University of Alberta

NMR investigations of porous materials using continuous-flow hyperpolarized Xe-129

by

Kristopher John Ooms

A thesis submitted to the Faculty of Graduate Studies and Research
in partial fulfillment of the requirements for the degree of

Doctor of Philosophy

Department of Chemistry

Edmonton, Alberta
Spring, 2007

Library and Archives Canada

Published Heritage Branch

395 Wellington Street
Ottawa ON K1A 0N4
Canada

Bibliothèque et Archives Canada

Direction du Patrimoine de l'édition

395, rue Wellington
Ottawa ON K1A 0N4
Canada

Your file Votre référence
ISBN: 978-0-494-29722-3
Our file Notre référence
ISBN: 978-0-494-29722-3

NOTICE:
The author has granted a non-exclusive license allowing Library and Archives Canada to reproduce, publish, archive, preserve, conserve, communicate to the public by telecommunication or on the Internet, loan, distribute and sell theses worldwide, for commercial or non-commercial purposes, in microform, paper, electronic and/or any other formats.

The author retains copyright ownership and moral rights in this thesis. Neither the thesis nor substantial extracts from it may be printed or otherwise reproduced without the author's permission.

AVIS:
L'auteur a accordé une licence non exclusive permettant à la Bibliothèque et Archives Canada de reproduire, publier, archiver, sauvegarder, conserver, transmettre au public par télécommunication ou par l'Internet, prêter, distribuer et vendre des thèses partout dans le monde, à des fins commerciales ou autres, sur support microforme, papier, électronique et/ou autres formats.

L'auteur conserve la propriété du droit d'auteur et des droits moraux qui protège cette thèse. Ni la thèse ni des extraits substantiels de celle-ci ne doivent être imprimés ou autrement reproduits sans son autorisation.

In compliance with the Canadian Privacy Act some supporting forms may have been removed from this thesis.

While these forms may be included in the document page count, their removal does not represent any loss of content from the thesis.

Conformément à la loi canadienne sur la protection de la vie privée, quelques formulaires secondaires ont été enlevés de cette thèse.

Bien que ces formulaires aient inclus dans la pagination, il n'y aura aucun contenu manquant.

Canada

For from Him and through Him
and to Him are all things.
To Him be the glory forever!

- Romans 10: 36

Abstract

The goal of this research was to use hyperpolarized ^{129}Xe NMR spectroscopy to answer questions about the nature of pore spaces in porous materials and the behaviour of Xe gas in the pores. To carry out this research an optical-pumping spin-exchange apparatus has been built in order to generate a continuous flow of hyperpolarized ^{129}Xe.

Hyperpolarized ^{129}Xe NMR is used to follow the formation of $AlPO_4$-18. The ^{129}Xe NMR indicates that the porous structure of the material evolves through an amorphous phase to the $AlPO_4$-5 structure, and finally is converted to $AlPO_4$-18. At an intermediate stage of the synthesis, the exchange of Xe between the bulk gas, $AlPO_4$-5 and $AlPO_4$-18 domains is studied by 2-D exchange spectroscopy.

The application of hyperpolarized ^{129}Xe NMR spectroscopy to investigate the pores of three shape-persistent organic macrocycles is described. Peaks with Xe chemical shifts between 160 and 200 ppm are assigned to Xe trapped in highly confined pores while NMR peaks with chemical shifts of 100 to 140 ppm are assigned to Xe present in channels. With the aid of molecular dynamics simulations and 2-D exchange spectroscopy, connections between the ^{129}Xe NMR spectra and the X-ray diffraction structure of one of the solvated macrocycles have been made.

The study was extended to metal-organic macrocycles where it was shown that all the materials studied are porous with respect to Xe and that multiple adsorption regions are present. The results indicate that for most of the materials, Xe can access both tightly confined spaces as well as the more open cavities formed when the co-crystallized solvent molecules are removed from the material.

Finally, hyperpolarized ^{129}Xe NMR spectroscopy was used to investigate the interaction of Xe with four zinc metal-organic frameworks, IRMOF-1, -7, -8, and -10, each of which consists of cubic cages of varying size. The ^{129}Xe NMR chemical shift is influenced by both the cage dimensions and Xe dynamics within the framework. Information about the adsorption energy and rates of diffusion is inferred from the behaviour of the Xe chemical shifts as a function of temperature and analysed for IRMOF-10.

Preface

Although researchers have been using nuclear magnetic resonance, NMR, to study solids since the mid-1940s, solid-state NMR is a technique that is under constant development. The steady advance of instrument technology, pulse sequence development, quantum chemical calculations, and theoretical understanding continues at a remarkable pace. During the past five years, I have been working to prepare myself for an active role in this field of scientific research. My goal has been to learn as much as possible about the field so that I can discover where I can best contribute to the future of solid-state NMR, SSNMR.

My research interests are unrestricted when it comes to using NMR to explore molecular properties. I have studied many inorganic and organometallic compounds in an attempt to understand how SSNMR can provide unique information about structure and bonding. I have investigated small organic molecules and complexes that are models for biological systems. This research has been published in numerous papers and has advanced my understanding of the place SSNMR holds in the wider discipline of chemistry.[1,2,3,4,5,6]

In the summer of 2002 I assisted a visiting scientist, Dr. Takahiro Ueda, in the construction of an optical pumping system that produced hyperpolarized ^{129}Xe gas for NMR studies. In the fall of 2002 Dr. Ueda returned to Japan and I was left to operate the system and develop an understanding of ^{129}Xe NMR spectroscopy in porous materials. Over the next year and a half I tested the optical pumping system, optimized its construction and operating parameters and explored possible systems for study. This was a completely new area of research in our laboratory and over time it became evident that there was much to learn. Whereas the other research I have performed involves precise measurements of interaction tensors and the extraction of NMR parameters that can be correlated to structure, the understanding of ^{129}Xe NMR in porous materials involves an understanding of how NMR is affected by gas dynamics and adsorption phenomena. These phenomena are not well understood at a molecular level so the interpretation of the NMR results has been complex.

The results presented in this thesis began in earnest in late 2003. Thanks to a key collaboration with the Tykwinski research group we have been able to apply ^{129}Xe NMR spectroscopy in a manner rarely used before, as a method of characterization used alongside the synthetic process of complex porous materials. This collaboration has proved extremely fruitful and represents one way the use of ^{129}Xe NMR spectroscopy for characterizing porous materials must go if it is to continue to be a relevant NMR technique.

---

[1] Ooms, K.J.; Wasylishen, R.E. "Solid-state Ru-99 NMR spectroscopy: a useful tool for characterizing prototypal diamagnetic Ru compounds". *J. Am. Chem. Soc.* **2004**, *126*, 10972-10980.

[2] Ooms, K.J.; Feindel, K.W.; Willans, M.J.; Wasylishen, R.E.; Hanna, J.V.; Pike, K.J.; Smith, M.E. "A Multiple-Magnetic Field ^{139}La NMR and Density Functional Theory Investigation of the Solid Lanthanum(III) Halides". *Solid State NMR*, **2005**, *28*, 125-134.

[3] Willans, M.J.; Feindel, K.W.; Ooms, K.J.; Wasylishen, R.E. "An Investigation of Lanthanum Coordination Compounds using Solid-State La-139 NMR and Relativistic Density Functional Theory", *Chem. Eur. J.* **2006**, *12*, 159-168.

[4] Ooms, K.J.; Wasylishen, R.E. "Solid-State NMR Spectroscopy of Nitrito- and Nitropentamminecobalt(III) Chloride Isomers", *Can. J. Chem.* **2006**, *84*, 300-308.

[5] Ooms, K.J.; Feindel, K.W.; Terskikh, V. V.; Wasylishen, R.E. "Ultrahigh-field NMR spectroscopy of quadrupolar transition metals: ^{55}Mn NMR of several solid manganese carbonyls", *Inorg. Chem.* **2006**, *45*, 8492-8499. (Cover article)

[6] Feindel, K. W.; Ooms, K. J.; Wasylishhen, R.E."Solid-state ^{55}Mn NMR spectroscopy and DFT investigation of several manganese pentacarbonyls". *Phys. Chem. Chem. Phys. To be submitted.*

Acknowledgments

There are two people whom I want to thank for their help during my Ph.D. research. The most influential person in my scientific career has undoubtedly been Rod Wasylishen. Rod has been an incredible supervisor; his excitement for NMR is truly infective. His ability to mentor me through the process of becoming an honest, rigorous researcher amazes me. I thank him for his patience with my failings and for helping me develop my skills. I also thank Rod for honestly caring about not only my science but also about me as person and for listening to my problems and encouraging me through the difficult times.

The second most important person during this time has been Kirk Feindel. Some of my best learning has come during my collaborations with Kirk. His different perspective and skills has been invaluable. The ability to bounce ideas around, to discuss our science and to evaluate each other's work has taught me a great deal about my research and has enabled me to learn the basics of his research. In some ways it feels like I have learned enough from him to write another thesis. Kirk's greatest contribution to my career though has been his friendship. The ability to work and learn with my best-friend has been invaluable and is a big reason why I was able to finish this thesis.

I would like to thank Rik Tykwinski and Katie Campbell for the opportunity to study the compounds they have been creating. Katie was a delight to work with, her keen interest in understanding NMR and the high quality of her research made it easy to discuss results and develop the projects with her.

I have had the opportunity to work at the Pacific Northwest National Laboratories and am thankful to David Hoyte, Nancy Isern, Joseph Ford, Andrew Lipton, and Paul Ellis for all their help and support. I also thank Drs.Victor Terskikh and Shane Pawsey of the National Ultrahigh field NMR centre for solids in Ottawa for their assistance.

I thank the other members of the solid-state NMR group at the U of A, both past and present for helpful discussions and coming to my group meetings and practice talks and reading my numerous drafts. Thanks go to David Bryce for being my first mentor in grad school and to Guy Bernard for always being a person who I could talk to.

Financial support has been graciously provided by many sources including the University of Alberta, Alberta Ingenuity, and NSERC.

I must thank my parents and family who encouraged me no matter what I did. From when I was a kid who could not sit still or get a mark better than a C, to the point where they now have no idea what I am doing, they have always supported me and loved me.

This work would not have been possible without my wife Martine. She has stood by me through the hard times and helped me celebrate the good times. She has given me the motivation to get up in the morning and a desire to succeed. I can never repay her for everything she has done for me.

Finally I am thankful for the gifts and skills I have been given and the ability to use them. I thank God for everything. Without Him I would never have been able to accomplish any of this and there would have been no reason to even bother. This work and my life I dedicate to His glory.

Table of contents

Abstract

Preface

Acknowledgments

Table of contents

List of tables

List of figures

List of symbols and abbreviations

Chapter 1: Introduction and objectives

1.1 Introduction 1

1.2 Objectives.....4

Chapter 2: Background

2.1 HP ^{129}Xe NMR spectroscopy: Theory.....9

2.1.1 The Zeeman interaction.....9

2.1.2 Producing hyperpolarized Xe: optical-pumping spin-exchange.....10

2.1.3 Magnetic shielding 15

2.1.4 The origin of magnetic shielding.....17

2.1.5 The chemical shift..... 18

2.2 The properties of Xe.....20

2.3 The NMR of ^{129}Xe in spaces on the order of the Xe diameter.....22

2.3.1 Clathrate compounds 22

2.3.2 Polymers 26

2.4 Models for Xe adsorption and the interpretation of Xe chemical shifts in porous materials.....28

2.4.1 Fast-exchange two-site models.....30

2.4.2 Surface curvature model.....32

2.4.3 Models based on Lennard-Jones potentials.....33

2.4.4 Ab initio calculations of Xe chemical shifts in porous materials.....36

2.5 Experimental examples of ^{129}Xe NMR of microporous materials.....39

2.5.1 Zeolites: cage structures.....39

2.5.2 Zeolites: channel structures.....43
2.5.3 Microporous materials with "organic" walls.....45
2.6 Examples of ^{129}Xe NMR in mesoporous materials.....48
2.6.1 MCM-41 and its analogues.....48
2.6.2 Amorphous porous silica materials.....50
2.7 Xe-129 NMR of multi-domain porous materials.....52
Chapter 3: General experimental procedures and considerations
3.1 Experimental equipment and procedures.....62
3.1.1 Optical pumping spin exchange apparatus.....62
3.1.2 Operating procedure.....66
3.1.3 NMR spectroscopy.....68
3.1.4 Computational methods.....70
3.2 Important considerations in interpreting continuous-flow HP ^{129}Xe NMR spectra ...71
3.2.1 Previous structural studies.....71
3.2.2 Alternative adsorption phenomena.....72
3.2.3 Crystallite size.....73
3.2.4 Sample purity.....73
3.2.5 Equilibrium vs. non-equilibrium adsorption dynamics.....76
Chapter 4: ^{129}Xe NMR spectroscopy used to monitor the formation of $AlPO_4$-18
4.1 Introduction.....80
4.2 Sample preparation.....81
4.3 1-D ^{129}Xe NMR spectra.....81
4.4 2-D ^{129}Xe EXSY spectra.....85
4.5 Conclusions.....87
Chapter 5: ^{129}Xe NMR spectroscopy of potentially porous organic macrocycles
5.1 Introduction.....90
5.2 Preparation of macrocycles.....92
5.3 ^{129}Xe NMR spectroscopy.....94
5.3.1 The ^{129}Xe NMR peak at $\delta \approx 190$ ppm.....95
5.3.2 The ^{129}Xe NMR peak with δ between 125 and 138 ppm.....98

*5.3.3 Compounds **2** and **3***.....100
5.4 Magnetic shielding calculations.....104
5.5 Conclusions.....106
Chapter 6: ^{129}Xe NMR spectroscopy of potentially porous metal-organic macrocycles
6.1 Introduction.....109
6.2 Sample preparation 112
6.3 ^{129}Xe NMR spectroscopy.....114
*6.3.1 Mono-platinate macrocycle **7***.....114
*6.3.2 Chiral mono-platinate macrocycle **8***.....118
*6.3.3 Di-platinate macrocycle **9*** 122
*6.3.4 Di-platinate macrocycle **10***.....125
*6.3.5 Super-molecular structure **11***.....127
6.4 Conclusions.....131
Chapter 7: ^{129}Xe NMR spectroscopy of IRMOFs
7.1 Introduction.....133
7.2 Sample preparation and characterization.....136
7.3 Structures of IRMOFs.....137
7.4 ^{129}Xe NMR spectroscopy.....139
7.4.1 IRMOF-1.....139
7.4.2 IRMOF-7.....143
7.4.3 IRMOF-8.....146
7.4.4 IRMOF-10.....149
7.4.5 Signal recovery experiment.....152
7.5 Conclusions.....154
Chapter 8: Concluding remarks.....159
Chapter 9: Future and ongoing research
9.1 Continued studies of MOF's.....161
9.2 HP ^{129}Xe NMR of titanosilicates 163
9.3 HP ^{129}Xe NMR studies of clays and minerals.....163

9.4 Development of a variable pressure NMR probe for thermally polarized ^{129}Xe NMR studies.....165

Appendix A: Optical-pumping spin-exchange apparatus: safety considerations ...167

Appendix B: Maple script for calculating two-site exchange spectra.....171

Appendix C: Pressure cell for elevated pressure gas NMR.....172

List of tables

Table 1. Relevant structural data for IRMOFs studied 136

List of figures

Figure 1.1	Examples of pore systems.	1
Figure 2.1	Zeeman energy level diagram for a spin ½ nucleus with a negative magnetogyric ratio.	10
Figure 2.2	A portion of the electronic energy level diagram for atomic ^{85}Rb.	11
Figure 2.3	A schematic of the optical pumping process.	12
Figure 2.4	Rubidium valence electron wave function in the vicinity of a Xe atom.	14
Figure 2.5	Diagrams representing the two mechanisms by which spin exchange can occur.	15
Figure 2.6	The polar angles that define the relative orientation of the magnetic shielding tensor with respect to B_0.	16
Figure 2.7	Simulated NMR spectra showing three possible chemical shift powder patterns.	19
Figure 2.8	Plots of the gas density and temperature dependencies of the Xe shielding.	22
Figure 2.9	Characteristic ^{129}Xe NMR spectra of structure I, II, and H hydrates.	24
Figure 2.10	^{129}Xe CP/MAS NMR spectra of Dianin's compound.	25

Figure 2.11	Schematic of Xe dissolved in a polymer.	26
Figure 2.12	^{129}Xe NMR spectra of HP Xe in rubbery polymer blends.	27
Figure 2.13	The two unique components of the shielding tensor that result from Xe approaching another atom or surface.	29
Figure 2.14	NMR spectra of a nuclei exchanging between two equally populated sites.	30
Figure 2.15	Schematic of the fast-exchange two-site model.	31
Figure 2.16	Schematic of the surface curvature model.	33
Figure 2.17	Calculated Lennard-Jones potential curves for a Xe atom in a spherical cage as a function of cage radius.	34
Figure 2.18	^{129}Xe NMR spectra of four samples of Xe in Zeolite NaA.	37
Figure 2.19	The structure of Zeolite A.	37
Figure 2.20	Xe NMR line shapes from GCMC simulations as a function of occupancy of Xe in ALPO-11.	39
Figure 2.21	^{129}Xe 1-D and 2D EXSY NMR spectrum of Xe adsorbed in zeolite NaA.	42
Figure 2.22	Xe in an elliptical 1-D channel such as ALPO-11.	44
Figure 2.23	Xe in a 1-D channel such as ALPO-5.	45

Figure 2.24	Continuous-flow hyperpolarized ^{129}Xe NMR spectra of Xe/He mixtures flowing in the 1-D channels of TPP.	46
Figure 2.25	Continuous-flow hyperpolarized ^{129}Xe NMR spectra of Xe in $Co(en)_3Cl_3$.	47
Figure 2.26	The experimental thermally polarized Xe NMR spectra of Xe in dipeptide nanochannels.	48
Figure 2.27	HP ^{129}Xe NMR spectrum of Xe in MCM-41.	49
Figure 2.28	^{129}Xe NMR chemical shift vs. Mean pore diameter for porous silica-based materials.	51
Figure 2.29	Variable temperature HP ^{129}Xe NMR spectra of Xe adsorbed in montmorillonite pillared with pyridinium ions.	53
Figure 2.30	Continuous flow HP ^{129}Xe NMR spectra of Xe in an RF aerogel.	54
Figure 3.1	Schematic diagram of the optical-pumping spin-exchange apparatus.	62
Figure 3.2	Diagram of the Rb well.	63
Figure 3.3	Diagram of the optical cell.	65
Figure 3.4	Vector diagram of the magnetization of a single spin during the EXSY pulse sequence.	69

Figure 3.5	^{129}Xe NMR spectra of Xe in different samples of IRMOF-1 acquired at multiple temperatures.	74
Figure 4.1	The different phases formed during the synthesis of $AlPO_4$-18.	81
Figure 4.2	^{129}Xe NMR spectra of HP Xe in calcined aluminophosphate samples after various heating times.	82
Figure 4.3	^{129}Xe EXSY spectra of Xe in the 60hr sample.	86
Figure 5.1	The structure of the three organic macrocycles studied.	90
Figure 5.2	The crystal structure of **1** determined by X-ray diffraction.	91
Figure 5.3	Scheme for the synthesis of **2**,	93
Figure 5.4	VT HP ^{129}Xe NMR spectra of **1**.	94
Figure 5.5	Xe one-body distribution plot of Xe in **1**.	97
Figure 5.6	VT HP ^{129}Xe NMR spectra of **2**.	100
Figure 5.7	VT HP ^{129}Xe NMR spectra of **3**.	101
Figure 5.8	The 2-D EXSY HP ^{129}Xe NMR spectra of **3**.	103
Figure 5.9	Plots of the isotropic Xe chemical shift as a function of distance from the nitrogen and C4 of pyridine and a carbon of benzene.	105
Figure 6.1	Molecular structure diagrams of two molecules which adsorb	109

molecules but do not have discernible channel structures.

Figure 6.2 The structures of the metal-organic macrocycles studied. 111

Figure 6.3 The scheme for the synthesis of **7**. 112

Figure 6.4 Crystal packing diagram of **7** and contour map of Xe in **7**. 114

Figure 6.5 VT ^{129}Xe NMR spectra of HP Xe in solid **7**. 115

Figure 6.6 The structure and crystal packing of **8** in the solid state. 119

Figure 6.7 VT ^{129}Xe NMR spectra of HP Xe in solid **8**. 120

Figure 6.8 Crystal packing diagram of **9**. 122

Figure 6.9 ^{129}Xe NMR spectra of HP Xe in solid **9**. 123

Figure 6.10 VT ^{129}Xe NMR spectra of HP Xe in solid **10**. 125

Figure 6.11 Crystal packing diagram of **10**. 126

Figure 6.12 Crystal packing diagram of **11** and contour map of Xe in **11**. 128

Figure 6.13 ^{129}Xe NMR spectra of HP Xe in solid **11**. 129

Figure 7.1 The structure of the four IRMOFs studied. 134

Figure 7.2 The zinc subunit and a corner of an α-cage of IRMOF-1. 134

Figure 7.3 The VT HP ^{129}Xe NMR spectra of IRMOF-1. 140

Figure 7.4	The VT HP ^{129}Xe NMR spectra IRMOF-7.	144
Figure 7.5	The VT HP ^{129}Xe NMR spectra IRMOF-8.	147
Figure 7.6	The HP ^{129}Xe EXSY NMR spectra IRMOF-8.	148
Figure 7.7	The VT HP ^{129}Xe NMR spectra IRMOF-10.	150
Figure 9.1	The VT HP ^{129}Xe NMR spectra IRMOF-2.	162
Figure 9.2	The VT HP ^{129}Xe NMR spectra of sepiolite.	164

List of abbreviations and symbols

A	A constant in the surface curvature model
$AlPO_4$	Aluminum phosphate
$\alpha(r)$	The coupling coefficient in the Fermi contact coupling term
α, ε	Constants in the Lennard-Jones potential energy equation that are characteristic of the Xe-surface atom potential energy interaction
B_0	The applied magnetic field
b	Ratio of adsorption over desorption rate constants, k_a/k_b
BDC	1,4-Benzenedicarboxylic acid or 1,4-Benzenedicarboxylate
BPDC	Biphenyldicarboxylic acid or Biphenyldicarboxylate
C	An intrinsic molecular property of Xe which is related to its polarizabillity
CS	Chemical shift
CSA	Chemical shift anisotropy
d	The distance between a Xe and a curved pore wall
D	Mean pore diameter
DEF	Diethylformamide
DFT	Density functional theory
δ, δ_{iso}	Isotropic chemical shift
δ_{11}, δ_{22}, δ_{33}	The principal components of the chemical shift tensor
δ_0	The chemical shift of an isolated Xe atom, also the chemical shift of Xe extrapolated to zero pressure
δ_A	The chemical shift of adsorbed Xe
δ_{av}	The average chemical shift resulting from exchange averaging
δ_s	The characteristic shift of an isolated Xe interacting with the framework
δ_t	Chemical shift component perpendicular to the direction of approach of Xe the surface of an elliptical channel and perpendicular to the channel axis

δ_V	The chemical shift of Xe in the free gas
δ_{Xe}	The chemical shift caused by Xe-Xe interactions
$\delta_{\parallel}$, $\sigma_{\parallel}$	Chemical shift or magnetic shielding tensor principal component parallel to the direction of approach of Xe and another atom, surface or the channel axis
$\delta_{\perp}$, $\sigma_{\perp}$	Chemical shift or magnetic shielding tensor principal component perpendicular to the direction of approach of Xe and another atom, surface or the channel axis
δ_{ij}	Kronecker delta
e	Charge of an electron
EXSY	Exchange spectroscopy
Et	Ethyl group
ΔE	Change or difference in energy
GCMC	Grand Canonical Monte Carlo
η	Pore geometry factor
γ_I	The magnetogyric ratio of nucleus I
h	Planck constant
$\hbar$	Planck constant divided by 2π
ΔH_{ads}	Heat of adsorption
$\boldsymbol{H}_Z$	The Zeeman Hamiltonian
$\boldsymbol{H}_{CS}$	The chemical shift Hamiltonian
$\boldsymbol{H}_{FC}$	The Fermi contact Hamiltonian
HP	Hyperpolarized
$\boldsymbol{I}$	Nuclear spin operator
I	Nuclear spin quantum number
I_Z	Azimuthal spin angular momentum operator
IRMOF	Iso-reticular metal-organic framework
I.D.	Inside diameter
K, K_0	Henry's constant and the pre-exponential factor of the Henry's law equation

k	Boltzmann constant
k_a	Adsorption rate constant
k_b	Desorption rate constant
k_{rep}	The rate constant used to describe the rate at which HP Xe is replenished within a porous material
κ	The skew of the magnetic shielding or chemical shift tensor
L, J, F	The quantum numbers used to describe the electronic energy levels of the Rb atom.
$\overline{\ell}$	Mean free path length
$\mathbf{L}$	Angular momentum operator
m	The mass of an electron
Δm	Angular momentum number of laser light which will induce a change in angular momentum when adsorbed by Rb electrons.
m_I, m_S	Magnetic quantum numbers
MR	Magnetic resonance
MOF	Metal-organic framework
N.A.	Natural abundance
n_i	Population in state i
NDC	Naphthalenedicarboxylic acid or Naphthalenedicarboxylate
NMR	Nuclear magnetic resonance
ν_L	The Larmor frequency
ν_{ref}	The frequency of the reference compound
ν_s	The frequency of the sample
O.D.	Outside diameter
Ω	The span of the magnetic shielding or chemical shift tensor
ω_1, ω_2	The frequencies recorded in the 2-D EXSY experiment obtained during the t_1 and t_2 evolution times
PAS	Principal axis system
PC	Personal computer
Ph	Phenyl group

r	Distance
r_k	Positional vector of electron k to the chosen origin
r_{ki}, r_{kj}	The indicated components of the positional vector, i,j = x, y, z
r_{min}	The distance at which the potential energy between two atoms is at a minimum
r_0	The distance at which the potential energy between two atoms is zero
R	The radius of a circular or spherical pore
ρ	Density
$\boldsymbol{S}$	The electron spin operator
S	The electron spin quantum number
S_a	Surface area
$^2S_{1/2}$, $^2P_{1/2}$, $^2P_{3/2}$	Important term symbols for the Rb electron states
s	The curvature factor of a curved pore wall
SSNMR	Solid-state nuclear magnetic resonance
σ	The magnetic shielding tensor
σ_1, σ_2, σ_3, etc.	The coefficients of the virial expansion of the Xe magnetic shielding as a function of Xe density
σ_{11}, σ_{22}, σ_{33}	The principal components of the magnetic shielding tensor
σ^d	The diamagnetic term of magnetic shielding
σ^p	The paramagnetic term of magnetic shielding
σ_{PAS}	The magnetic shielding tensor in its principal axis system
σ_{ref}	The magnetic shielding of the reference compound
σ_s	The magnetic shielding of the sample
T	Temperature
T_1	Spin lattice relaxation time
t_1	The first evolution time in the EXSY experiment
t_2	The second evolution time in the EXSY experiment (acquisition time)
t_{rep}	The time constant used to describe the time it takes to replenish

	the HP Xe within a porous material
τ_0	Pre-exponential factor in the residence time equation
TEAH	Tetraethyl ammonium hydroxide
τ_{mix}	Mixing time
τ_{surf}	Residence time on the surface
TPP	Tris(o-phenylenedioxy)cyclophosphazene
θ, ϕ	The angles that relate the orientation direction of B_0 with respect to the magnetic shielding tensor
W	Interaction energy between Xe and a curved pore wall
U, U(x)	Adsorption potential energy
UV/Vis	Ultraviolet/visible
μ_0	Permeability of vacuum
VT	Variable temperature
x, y, z	Cartesian coordinates
$\langle 0\|,\|n\rangle$	Ground state and excited state wave functions, respectively

Chapter 1: Introduction and objectives

1.1 Introduction

A porous material is any material that has cavities, channels, or interstices which are deeper than they are wide.[1] There are two classes of porous materials, amorphous and crystalline. Amorphous frameworks exhibit aperiodic arrangement of the atoms and include materials such as charcoals, silicas (such as Xerogels and Aerogels) and M41S materials. Crystalline frameworks have a periodic arrangement of atoms in the framework[1] and include zeolites, aluminum phosphates, and many of the organic-based porous frameworks. The size of the pores is generally divided into three categories: micropores have pore diameters less than 20 Å, mesopores have average pore diameters of 20 to 500 Å, and macropores are pore systems that have free space diameters greater than 500 Å.[1] The geometry of the pores can also vary widely and be either ordered or disordered; some examples of common ordered pore structures are shown in Figure 1.1.

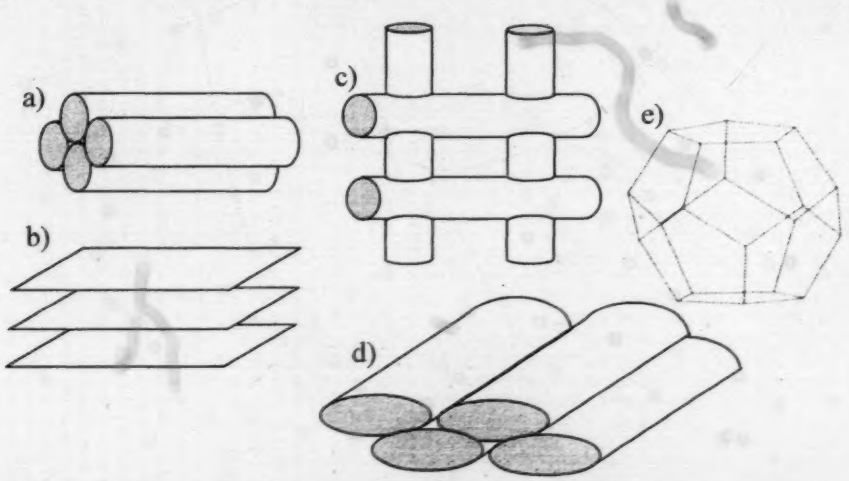

Figure 1.1: Examples of pore systems: a) circular 1-D channels, b) inter-lamellar space, c) 2-D channels, d) elliptical 1-D channels, and e) clathrate cages (while not technically porous, clathrates can include guest molecule).

The ability to systematically synthesize inorganic porous materials began when Barrer first synthesized mordenite in 1948.[2] The techniques used in this initial discovery were widely applied and by the late 1970s many inorganic porous materials had been synthesized in laboratories around the world. Recently there has been interest in the

design and synthesis of materials that have specific chemical functionality in the pores or have specific pore diameters.[3,4] These materials are finding applications as catalysts and in the areas of molecular sensing, separation, and gas storage.[3,4,5] The preparation of porous materials that are assembled by the aggregation of organic[6,7] or metal-organic[8,9] building blocks has become a particularly intriguing area of research due to the possibility of tuning both the dimensions and the chemical functionality of the pores.

The most widely used method for studying porosity is gas/liquid adsorption.[10] While adsorption measurements can provide information about pore size distributions, total surface area and void space volume, the technique has a number of drawbacks. First the analysis of adsorption isotherms relies on assumptions about pore geometry and is often based on oversimplifications of the adsorption mechanisms.[1] Adsorption methods also provide only bulk measurements. While in some instances large differences in pore size can be detected, generally only a distribution of pore sizes can be discerned from the analysis. Typical isotherm analysis is also incompatible with the heterogeneity in adsorption energies exhibited by most solids.[10] Information about specific adsorption regions, gas dynamics within the pores, and interactions between the frameworks and the guest molecules can not be obtained. It has become clear that relying on adsorption techniques to characterize the porosity of new, functionalized materials is insufficient. More detailed information about the pore networks is required to understand and tailor new materials for specific applications.

In the late 1970's Jacques Fraissard explored the possibilities of using nuclear magnetic resonance, NMR, spectroscopy to explore zeolites using an NMR-active gas:[11,12]

> "The central idea behind this research was to find a non-reactive molecule, particularly sensitive to its environment and to collisions with other chemical species, which could serve as a probe for determining in a new way certain properties of solid catalysts, and, especially, zeolites."[12]

After exploring numerous possible gases, Ito and Fraissard settled on using $^{129}Xe(0)$ which has a van der Waals diameter of 2.16 Å[13] and a chemical shift range of over 300 ppm,[14] making it an ideal non-destructive probe of pore spaces. Xe-129 has a nuclear spin $I = ½$, an NMR resonance frequency close to that of ^{13}C and a natural abundance of 26.44%.[15] Ito and Fraissard's initial studies were performed by sealing samples of

zeolites with varying pressures of Xe gas and then recording the chemical shifts of ^{129}Xe.[11,12] Plots of chemical shift as a function of the average xenon loading, determined from adsorption methods, showed that the Xe chemical shift was highly sensitive to the local environment of the Xe atoms. Soon after this initial publication,[12] Ripmeester showed that ^{129}Xe could be used to study other inclusion compounds and that experiments associated with solid-state NMR, such as the analysis of powder lineshapes and magic angle spinning of the sample, could be applied to ^{129}Xe gas atoms confined in solid materials.[16,17] Since these initial demonstrations, hundreds of studies have been performed using the chemical shift of Xe to explore a wide range of porous materials. A discussion of the models used to interpret ^{129}Xe chemical shifts and select experimental results obtained over the past thirty years are presented in Chapter 2. The most general conclusion that can be made from these studies is that the more confined the void space, the greater the Xe chemical shift (i.e., the less shielded the Xe nucleus).

While the process of sealing porous samples under a known pressure of Xe has continued to be an important method for performing ^{129}Xe NMR experiments, the application of optical-pumping spin-exchange to produce hyperpolarized, HP, ^{129}Xe gas for NMR detection revolutionized the field; the process is briefly described in Chapter 2.[18,19] In 1991 Pines and coworkers showed that HP ^{129}Xe gas could be used to explore porous materials at very low Xe partial pressures.[20] In subsequent years, researchers have optimized the methods for preparing and transporting HP ^{129}Xe. Both batch[20] and continuous flow[21] techniques have been used for delivering the HP gas to the sample and have resulted in signal enhancements ranging from 10^3 to 10^5 times that observed in conventional ^{129}Xe NMR experiments.[22] This enhanced NMR signal has allowed researchers to perform a wider range of NMR experiments[23] and to examine smaller quantities of sample.[24,25] Researchers have investigated the interaction of Xe with solid surfaces,[20] the NMR of ^{129}Xe bound to low concentration molecules in solution, and the use of ^{129}Xe NMR for materials[26,27] and medical[28,29] magnetic resonance imaging.

As a result of the enhanced signal-to-noise available from the optical-pumping spin-exchange process, ^{129}Xe NMR is finding an increasingly important role in the characterization of porous materials. In particular, as researchers move away from relatively simple inorganic frameworks to functionalized inorganic, organometallic, and

organic materials, ^{129}Xe NMR spectroscopy will no doubt become an increasingly important characterization technique.

1.2 Objectives

The goal of this thesis is to use continuous-flow HP ^{129}Xe NMR spectroscopy to obtain information about the pores in solid materials. Specifically, ^{129}Xe NMR spectroscopy allows us to address four general questions:

1) Is the material porous?

While this question may appear trivial, its importance cannot be overstated. With the rapid development of new, potentially porous materials, the success of a particular line of research can often be determined by answering this one question. For example, if a synthetic chemist cannot show that the structure of a material is porous or at least has the potential for being porous, a new compound might be abandoned in the search for other novel porous materials.

2) What is the general size of the pores?

An answer to this question provides researchers with a means of classifying a new material and a guide for what types of applications such a material may have. The size of the pores dictates what molecules can access the free space within the solid and interact with the inner surfaces. The answer to this basic question can determine what kinds of catalytic applications a material could be used for, what types of molecular separations might be possible, or what gases could be stored within the solid.

3) What is the geometry and functionality of the pore space?

After general conclusions have been made about the existence of the pores within a solid, researchers desire to understand details about the pores. Determining such properties as pore dimension, geometry, and connectivity can lead to understanding how a particular material can function in various applications (see Figure 1.1 for a few examples of pore geometry). For example, a material with two unconnected channel systems of different sizes will function differently as a gas separation material than a material with two connected channel systems. Additionally, information about the chemical functionality of different regions of the pore space can be important for tailoring materials for specific applications.

4) How does the Xe gas behave within the framework?

This question is closely related to question *c* but focuses on the guest, i.e., Xe, rather than the framework. Understanding gas dynamics and mobility within different frameworks can be extremely important for understanding how a porous material might be applied for scientific or industrial use. Xe can act as a model for other small molecules such as CH_4, CO_2 and H_2.

We have built an optical-pumping spin-exchange apparatus to produce HP ^{129}Xe, described in Chapter 3, and then applied HP ^{129}Xe NMR spectroscopy to four types of porous materials for which answers to some or all of the above questions can be obtained. The first material studied, see Chapter 4, is an inorganic aluminum phosphate material, AlPO-18. The formation of AlPO-18 was shown to proceed through a number of intermediate structures.[30] It was unclear whether these intermediates were porous themselves or whether just the final product contained accessible pores. Xe-129 NMR spectroscopy was used to study the porosity throughout the synthesis of AlPO-18.

The synthesis of organic and metal-organic porous materials is a relatively new and growing field of synthetic chemistry. Recent efforts to use organic and metal-organic macrocycles to form ordered porous materials have resulted in a number of potentially porous solids.[31,32,33,34,35] The challenges that face researchers in this field are twofold. Initial synthesis of new solids is time consuming and often only small amounts of material are prepared, typically tens to hundreds of milligrams. This quantity of material makes conventional porosity techniques such as adsorption methods and thermally polarized ^{129}Xe NMR spectroscopy extremely difficult if not impossible to use. Characterization of the materials relies almost exclusively on single-crystal X-ray diffraction. Single crystals of these materials are often difficult to grow. Even when single crystals are obtained, the solids often include guest molecules in the proposed pores, typically from the solvent used for crystallization. Obtaining structures of the material without the guests is difficult and therefore the question must be asked, is the material truly porous? This is an ideal problem for HP ^{129}Xe NMR spectroscopy. Chapter 5 describes the study of three similar organic macrocycles. The results obtained from HP ^{129}Xe NMR spectroscopy clearly show the presence of pores and channels and

analysis of the spectra allows a model for Xe adsorption to be proposed. In Chapter 6 a variety of metal-organic macrocycles are studied. Again all the samples are shown to be porous to Xe gas, even though some of the samples do not exhibit clear channel structures. The ^{129}Xe NMR spectra show Xe adsorbing in multiple environments in most of the samples, many of which can be correlated to void spaces created when the co-crystallized solvent molecules are removed from the solid.

Chapter 7 describes the HP ^{129}Xe NMR investigation of a series of materials formed *via* coordination of dicarboxylic acid molecules to Zn_4O^{6+} subunits.[36] While the porosity of these materials has been widely investigated, further experimental characterization of the gas adsorption in these frameworks is important. Also, methods for determining framework stability and the presence of structural defects are critical for properly applying these new materials. The ability of ^{129}Xe NMR spectroscopy to identify different adsorption sites using the Xe chemical shift makes gaining information about the adsorption process in these materials feasible.

At the end of the thesis conclusions will be made and future research will be laid out in Chapters 9 and 10, respectively. The thesis clearly demonstrates how HP ^{129}Xe NMR spectroscopy can be used as a technique to characterize new porous materials and how it is feasible to use ^{129}Xe NMR in a way that can provide vital information to researchers engaged in the development of new porous materials.

---

[1] Rouquerol, J.; Avnir, D.; Fairbridge, C. W.; Everett, D. H.; Haynes, J. H.; Pernicone, N.; Ramsay, J. D. F.; Sing, K. S. W.; Unger, K. K. *Pure Appl. Chem.* **1994**, *66*, 1739-1758.

[2] Barrer, R. M. *J. Chem. Soc.* **1948**, 2158-2163.

[3] Davis, M. E. In *Sci. Tech. Catal. 1998*, **1999**, *121*, 23-32.

[4] Stein, A. *Adv. Mater.* **2003**, *15*, 763-775.

[5] Bong, D. T.; Clark, T. D.; Granja J. R.; Ghadiri, M. R. *Angew. Chem. Int. Ed.* **2001**, *40*, 988-1011.

[6] Höger, S. *J. Polym. Sci. Part A: Poly. Chem.* **1999**, *37*, 2685-2698.

[7] Kitagawa S.; Uemura, K. *Chem. Soc. Rev.* **2005**, *34*, 109-119.

[8] Eddaoudi, M.; Li H.; Yaghi, O. M. *J. Am. Chem. Soc.* **2000**, *122*, 1391-1397.

[9] Rosi, N. L.; Eckert, J.; Eddaoudi, M.; Vodak, D. T.; Kim, J.; O'Keeffe M.; Yaghi, O. M. *Science* **2003**, *300*, 1127-1129.

[10] Rouquerol, F.; Rouquerol, J.; Sing, K. In *Adsorption by Powders & Porous Solids.* Academic Press: London, **1999**.

[11] Ito, T.; Fraissard, J. In *Proceedings of the 5th International Zeolite Conf., Naple.*, Reese, L. V. C., Ed.; Heyden; London. 1980, p. 510.

[12] Ito, T.; Fraissard, J. *J. Chem. Phys.* **1982**, *76*, 5225-5229.

[13] Sears D. R.; Klug, H. P. *J. Chem. Phys.* **1962**, *37*, 3002-3006.

[14] Ratcliffe, C. I.; *Annu. Rep. NMR Spectrosc.* **1998**, *36*, 123-221.

[15] Harris, R. K.; Becker, E. D.; De Menezes, S. M. C.; Goodfellow, R.; Granger, P. *Pure Appl. Chem.* **2001**, *73*, 1795-1818.

[16] Ripmeester, J. A.; Davidson, D. W. *Bull. Magn. Reson.* **1981**, *2*, 139

[17] Ripmeester, J. A. *J. Am. Chem. Soc.* **1982**, *104*, 289-290.

[18] Appelt, S.; Baranga, A. B.; Erickson, C. J.; Romalis, M. V.; Young, A. R.; Happer, W. *Phys. Rev. A* **1998**, *58*, 1412-1439.

[19] Walker, T. G.; Happer, W. *Rev. Mod. Phys.* **1997**, *69*, 629-642.

[20] Raftery, D.; Long, H.; Meersmann, T.; Grandinetti, P. J.; Pines, A. *Phys. Rev. Lett.* **1991**, *66*. 584-587.

[21] Driehuys, B.; Cates, G. D.; Miron, E.; Sauer, K.; Walter, D. K.; Happer, W. *Appl. Phys. Lett.* **1996**, *69*, 1668-1670.

[22] Zook, A. L.; Adhyaru, B. B.; Bowers, C. R. *J. Magn. Reson.* **2002**, *159*, 175-182.

[23] Navon, G. Song, Y.-Q.; Rooms, T.; Appelt, S.; Taylor, R. E.; Pines, A. *Science* **1996**, *271*, 1848-1851.

[24] Ooms, K. J.; Campbell, K.; Tykwinski, R. R.; Wasylishen, R. E. *J. Mater. Chem.* **2005**, *15*, 4318-4327.

[25] Nossov, A.; Haddad, E.; Guenneau, F.; Mignon, C.; Gédéon, A.; Grosso, D.; Badonneau, F.; Bonhomme, C.; Sanchez, C. *Chem. Commun.* **2002**, 2476-2477.

[26] Pavlovskaya, G. E.; Meersmann, T. In *NMR Imaging in Chemical Engineering.* Stapf, S., Han, S., Eds.; Wiley-VCH; Weinheimm 2006, pp 551.

[27] Song, Y.-Q.; Gaede, H. C.; Pietraß, T.; Barrall, G. A.; Chingas, G. C.; Ayers, M. R.; Pines, A. *J. Magn. Reson. A* **1995**, *115*, 127-130.

[28] Wagshul, M. E.; Button, T. M.; Li, H. F.; Liang, Z.; Springer, C. S.; Zhong, K.; Wishnia, A. *Magn. Reson. Med.* **1996**, *36*, 183-191.

[29] Albert, M. S.; Cates, G. D.; Driehuys, B.; Happer, W.; Saam, B.; Springer, C. S.; Wishnia, A. *Nature* **1994**, *370*, 199-201.

[30] Huang, Y.; Demko, B. A.; Kirby, C. W. *Chem. Mater.* **2003**, *15*, 2437-2444.

[31] Campbell, K.; McDonald R.; Tykwinski R. R. *J. Org. Chem.* **2002**, *67*, 1133-1140.

[32] Campbell, K.; McDonald R.; Ferguson, M. J.; Tykwinski R. R. *Organometallics* **2003**, *22*, 1353-1355.

[33] Campbell, K.; McDonald R.; Ferguson, M. J.; Tykwinski R. R. *J. Organomet. Chem.* **2003**, *683*, 379-387.

[34] Campbell, K.; Tiemstra, N. M.; Prepas-Strobeck, N. S.; McDonald, R.; Ferguson, M. J.; Tykwinski, R. R.; *Syn. Lett.* **2004**, 182-186.

[35] Campbell, K.; Kuehl, C. J.; Ferguson, M. J.; Stang, P. J.; Tykwinski, R. R. *J. Am. Chem. Soc.* **2002**, *124*, 7266-7267.

[36] Eddaoudi, M.; Kim, J.; Rosi, N.; Vodak, D.; Wachter, J.; O'Keeffe, M.; Yaghi, O. M. *Science* **2002**, *295*, 469-472.

Chapter 2: Background

The interpretation of the ^{129}Xe NMR spectra of Xe adsorbing to porous materials is complicated by many physical phenomena that affect the observed chemical shifts. The understanding of ^{129}Xe NMR spectra, perhaps more so than any other type of solid-state NMR spectra, has relied on incremental steps in our understanding of Xe adsorption and the origin of chemical shifts in atomic gases. To properly understand how the Xe chemical shift relates to the structure of porous materials a thorough knowledge of previous experimental and theoretical studies is required. The following background is intended to highlight some of the major advances made in the interpretation of ^{129}Xe NMR spectra of Xe in porous materials from both a theoretical and experimental point of view. There are many reviews of ^{129}Xe NMR spectroscopy which the reader is referred to for a more comprehensive summary of the field or a more thorough analysis of a specific topic.[1,2,3,4,5,6,7,8,9]

2.1 HP ^{129}Xe NMR spectroscopy: theory

2.1.1 The Zeeman interaction

The fundamental interaction in nuclear magnetic resonance spectroscopy is the Zeeman interaction which gives rise to a spectroscopic signal that resonates in the radio frequency range of the electromagnetic spectrum. The frequency that a particular nucleus resonates at is largely determined by the Zeeman Hamiltonian which describes the interaction of a nuclear spin I with an external magnetic field $\mathbf{B_0}$. The direction along which $\mathbf{B_0}$ points is designated the z-direction and the component of the applied magnetic field along z is referred to as B_0. The Zeeman Hamiltonian can be expressed as

$$\boldsymbol{H}_Z = -\gamma_I \hbar B_0 I_Z \qquad 2.1$$

where I_Z is the azimuthal spin angular momentum operator in the z-direction, $\hbar$ is the Planck constant divided by 2π and the magnetogyric ratio, γ_I, is unique for every NMR active isotope. For a spin $I = 1/2$ nucleus such as ^{129}Xe, with a negative γ_I, equation 2.1

yields two possible spin states corresponding to the magnetic dipole moment of the nucleus being aligned with B_0, $m_I = -½$, or against B_0, $m_I = +½$, Figure 2.1.

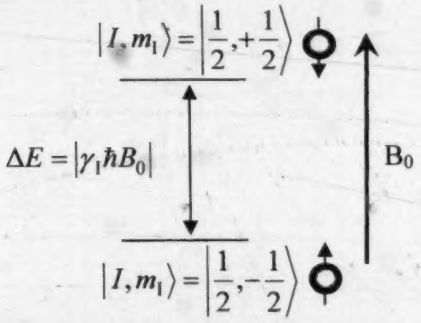

Figure 2.1: Zeeman energy level diagram for a spin ½ nucleus with a negative magnetogyric ratio such as ^{129}Xe.

The energy difference between these two spin states, which in NMR is often expressed in frequency units, is referred to as the Larmor frequency, ν_L, and can be expressed as

$$\nu_L = \frac{|\gamma_I| B_0}{2\pi} \qquad 2.2$$

2.1.2 Producing hyperpolarized ^{129}Xe: optical-pumping spin-exchange

The use of the optical-pumping spin-exchange process to obtain HP ^{129}Xe has become extremely important in the application of ^{129}Xe NMR spectroscopy. The ability to rapidly acquire spectra of materials with low ^{129}Xe densities is invaluable. Typically a signal enhancement of 10,000 can be obtained over conventional thermally polarized ^{129}Xe.

In conventional NMR experiments the magnitude of the bulk nuclear magnetization when a sample is placed in an external magnetic field is determined by the Boltzmann distribution and governed by the Zeeman interaction energy,

$$\frac{n_{+1/2}}{n_{-1/2}} = \exp\left(-\frac{\Delta E}{kT}\right) = \exp\left(-\frac{|\gamma_I| \hbar B_0}{kT}\right) \qquad 2.3$$

where $n_{+1/2}$ and $n_{-1/2}$ are the populations of the two nuclear spin states ($n_{-1/2} + n_{+1/2} = N$, the total number of spins), k is the Boltzmann constant, and T is the temperature. In a magnetic field of 4.7 T at room temperature the population difference, $(n_{-1/2} - n_{+1/2})/N$, of ^{129}Xe is 4.5×10^{-6}. The goal of optical-pumping spin-exchange is to create ^{129}Xe that has a population difference on the order of 0.1 which equates to a signal enhancement of 10^4 to 10^5.

There are two parts to the optical-pumping spin-exchange process. The first step involves the optical-pumping of the electron-spins of an appropriate alkali metal atom. The second step transfers the accumulated electronic-spin polarization from the alkali metal to the nucleus of a NMR active noble gas atom such as Xe. The theory of optical-pumping spin-exchange has been worked out by Happer and co-workers and the reader is referred to their publications for a more detailed description of the process.[10,11,12,13,14]

In most optical-pumping spin-exchange systems, the alkali metal atom of choice is Rb. This is because Rb has a sufficiently high vapor pressure (m.p. = 39 °C)[15] and an electronic transition that falls at a convenient energy level for commercial laser systems, 794 nm.

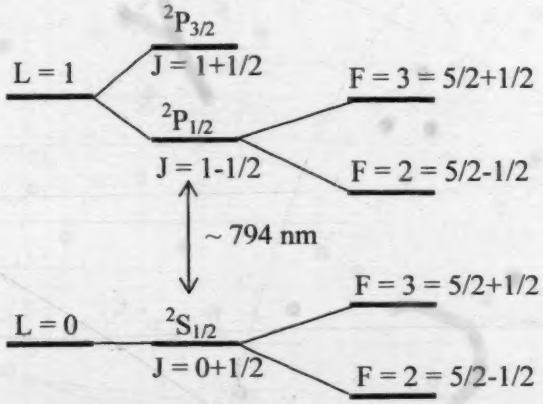

Figure 2.2: A portion of the electronic energy level diagram for ^{85}Rb.[10]

A portion of the electronic energy level diagram of Rb is shown in Figure 2.2. There are two energy levels that are of interest corresponding to electronic orbitals with angular momentum L = 0 and the L = 1. These energy levels are given the symbols ^2S

and ^2P for L = 0 and L = 1 respectively (the 2 is the multiplicity, 2S + 1, and arises from the fact that there is one unpaired electron in Rb(0) resulting in a net spin of S = ½). The energy levels are perturbed by the coupling between the orbital and the spin angular momentum of the electron and the resultant momentum is given the term, J, where J can equal L ± ½; the three resultant energy levels, from lowest to highest energy, are given the terms $^2S_{1/2}$, $^2P_{1/2}$, and $^2P_{3/2}$. The splitting between the $^2S_{1/2}$ and $^2P_{1/2}$ energy levels has an energy corresponding to a wavelength of 794 nm. This is the transition that is employed in the optical pumping process.

The next perturbation to the energy levels arises from the hyperfine coupling between the electrons and the nucleus. For ^{85}Rb which has a nuclear spin of 5/2, the coupling results in a splitting of the $^2S_{1/2}$ and $^2P_{1/2}$ energy levels. The resultant quantum number F equals I ± J, and has the values of F = 2 and F = 3 for the two energy levels. There are thus four energy levels of interest in the ^{85}Rb electronic energy level diagram, two for the electronic ground state $^2S_{1/2}$ F = 2 and 3 and two for the excited state $^2P_{1/2}$ F = 2 and 3, Figure 2.3.

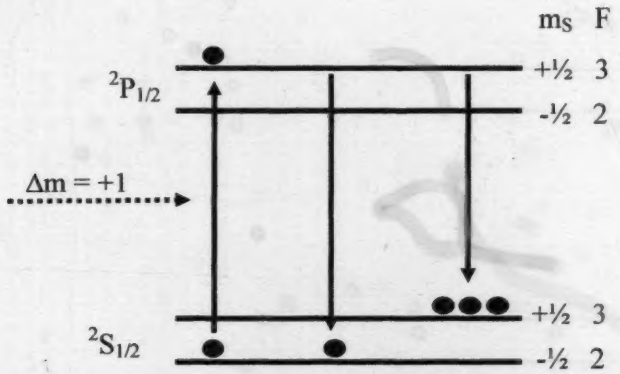

Figure 2.3: A schematic of the optical pumping process for the electrons of ^{85}Rb.[10]

The optical pumping process involves the excitation of electrons from the lowest energy ground state, $^2S_{1/2}$ F = 2, to the $^2P_{1/2}$ excited state. The light used for this excitation process is circularly polarized which means that the light absorbed by the electron to induce the excitation has an angular momentum number associated with it. Right-handed circularly polarized light is said to have Δm = +1 angular momentum and

left-handed circularly polarized light has an angular momentum of $\Delta m = -1$; we will consider right circularly polarized light. This angular momentum is transferred to the electrons during the excitation and a change in the spin angular momentum occurs. The electron is therefore excited from the lowest energy level $^2S_{1/2}$ F = 2 to the $^2P_{1/2}$ F = 3 level.

The relaxation process by which the electrons return to the ground electronic state can occur via three mechanisms: simple remittance of the energy, fluorescence at a lower energy, or non-radiative methods. In the optical-pumping spin-exchange apparatus where a buffer gas is present in the optical pumping cell, the non-radiative relaxation mechanism dominates; the energy is transferred through collisions with the buffer gas. This form of relaxation may involve either a change in the angular momentum or not. When no change in momentum occurs, the electron relaxes to the $^2S_{1/2}$ F = 3 state, if a change in angular momentum takes place the electron returns to the $^2S_{1/2}$ F = 2 state where it can be excited again by the laser. The electrons that end up in the $^2S_{1/2}$ F = 3 state become trapped because they can not absorb the light that has an angular momentum of +1. Over time this leads to a build-up of electrons in the $^2S_{1/2}$ F = 3 state and therefore a net electronic spin polarization.

After the Rb electrons have been spin polarized the net angular momentum can be transferred to the nucleus of a NMR active noble gas such as ^{129}Xe. In order for the spin to be effectively transferred, a Fermi-contact mechanism is required between the electron on the Rb and the nucleus of the Xe. This mechanism requires that there is a finite Rb electron density at the Xe nucleus. The Hamiltonian that describes this interaction has the form:

$$\boldsymbol{H}_{FC} = \alpha(r)\boldsymbol{I}\cdot\boldsymbol{S} \qquad 2.4$$

where $\boldsymbol{I}$ is the nuclear spin operator of the nucleus, $\boldsymbol{S}$ is the electron spin operator of the Rb electron and $\alpha(r)$ is a coupling coefficient that depends on the inter-nuclear separation between the two atoms. Figure 2.4 shows the Rb 5s electron density after being orthoganalized to all of the Xe electrons. It is clear that there is significant electron density at the Xe nucleus which results in the Fermi-contact contribution.

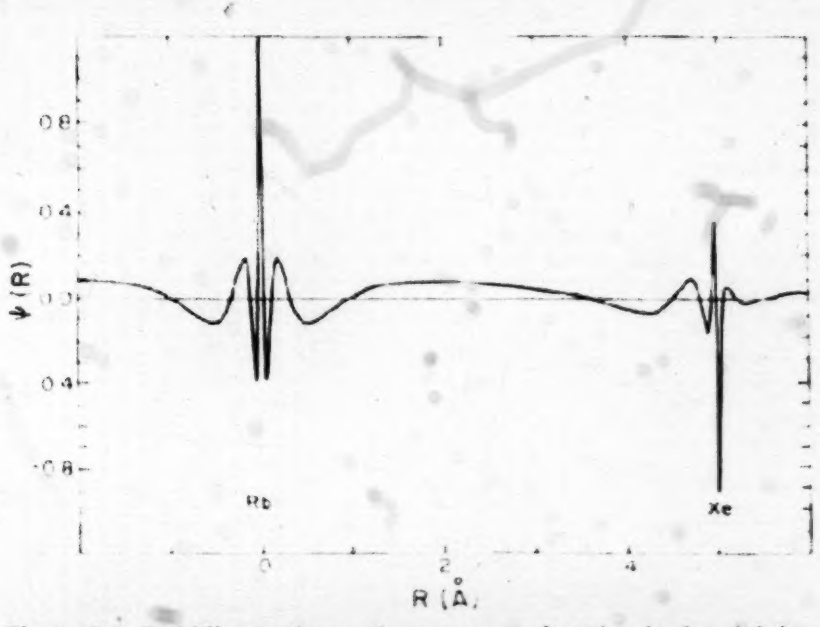

Figure 2.4: Rubidium valence electron wave function in the vicinity of a Xe atom. The function plotted is the Rb 5s wave function after being orthogonolized to all the Xe electron orbitals. Figure reprinted with permission from Ref 11.

The time that the Rb and Xe atoms spend within the distance required for the Fermi contact mechanism to transfer the electron spin polarization to the ^{129}Xe nucleus depends on the overall gas pressure in the optical-pumping spin-exchange cell. When the total pressure of the optical-pumping chamber is low, less than a few tens of torr, the Fermi-contact interaction acts when the two atoms are bound in a van der Waals complex. At low pressures, the lifetime of these van der Waals complexes can be greater than 10^{-9} s and therefore the spin transfer is dominated by the formation of these complexes, Figure 2.5.[11] With an increase in the total pressure, the lifetime of the van der Waals complexes decreases due to the rapid breakup of the complexes caused by collisions with other gas atoms. At total pressures of a few atmospheres the lifetime of the van der Waals complexes decreases to approximately 10^{-12} s which is the average lifetime two atoms remain within the Fermi contact distance during a binary collision.[11] Therefore at pressures above a few atmospheres the transfer of spin polarization occurs during binary collisions, the lifetimes of which are generally not dependent on total gas pressure. At the pressures used for the optical-pumping experiment, generally a few

atmospheres, the spin polarization transfer likely occurs during both binary collisions and the formation of van der Waals complexes.

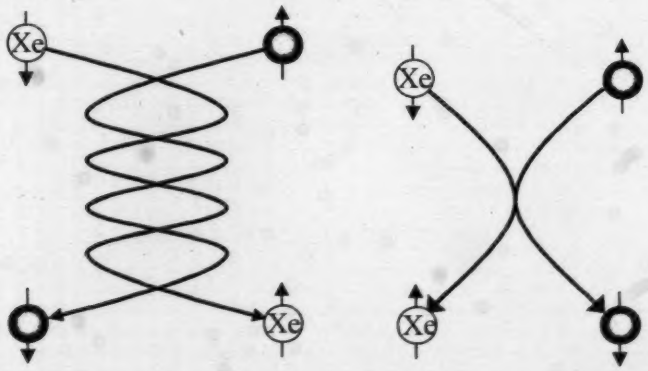

Figure 2.5: Diagrams illustrating the two mechanisms by which electron-nuclear spin exchange can occur; the formation of van der Waals complexes, left, and during 2-body collisions, right. The exchange is mediated by the Fermi-contact interaction between the Rb unpaired electron and the ^{129}Xe nucleus. The exchange acts during the time the atoms are within ~4.5 Å.[11]

2.1.3 Magnetic shielding

The power of the NMR experiment from a chemist's point of view is that the Larmor frequency can be perturbed by other interactions that in turn can be correlated to the chemical environment a nucleus resides in. Arguably the most important of these interactions is the magnetic shielding interaction. The magnetic shielding interaction modifies the effective magnetic field that a nucleus experiences due to the magnetic field induced motion of electrons surrounding the nucleus. The magnetic shielding Hamiltonian can be expressed as

$$\boldsymbol{H}_{CS} = \gamma_I \hbar \boldsymbol{I} \cdot \boldsymbol{\sigma} \cdot \boldsymbol{B}_0 \qquad 2.5$$

where $\boldsymbol{\sigma}$ is the magnetic shielding tensor, a second rank tensor that describes the magnitude of the magnetic shielding interaction in three dimensions.

$$\sigma = \begin{bmatrix} \sigma_{xx} & \sigma_{xy} & \sigma_{xz} \\ \sigma_{yx} & \sigma_{yy} & \sigma_{yz} \\ \sigma_{zx} & \sigma_{zy} & \sigma_{zz} \end{bmatrix} \qquad 2.6$$

In the NMR experiment only the symmetric portion of this tensor can be characterized under normal conditions, i.e., $\sigma_{ij} = \sigma_{ji}$ where i, j = x, y, z. If the symmetric magnetic shielding tensor is diagonalized, the tensor is said to be in its principal axis system, PAS. In the PAS, the three diagonal components of the tensor are referred to as the principal components and are defined such that $\sigma_{11} \leq \sigma_{22} \leq \sigma_{33}$.

$$\sigma_{PAS} = \begin{bmatrix} \sigma_{11} & 0 & 0 \\ 0 & \sigma_{22} & 0 \\ 0 & 0 & \sigma_{33} \end{bmatrix} \qquad 2.7$$

To relate the PAS of the magnetic shielding tensor to the laboratory frame, where B_0 defines the z-direction, two polar angles are required (see Figure 2.6).

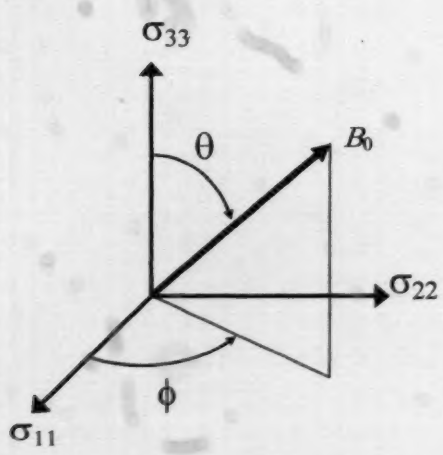

Figure 2.6: The polar angles that define the orientation of the magnetic shielding tensor with respect to B_0.

A new expression for the resonance frequency of a nucleus in a particular chemical environment can be derived from Equation 2.2 by including the magnetic shielding:

$$\nu(\theta,\phi) = \frac{\gamma_1 B_0}{2\pi}\left[1 - \left(\sigma_{11}\sin^2\theta\cos^2\phi + \sigma_{22}\sin^2\theta\sin^2\phi + \sigma_{33}\cos^2\theta\right)\right] \qquad 2.8$$

In the solid state, each crystallite in a powder will have a different orientation with respect to B_0, and therefore a range of θ and ϕ values exists. These orientations result in a range of frequencies according to Equation 2.8 and the resulting spectrum is referred to as the NMR powder pattern.

2.1.4 The origins of magnetic shielding

The theoretical understanding of magnetic shielding was first developed by Ramsey.[16] Ramsey described shielding in terms of a diamagnetic and paramagnetic term

$$\sigma = \sigma^d + \sigma^p \qquad 2.9$$

The diamagnetic term depends solely on the ground electronic state of the molecule or atom and is given by[17]

$$\sigma^d{}_{ij} = \left(\frac{\mu_0}{4\pi}\right)\left(\frac{e^2}{2m}\right)\langle 0|\sum_k \frac{\left(r^2\delta_{ij} - r_{ki}r_{kj}\right)}{r_k^3}|0\rangle \qquad 2.10$$

where e and m are the charge and mass of an electron, respectively, μ_0 is the permeability of vacuum, k indicates a sum over all electrons, r_k is the distance vector of electron k from the nucleus, i and j represent the appropriate components of the tensor, x, y, or z, and δ_{ij} is the Kronecker delta. The diamagnetic shielding is easily calculated, relatively constant, and always positive for any given atom.

The paramagnetic contribution to shielding, which is normally negative, is related to the magnetic-dipole allowed mixing between symmetry appropriate occupied and virtual molecular orbitals and can be expressed as[16,17,18]

$$\sigma^{p}_{ij} = -\left(\frac{\mu_0}{4\pi}\right)\left(\frac{e^2}{2m^2}\right)\sum_{n\neq 0}\left[\frac{\langle 0|\sum_k r_k^{-3} L_{ki}|n\rangle\langle n|\sum_k L_{kj}|0\rangle + \langle 0|\sum_k L_{kj}|n\rangle\langle n|\sum_k r_k^{-3} L_{ki}|0\rangle}{E_n - E_0}\right] \quad 2.11$$

where $\boldsymbol{L}$ is the angular momentum operator, n indicates the sum over excited electronic states and E is the energy of the indicated electronic state. Qualitatively, the magnitude of the paramagnetic term is dependent both on the energy difference between the occupied and virtual molecular orbitals and the matrix elements of the form $\langle 0|\boldsymbol{L}_i|n\rangle$, where $\boldsymbol{L}_i$ is the angular momentum operator acting along i.[16,18]

For Xe(0) in the gas phase at zero density the paramagnetic shielding term is zero and the shielding arises solely from the diamagnetic contribution. Based on quantum chemical calculation, the shielding of a isolated Xe(0) atom is approximately 5642 ppm or 6938 ppm based on non-relativistic and relativistic calculations, respectively.[19,20,21]

Whenever the electrons associated with a Xe nucleus are disturbed from perfect spherical symmetry, a paramagnetic shielding contribution exists. Thus, when Xe atoms approach other atoms the electronic orbitals about the Xe nucleus will be perturbed and a paramagnetic term will contribute to the overall Xe magnetic shielding. Thus the measured chemical shift will contain information about the local environment.

2.1.5 The chemical shift

While magnetic shielding is the physical property that describes the influence of the electronic structure on the nucleus, it is not measured directly in the NMR experiment. Instead, the difference in NMR frequencies between the sample of interest and a standard reference is measured; this is called the chemical shift, δ, and is usually expressed in units of ppm.[22]

$$\delta = \frac{(\nu_s - \nu_{ref})}{\nu_{ref}} \quad 2.12$$

The chemical shift is related to the magnetic shielding by the following equation:

$$\delta = \frac{(\sigma_{ref} - \sigma_s)}{(1 - \sigma_{ref})} \qquad 2.13$$

Like the magnetic shielding, the chemical shift can be expressed as a second-rank tensor with all of the same angular dependencies. The principal components of the chemical shift tensor are defined such that $\delta_{11} \geq \delta_{22} \geq \delta_{33}$. It is convenient to define three terms to characterize the chemical shift tensor in its principal axis system, δ_{iso}, which describes the average position of the powder pattern, the span, Ω, which indicates the breadth of the pattern and the skew, κ, which describes the shape of the pattern.[22]

$$\delta_{iso} = (\delta_{11} + \delta_{22} + \delta_{33})/3 \qquad 2.14$$

$$\Omega = \delta_{11} - \delta_{33} \qquad 2.15$$

$$\kappa = 3(\delta_{22} - \delta_{iso})/\Omega \qquad 2.16$$

The skew can take on values from -1 to +1, the two extremes representing axially symmetric tensors, Figure 2.7.

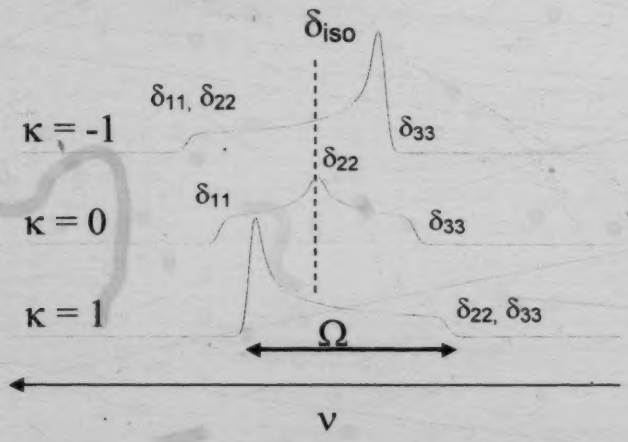

Figure 2.7: Simulated spectra showing three possible chemical shift powder patterns.

The chemical shift observed for ^{129}Xe interacting with porous materials is often partitioned into the shifts arising from different interactions

$$\delta = \delta_0 + \delta_s + \delta_{Xe} \qquad 2.17$$

δ_0 is the chemical shift of a free Xe atom at zero loading, and is typically used as the reference (δ_0 = 0 ppm) when performing NMR of Xe(0); the conventional chemical shift reference for ^{129}Xe NMR spectroscopy is $XeOF_4$ which is ~5460 ppm less shielded than Xe gas at 0 pressure.[17] δ_s is the chemical shift induced when a lone Xe atom interacts with the framework or surface. This contribution is often obtained from extrapolating the chemical shift of Xe in the material as a function of Xe loading to the zero-loading limit or by using low partial pressures of Xe gas as is done in the HP ^{129}Xe experiments. δ_{Xe} represents the chemical shift introduced from Xe-Xe interactions which are significant at elevated pressures or at low temperatures where Xe loading increases. Other contributors to δ can also be proposed such as an electric field effect caused by charged ions in the framework, δ_E, or the shift caused by interaction with paramagnetic centres.

2.2 The properties of Xe

Xe is element 54 in the periodic table. It is a noble gas with a van der Waals radius of 2.16 Å[23] making it an ideal non-destructive probe of pore spaces that are large enough to accommodate small molecular gases such as methane. Xe has two NMR active isotopes, ^{129}Xe and ^{131}Xe.[24] Xe-129 is the most commonly used isotope of Xe for NMR experiments because of its favorable NMR properties, I = ½, Ξ = 27.810186 MHz, N.A. = 26.44%.[24] Xe-131 is a quadrupolar nucleus (I = 3/2) with a moderate quadrupole moment (Q = -11.4 fm^2) a natural abundance of 21.18% and a low NMR frequency, Ξ = 8.243921 MHz.[24] In the solid state, ^{131}Xe NMR spectra typically yield broad second-order quadrupolar lineshapes.[25] Additionally, maintaining the hyperpolarization of ^{131}Xe is much more difficult because its rate of relaxation is several orders of magnitude greater than that of ^{129}Xe.

Due to the large number of electrons surrounding the nucleus, Xe has a high polarizability. Compared to other small non-polar molecules, the inter-atomic forces of attraction between Xe and other atoms are quite large, e.g., the Xe-Xe potential energy

minimum is 2.357 kJ mol^{-1} while that of Ne-Ne is 0.329 kJ mol^{-1}.[26,27] As a result Xe has a much higher melting and boiling point than many other atoms or non-polar small molecules. At 1 atm the melting point and boiling point are within 5° of each other, 161.2 and 166.0 K respectively.[15] The triple point occurs at 160.3 K and 0.8053 atm which implies that at Xe pressures below 0.8053 atm Xe does not exist in the liquid state.[15] The enthalpy of sublimation for solid xenon is 14.98 kJ mol^{-1}.[28]

Another consequence of the high polarizability of Xe is that its chemical shift range is large. For atomic Xe the chemical shifts range from 0 ppm for isolated Xe atoms to approximately 310 ± 10 ppm for Xe(s);[29,30] examples of Xe interacting with Ag^+ or Cu^+ ions in zeolites have shown that negative chemical shifts are also possible.[31] It is this high sensitivity of atomic Xe to its environment that makes ^{129}Xe such a desirable NMR probe for exploring void spaces in solids.

The magnetic shielding of Xe(g) has been shown to have a large temperature and density dependence. The best analysis of the density dependence is that proposed by Jameson and co-workers who described the dependence in terms of virial coefficients

$$\sigma = \sigma_0 + \sigma_1(T)\rho + \sigma_2(T)\rho^2 + \sigma_3(T)\rho^3 \qquad 2.18$$

where (at 298 K) σ_0 = reference shielding, σ_1 = -0.548 ± 0.004 ppm/amagat, σ_2 = (-0.169 ± 0.02) × 10^{-3} ppm/amagat^2, σ_3 = (0.163 ± 0.01) × 10^{-5} ppm/amagat^3 (One amagat is the density of an ideal gas at 273.15 K and 1 atm, 2.689 × 10^{19} atoms cm^{-3}).[32] This equation is linear over Xe densities of one hundred amagat or less, Figure 2.8a. Because of the temperature independence of σ_0, the chemical shift of Xe(g) extrapolated to zero density is used as the chemical shift reference value for ^{129}Xe NMR of atomic Xe. Equation 2.18 is widely used for standardizing the observed chemical shift of Xe(g) at various pressures to this reference value.

The temperature dependence of the first virial coefficient has also been derived by Jameson using a polynomial dependence on temperature; in units of ppm/amagat it is

$$\sigma_1(T) = -0.553 + 0.1114\times10^{-2}\tau - 0.765\times10^{-5}\tau^2 + 0.436\times10^{-7}\tau^3 - 0.132\times10^{-9}\tau^4 - 0.545\times10^{-12}\tau^5 \qquad 2.19$$

where τ = T-300 K.[33]

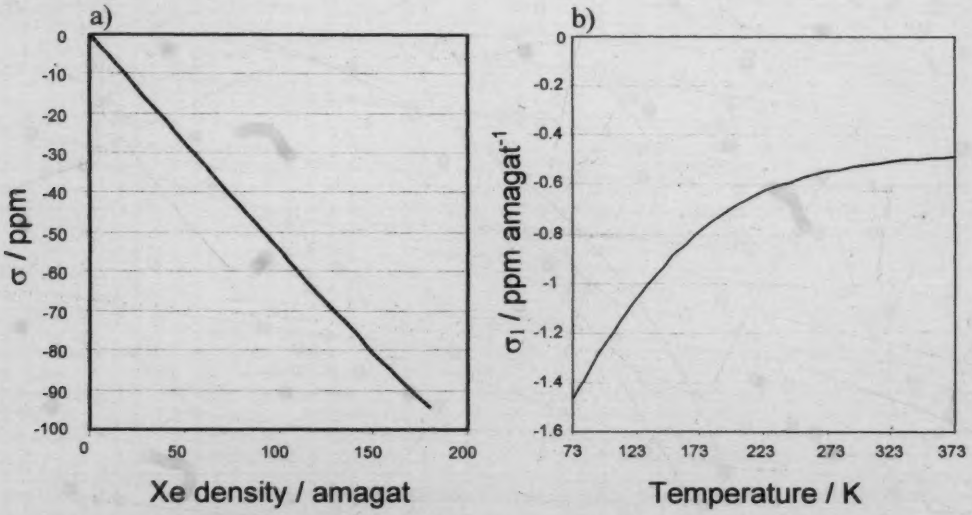

Figure 2.8: Plots of the density and temperature dependencies of the Xe shielding using equation a) 2.18 and b) 2.19. [32,33]

In the hyperpolarized Xe experiment the partial pressure of Xe is low: 0.01 atm in this work (the gas mixture used is 1% Xe, 1% N_2 and 98% He). To a good approximation the chemical shift observed for Xe in the gas mixture can be assumed to be equivalent to Xe at zero density, and therefore used as an internal reference. This also implies that no significant variation in chemical shift is expected in the NMR peak of free Xe gas as a function of temperature.

2.3 The NMR spectra of ^{129}Xe in spaces on the order of the Xe diameter

2.3.1 Clathrate compounds

The study of Xe clathrate compounds began soon after the first published uses of ^{129}Xe as an NMR probe of porous materials.[34,35] Clathrate compounds can accommodate Xe atoms within the molecular cages. A number of clathrates have been studied using

solution ^{129}Xe NMR spectroscopy, most notably Xe in cryptophane-A,[36,37,38] which are leading to biological applications.[39,40,41,42,43]

In the solid state, clathrates represent some of the smallest cages Xe can occupy. The chemical shift of Xe interacting with a solid is dependent on the number of close contacts the Xe atom can make with the solid. Clathrates often have cages of similar size to Xe, thereby maximizing the number of close contacts and creating large chemical shifts, typically between 150 and 250 ppm. Since the Xe atom is trapped in the cage, there is very little motional averaging of the chemical shift and consequently chemical shift anisotropies can be observed in many cases.

Clathrate hydrates are ice-like cages of water molecules that form around small molecules. They form at elevated pressures, 25 to 100 atm, and at a temperature between 275 and 285 K.[44,45] Using ^{129}Xe NMR spectroscopy, Ripmeester and coworkers have performed extensive studies of type I, II, and H clathrates hydrates;[34,35,46,47,48] the existence of type H clathrate hydrates was proven, in part, by ^{129}Xe NMR spectroscopy.[49] Studies of the hydrates show that the isotropic chemical shift depends on the cage size and ranges from ~152 ppm for larger cages to ~240 ppm for the smaller cages.[47] For Xe trapped in some of the non-spherical cages, measurable chemical shift anisotropies are often obtained. For example, when xenon occupies the oblate $5^{12}6^2$ cage of type I hydrate an axially symmetric, $\kappa = 1.0$, lineshape is observed, Fig. 2.9 top.

The increased signal-to-noise afforded by the use of HP ^{129}Xe NMR spectroscopy has allowed researchers to study the formation of clathrate hydrates on the surface of ice.[50] Spectra acquired every second show variations in signal intensity as the clathrate hydrate forms. From these data, conclusions about the formation process and the kinetics of formation and decomposition were made.

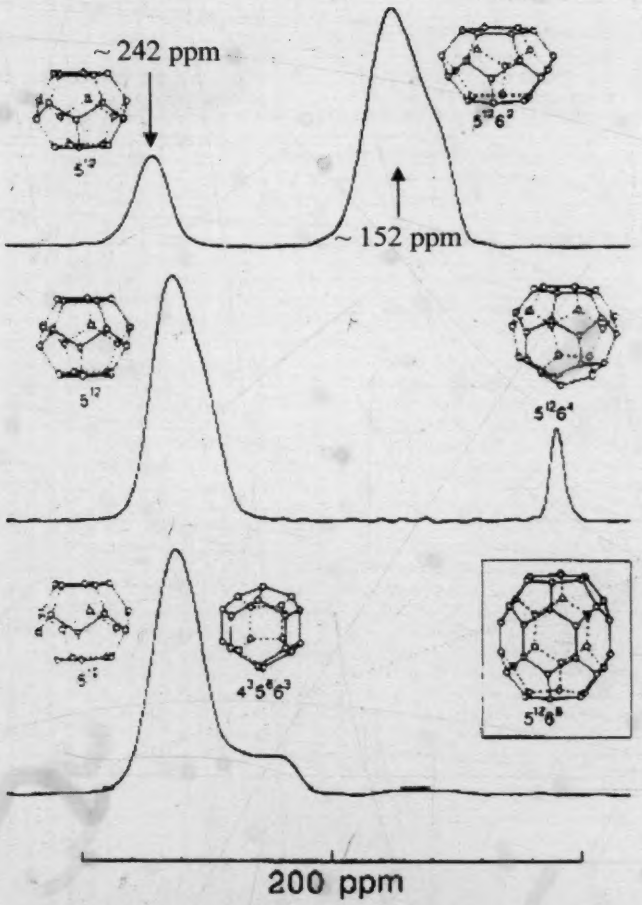

Figure 2.9: Characteristic ^{129}Xe NMR spectra of structure I, II, and H hydrates recorded at 77 K: (top) Xe structure I hydrate; (middle) double hydrate of n-butane and xenon, type II; (bottom) double hydrate of bicyclo-[2.2.2]oct-2-ene and xenon, type H. There is no evidence that Xe occupies the large cage of structure H hydrate (insert). Figure reprinted with permission from Ref 48.

A number of other clathrates have also been studied.[46,47,51] Dianin's compound (4-*p*-hydroxy-phenyl-2,2,4-trimethylchroman) is an example of an organic clathrate that can accommodate two Xe atoms within the hour-glass shaped cages; the cross-section dimensions of the cage are 6.3 Å at the two ends with the "neck" being approximately 4.2 Å across.[52] The ^{129}Xe NMR spectra of Xe in Dianin's compound, acquired when the overhead Xe pressure is below 1 atm, contain two NMR peaks at 134 and 152 ppm,

Figure 2.10.[52] The peak at 134 ppm is from a single Xe occupying the hour-glass shaped cage. The peak at 152 ppm, which becomes the only peak observed when the Xe loading is increased, arises when two Xe atoms are occupying the cage. The increased chemical shift is a result of the deshielding introduced by the Xe-Xe interaction.

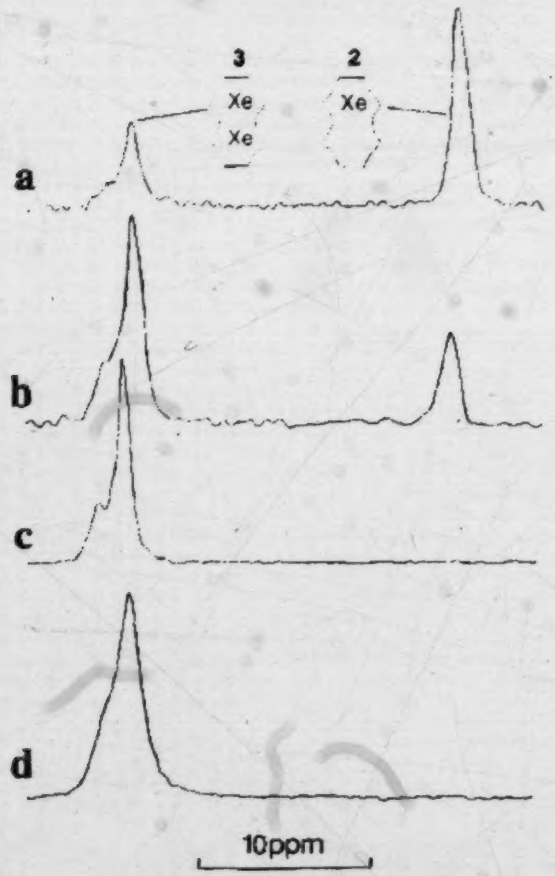

Figure 2.10: ^{129}Xe CP/MAS NMR spectra of Dianin's compound clathrates of Xe prepared from dodecane under different xenon pressures: (a) 0.3, (b) 0.7, (c) 3, (d) 20 atm. Figure reprinted with permission from Ref. 51.

Based on the studies of Xe in clathrate compounds a general trend has emerged that correlates Xe chemical shifts to the van der Waals diameter of the cage. The trend is linear over a range of 200 ppm and cage diameters of 5.0 to 6.7 Å.[47]

2.3.2 Polymers

Many polymers adsorb large amounts of Xe, especially when exposed to several atmospheres of Xe gas. Intercalation into the polymer results in the Xe atoms experiencing a highly confined "void" space between the polymer chains, Figure 2.11, which can more accurately be described as Xe dissolved in the polymer. The chemical shift values of Xe adsorbed into polymers range from 150 to 250 ppm with the majority of the shifts falling between 200 and 230 ppm.

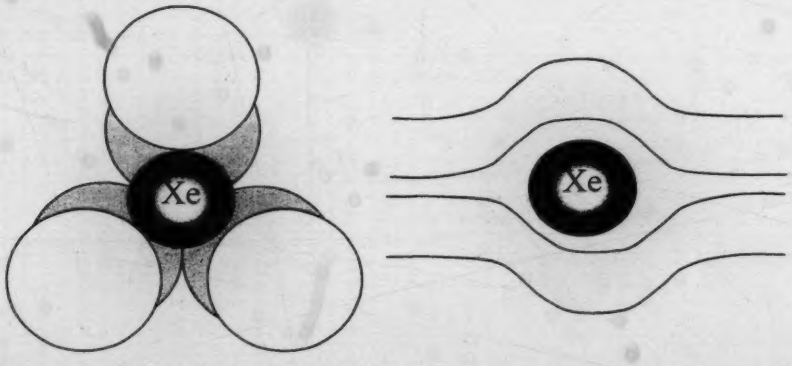

Figure 2.11: Schematic of Xe dissolved in a polymer. The Xe displaces the polymer chains during adsorption resulting in a highly confined Xe environment. The flexibility of the polymer chains and the temperature of the sample influence the amount of space created by the Xe and therefore influence the chemical shift.[55]

The Xe chemical shift decreases with increasing temperature of the polymer due to the thermal expansion of the polymer and the subsequent increase in free space. The dependence of chemical shift and line width on temperature is typically linear with a change in slope at the glass transition temperature of the polymer.[53] Below the glass transition temperature, Xe linewidths can be large due to the presence of many different environments within the disordered polymers.[53,54] Above the glass transition temperature narrow lines are observed in the ^{129}Xe NMR spectra, corresponding to the rapid motion of Xe within the mobile polymer phase. This rapid motion averages distributions in chemical shift and chemical shift anisotropy.[55]

Since different polymers give different characteristic Xe chemical shifts, ^{129}Xe NMR spectroscopy can be used to study the miscibility of polymer blends. Highly miscible polymers yield a single ^{129}Xe NMR peak while immiscible polymers yield multiple peaks corresponding to the multiple, separate polymer phases. This behavior has been employed to study rubbery polymer blends of polypropylene and

ethylene/propylene.[56] It was shown that the two phases in the polymer blends gave rise to two ^{129}Xe NMR peaks, Figure 2.12. When HP ^{129}Xe was dissolved in the polypropylene phase of the polymer blends a peak near 222 ppm was observed while the peak from ^{129}Xe in the ethylene/propylene phase produced an NMR peak at 206 to 215 ppm. The intensity of the peaks as a function of temperature was used to extrapolate the glass transition temperature of the phases.[56] The diffusion of Xe through the polypropylene was determined to be slow based on the signal intensity of the dissolved ^{129}Xe NMR peak as a function of polymer treatment. When the polymer was pretreated at 140, 150 and 160 °C, the signal intensity decreased due to a decrease in the polymer surface area. This suggested that the ^{129}Xe NMR signal originates solely from ^{129}Xe in the first few hundred nanometers of the polymer surface; the recycle delay was 0.5 s which is the amount of time the Xe is allowed to diffuse before the HP signal is used up by the NMR experiment.

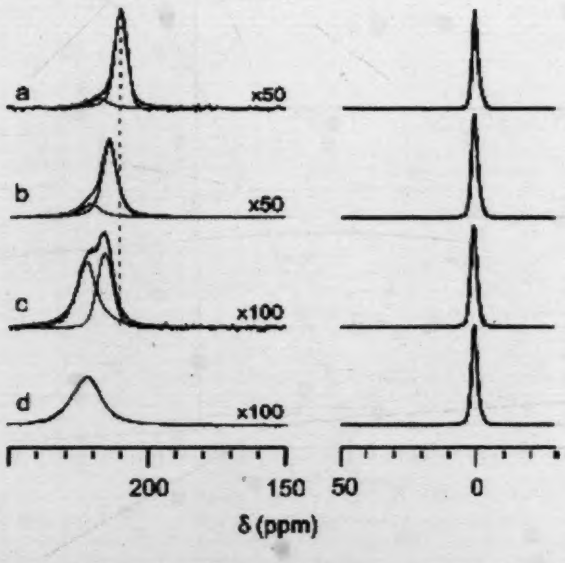

Figure 2.12: ^{129}Xe NMR spectra of HP Xe in rubbery polymer blends of polypropylene, ~222 ppm, and ethylene/propylene, ~210 ppm, with different fractions of the two polymers. Figure reprinted with permission from Ref 56.

Exchange between the two polymer phases and the free xenon gas has also been studied using 2-D exchange spectroscopy.[56] The spectra revealed that Xe exchanges first

between the free gas and the ethylene/propylene phase and subsequently into the polypropylene phase. From these results it was suggested that the ethylene/propylene phase was coated on the surface of the polymer particles.

Other NMR studies of polymers include using ^{129}Xe chemical shifts to understand cross-linked polymers[57,58] and to study permeability in different types of polymers.[59,60,61]

2.4 Models for Xe adsorption and the interpretation of Xe chemical shifts in porous materials

The biggest challenge to interpreting Xe chemical shifts in porous materials is to understand how exchange of the Xe affects the chemical shift. There are few instances where it can be stated that Xe occupies a single site within a porous material. In the case of clathrate hydrates and other small cage compounds, where the Xe atoms are trapped in tight spaces this can be a good approximation. Also, if there is a strong adsorption site that can effectively trap Xe, exchange averaging may be of minimal importance. These cases are relatively rare and therefore Xe exchange must be considered when interpreting ^{129}Xe NMR spectra. The development of models that account for Xe dynamics has been progressive, beginning with simple models that were incrementally expanded to explain new data and progressing to the current state where computer simulations can be used to model Xe dynamics or distributions and predict Xe chemical shifts.

The magnetic shielding of Xe gas is determined by interactions with the other atoms. Each diatomic interaction creates a response in the Xe magnetic shielding tensor with the shielding along the inter-nuclear vector being different than that perpendicular to the vector, Figure 2.13. A similar effect is observed when Xe approaches an ideal surface. In general the shielding components in the plane perpendicular to the vector of approach are deshielded while the component parallel to the vector changes only slightly. The magnitude of the shielding response is related to the distance between the Xe and the other atom or surface, with shielding generally decreasing as the separation decreases, i.e., chemical shift increases as Xe approaches the atom or surface due to an increase in σ^p, which is negative. To a good approximation, the overall Xe chemical shift can be

determined by summing up all the different three dimensional diatomic shielding contributions.[62]

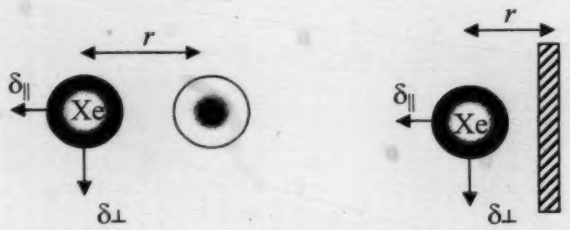

Figure 2.13: The two components of the shielding tensor that result from Xe approaching another atom (left) and Xe approaching an ideal surface (right). The magnitude of the shielding response depends on the separation, *r*.

The simplest case for Xe adsorption is that of adsorption on a flat surface. The adsorption can be described as an exchange process between a Xe atom on and off the surface as well as Xe motion on the surface. The exchange rate of Xe on and off the surface is governed by the temperature and the heat of adsorption, ΔH_{ads}, which is a positive value and is the amount of energy released when a Xe atoms adsorbs to a surface; the adsorption potential, $U = -\Delta H_{ads}$, is determined by the potential energy between Xe and the surface. For a perfectly smooth surface, i.e. ΔH_{ads} is the same over the entire surface, there is no barrier to translational motion along the surface while on any real surface variations in adsorption energy at different positions on the surface restrict the motion.

The motion of the Xe on the surface as well as the exchange of Xe between the adsorbed and free gas phases can result in averaging of the Xe chemical shift tensor. Exchange averaging in NMR arises when the rate of exchange between two sites, A and B is faster than the separation between the chemical shifts at the two sites, δ_A and δ_B, in Hz. For example, if Xe exchanges between an adsorbed state with δ_A = 50 Hz and free gas state δ_B = 0 Hz faster than ~ 50 times a second, the NMR signal will be averaged, see Figure 2.14. If the exchange, *k*, is significantly greater than 50 Hz, a single peak will be observed at $\delta_{av} = n_A\delta_A + n_B\delta_B$, where n_A and n_B are the populations of the two sites. Equations that model the exchange process can be used to calculate the NMR spectra of a

system undergoing chemical exchange, see Appendix B. Motion on the surface also results in exchange averaging if there are different positions on the surface that give different magnetic shielding responses. A result of the various exchange modes for Xe adsorbing in porous materials is that the chemical shift anisotropy is averaged or obscured and isotropic lineshapes are often observed.

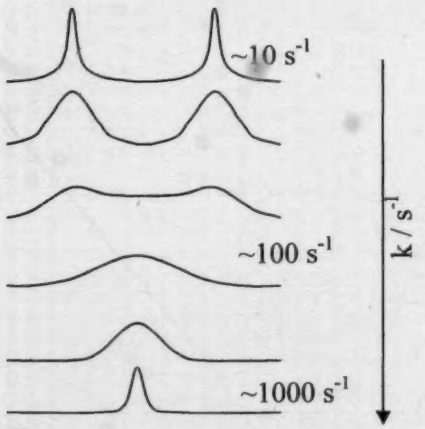

Figure 2.14: NMR spectra of a nuclei exchanging between two equally populated sites with chemical shifts that are 50 kHz apart.

2.4.1 Fast-exchange two-site models

The first model to include Xe exchange in the analysis of the observed chemical shift was proposed by Fraissard to describe the ^{129}Xe NMR chemical shift in zeolites.[63] The model supposes that at room temperature the Xe chemical shift arises from a rapid exchange between Xe on the pore walls and in the free volume of the pore (see figure 2.15). The observed chemical shift arises from an average of the chemical shifts at the two positions, δ_a and δ_v for adsorbed and free volume, respectively, [63,64]

$$\delta = \frac{n_a\delta_a + n_v\delta_v}{n_a + n_v} \qquad 2.20$$

where n_a and n_v are the numbers of Xe in the adsorbed or free volume, respectively. The value of δ_v is related to δ_a and the distance the Xe atom is away from the wall; because of this dependence a mean value, $\langle\delta_v\rangle$, is defined as a function of δ_a and $\bar{\ell}$, the mean free path which is related to the pore diameter.[64]

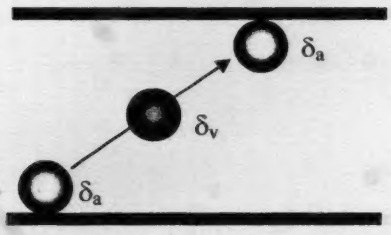

Figure 2.15: Schematic of the fast-exchange two-site model.

By using the same fast-exchange assumption and noting that the chemical shift of free Xe gas is zero, Cheung and coworkers described the observed δ as a function of temperature and Xe density [65]

$$\delta(T,\rho)=\frac{bn_a\delta_a+(1+b\rho_g)\delta_g\rho_g}{1+bn_a+b\rho_g} \qquad 2.21$$

where $b = k_a/k_b$ is the ratio of the adsorption and desorption rate constants and n_a is the number of adsorption sites within a given volume, ρ_g is the density of Xe gas in the free volume within the pores, and δ_g corresponds to the coefficient σ_1 of Jameson's virial expression (equation 2.18) which contains the temperature dependencies (equation 2.19). When ρ_g is zero, i.e., low Xe loading, equation 2.21 reduces to

$$\delta=\frac{bn_a}{1+bn_a}\delta_a \qquad 2.22$$

which is similar to equation 2.20 when δ_v is assumed to be 0 ppm.

Other fast-exchange two-site models have been proposed to explain Xe chemical shifts including that of Raftery and co-workers who related the distribution between the adsorbed and free sites to temperature using the residence time of the Xe on the surface, τ_{surf}, which they described using a Boltzmann distribution.[66]

$$\tau_{surf} = \tau_0 e^{\Delta H_{ads}/RT} \qquad 2.23$$

The fast-exchange models contain assumptions that make their application problematic for some systems. First they incorrectly assume that the distribution of Xe within a porous system can be described by two sites, adsorbed and free Xe. In porous systems the walls of the pores and cavities are rarely uniform and some variation in adsorption potential is expected. This produces not one but numerous sites each with a different value of δ_a. Also, while the value δ_v does not have to be assumed to be 0 ppm, as is the case in Fraissard's model, most applications do make this assumption for simplicity. This clearly assumes that when the Xe is not in an adsorbed state, it does not experience any interaction with the walls. This may be an acceptable assumption for large porous systems where the non-adsorbed Xe can be approximated as "free" but it is clearly not accurate for smaller pores. Despite these problems many empirical correlations have been explained using variations of the fast-exchange two-site model.

2.4.2 Surface curvature model

The chemical shift of ^{129}Xe in micropores on the same size scale as Xe atoms was explained by Derouane and coworkers using a van der Waals model that incorporated the polarizability of Xe and the curvature of the micropore walls.[67,68,69] According to the model, the van der Waals interaction energy between the Xe and the pore walls, *W*, is related to the intrinsic molecular property, *C*, which is proportional to the Xe polarizability, and the curvature factor, *s*, which is related to *d/a* where *d* is the distance from the Xe to the pore wall and *a* is the radius of the pore, Figure 2.16.[67,68,69]

$$W = -\frac{C}{4d^3}\left(1-\frac{s}{2}\right)^{-3} \qquad 2.24$$

The chemical shift that results from Xe interacting with the pore walls is then expressed simply as[68]

$$\delta_s = AW \qquad 2.25$$

where A is a constant that can be obtained from a plot of δ_s against W. For some microporous zeolites this linear correlation appears to hold.[69] The main problem with this model is that it all but ignores the fact that Xe atoms may not be in "direct" contact with the surface at all times which, as stated previously, only occurs for extremely strong adsorption sites or small cages such as clathrates.

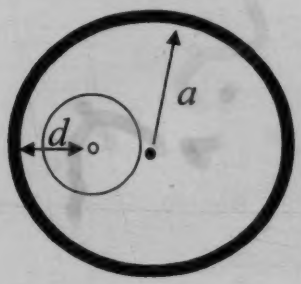

Figure 2.16: Schematic of the surface curvature model; *d* is the distance from the center of the Xe atom to the pore wall and *a* is the radius of the pore.

2.4.3 Models based on Lennard-Jones potentials

To produce a unified description of how Xe interacts with porous materials and thereby correlate the observed Xe chemical shift to pore structure, a more molecular approach was required. The first step in this direction was taken by Ripmeester and Ratcliffe when they examined the data available for clathrates and zeolites.[70] They noted that the early fast-exchange two-site models and pore wall curvature models were proving ineffectual for explaining newer chemical shift *vs.* temperature and chemical shift *vs.* density data. In particular, erroneous conclusions were being drawn by extending the simple models to more complex systems where different adsorption sites were present within the same pore structure.

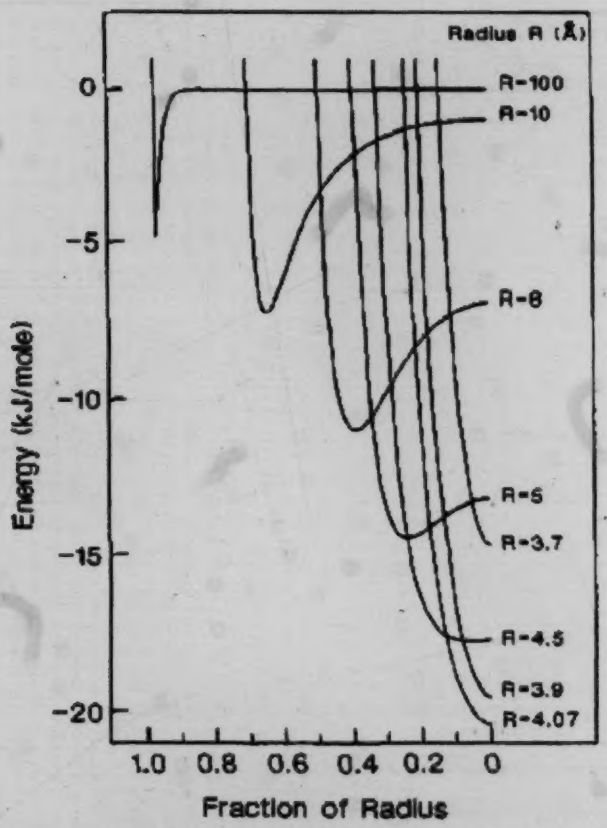

Figure 2.17: Calculated Lennard-Jones potential curves for a Xe atom in a spherical cage as a function of cage radius. It is assumed that oxygen atoms are smeared out over the cage surface at a constant density similar to that in zeolites. Figure reprinted with permission from Ref. 70.

Instead of relying solely on the pore geometry, Ripmeester and Ratcliffe used the interaction potentials between Xe and the pore wall atoms to explain both the behavior of Xe in clathrate cages and in larger zeolite pores. They derived a net interaction potential based on the Lennard-Jones potential energy function[71] between Xe and the oxygen atoms of the pore walls; this interaction is sufficient for most zeolites and clathrate hydrates where the walls are formed by oxygen atoms. The interaction energy is expressed as

$$U(x) = 4\varepsilon\left[\frac{\alpha^{12}}{r^{12}} - \frac{\alpha^{6}}{r^{6}}\right] \qquad 2.26$$

where ε = 0.8975 kJ/mol, α = 3.49 Å and r is the distance between the two atoms.[72] Lennard-Jones potential energy functions are widely used to describe the interaction energy between two atoms. The potentials are composed of a long range attractive term, with the r^{-6} dependence, and a short range repulsion term, with the r^{-12} dependence, and are considered adequate for many purposes when describing pairwise inter-atomic interactions.[73]

Models of Xe in a spherical shell revealed that by using the potential energy interactions a description of Xe adsorption behavior as a function of pore radius, R, could be obtained, Figure 2.17. For small cages, R less than ~4.5 Å, the Xe atom can be considered to be in the center of the cage and a result similar to that obtained using the surface wall curvature model is obtained. When R > ~6 Å, there is a non-uniform potential across the diameter of the cage and the potential energy is lower along the walls, with a significant potential energy hump in the centre of the cage. This leads to a model for the Xe distribution similar to that proposed by the fast-exchange two-site model where Xe exists in an adsorbed state, in the potential energy wells, and in a free state, on the potential energy hump in the middle of the cage. In the extreme case where R ~100 Å, the Xe atom behaves as if it is adsorbed on a flat surface.

The calculated potential energy curves were used to explain the dependence of chemical shift on temperature for Xe in a spherical cage with a radius large enough to give a large potential energy barrier in the centre of the cage (the width of the potential barrier is $2r$). Using the Boltzmann equation to obtain the population of Xe atoms with kinetic energies above and below the energy barrier as a function of temperature, various experimental temperature dependencies were explained for different cage sizes and potential energy barriers. As the temperature approached zero Kelvin, the results showed that the Xe chemical shift would approach that of Xe trapped in the potential energy wells. At the high temperature limit, where the temperature approached infinity, the chemical shift approached a value of

$$\delta = \frac{2}{1 + R^3/(R^3 - r^3)} \qquad 2.27$$

Therefore only in the high temperature limit does the chemical shift truly reflect the cage dimensions while at all lower temperatures both the cage dimensions and adsorption energies are important. This was a critical development in the modeling of ^{129}Xe chemical shifts because it emphasized the fact that in almost all systems both pore geometry and the potential energy surface within the pores are important.

In a second example, Ripmeester and Ratcliffe showed that by using an energy curve model the presence of multiple weak and strong adsorption sites could be accounted for.[70] Cheung used Lennard-Jones potentials to calculate the potential energy for Xe residing between two parallel plates.[74] The model was then extended to calculating the potential energy curve of Xe in a cylinder. Both models were used to explain experimental temperature dependencies of the Xe chemical shift.

2.4.3 Ab initio calculations of Xe chemical shifts in porous materials

The most thorough theoretical model for explaining Xe chemical shifts to date has been developed by Jameson and coworkers over the past fifteen years. The model resulted from early experimental evidence showing that the variable pressure ^{129}Xe NMR spectra of Xe in zeolite NaA contained multiple peaks, the intensities of which changed as a function of Xe loading, Figure 2.18 and 2.19 (see section 2.5.1 for a discussion of the experimental results).[75]

Due to the position of the Na^+ ions, the exchange of Xe between the large α-cages in zeolite NaA is slow, resulting in cages with different numbers of Xe atoms. These different occupancies result in different peaks in the ^{129}Xe NMR spectrum. Attempts were made to explain the distribution of Xe occupancies using different statistical models. It was concluded that to model the Xe distributions Xe-Xe inter-atomic potentials needed to be considered in addition to the Xe-wall potentials. This initial study was one of the first examples of using *ab initio* magnetic shielding calculations to correlate the observed chemical shifts to the Xe distributions. While the calculations were performed on the Ar-Ar diatomic pair as a function of inter-atomic distance as a model for the Xe-Xe interaction,[76] it represented an important step towards establishing

the theoretical connection between the experimental chemical shift and Xe distribution, which can be in turn correlated to the pore dimensions.

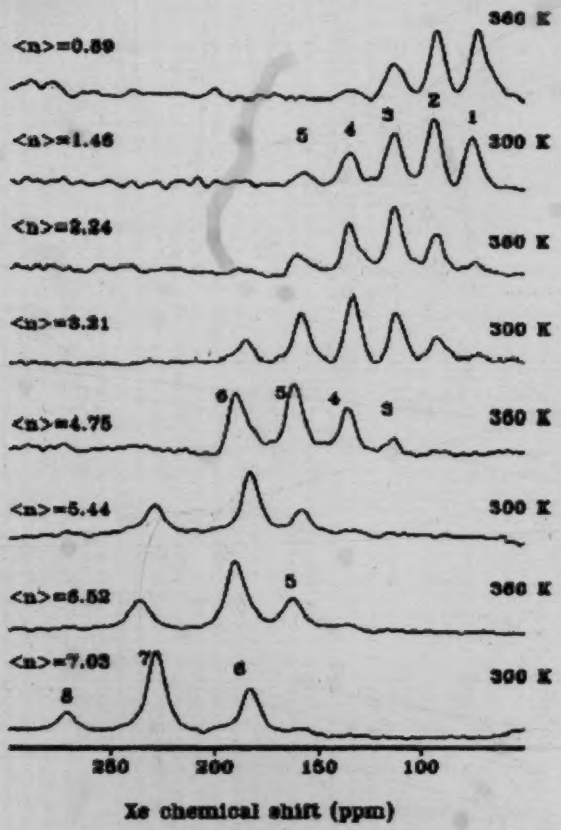

Figure 2.18: ^{129}Xe NMR spectra of four samples of Xe in Zeolite NaA. Each spectrum was observed at equilibrium conditions at 300 and at 360 K. Figure reproduced from Ref. 75.

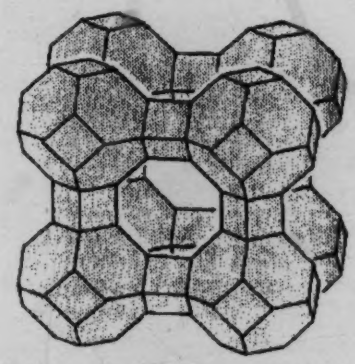

Figure 2.19: The structure of Zeolite A. The centre α-cage is large enough to accommodate up to 8 Xe atoms. The Na^+ ions occupy positions partially blocking the windows to the α-cage.

In order to provide a better model for the distribution of Xe inside pores, Jameson has employed Grand Canonical Monte Carlo, GCMC, simulations.[77,78] The simulations use inter-atomic potentials to describe the Xe-O_{zeol}, Xe-Na^+ and Xe-Xe interactions which have yielded potential energy surfaces which have been used to calculate the distribution of Xe as a function of temperature and loading. The results clearly show that Xe clusters form inside the α-cages of zeolites NaA.[78] The distribution of a single Xe atom in the α-cage is similar to what can be extrapolated based on the previous Lennard-

Jones models; the Xe atoms spend the majority of their time around the walls of the cage where potential energy wells exist due to the attractive forces between Xe and the walls.[78]

The chemical shifts of the xenon in different configurations were calculated based on the pairwise-additivity of the intermolecular shielding functions. The Xe-Xe, Xe-O_{zeol}, Xe-Na^+ inter-atomic shielding functions were obtained by scaling the shielding functions of Ar-Ar, Ar-OH_2 and Ar-Na^+.[76] The chemical shifts calculated using the GCMC method were in excellent agreement with the experimental chemical shifts, although the authors claim the agreement was fortuitous.[77] The model also explains the general experimentally observed chemical shift vs. pore size trends; the smaller the void space, the more Xe-wall close contacts are present and, because of the additivity of the shielding functions, the greater the Xe chemical shift.[62]

The excellent results obtained in these early studies have been successively improved upon and expanded to other systems. Among the many conclusions is that it is extremely important not only to properly describe the inter-atomic shielding functions but to also use very accurate potential energy functions. Even small errors in the functional descriptions of the two interactions can lead to systematic errors in the calculated chemical shifts.[79] The availability of these functions is the primary limit to applying these types of calculations to a wider range of porous materials. While results for zeolites, where the walls are primarily composed of oxygen atoms have been in good agreement with experiment, applying these calculations to more complex frameworks can be problematic due to the lack of proper potential and shielding functions. Recent results have shown that Xe-CH_4 potential and shielding functions are adequate to reproduce the experimental results for Xe in dipeptide channels and in the channels of $Co(en)_3Cl_3$.[80,81]

In addition to reproducing relative isotropic chemical shifts, the greatest potential of the GCMC method for calculating Xe chemical shifts is in its ability to reproduce experimentally observed Xe lineshapes. Anisotropic chemical shift lineshapes have been observed for Xe in a number of porous materials (see below). Jameson first demonstrated the calculation of Xe chemical shift lineshapes for AlPO-11.[62] Not only was Jameson able to reproduce the lineshape of a single Xe in the one-dimensional channel, but she was also able to reproduce the effects that increased Xe loading have on the lineshape, Figure 2.20.[62] The calculations accurately reproduced the experimental Ω

and κ observed by Ripmeester and coworkers for Xe in $AlPO_4$-11 at various Xe loadings. The GCMC simulations have been used to calculate Xe chemical shift lineshapes in a variety of simple pore geometries including narrow-bore and medium-bore pipes, capped pipes and disks, and parallel plates, many of which can be used as models for porous materials.[82]

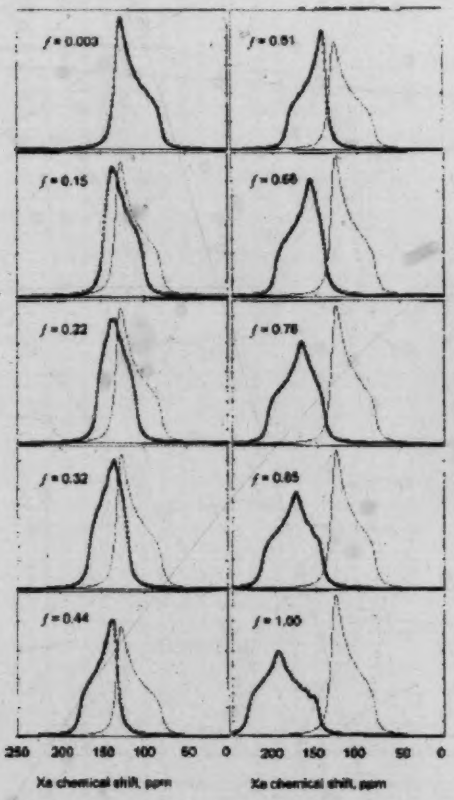

Figure 2.20: Xe NMR lineshapes from GCMC simulations as a function of occupancy of Xe in $AlPO_4$-11. The Xe–channel contribution (shown in gray) is displayed together with the total spectrum (shown in black). Occupancies are shown as fractions of maximum occupancy. Figure reprinted with permission from Ref. 62.

2.5 Experimental examples of ^{129}Xe NMR of microporous materials

2.5.1 Zeolites: cage structures

The term microporous refers to materials which have accessible pore spaces with diameters between 2.5 and 20 Å.[83] The most important and widely studied microporous materials are zeolites and other zeotype structures. Zeolites are Si/AlO_4 materials that can be synthesized or obtained from natural sources. The host framework is formed by TO_4 tetrahedra, **T** = Al or Si, that connect through the corners of the tetrahedra to form

infinite networks, yielding an overall formula of TO_2. If all the **T** atoms have a formal charge of 4+, such as Si^{4+}, then the framework is neutral. When other cations are substituted, such as Al^{3+}, then the negative framework charge has to be balanced by counterions such as Na^+. Other zeotype structures are formed with aluminum and phosphorus atoms occupying the **T** sites and are referred to as $AlPO_4$s. In addition to these common **T** atoms, frameworks with a wide variety of cations occupying the **T** sites in tetrahedral frameworks have been reported.[84]

The study of the pores in zeolites was the impetus for the development of ^{129}Xe NMR spectroscopy of porous materials and the first systems investigated were zeolites X and Y.[85] Zeolite X/Y structures, the X and Y refer to the Al/Si ratio, form a large spherical α-cage with a free space diameter of 11.2 Å which has 12 member ring windows that can allow molecules as large as 7.3 Å to enter the cage.[86] The counter-ions present in zeolite X/Y can be changed and can influence the ^{129}Xe chemical shift. The chemical shift dependence on Xe loading is linear for the alkali-ion and H^+ exchanged zeolite X/Y. For H^+, Li^+ and Na^+, the δ_s values, δ extrapolated to zero loading, are approximately 58 ppm and show little dependence on the Si/Al ratios.[85] For larger cations δ_s increases, 78 ppm for the K^+ and 90 ppm for the Rb^+ exchangd zeolites.[87]

Exchanging singly charged cations for doubly-charged Ca^{2+} and Mg^{2+} ions leads to non-linear chemical shift vs. Xe loading plots.[65,87,88] It has been suggested that these curved dependencies are a result of strong adsorption sites associated with the M^{2+} ions. It is from the differences between the M^+ and M^{2+} ions that the some researchers have proposed a δ_E term be added to equation 2.17.[65,87] Xe-129 NMR spectroscopy has been shown to be sensitive to both the extent of exchange, i.e. the M^+/M^{2+} ratio, and on the level of hydration.[87]

When Ag^+ or Cu^+ are exchanged into zeolite X, there is a remarkable increase in the shielding of the Xe nucleus.[31,89,90,91,92] At low Xe concentrations chemical shifts of -40 to -50 ppm are observed for Xe in zeolite AgX.[31] It has been postulated that these unusual shifts arise when Xe atoms form short lived complexes with the cations and there is back donation of *d* electrons from the Ag^+ ($4d^{10}$) or Cu^+ ($3d^{10}$) ions to the Xe ($5d^0$).[90,92]

The studies of zeolite A are important because they provided some of the first systems where the correlations between ^{129}Xe NMR chemical shift and zeolite structure were made at an atomic level; this included the first system described using GCMC simulations to reproduce the experimental ^{129}Xe NMR results, see Section 2.4.3. Zeolite A consists of α-cages that are large enough to accommodate ~8 Xe atoms and are connected by 8 member ring windows that are large enough to allow Xe to enter, Figure 2.19. Smaller β-cages are accessed through six-membered rings which are too small for Xe to pass through. Some of the Na^+ ions occupy positions in the large windows of the α-cages, partially blocking them and greatly reducing the ability of Xe to exchange from cage to cage.[48,93,94] Due to the slow cage-to-cage exchange it can take months for the samples to reach thermal equilibrium. Even when the samples are heated to 500 K first, to establish a high temperature equilibrium distribution of Xe atoms, and then allowed to cool to 300 K, it can take two months to establish thermal equilibrium at 300 K.[75]

The ^{129}Xe NMR spectra of Xe in zeolite NaA show multiple peaks resulting from cages with different numbers of Xe atoms. Even when the average number of Xe atoms per cage is below one, a distribution could be observed, Figure 2.18. When the average number of Xe atoms is increased, the distribution of Xe cage occupancies changes.[75] The distribution of cage occupancies, as determined from the NMR signal intensities, does not follow a completely statistical distribution for hard spheres in a confined space for either a specific site or a freely moving Xe adsorption model. This suggests that Xe-Xe attractive interactions are important and that the formation of Xe clusters is favoured at medium and high Xe loadings.[75]

The Xe exchange rate for Xe atoms moving between different Xe clusters has been measured using ^{129}Xe 2-D exchange spectroscopy, EXSY, experiments, Figure 2.21.[95] By varying the amount of time Xe was allowed to exchange during the experiment, τ_{mix}, and performing a rigorous analysis of the cross-peak intensities, the rate of exchange between different Xe clusters was obtained. The data was used to calculate the adsorption separation energies for the different Xe clusters, i.e., the energy required for Xe to move from one cage to a cage with a different Xe loading, which varied from -16 to -23 kJ/mol.[95] Further studies of the exchange process using one-dimensional techniques were able to determine all of the exchange rates and found that the exchange

varied as a function of loading and depended on the occupancy of both the cage the Xe atom was moving from and the one it was moving to.[96] The exchange rates varied from 2.5 s^{-1}, for a Xe atom leaving a cage with 8 Xe atoms, to 0.1 s^{-1}, for Xe atoms moving from cages with a single Xe to cages with 7 Xe atoms.[96]

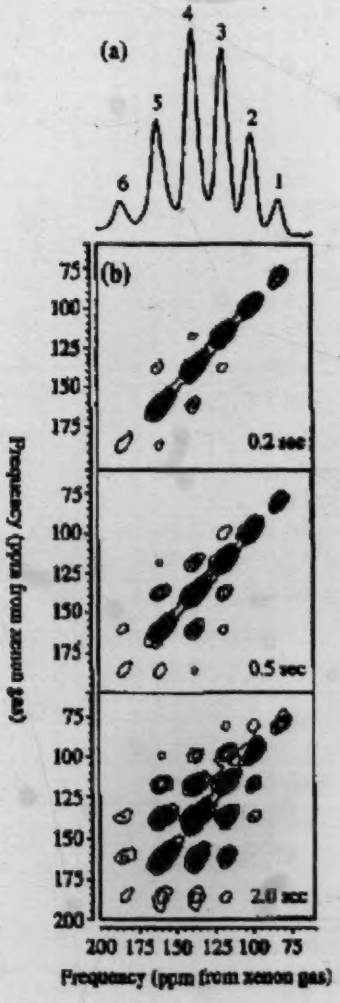

Figure 2.21: a) ^{129}Xe 1-D NMR spectrum of Xe adsorbed in zeolite NaA. b) ^{129}Xe 2-D exchange NMR spectra of Xe as a function of τ_{mix}. The diagonal peaks correspond to the ^{129}Xe resonances from α-cages with different numbers of Xe atoms. The cross-peak intensities provide an indication of the number of Xe atoms that are exchanging between the corresponding cages during the indicated τ_{mix}. Figure reprinted with permission from Ref. 95.

The study of zeolite KA, which is isostructural to zeolite NaA, revealed analogous behaviour of the ^{129}Xe NMR spectra as a function of Xe loading and temperature.[97] The study allowed two important observations to be made, (1) an increase in the slopes of the chemical shift vs. Xe loading as a function of cation size, (2) an increase in the chemical shifts at the zero loading limit due to increasing cation size; this was later proven theoretically with GCMC simulations.[97] These results provided a basis for understanding

the chemical shift changes observed previously for zeolite X/Y when the cation was changed from Na^+ to K^+ or Rb^+.

When the twelve Na^+ ions in zeolite NaA are exchanged for six Ca^{2+} ions the ^{129}Xe NMR spectra no longer contain different peaks for the different Xe occupancy numbers.[85,98,99,100] While the framework structure of zeolite NaA and CaA is the same, the position of ions is different. Most notably, no Ca^{2+} ions occupy positions blocking the eight-member windows of the α-cage. As a result the exchange of Xe between cages is faster and only one isotropic peak is observed. The chemical shift as a function of Xe loading and temperature can be explained using the distribution model developed by Jameson for zeolite NaA. It was found that the free space within the α-cage was slightly greater for CaA due to the lower number and smaller size of Ca^{2+} ions. This allowed for an average loading of greater than eight Xe atoms to be reached. The chemical shift as a function of Xe loading varied from 90 ppm at the zero loading limit, to ~280 ppm for a loading of nine Xe atoms per cage.[98] The systematic substitution of Ca^{2+} for Na^+ has been studied both experimentally and theoretically.[100,101] The results point to significant polarization of the Xe atoms by the divalent cations, leading to a deviation from the pairwise-additivity model of the inter-atomic potential energies. Using GCMC simulations the different influences of the Na^+ and Ca^{2+} ions on the ^{129}Xe chemical shifts were shown to be useful in determining the location of the cations as the Na^+ ions were systematically replaced by Ca^{2+} ions.[101]

2.5.2 Zeolites: channel structures

Many zeolites contain well defined channels rather than interconnected cages. These channel systems can range from one-dimensional to three-dimensional systems. The geometry of the microporous channel systems is reflected in the Xe chemical shift anisotropy. This anisotropy has been observed mainly for 1-D channels.

The first 1-D channel studied for which anisotropic ^{129}Xe chemical shifts were observed was AlPO/SAPO-11; [102] SAPO-11 is iso-structural to AlPO-11 but with some of the Al atoms replaced by Si atoms. In the initial study the spectra were observed to be axially symmetric both at high and low Xe loading; at low loading the lineshape had a skew, κ, of 1 while at high loading the κ changed sign to -1.[102] This change in the skew

arises from increased Xe-Xe interactions. A subsequent study by Ripmeester and Ratcliffe characterized the loading dependence of the ^{129}Xe lineshape using ten different Xe loadings.[103] At the lowest loadings the lineshape was axially symmetric with a skew of 1.0. As the Xe pressure was raised, δ_{33} increased, eventually reaching a point where the chemical shift tensor had a skew of -1.0. With continued Xe loading, however, the lineshape continued to change until a non-axially symmetric lineshape was observed.

While an initial explanation for the change in lineshape was made based on a simple distribution model, a more thorough correlation of the lineshape and pore geometry was proposed based on GCMC simulations.[62,82] The ALPO-11 channel is elliptical, with a cross-section of 6.7 by 4.4 Å. At low loading the Xe atoms preferentially reside along the walls of the channel resulting in three unique shielding components, two of which are very close to each other in magnitude, Figure 2.22b; this gives rise to the nearly axially symmetric lineshape observed. As the Xe loading is increased, the shielding component parallel to the channel, $\delta_{\|}$, remains constant while the other two components, $\delta_{\perp}$, and δ_t, change due to increased Xe-Xe interactions, Figure 2.22, resulting in the changes in lineshape observed experimentally.

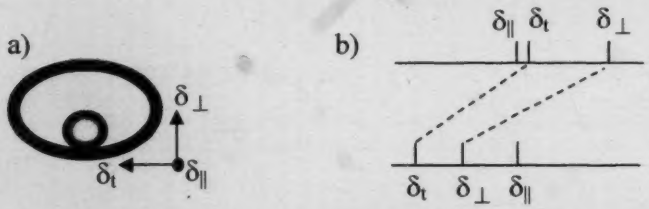

Figure 2.22: Xe in an elliptical 1-D channel such as ALPO-11 a) Diagram showing the orientation of the three tensor components; $\sigma_{\|}$, the component along the channel; $\sigma_{\perp}$, the component perpendicular to the channel axis and the wall; σ_t the component tangential to the wall. b) The relative positions of the components at low (top) and high (bottom) Xe loading.[82]

One of the simplest channel systems investigated using ^{129}Xe NMR spectroscopy is that of AlPO/SAPO-5.[104,105,106] Most of the studies show that an anisotropic lineshape is observed that changes as a function of Xe loading. The channels are cylindrical with a diameter of approximately 7.3 Å. Unlike for AlPO-11, the Xe is uniformly distributed about the cross-section of the channel, i.e., there are no potential wells along the walls of

the channels. The Xe chemical shift along the channel, which results from Xe interactions perpendicular to the channel axis, is different than the chemical shift components perpendicular to the channel axis, which result from interactions along the channel.[82,106] At low Xe pressure the deshielding caused by Xe-wall interactions is greater than any shielding caused by interactions along the channel axis, Figure 2.23a. At elevated Xe loadings, a nearly isotropic peak is observed.[106] This is because the deshielding perpendicular to the channel increases as a result of increased Xe-Xe interactions along the channel; the perpendicular and parallel components are fortuitously the same value, Figure 2.23b. The isotropic peak could also indicate that at elevated pressures the Xe atoms are no longer restricted to single file diffusion but could be passing one another, thereby making Xe-Xe interactions the dominant interaction both perpendicular and parallel to the channel, Figure 2.23c.

Figure 2.23: a) Xe in a 1-D channel such as ALPO-5 at low Xe loading. b) and c) the two models to explain the origin of the isotropic peak observed in the ^{129}Xe NMR spectrum at high loading.

Other zeolites that posses 1-D channels have also been studied and show similar characteristic lineshapes to those observed for AlPO-11 and AlPO-5. Some of these include silicalite,[107,108] ZSM-12,[109] SSZ-24,[110,111,112] AlPO/SAPO-31,[106] and AlPO/SAPO-41.[113,106]

2.5.3 Microporous materials with "organic" walls

Whereas there are many studies using ^{129}Xe NMR spectroscopy to investigate inorganic micropores there are few reports of ^{129}Xe NMR spectroscopy of Xe in organic based porous systems. Since the Xe chemical shift at low loading depends on the intermolecular shielding between Xe and the walls, the chemical shifts of Xe in organic

systems are expected to be different than for inorganic systems. The wide variety of organic functional groups that can make up the framework leads to many complications when trying to analyze and interpret chemical shifts in such systems. Xe will have different shielding responses to the different functional groups along with different potential energy interactions. While recent attempts to calculate ^{129}Xe chemical shifts in organic systems using the GCMC method have met with some success, they have relied on modeling the channel walls using CH_4 molecules,[80,81] this type of model is only adequate for a subset of microporous organic materials.

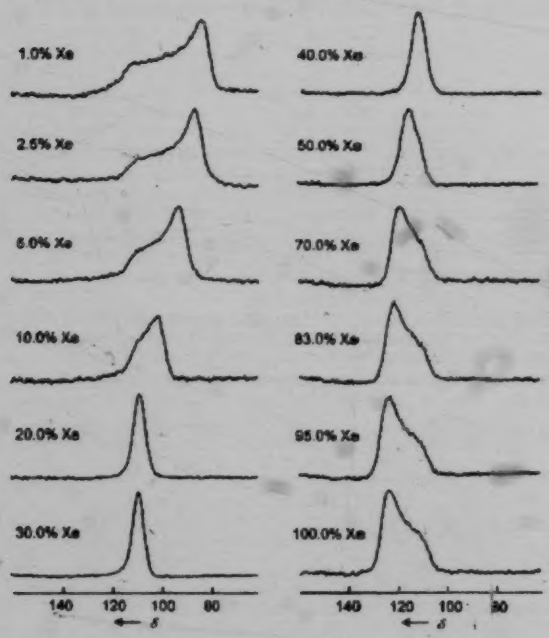

Figure 2.24: Continuous-flow hyperpolarized ^{129}Xe NMR spectra of Xe/He mixtures flowing in the 1-D channels of TPP. Figure reproduced from Ref. 114.

The study of tris(o-phenylenedioxy)cyclophosphazene, TPP, using ^{129}Xe NMR spectroscopy is one of the best examples of using ^{129}Xe NMR spectroscopy to study an "organic" channel system.[114] The TPP molecules form hexagonal, one-dimensional channels in the solid state that have a van der Waals diameter of ~5 Å. The ^{129}Xe NMR spectra of HP Xe show axially symmetric ^{129}Xe NMR powder patterns that change as a function of Xe concentration and are generally centered near 110 ppm, Figure 2.24.[114] The change in lineshape is similar to that observed for one-dimensional zeolite channels as a function of Xe loading, see Section 2.5.2. These results reveal that the continuous-

flow HP Xe experiment can be used to obtain Xe loading data that are comparable to these obtained from samples sealed with varying pressures of Xe gas.

Because of the unique nature of the HP Xe NMR experiment, researchers were able to determine that the diffusion of Xe within the TPP channel was single-file.[115] Once the HP-Xe has been exposed to an NMR pulse sequence it is effectively "dead" and will not contribute to the signal from future pulse sequences. By measuring the signal intensity of the adsorbed Xe peak as a function of recycle time, estimates of the time it takes for fresh HP Xe to diffuse into the channels could be obtained. The resulting curves could only be fit with an equation that described single-file diffusion.[115]

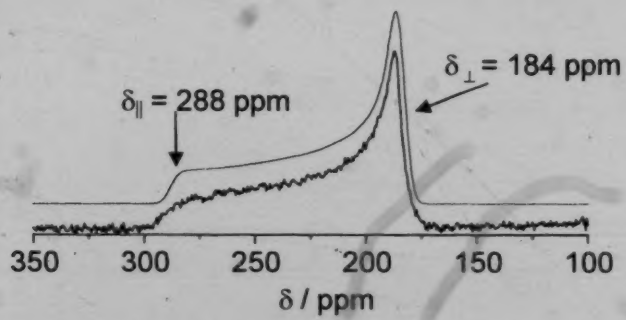

Figure 2.25: Continuous-flow hyperpolarized ^{129}Xe NMR spectra of Xe in $Co(en)_3Cl_3$.

Cobalt(III) ethylenediamine chloride crystallizes to form one-dimensional channels along the crystallographic *c*-axis which contain alternating segments with channel diameters of 3.7 and 4.0 Å. The $Co(en)_3Cl_3$ channels are smaller than those formed in TPP, and as a result the isotropic chemical shifts are much larger, δ_{iso}(0 atm) = 212 ppm.[116] The span of the Xe chemical shift tensor is 104 ppm and also indicates how tight the fit is for Xe in the channels, Figure 2.25. The changes in the lineshape as a function of Xe loading were much smaller than for other 1-D channel systems. Using GCMC simulations this was correlated to the fact that even at high pressures, Xe atoms only resided in the larger of the two segments; the smaller segment being too narrow for Xe to occupy for significant amounts of time; this leads to minimal Xe-Xe interactions even when the sample is exposed to high Xe pressures.[81]

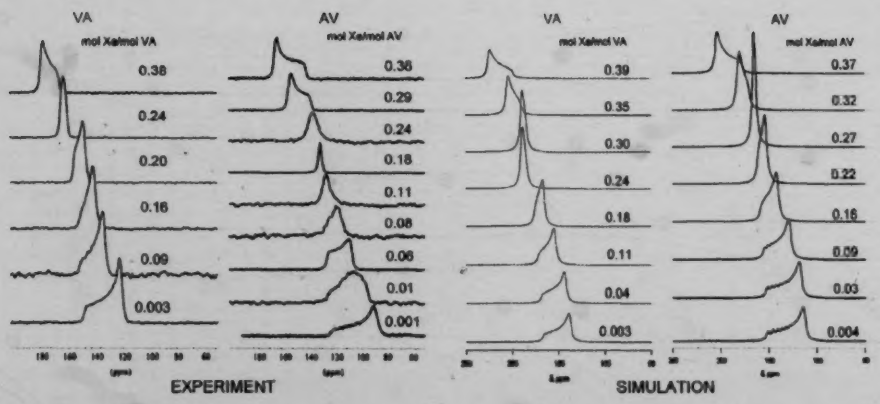

Figure 2.26: The experimental thermally polarized Xe NMR spectra at room temperature, at various Xe occupancies in VA and AV crystals, are compared with the Xe NMR spectra calculated by GCMC simulations. Figure reprinted with permission from Ref. 80.

Crystalline peptide nanochannels are formed when certain pairs of amino acids hydrogen bond in the solid state to form stacks that contain 1-D channels. These channels range in diameter from 3.0 to 5.36 Å and can accommodate Xe atoms.[117] The ^{129}Xe NMR spectra of eight different channels reveal that the Xe chemical shift tensors are axially symmetric with spans that ranged from 18 to 70.5 ppm and isotropic chemical shifts that ranged from 98.7 to 264.3 ppm.[117] A good correlation was observed between the pore diameter and δ_{iso}. The presence of strong ^{129}Xe NMR signals for channels with diameters less that the van der Waals diameter of Xe indicate that the channels are flexible and can change dimensions slightly to accommodate the Xe atoms. GCMC calculations of Xe in the Ala-Val and Val-Ala channels, two retroanalogues that have slightly different channel dimensions, were able to reproduce the trends observed in the ^{129}Xe powder lineshapes as a function of Xe loading, Figure 2.26.

2.6 Examples of ^{129}Xe NMR in mesoporous materials

2.6.1 MCM-41 and its analogues

In 1992 Kresge and coworkers reported the synthesis of a new class of porous materials prepared using a liquid crystal as a templating agent.[118] The resulting material had 1-D channels with diameters up to ~100 Å. This family of materials, designated

M41S, represented the first examples of synthetic ordered mesoporous materials. While the channel structures are ordered, the materials are not crystalline. The positions of the Si and O atoms in the walls of the pores are disordered and the geometries of the SiO_4^{4-} tetrahedra also vary. As a result, it is not possible to obtain single-crystal X-ray diffraction structures of these materials.

Pietraß and coworkers have used ^{129}Xe NMR spectroscopy to study pores created when different quantities of methanol are used in the aqueous surfactant solution during the synthesis of M41S materials.[119] For preparations which were known to form hexagonal mesophases, Xe was observed adsorbing into the mesopores. The sample obtained when 70% methanol was used in the synthesis had a more disordered structure and there was little sign that Xe could access a porous environment, a conclusion that could not be drawn from N_2 adsorption measurements. For samples that were not dehydrated an increased chemical shift was observed; it was hypothesized that a layer of water formed on the inside of the channels, changing the interaction of Xe with the walls. In addition to the chemical shifts, the Xe T_1 relaxation times were used to support the conclusions about pore accessibility and the influence of hydration.[119]

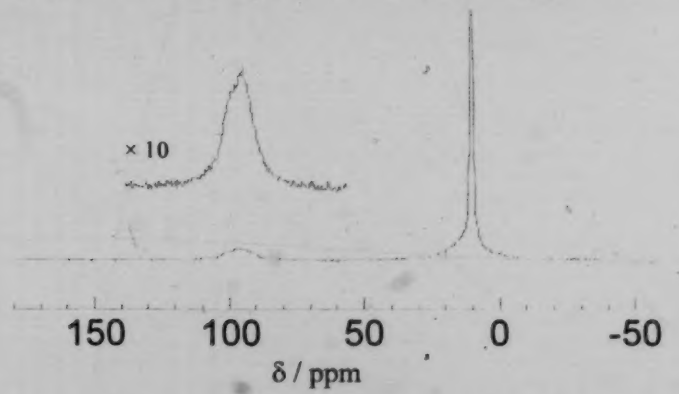

Figure 2.27: HP ^{129}Xe NMR spectrum of Xe in MCM-41.

Another study of M41S materials with 1-D and 2-D channels used EXSY experiments to determine the presence of surface roughness.[120] For many mesoporous materials, such as MCM-41, broad ^{129}Xe NMR linewidths and asymmetries in the lineshape arise from variation in the Xe adsorption environments, Figure 2.27. It was concluded based on EXSY experiments that the exchange between different

environments was rapid. For the bimodal sample, SBA-15, before hydrothermal treatment, the EXSY experiments revealed much longer exchange times, implying greater surface roughness.[120]

Other studies have used HP ^{129}Xe NMR to study different ordered mesoporous materials and supported mesoporous silica thin films.[121,122] The thin film study demonstrated how HP ^{129}Xe could be used to study 0.1 to 0.2 mg of mesoporous sample, a quantity that could not be studied effectively using conventional thermally polarized ^{129}Xe NMR spectroscopy.

2.6.2 Amorphous porous silica materials

Amorphous porous silica materials contain pores that have no regular, repeating structure. Some materials that fall into this category are silica gels, controlled pore glasses, and Vycor glasses. The first such systems to be studied were aerosils, porous spheres of silica with diameters of 12 and 7 nm, that were compressed to form disordered pore spaces between the beads.[123] This study recognized that the adsorption dynamics of the Xe at low loadings could be described using Henry's law to determine the fraction of Xe atoms adsorbed on the surface. Henry's law is a common set of equations used to describe gas adsorption at low loadings, when gas-gas interactions are minimal.[73] The use of Henry's law was later extended by Terskikh and coworkers who performed the most extensive study of amorphous porous silica materials.[124] Xe-129 NMR spectra were acquired at room temperature for thirty-four different samples and the chemical shifts were plotted against the mean pore diameters, Figure 2.28.

The data was analyzed using a fast-exchange two-site model, assuming that equation 2.20 was valid. In the low loading limit, Henry's law was used to determine the number of Xe atoms adsorbed on a surface

$$n_a = KP_g S_a \qquad 2.28$$

$$K = K_0 \exp(\Delta H_{ads} / RT) / T^{1/2} \qquad 2.29$$

where P_g is the Xe gas pressure, S_a is the specific surface area, K is Henry's constant, ΔH_{ads} is the heat of adsorption, R is the ideal gas constant, and K_0 is the pre-exponential

term. Since K is temperature dependent, the chemical shift also changes with temperature.[125] When applied to porous materials Henry's law is only valid in the low loading regime, therefore, at low temperatures or high gas pressures other adsorption models must be used such as the Langmuir theory for adsorption in porous materials. The book by Rouquerol et. al. is useful for understanding adsorption phenomena in porous materials.[73]

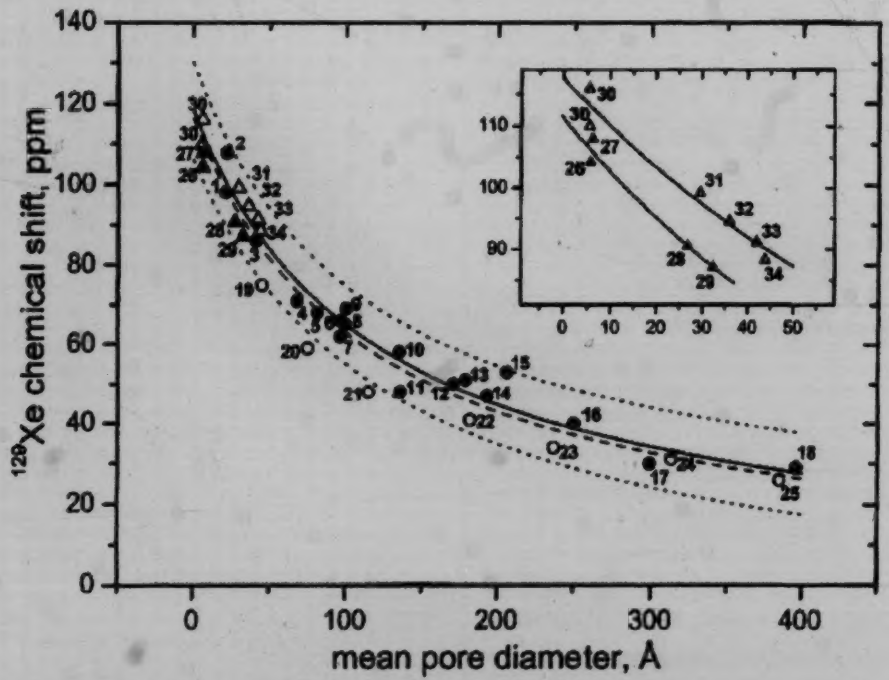

Figure 2.28: ^{129}Xe NMR chemical shift vs. mean pore diameter for porous silica-based materials, •, silica gel; ○, Vycor/controlled pore glass; ▲, porous organosilicates (akin to ordered mesoporous silica materials). Figure reprinted with permission from Ref. 124.

For the thirty-four silica samples studied the correlation between chemical shift and pore size was found to follow the equation:

$$\delta = \frac{\delta_s}{(1 + D/\eta KRT)} \qquad 2.30$$

where δ_s is the chemical shift characteristic of the interaction of Xe with the silica surface (replaces δ_a in equation 2.20), D is the mean pore diameter, η is a pore geometry factor, K

is the adsorption constant, and T is the temperature. As a result of the analysis a value for δ_s of 116 ppm was obtained. Although the analysis relies on a fairly simplistic description of Xe distribution within the pores, the resulting correlation clearly shows the utility of using simple models for interpreting experimental results. The fast-exchange two-site model works for mesoporous materials because the potential energy surface has two distinct regimes, the low energy wells along the walls where adsorption occurs and large flat potential energy humps in the center of the pores where the Xe acts as a free gas. The minimum pore size where the model can be used is still unclear, but as has been shown by Jameson and coworkers, for small micropores the model is inadequate.

2.7 Xe-129 NMR in multi-domain porous materials

Many porous materials cannot be classified as solely microporous or mesoporous due to the presence of different adsorption regions within the material. This is particularly true for many naturally occurring porous minerals. Montmorillonite is a pillared clay that can form different sized cavities between the layers of the clay depending on the molecules adsorbed by the material; this space is referred to as the interlamellar space. When montmorillonite pillared with pyridinium ions was studied using HP ^{129}Xe NMR spectroscopy, two different porous regimes were distinguished, Figure 2.29.[110] At elevated temperatures the Xe was observed preferentially adsorbing in the microporous interlammellar space; a chemical shift of 170 ppm was observed. As the temperature was lowered, the Xe condensed within the micropores, leading to a loss in the HP ^{129}Xe signal. At low temperatures, Xe was then observed adsorbing into mesoporous void spaces in the sample; a chemical shift of ~90 ppm appeared. This example of using HP ^{129}Xe to explore the behavior of Xe in a material emphasizes how information about gas-framework interactions can be obtained.

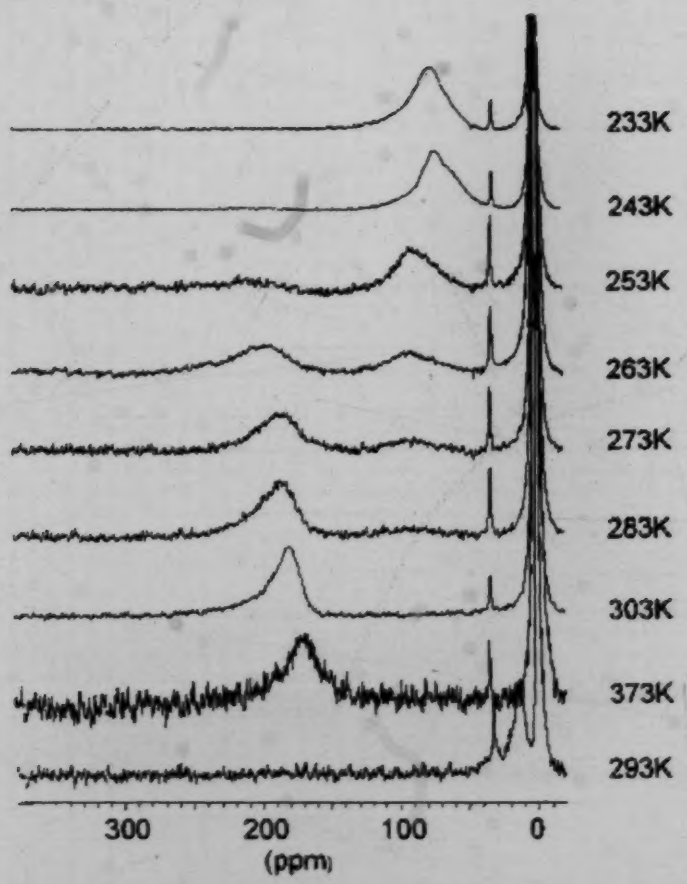

Figure 2.29: Variable temperature HP ^{129}Xe NMR spectra of Xe adsorbed in montmorillonite pillared with pyridinium ions under magic angle spinning conditions. Figure reprinted with permission from Ref. 110.

Many silicas also contain multiple porous domains. A HP ^{129}Xe NMR study of resorcinol-formaldehyde, RF, aerogels revealed the presence of both microporous regions, with a large variation in pore size, as well as mesoporous space.[126,127] Variable temperature HP ^{129}Xe experiments were used to characterize the Xe chemical shift as a function of temperature. Analysis of the variation using the Henry's law chemical shift equations, equations 2.28 and 2.29, allowed for estimates of the adsorption energy and δ_s of the mesoporous phase to be obtained. 2-D EXSY experiments provided information on the connectivity of the microporous and mesoporous spaces. At zero mixing time, τ_{mix} = 0 ms, no cross-peaks were observed. At τ_{mix} = 1 ms cross-peaks between the Xe gas

peak and the peak from Xe in the mesopores was observed. When τ_{mix} was increased to 8 ms, cross-peaks between the mesoporous space and the microporous space peaks were present but no cross-peaks between the free gas and the micropore peaks were evident, Figure 2.30. This led researchers to conclude that the micropores are only accessible through the mesoporous space.

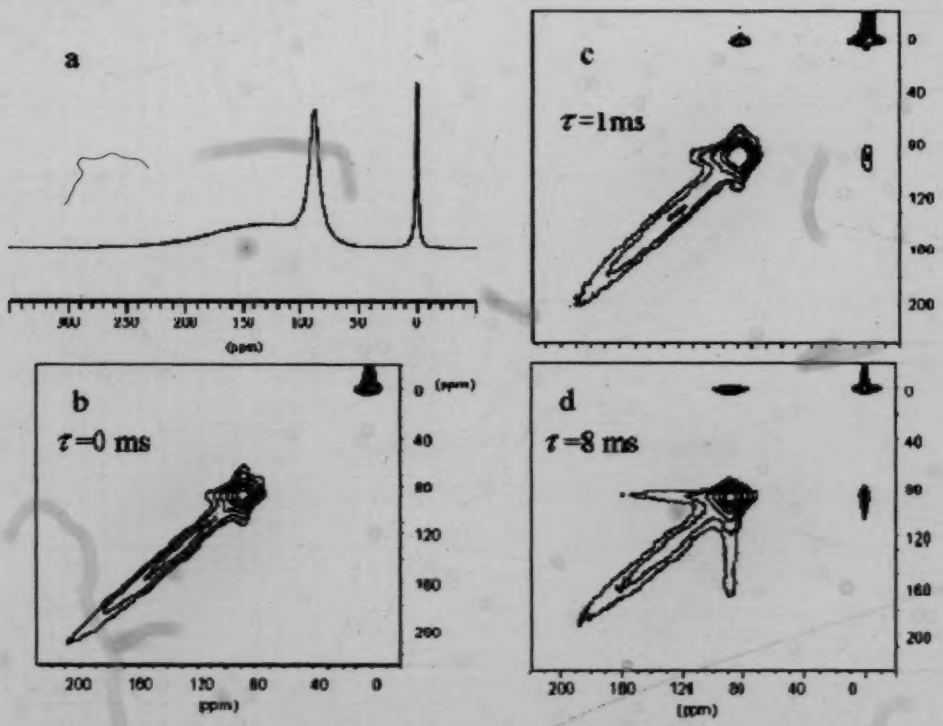

Figure 2.30: Continuous flow HP ^{129}Xe NMR spectra of Xe in an RF aerogel. a) the 1-D spectrum. b-d) 2D EXSY spectra acquired with the indicated mixing times. Figure reprinted with permission from Ref. 126.

Another class of materials that contain different adsorption regions is functionalized mesoporous materials. In a drive to add different functional groups to inorganic porous materials, many researchers have grafted inorganic or organic functional groups onto the walls of ordered mesoporous materials. Xe atoms can reside in the remaining mesoporous regions, or they can be closely associated with the functional groups grafted on the walls. Mesoporous silica functionalized with long chain organic surfactant molecules contain both Xe in the mesoporous cavity and Xe

intercalated between the flexible organic chains.[128,129] Similar ^{129}Xe NMR spectra are obtained for calixarene-based solid lipid nanoparticles.[130]

---

[1] Dybowski, C.; Bansal, N.; Duncan, T. M. *Annu. Rev. Phys. Chem.* **1991**, *42*, 433-464.

[2] Barrie P. J.; Klinowski, J. *Prog. Nuçl. Magn. Reson. Spectrosc.* **1992**, *24*, 91-108.

[3] Springuel-Huet, M. A.; Bonardet J. L.; Fraissard, J. *Appl. Magn. Reson.* **1995**, *8*, 427-456.

[4] Ratcliffe, C. I.; *Annu. Rep. NMR Spectrosc.* **1998**, *36*, 123-221.

[5] Bonardet, J.-L.; Fraissard, J.; Gédéon A.; Springuel-Huet, M.-A. *Catal. Rev.–Sci. Eng.* **1999**, *41*, 115-225.

[6] Springuel-Huet, M.-A.; Bonardet, J.-L.; Gédéon A.; Fraissard, J. *Magn. Reson. Chem.* **1999**, *37*, S1-S13.

[7] Brunner, E. *Magn. Reson. Chem.* **1999**, *37*, S14-S22.

[8] Goodson, B. M. *J. Magn. Reson.* **2002**, *155*, 157-216.

[9] Oros, A.-M.; Shah, N. J. *Phys. Med. Biol.* **2004**, *49*, R105-R153.

[10] Happer, W.; Miron, E.; Schaefer, S.; Schreiber, D.; van Wijngaarden, W. A.; Zeng, X. *Phys. Rev. A* **1984**, *29*, 3092-3110.

[11] Knize, R. J.; Wu, Z.; Happer, W. in *Advances in Atomic and Molecular Physics,* Vol. 24; Bates, D.; Bederson, B. Eds. Academic Press: Boston, 1988; 223-267.

[12] Driehuys, B.; Cates, G. D.; Miron, E.; Sauer, K.; Walter D. K.; Happer, W. *Appl. Phys. Lett.* **1996**, *69*, 1668-1670.

[13] Walker T. G.; Happer, W. *Rev. Mod. Phys.* **1997**, *69*, 629-642.

[14] Appelt, S.; Ben-Amar Baranga, A.; Erickson, C. J.; Romalis, M. V.; Young, A. R.; Happer, W. *Phys. Rev. A* **1998**, *58*, 1412-1439.

[15] *The Merck Index, 8th edition*, Stecher, P. G., Ed., Merck & Co., Inc. Rahway, New Jersey. 1968.

[16] Ramsey, N. F. *Phys. Rev.* **1950**, *78*, 699-703.

[17] Jameson, C. J. In *Multinuclear NMR*; Mason, J., Ed. Plenum: New York, 1989, pp 463-477.

[18] Jameson, C. J.; Gutowsky, H. S. *J. Chem. Phys.* **1964**, *40*, 1714-1724.

[19] Kolb, D.; Johnson, W. R.; Shorer, P. *Phys. Rev. A* **1994**, *26*, 19-31.

[20] Bishop, D. M.; Cybulski, S. M. *J. Magn. Reson. A* **1994**, *107*, 99-101.

[21] Vaara, J.; Pyykkö, P. *J. Chem. Phys.* **2003**, *118*, 2973-2976.

[22] Mason, J. *Solid State Nucl. Magn. Reson.* **1993**, *2*, 285-288.

[23] Sears D. R.; Klug, H. P. *J. Chem. Phys.* **1962**, *37*, 3002-3006.

[24] Harris, R. K.; Becker, E. D.; De Menezes, S. M. C.; Goodfellow, R.; Granger, P. *Pure Appl. Chem.* **2001**, *73*, 1795-1818.

[25] Moudrakovski, I. L.; Ratcliffe, C. I.; Ripmeester, J. A. *J. Am. Chem. Soc.* **2001**, *123*, 2066-2067.

[26] Aziz, R. A.; Slaman, M. J. *Mol. Phys.* **1986**, *57*, 825-840.

[27] Maitland, G. C. *Mol. Phys.* **1973**, *26*, 513-528.

[28] Schwalbe, L. A.; Crawford, R. K.; Chen, H. H.; Aziz, R. A. *J. Chem. Phys.* **1977**, *66*, 4493-4502.

[29] Davies, G. R.; Halstead, T. K.; Greenhow, R. C.; Packer, K. J. *Chem. Phys. Lett.* **1994**, *230*, 237-242.

[30] Gatzke, M.; Cates, G. D.; Driehuys, B.; Gox, D.; Happer, W.; Saam, B. *Phys. Rev. Lett.* **1993**, *70*, 690-693.

[31] Gédéon, A.; Burmeister, R.; Grosse, R.; Boddenberg, B.; Fraissard, J. *Chem. Phys. Lett.* **1991**, *179*, 191-194.

[32] Jameson, A. K.; Jameson, C. J.; Gutowsky, H. S. *J. Chem. Phys.* **1970**, *53*, 2310-2321.

[33] Jameson, C. J. *J. Chem. Phys.* **1975**, *63*, 5296-5301.

[34] Ripmeester, J. A.; Davidson, D. W. *Bull. Magn. Reson.* **1981**, *2*, 139

[35] Ripmeester, J. A.; Davidson, D. W. *J. Mol. Struct.* **1981**, *75*, 67-72.

[36] Bartik, K.; Luhmer, M.; Heyes, S. J.; Ottinger, R.; Reisse, J. *J. Magn. Reson. B.* **1995**, *109*, 164-168.

[37] Song, Y.-Q.; Goodson, B. M.; Taylor, R. E.; Laws, D. D.; Navon, G.; Pines, A. *Angew. Chem. Int. Ed. Engl.* **1997**, *36*, 2368-2370.

[38] Luhmer, M.; Goodson, B. M.; Song, Y.-Q.; Laws, D. D.; Kaiser, L.; Cyrer, M. C.; Pines, A. *J. Am. Chem. Soc.* **1999**, *121*, 3502-3512.

[39] Bowers, C. R.; Storhaug, V.; Webster, C. E.; Bharatam, J.; Cottone, A. III; Gianna, R.; Betsey, K.; Gaffney, B. J. *J. Am. Chem. Soc.* **1999**, *121*, 9370-9377.

[40] Rubin, S. M.; Spence, M. M.; Goodson, B. M.; Wemmer, D. E.; Pines, A. *Proc. Natl. Acad. Sci.* **2000**, *97*, 9472-9475.

[41] Sears, D. N.; Jameson, C. J. *J. Chem. Phys.* **2003**, *119*, 12231-12244.

[42] Montet, Y.; Amara, P.; Volbeda, A.; Vernede, X.; Hatchikian, E. C.; Field, M. J.; Frey, M.; Fontecilla-Camps, J. C. *Nat. Struct. Biol.* **1997**, *4*, 523-526.

[43] Rubin, S. M.; Lee, S. Y.; Ruiz, E. J.; Pines, A.; Wemmer, D. E. *J. Mol. Biol.* **2002**, *322*, 425-440 (2002).

[44] Koh, C. A. *Chem. Soc. Rev.* **2002**, *31*, 157-167.

[45] Hammerschmidt, E. G. *Ind. Eng. Chem. Res.* **1934**, *26*, 851-855.

[46] Ripmeester, J. A. *J. Am. Chem. Soc.* **1982**, *104*, 289-290.

[47] Ripmeester, J. A.; Ratcliffe, C. I.; Tse, J. S. *J. Chem. Soc., Faraday Trans. 1* **1988**, *84*, 3731-3745.

[48] Ripmeester, J. A.; Ratcliffe, C. I. *J. Phys. Chem.* **1990**, *94*, 8773-8776.

[49] Ripmeester, J. A.; Tse, J. S.; Ratcliffe, C. I.; Powell, B. M. *Nature* **1987**, *325*, 135-136

[50] Moudrakovski, I. L.; Sanchez, A. A.; Ratcliffe, C. I.; Ripmeester, J.A. *J. Phys Chem. B* **2001**, *105*, 12338-12347.

[51] Storhaug, V. J.; Liebig, F.; Bowers, C. R. *J. Phys. Chem. B* **2002**, *106*, 2884-2891.

[52] Lee, F.; Gabe, E.; Tse, J. S.; Ripmeester, J. A. *J. Am. Chem. Soc.* **1988**, *110*, 6014-6019.

[53] Stengle, T. R.; Williamson, K. L. *Macromolecules* **1987**, *20*, 1430-1431.

[54] Kentgens, A. P. M.; van Boxtel, H. A.; Verweel, R.-J.; Veeman, W. S. *Macromolecules* **1991**, *24*, 3712-3714.

[55] Miller, J. B.; Walton, J. H.; Roland, C. M. *Macromolecules* **1993**, *26*, 5602-5610.

[56] Simonutti, R.; Bracco, S.; Comotti, A.; Mauri, M.; Sozzani, P. *Chem. Mater.* **2006**, *18*, 4651-4657.

[57] Urban, C.; McCord, E. F.; Webster, O. W.; Abrams, L. *Chem. Mater.* **1995**, *7*, 1325-1332.

[58] Morgan, D. R.; Stejskal, E. O.; Andrady, A. L.; *Macromolecules* **1999**, *32*, 1897-1903.

[59] Wang, Y.; Inglefield, P. T.; Jones, A. A. *Polymer* **2002**, *43*, 1867-1872.

[60] Wang, Y.; Inglefield, P. T.; Jones, A. A. *J. Polymer Sci Part B: Polym. Phys.* **2002**, *40*, 1965-1974.

[61] Lin, G.; Jones, A. A. *Solid State Nucl. Magn. Reson.* **2004**, *26*, 87-98.

[62] Jameson, C. J. *J. Chem. Phys.* **2002**, *116*, 8912-8929.

[63] Chen, Q. J.; Fraissard, J. *J. Phys. Chem.* **1992**, *96*, 1809-1814.

[64] Demarquay, J.; Fraissard, J. *Chem. Phys. Lett.* **1987**, *136*, 314-318.

[65] Cheung, T. T. P.; Fu, C. M.; Wharry, S. *J. Phys. Chem.* **1988**, *92*, 5170-5180.

[66] Raftery, D.; Reven, L.; Long, H.; Pines, A.; Tang, P.; Reimer, J. A. *J. Phys. Chem.* **1993**, *97*, 1649-1655.

[67] Derouane, E. G.; André, J.-M. *Chem. Phys. Lett.* **1987**, *137*, 336-340.

[68] Derouane, E. G.; Nagy, J. B. *Chem. Phys. Lett.* **1987**, *137*, 341-343.

[69] Derouane, E. G. *Chem. Phys. Lett.* **1987**, *142*, 200-204.

[70] Ripmeester, J. A.; Ratcliffe, C. I. *J. Phys. Chem.* **1990**, *94*, 7652-7656.

[71] Lennard-Jones, J. E. *Trans. Faraday Soc.* **1932**, *28*, 333-359.

[72] Tse, J. S.; Klein, M. L.; McDonald, I. R. *J. Chem. Phys.* **1983**, *78*, 2096.

[73] Rouquerol, F.; Rouquerol, J.; Sing, K. in *Adsorption by Powders & Porous Solids.* Academic Press, London, 1999.

[74] Cheung, T. T. P. *J. Phys. Chem.* **1995**, *99*, 7089-7095.

[75] Jameson, C. J.; Jameson, A. K.; Gerald, R. II; de Dios, A. C. *J. Chem. Phys.* **1992**, *96*, 1676-1689.

[76] Jameson, C. J.; de Dios, A. C. *J. Chem. Phys.* **1992**, *97*, 417-434.

[77] Jameson, C. J.; Jameson, A. K.; Baello, B. I.; Lim. H.-M. *J. Chem. Phys.* **1994**, *100*, 5965-5976.

[78] Jameson, C. J.; Jameson, A. K.; Baello, B. I.; Lim. H.-M. *J. Chem. Phys.* **1994**, *100*, 5977-5987.

[79] Sears, D. N.; Demko, B. A.; Ooms, K. J.; Wasylishen, R. E.; Huang, Y. *Chem. Mater.* **2005**, *17*, 5481-5488.

[80] Moudrakovski, I. L.; Soldatov, D. V.; Ripmeester, J. A.; Sears, D. N.; Jameson, C. J. *Proc. Natl. Acad. Sci.* **2004**, *101*, 17924-17929.

[81] Sears, D. N.; Wasylishen, R. E.; Ueda, T. *J. Phys. Chem. B* **2006**, *110*, 11120-11127.

[82] Jameson, C. J.; de Dios, A. C. *J. Chem. Phys.* **2002**, *116*, 3805-3821.

[83] Rouquerol, J.; Avnir, D.; Fairbridge, C. W.; Everett, D. H.; Haynes, J. H.; Pernicone, N.; Ramsay, J. D. F.; Sing, K. S. W.; Unger, K. K. *Pure Appl. Chem.* **1994**, *66*, 1739-1758.

[84] Depmeier, W. *Handbook of Porous Solids*, Vol. 2. Schüth, F.; Sing, K. S. W.; Weitkamp, J. Eds. Wiley-VCH, Weinheim, 2002, 699-736.

[85] Ito, T.; Fraissard, J. *J. Chem. Phys.* **1982**, *76*, 5225-5229.

[86] Foster, M. D.; Rivin, I.; Treacy, M. M. J.; Delgado Friedrichs, O. *Microporous Mesoporous Mater.* **2005**, *90*, 32-38.

[87] Ito, F.; Fraissard, J. *J. Chem. Soc., Faraday Trans. 1*, **1987**, *83*, 451-462.

[88] Bansal, N.; Dybowski, C. *J. Phys. Chem.* **1988**, *92*, 2333-2337.

[89] Gédéon, A.; Bondardet, J. L.; Lepetit, C.; Fraissard, J. *Solid State Nucl. Magn. Reson.* **1995**, *5*, 201-212.

[90] Gédéon, A.; Fraissard, J. *Chem. Phys. Lett.* **1994**, *219*, 440-444.

[91] Hartmann, M.; Boddenberg, B. *Microporous Mater.* **1994**, *2*, 127-136.

[92] Gédéon, A.; Bondardet, J. L.; Fraissard, *J. Phys. Chem.* **1993**, *97*, 4254-4255.

[93] Samant, M. G.; de Ménorval, L.-C.; Dalla Betta, R. A.; Boudart, M. *J. Phys. Chem.* **1988**, *92*, 3937-3938.

[94] Chmelka, B. F.; Raftery, D.; McCormick, A. V.; de Ménorval, L.-C.; Levine, R. D.; Pines, A. *Phys. Rev. Lett.* **1991**, *66*, 580-583.

[95] Larsen, R. G.; Shore, J.; Schmidt-Rohr, K.; Emsley, L.; Long, H.; Pines, A.; Janicke, M.; Chmelka, B. F. *Chem. Phys. Lett.* **1993**, *214*, 220-226.

[96] Jameson, A. K.; Jameson, C. J.; Gerald, R. E. II *J. Chem. Phys.* **1994**, *101*, 1775-1786.

[97] Jameson, C. J.; Jameson, A. K.; Gerald, R. E. II; Lime, H.-M. *J. Chem. Phys.* **1995**, *103*, 8811-8820.

[98] Jameson, C. J.; Jameson, A. K.; Gerald, R. II; de Dios, A. C. *J. Chem. Phys.* **1992**, *96*, 1690-1697.

[99] Cheung, T. T. P. *J. Phys. Chem.* **1990**, *94*, 376-380.

[100] Tsaio, C.; Corbin, D. R.; Dybowski, C. R. *J. Phys. Chem.* **1990**, *94*, 867-869.

[101] Jameson, C. J.; Lim, H.-M.; Jameson, A. K. *Solid State Nucl. Magn. Reson.* **1997**, *9*, 277-301.

[102] Springuel-Huet, M.; Fraissard, J. *Chem. Phys. Lett.* **1989**, *154*, 299-302.

[103] Ripmeester, J. A.; Ratcliffe, C. I.*J. Phys. Chem.* **1995**, *99*, 619-622.

[104] Davis, M. E.; Saldarriaga, C.; Montes, C.; Hanson, B. E. *J. Phys. Chem.* **1988**, *92*, 2557-2560.

[105] Chen, Q. J.; Springuel-Huet, M. A.; Fraissard *J. Chem. Phys. Lett.* **1989**, *159*, 117-121.

[106] Koskela, T.; Jokisaari, J.; Satyanarayana, C. *Microporous Mesoporous Mater.* **2004**, *67*, 113-122.

[107] Jameson, C. J.; Jameson, A. K.; Gerald, R. E. Jr.; Lin. H.-M. *J. Phys. Chem.* B **1997**, *101*, 8418-8437.

[108] Terkikh, V. V.; Moudrakovski, I. L.; Du. H.; Ratcliffe, C. I.; Ripmeester, J. A. *J. Am. Chem. Soc.* **2001**, *123*, 10399-10400.

[109] Moudrakovski, I. L.; Ratcliffe, C. I.; Ripmeester, J. A. *Appl. Magn. Reson.* **1996**, *10*, 559-574.

[110] Moudrakovski, I. L.; Nossov, A.; Lang, S.; Breeze, A. R.; Ratcliffe, C. I.; Simard, B.; Santyr, G.; Ripmeester, J. A. *Chem. Mater.* **2000**, *12*, 1182-1183.

[111] Terskikh, V. V.; Moudrakovski, I. L.; Du, H.; Ractcliffe, C. I.; Ripmeester, J. A. *J. Am. Chem. Soc.* **2001**, *123*, 10399-10400.

[112] Jameson, C. J. *J. Am. Chem. Soc.* **2004**, *126*, 10450-10456.

[113] Nossov, A.; Guenneau, F.; Springuel-Huet, M.-A.; Haddad, E.; Montouillout, V.; Knott, B.; Engelke, F.; Fernandez, C.; Gédéon, A. *Phys. Chem. Chem. Phys.* **2003**, *5*, 4479-4483.

[114] Sozzani, P.; Comotti, A.; Simonutti, R.; Meersmann, T.; Logan, J. W.; Pines, A. *Angew. Chem. Int. Ed.* **2000**, *39*, 2695-2698.

[115] Meersmann, T.; Logan, J. W.; Simonutti, R.; Caldarelli, S.; Comotti, A.; Sozzani, P.; Kaiser, L. G.; Pines, A. *J. Phys. Chem. A* **2000**, *104*, 11665-11670.

[116] Ueda, T.; Eguchi, T.; Nakamura, N.; Wasylishen, R. E. *J. Phys. Chem. B* **2003**, *107*, 180-185.

[117] Soldatov, D. V.; Moudrakovski, I. L.; Grachev, E. V.; Ripmeester, J. A. *J. Am Chem. Soc.* **2006**, *128*, 6737-6744.

[118] Kresge, C. T.; Leonowicz, M. E.; Roth, W. J.; Vartuli, J. C.; Beck, J. S. *Nature* **1992**, *359*, 710-712.

[119] Pietraß, T.; Kneller, J. M.; Assink, R. A.; Anderson, M. T. *J. Phys. Chem. B* **1999**, *103*, 8837-8841.

[120] Davidson, A.; Berthault, P.; Desvaux, H. *J. Phys. Chem. B* **2003**, *107*, 14388-14393.

[121] Nossov, A.; Haddad, E.; Guenneau, F.; Gédéon, A. *Phys. Chem. Chem. Phys.* **2003**, *5*, 4473-4478.

[122] Nossov, A.; Haddad, E.; Guenneau, F.; Mignon, C.; Gédéon, A.; Grosso, D.; Badonneau, F.; Bonhomme, C.; Sanchez, C. *Chem. Commun.* **2002**, 2476-2477.

[123] Conner, W. C.; Weist, W. L.; Ito, T.; Fraissard, J. *J. Phys. Chem.* **1989**, *93*, 4138-4142.

[124] Terskikh, V. V.; Moudrakovski, I. L.; Breeze, S. R.; Lang, S.; Ratcliffe, C. I.; Ripmeester, J. A.; Sayari, A. *Langmuir* **2002**, *18*, 5653-5656.

[125] Terskikh, V. V.; Moudrakovski, I. L.; Mastikhin, V. M. *J. Chem. Soc. Faraday Trans.* **1993**, *89*, 4239-4243.

[126] Moudrakovski, I. L.; Wang, L.-Q.; Baumann, T.; Satcher, J. H. Jr.; Exarhos, G. J.; Ratcliffe, C. I.; Ripmeester, J. A. *J. Am. Chem. Soc.* **2004**, *126*, 5052-5053.

[127] Moudrakovski, I. L.; Ratcliffe, C. I.; Ripmeester, J. A.; Wang, L.-Q.; Exarhos, G. J.; Baumann, T.; Satcher, J. H. Jr. *J. Phys. Chem. B* **2005**, *109*, 11215-11222.

[128] Moudrakovski, I. L.; Terskikh, V. V.; Ratcliffe, C. I.; Ripmeester, J. A.; Wang, L.-Q.; Shin, Y.; Exarhos, G. J. *J. Phys. Chem. B* **2002**, *106*, 5938-5946.

[129] Huang, S.-J.; Huh, S.; Lo, P.-S.; Liu, S.-H.; Lin, V. S.-Y.; Liu, S.-B. *Phys. Chem. Chem. Phys.* **2005**, *7*, 3080-3087.

[130] Dubes, A.; Moudrakovski, I. L.; Shahgaldian, P.; Coleman, A. W.; Ratcliffe, C. I.; Ripmeester, J. A. *J. Am. Chem. Soc.* **2004**, *126*, 6236-6237.

Chapter 3: General experimental procedures and considerations

3.1 Experimental equipment and procedures

3.1.1 The optical-pumping spin-exchange apparatus

The optical-pumping spin-exchange apparatus used in this work was constructed based on the system built in the laboratory of Dr. John Ripmeester at the National Research Council in Ottawa. The design is a simple, relatively low cost variant of the traditional apparatus developed by numerous groups.[1,2] The system was constructed under the supervision of Dr. Takahiro Ueda, a visiting scientist in the Wasylishen lab. We are grateful to Dr. Ripmeester and his colleagues at the NRC for providing us with detailed instructions on the construction and operation of the apparatus.

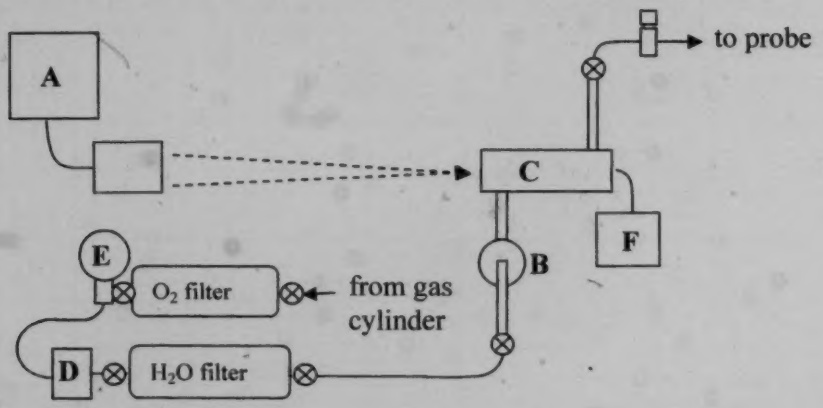

Figure 3.1: Schematic diagram of the optical-pumping spin-exchange apparatus. A) the dual diode laser; B) the Rb well; C) the optical cell; D) the flow meter; E) the pressure gauge; F) UV/Vis spectrometer.

The apparatus which optically pumps the Rb metal electrons and transfers the spin polarization to the Xe nuclei contains three main components, a laser tuned to the wavelength used to excite the unpaired $5s^1$ electron ($^2S_{1/2} \rightarrow {}^2P_{1/2}$) of gaseous atomic Rb, 794.5 nm, a well of Rb metal that can be heated to obtain an adequate vapor pressure of Rb gas, and an optical cell where the Rb can be irradiated by the laser and mixed with the Xe gas to allow spin-exchange to occur. A schematic of the design is presented in Figure 3.1.

A) The laser used in the system is a 60 W dual diode laser purchased from Coherent laser systems. Diode lasers, while much less expensive than other types of lasers, do not provide highly monochromatic light; the wavelength profile was approximately 3 to 5 nm. To obtain a maximum intensity at 794.5 nm, the laser was operated at 80% of maximum power. The laser is connected to a polarizer which converts the light to circularly polarized laser light which also acts to focus the laser beams on the face of the optical cell.

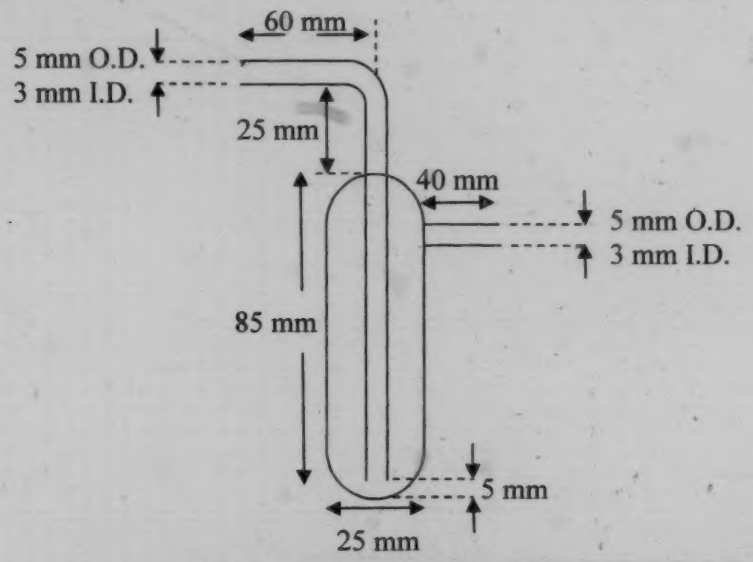

Figure 3.2: Diagram of the Rb well. The well itself is made of 5 mm thick Pyrex glass and contains 1 to 2 g of Rb metal.

B) The Rb well, shown in Figure 3.2, is used to hold the solid Rb under an inert atmosphere. This well is designed to hold between 1 and 2 g of Rb. The well is surrounded by a heating mantel that is used to increase the temperature of the well to ~180 °C. The Rb well, along with the optical cell, is made of 5mm thick Pyrex glass, with 1 mm thick, 5 mm O.D. Pyrex tubes used for the gas inlet and outlet and was constructed in the department of chemistry glass shop at the University of Alberta. The well is 85 mm deep, and 25 mm in diameter. It is rounded at the top and bottom to provide the strength necessary to handle the elevated gas pressures used in the apparatus. The gas inlet extends down the center of the well to a point 5 mm from the bottom. This allows the Xe gas mixture to bubble through the molten Rb and thus saturate the gas stream with Rb atoms. The inlet tube is bent 25 mm above the top of the well and

extends an additional 60 mm, see Figure 3.2. The length of the inlet tube provides a buffer region in the event that liquid Rb bubbles up the tube, and provides a region outside the heating mantle that can condense any Rb gas before it can evaporate into the gas line, upstream of the well. The dimensions of the Rb well play an important role in the lifetime of the optical pumping cell. Figure 3.2 shows the dimensions that have proven to provide a cell with the longest lifetime.

The Rb well was pressure tested at 120 psi before filling it with Rb. Rb was obtained from Aldrich as an ingot in a sealed glass ampoule. All procedures for loading the well were performed in a glove box and all the glassware used was dried in an oven. The ampoule was opened and the Rb was melted using a heat gun; the melting point of Rb is 38.8 °C. The liquid Rb was transferred to the Rb well using a glass pipette. Swagelock™ valves connected to the gas inlet and outlets were used to seal the well/optical cell before it was removed from the glove box.

After extended use of the apparatus, the Rb in the well becomes oxidized due to small amounts of O_2 and H_2O that enter the system. Some Rb also condenses and oxidizes in the glass inlet and outlet tubes, blocking gas flow. In the initial stages of oxidation, the Rb takes on a golden appearance and the melting point drops so that liquid Rb/Rb_2O is present even at room temperature. The performance of the system is not significantly affected by small amounts of Rb_2O. Further oxidation and exposure to trace moisture results in grey white $Rb_2O/RbOH$ forming. This occurs predominantly in the narrow gas tubes and is the primary cause of cell failure.

After a cell ceases to work it can be cleaned and reused. The cell is removed from the apparatus and taken to a fume hood where one of the valves is momentarily opened to allow air to enter the well. The air oxidizes some of the remaining Rb without igniting it, forming a $Rb_2O/RbOH$ coating over the Rb metal. This process is repeated several times and the well is then left open to the air for a period of several days.

Octanol can be used to slowly dissolve the $Rb_2O/RbOH$ layer, and expose the underlying Rb to small amounts of O_2 and H_2O dissolved in the octanol. Small volumes of octanol are introduced repeatedly to slowly oxidize and remove the Rb. When all the residue is removed, the cell is washed in water and placed in an oven to dry.

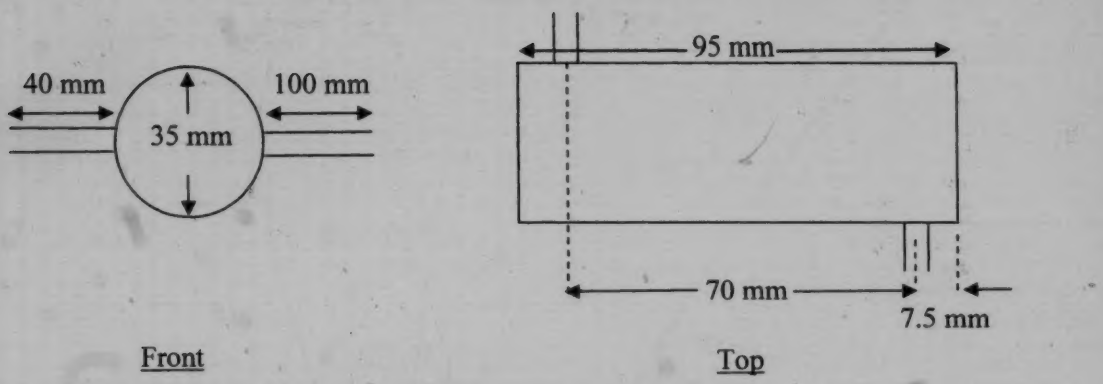

Figure 3.3: Diagram (not to scale) of the optical cell. The cell is made of 5 mm thick Pyrex and is connected to the Rb well by the 40 mm tube.

C) Figure 3.3 shows a schematic of the optical cell. The optical cell is connected to the Rb well, forming a single glass unit, and is the container in which the Rb gas is irradiated by the laser light and then allowed to mix with the Xe gas. The dimensions of the chamber are optimized based on the specifics of the laser used in the system. The cell is cylindrical with a diameter of 35 mm, a length of 95 mm and has flat faces at either end. As with the Rb well, the optical cell is made of 5 mm thick Pyrex glass. The inlet and outlet tubes are staggered with the inlet at the front of the cell (the face which the laser light irradiates) and the outlet at the back of the cell. The cell is spaced 40 mm from the Rb well and the outlet tube is 100 mm long. As with the Rb well, the optical cell is surrounded by a heating mantel; the temperature of the cell is maintained at ~ 140 °C. A cold trap could be placed after the optical pumping cell in order to condense any Rb gas but with the system described here, no trap was required and no Rb was ever detected after the first 3 mm of the outlet tube. The optical cell was placed in the fringe field of the superconducting NMR magnet so that the magnetic field at the cell was approximately 30 gauss (~40 cm from the bottom edge of the 4.7 T superconducting magnet).

The gas mixture used in the apparatus was composed of 1% Xe (partial pressure 0.01 atm or 7 torr), 1% N_2, and 98% He and was obtained from Praxair. The gas was passed through oxygen and water filters to remove any O_2 and H_2O which would oxidize the Rb. The gas was also passed through a gas flow meter, **D**, and pressure gauge, **E**, see Figure 3.1. The system was set up on a moveable cart and connected using Teflon tubing

and Swagelock™ gas fittings and valves which were placed on either end of the O_2 and H_2O filters and at either end of the Rb well/optical cell. After the outlet valve on the optical cell, a needle valve was placed in order to provide fine control over the gas flow rate. The gas then passed through rubber tubing, approximately 2 m in length, to the probe head where it was introduced into the sample holder. The gas temperature was approximately at room temperature by the time it entered the sample holder.

To monitor the performance of the system, electronic thermometers were placed along the heater control thermometers in both the Rb well and optical cell. The polarization of the Rb was monitored indirectly by observing the light absorption profile of the optical cell. A fiber optic wire was placed at the back of the optical cell and was connected to an Ocean Optics UV/Vis spectrometer, **F**. The adsorption spectrum was monitored on a PC connected to the spectrometer and showed a noticeable drop in light intensity at 794.5 nm when the system was operating properly.

The optical cell was housed in an aluminum case which was supported on a plastic utility jack. The aluminum casing allowed for dissipation of heat as well as providing a mount for the fiber optic detector and a rubber tube which was used to flow air over the optical cell if the temperature became too high as a result of laser irradiation.

The Rb well/optical cell was housed at the end of a stainless steal container with openings for the gas tubes and detectors and a door on the top to provide access to the Rb well/optical cell. At the opposite end of the box, the optical polarizer from the laser was placed on an aluminum jack. The distance from the polarizer to the optical cell was approximately 70 cm. The box was painted matte black in order to adsorb any stray laser radiation.

3.1.2 Operating procedure

Before operation, the glass cell and laser path were visually inspected to ensure nothing was obstructing the laser's path and that the cell was in good condition. All the gas lines were also checked to ensure that they were in good condition and that the valves were closed. The doors to the room were closed and the laser warning sign was placed outside on the door. Laser safety glasses were worn throughout the operation of the system.

The laser was aligned so that the two laser beams converged on the front of the optical cell. This was done by turning the laser on at low power, placing a black plate in front of the cell and focusing and aligning the laser. The laser power was changed by adjusting the electrical current of each laser. After the laser had been aligned, the door on the stainless steal case was closed and the laser system was allowed to warm up for 5-10 minutes.

While the laser was warming up, the OOIbase32 program on the PC was started; this program controls the UV/Vis spectrometer which allows for the Rb adsorption spectrum to be monitored. The laser alignment was confirmed by ensuring that the light intensity as measured by the UV/Vis spectrometer was maximized; the integration time on the OOI program was adjusted so that the absorbance filled the screen. The power of the two lasers was adjusted so that the maximum light intensity was approximately 794.5 nm. Both laser power levels could be adjusted independently during optimization. The optimal settings at the time of writing were 32.3 A on laser 1 and 31.1 A on laser 2.

Once the laser was aligned it was turned off. A protective face shield was put on and the valves on the gas line were checked to ensure they were tightly closed. The gas regulator in the gas cylinder was opened and the pressure was set to between 50 and 70 psi. Each valve was then opened in sequence up to the inlet valve on the Rb well to charge the line. The heaters were turned on and the temperature of both the well and optical cell was increased to 90 °C. The Rb well inlet valve was carefully opened to allow a small amount of gas to flow into the Rb well. After the pressure equalized the outlet valve on the optical cell was opened and the flow rate was adjusted using the needle value. Typically the flow rate was set in the 2 to 5 ml sec^{-1} range, which is fast enough to completely cycle the gas in the NMR sample holder ten or more times per second.

Finally, the temperature of the Rb well was adjusted to approximately 180 °C and the optical cell to approximately 140 °C. During operation the exposure of the optical cell to the intense laser light resulted in overheating of the cell and cool air from the in-house air line was blown over the cell to maintain the temperature. The system typically took 10 to 20 min to reach a stable level of polarization. For further safety instruction see Appendix A.

3.1.3 NMR spectroscopy

^{129}Xe NMR spectroscopy was performed using a Chemagnetics CMX Infinity 200 wide-bore spectrometer operating at a ^{129}Xe frequency of 55.36 MHz, employing a modified Chemagnetics 5 mm double-resonance solenoid probe. The ^{129}Xe NMR chemical shifts were referenced to the gas peak for ^{129}Xe in the gas mixture at room temperature, 0.0 ppm, prior to placing the samples of interest in the spectrometer. Bloch-decay spectra ($\pi/2$ – acquire – delay) were obtained using $\pi/2$ pulse widths of 2.2 μs, calibrated using the free gas peak. HP ^{129}Xe (~7% spin polarization) was generated using the home-built continuous-flow optical-pumping system, see above.[1,2] The sample temperature at which the spectra were acquired was determined using the Chemagnetics temperature controller which was calibrated using the ^{207}Pb NMR peak of solid lead nitrate.[3]

The acquisition of ^{129}Xe NMR spectra using continuous-flow HP ^{129}Xe requires special experimental considerations. The experimental recycle delay is limited by the flow rate and not the ^{129}Xe spin-lattice relaxation time, T_1. This can make spectral acquisitions significantly faster than using thermally polarized ^{129}Xe since the relaxation times of ^{129}Xe can be long.[4] Additionally, hyperpolarization of the ^{129}Xe nuclei means that if $\pi/2$ excitation pulses are used, any given HP ^{129}Xe nucleus can only be "observed" once.[5] Therefore if the Xe atoms are not replaced by freshly polarized ^{129}Xe nuclei from the optical pumping system, no signal enhancement will be observed when signal averaging is performed. Some of the lost intensity can be recovered if longer experimental recycle times are employed, which allows for more "used" Xe to be replaced by freshly polarized Xe; at some point the Xe T_1 relaxation limits the signal intensity. Typically, 1 s recycle times were used when acquiring ^{129}Xe NMR spectra and longer recycle times were used to check if the loss of signal intensity was a result of exchange times or exclusion of Xe from the structure.

2-D EXSY ($\pi/2$-t_1-$\pi/2$-τ_{mix}-$\pi/2$-acquire-delay) ^{129}Xe NMR experiments were conducted using a "hypercomplex" pulse sequence employing mixing times, τ_{mix}, of 1 to 400 ms.[6,7,8,9] Each spectrum consisted of 64 to 256 points in the t_1 dimension and 2 k

points in the t_2 dimension. The spectra were zero filled to 2048 points in the t_1 dimension, processed with 10 to 100 Hz of line broadening, and symmetrized when necessary to overcome distortions caused by low signal-to-noise and t_1 noise.[10]

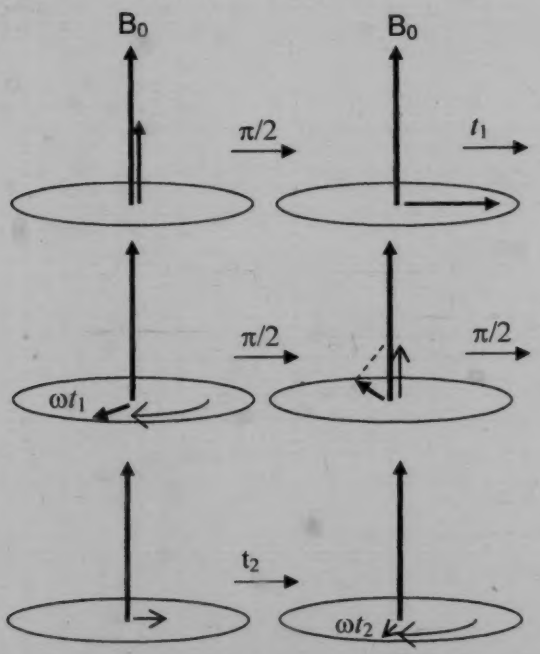

Figure 3.4: Vector diagram of the magnetization of a single spin during the EXSY pulse sequence. The mixing time, τ_{mix}, occurs between the second and third $\pi/2$ pulses and allows for exchange when there is more than one magnetic environment.[11]

To understand how the EXSY experiment works consider the behaviour of an isolated spin system that is not undergoing exchange during the experiment ($\pi/2$-t_1-$\pi/2$-τ_{mix}-$\pi/2$-t_2), Figure 3.4.[11] The first $\pi/2$ pulse causes the net magnetization vector to rotate from equilibrium along B_0 (the *z*-axis), to the *xy*-plane. The magnetization is allowed to precess about B_0 for a time t_1, this imparts a phase dependence related to the precession frequency ω, relative to the carrier, and the time t_1. After a second $\pi/2$ pulse the magnetization is rotated into the *xz*-plane where only the *z* component of this magnetization is important. The magnitude of the magnetization along *z* now contains a $\cos(\omega t_1)$ component. The magnetization is kept along the *z*-axis for a specific mixing

time, τ_{mix}, after which a $\pi/2$ pulse rotates the magnetization back down into the *xy*-plane where it is recorded by the spectrometer with an evolution time of $\cos(\omega t_2)$, where t_2 is the acquisition period. When a double Fourier transform is performed along t_1 and t_2, the resulting 2-D frequency spectrum contains a peak at $\omega_1 = \omega$ and $\omega_2 = \omega$.

When there are two chemically unique sites, A and B, the resulting spectrum consists of two peaks at frequencies of $\omega_1, \omega_2 = \omega_A$ and $\omega_1, \omega_2 = \omega_B$, i.e., two peaks along the diagonal of the 2-D spectrum. If there is chemical exchange between the sites, as is the case for Xe atoms exchanging between two different environments, then the spectrum will consist of the two diagonal peaks, representing Xe atoms that do not exchange between the two sites during the mixing time, and cross-peaks that arise from Xe atoms that are in one site during t_1 and the other site during t_2, i.e., these peaks have a frequency of $\omega_1, \omega_2 = \omega_A, \omega_B$ or $\omega_1, \omega_2 = \omega_B, \omega_A$ depending on the order of exchange (i.e., A → B or B → A). The intensities of the peaks can therefore be used to determine the number of Xe atoms exchanging during τ_{mix} and by extension the exchange rate.

3.1.4 Computational details

Calculations of the Xe magnetic shielding tensors were performed using Gaussian 98W (revision A.7).[12] The DFT B3LYP[13,14] calculations were performed on a Windows-based Intel PC using the uncontracted 29*s*21*p*17*d*9*f* basis set used extensively by Jameson for Xe.[15] This basis set uses the core (25*s*18*p*13*d*) of Partridge and Faegri[16] and was augmented with *3s*, *2p*, *4d*, and *9f* functions, with exponents taken from Bishop.[17] For all other atoms, 6-311++G(d,p) basis sets, as available in the Gaussian package, were used. Calculated magnetic shielding values, σ, were converted to chemical shifts, δ, by calculating the magnetic shielding constant of an isolated Xe atom, σ_{ref}, and using the relationship $\delta = (\sigma_{ref} - \sigma)/(1 - \sigma_{ref})$.

Molecular dynamics simulations were performed using the MM+ force field as available in the Hyperchem computational chemistry program on a Windows-based Intel PC.[18] The MM+ force field is derived from the MM2(1977) code developed by Allinger[19] with additional parameters from the MM2(1991) parameter set.[20] It is known that the use of Lennard-Jones and other similar potential energy equations such as

exponential-6 functions to describe the potential energy interactions between Xe and another atom will overestimate the value of the inter-atomic distance at the lowest potential energy, r_{min}, and the point where the potential energy is zero, r_0.[21] For comparison, the r_{min} for two Xe atoms calculated using the MM+ force field is 4.600 Å, while the experimental value is 4.363 Å, and the r_0 is 4.048 Å while the experimental value is 3.892 Å.[22] Therefore, using these simulations the Xe atoms are not expected to sample all of the space that they can experimentally. The simulations were performed by allowing Xe atoms to move under the influence of the interatomic potentials inside the static framework. The framework consisted of 3 x 3 x 3 unit cells and only the center cavities were used, no other boundary conditions were employed. The Xe was allowed to reach equilibrium for 5 ps, the simulation was performed for 100 ps using 0.01 ps time steps, and the temperature was maintained using a temperature bath with a T-bath constant of 0.01 ps.

3.2 Important consideration when interpreting continuous-flow HP ^{129}Xe NMR spectra

3.2.1 Previous structural studies

Of the four questions this thesis will attempt to answer using HP ^{129}Xe NMR spectroscopy, the first two regarding the presence of accessible pore space and general pore size can be answered without extensive knowledge of the solid-state structure of the framework. The answers can be inferred based on the chemical shift of the ^{129}Xe provided that a few checks are preformed to rule out unusual adsorption behavior, see section 3.2.2.

To access more detailed information about pore geometry and functionality as well as the behaviour of Xe inside the framework, some knowledge of the solid-state structure of the material must be known. In Chapters 4 through 7, a number of different models for the framework structure will be used. For the $AlPO_4$ and IRMOF samples, a great deal is known about the framework structures, including the fact that the structure is stable when different guest molecules are adsorbed or desorbed.

When the exact structure of the evacuated framework is not known, such as in the case of the macrocycle compounds studied in Chapters 5 and 6, correlation of the ^{129}Xe

NMR spectra to structure is more tenuous. However, models can be proposed based on molecular structures of the subunits, or on the solid-state structure of the framework with co-crystallized solvent molecules. These models often provide a good approximation upon which a mechanism for Xe adsorption can be based. The risk one encounters is that over-interpretation of the results is easy. It must always be remembered that a framework structure with co-crystallized solvent may not be exactly the same as the structure without any guests or with Xe guest atoms. This can sometimes be beneficial because the flexibility in the solid-state structure allows guest adsorption and desorption through structures that do not appear to have channels large enough for Xe based on the single-crystal structure of the framework with co-crystallized solvent molecules, as has been shown for some of the metal-organic macrocycles studies in Chapter 6.

3.2.2 Alternative adsorption phenomena

One key factor that must be recognized is that Xe gas can adsorb in regions that are not associated with the internal porosity of the materials; for example, at low temperatures Xe can adsorb on the crystallite surfaces.[23,24,25,26,27,28,29,30,31,32,33] As with Xe in pores, the extent of adsorption and the dynamics of the adsorbed Xe depend on the potential energy of interaction between Xe and the surface. For materials with relatively small pores, micropores or small mesopores, the heat of adsorption of Xe on the surface of the crystallites is much lower than for Xe in the cavities and therefore Xe will invariably adsorb inside the materials before it adsorbs to the exterior crystallite surfaces.

Many crystallite surfaces contain defects, such as ledges and surface impressions, which can result in stronger adsorption sites than Xe on a flat surface would experience. Adsorption in these sites can sometimes become significant and may interfere with the analysis of the ^{129}Xe NMR spectra. If there is rapid exchange between Xe on the surfaces and Xe in the pores, then the observed ^{129}Xe chemical shift could also be affected. Since surface condensation could lead to a large number of Xe-Xe interactions at low temperature, a large ^{129}Xe chemical shift for the atoms on the surface can be observed. Exchange averaging with Xe in the pores can lead to an apparent chemical shift that is larger than is characteristic of Xe in the pore space.

3.2.3 Crystallite size

When performing NMR experiments with Xe gas, the average crystallite size can have an important effect on the NMR signal. [34,35] As has been discussed, if the exchange of Xe atoms between two sites, such as the pore space and the free gas, is faster than the separation of the NMR signals for Xe in the two sites in Hz, then the ^{129}Xe NMR signals will be motionally averaged. This is commonly observed for mesoporous materials. However, if the crystallite size of microporous materials is too small, the exchange rate can be artificially high, simply due to the lack of extended pore structure. The research groups of Ripmeester and Jameson have both studied the influence of crystallite size on the ^{129}Xe NMR spectra of Xe in microporous materials.[34,35] The average crystallite size at which this type of exchange becomes a problem depends on the diffusion rate of Xe through the pores of the solid. For materials with strong adsorption sites or restricted openings in the pores, such as the macrocycles described in Chapters 5 and 6, the diffusion rate is expected to be slower and therefore smaller crystallites can be expected to give spectra characteristic of the sample. For materials with more open porous structure, such as the IRMOFs discussed in Chapter 7, larger crystallites are desirable in order to obtain spectra truly representative of the sample.

When the crystallites are small enough for fast inside-outside exchange to be a consideration, the ^{129}Xe NMR spectra can be affected in two ways. First, if the crystallite size is homogenous, a single, narrow NMR peak is observed with a chemical shift that is an average between Xe in the pores and Xe in the gas; the same as for Xe in fast-exchange in and out of mesoporous materials.[34] If the crystallite size is highly heterogeneous then each crystallite could have a different exchange rate with the gas and therefore each set of crystallite sizes will give rise to an average chemical shift that is slightly different resulting in broad ^{129}Xe NMR peaks.[34,35]

3.2.4 Sample purity

Sample purity is always important in solid-state NMR studies. The presence of multiple NMR signals from impurities or different polymorphs can greatly complicate the interpretation of NMR spectra. This is also true when using HP ^{129}Xe NMR spectroscopy

to explore porous materials. However, due to the influence Xe exchange rate has on the chemical shift, identifying sample impurities can be more difficult. If the impurity exists as separate crystallites within the powder, and exchange between crystallites is slow, different ^{129}Xe NMR peaks are observed for Xe in the different structures. Provided one knows the structure of the sample, the presence of the impurity peaks can usually be identified. However, if there is uncertainty about the structure, it cannot be conclusively stated whether the different peaks arise from impurities or from different pore regions in the sample.

Figure 3.5b shows spectra acquired on a sample of IRMOF-1 for which the diethyl formamide, DEF, was removed by heating the sample at temperatures greater than 150°C; this was determined by elemental analysis and took approximately one week. Above 200 K the ^{129}Xe NMR spectra are the same as for the pure sample shown in Figure 3.5a. However, when the temperature is lowered, a second peak is observed with a chemical shift near 90 ppm. This peak is quite broad, likely a result of a distribution of sites in the impurity. The chemical shift indicates that Xe is residing in a more open structure than the IRMOF-1 cage; the behaviour of the two peaks as a function of temperature resembles that of a multi-domain material.

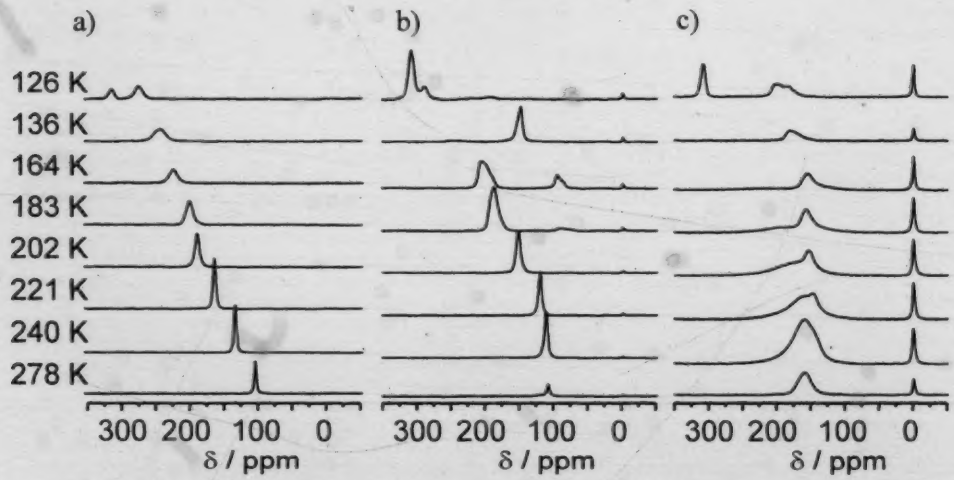

Figure 3.5: ^{129}Xe NMR spectra of Xe in different samples of IRMOF-1 acquired at multiple temperatures. a) IRMOF-1 prepared as described in Chapter 7. b) IRMOF-1 when the DEF guest was removed by heating the sample at 150 °C for 1 week. c) IRMOF-1 with 2 DEF molecules included in each cage.

The powder X-ray diffraction pattern of the sample revealed the presence of another crystalline structure in addition to the IRMOF-1. Since the ^{129}Xe NMR spectra reveal that the defect has a large pore size, the second phase likely results from opening the cubic framework, possibly by hydrolysis of the carboxylate-metal bonds. Such a hydrolysis, which may occur during the prolonged heating of the sample, could create large cages in the framework while maintaining the overall crystallinity of the sample.

If there is fast exchange between the defect and the sample, a change in Xe chemical shift can occur. This phenomenon is exactly the same as would be observed for fast exchange between Xe in the pore and Xe on the surface of the crystallites except that the second site would be a pore. This type of impurity is the most difficult to identify based on ^{129}Xe NMR spectra because only a single peak is observed, which can be mistakenly attributed to Xe in the pure framework.

Incomplete guest removal is another source of an "impurity". Co-adsorbed species can have a significant effect on the ^{129}Xe NMR spectrum of Xe adsorbed in a porous material. This has been shown by previous researchers and is often used to characterize the interaction, preferential adsorption behaviour, or displacement of Xe and the co-adsorbed species.[36] When the goal is to explore the empty framework, the presence of co-adsorbed species is clearly undesirable. Figure 3.5c shows a series of spectra acquired on a sample of IRMOF-1 for which approximately 2 DEF molecules were still included in the cavity.

At elevated temperatures, a peak is observed at 158 ppm, 50 ppm greater than the chemical shift value in the DEF-free sample. This suggests that the presence of DEF reduces the free space available for the Xe leading to the larger ^{129}Xe chemical shift. While the peak appears to be isotropic, the breadth is much greater than that observed in the DEF-free sample, suggesting that disorder in the DEF molecules causes a range of non-equivalent Xe adsorption sites. As the temperature is lowered, only a small change in the chemical shift is observed. The presence of DEF blocks most of the Xe-Xe interactions responsible for the change in chemical shift observed. There also appear to be two peaks which could be from cages with different DEF loadings or from impurities in the framework structure brought on by the heating process used to remove the other

five DEF molecules. The ^{129}Xe NMR peaks observed in Figure 3.5 near 313 ppm are from solid Xe.

3.2.5 Equilibrium vs. non-equilibrium adsorption dynamics

One question that has yet to be adequately addressed by researchers is the difference in adsorption phenomena when using pressurized thermally polarized Xe samples compared to continuous-flow experiments. Most studies which compare the ^{129}Xe NMR spectra between ~180 K and 300 K indicated that the ^{129}Xe spectra are similar.[37,38] The best comparison between results obtained using continuous-flow experiments below 180 K and sealed sample thermally polarized experiments is for silicalite.[34,39] It was shown that even using a 1% Xe gas mixture, a full loading of 16 Xe atoms per unit cell could be achieved by lowering the sample temperature to 140 K. The lineshape was similar to that obtained on samples sealed under high pressure so that the pores also had 16 Xe atoms per unit cell.[34,39]

It is likely that the behaviour of Xe in continuous-flow experiments will be increasingly different from that in pressurized experiments as the temperature is lowered. At high temperatures, the partial pressure of Xe in the gas will dictate the loading of Xe in the framework, i.e., it is expected that Xe will remain in the low-loading regime when using low pressures. However, as the temperature is lowered, the Xe atoms will become increasingly confined to the pores by the potential energy of attraction and the amount of Xe adsorbed during continuous-flow experiments may be significantly different from that adsorbed during a sealed-sample experiment. This is because in the low-temperature regime, the amount of Xe the framework has access to becomes important. In sealed samples, the amount of Xe atoms is dictated by the amount sealed into the tube, but, in the continuous-flow experiment this is determined by how fast Xe is flowed over the system. Because of the high adsorption potential of Xe compared to the He and N_2 in the gas stream, the framework can act as a filter, adsorbing a disproportionate amount of Xe from the overhead gas. If the diffusion of Xe out of the pores or off the surfaces is slow, there is a significant build-up of Xe in the porous material and higher Xe loadings. Even if the Xe becomes depolarized due to low residence times in the pores, the Xe-Xe interactions will still cause large chemical shifts for any freshly HP Xe atoms that enter

the framework. A careful study of adsorption phenomena under constant pressure and continuous-flow conditions as a function of temperature is required to better understand the different behaviours that may be present at low temperatures.

The role that continuous flow has on Xe exchange dynamics is also unresolved. At higher temperatures, where the continuous-flow and sealed samples yield the same Xe loadings, the exchange rates may still be affected by the differences in the overhead gas. This will be particularly true for any exchange process that involves Xe passing through the gas phase. The different overhead gas conditions will not significantly affect the exchange between intra-crystallite domains because the exchange rates will be governed by the potential energy differences and Xe populations of the different sites. As long as the populations of the sites do not change significantly when using continuous-flow or sealed samples, the exchange rates will be similar; this can be checked by comparing the chemical shifts observed from a sealed and continuous-flow experiment extrapolated to the same Xe pressures.

In conclusion, the experimental procedures used in this thesis have been described in this chapter. Some of the pitfalls and possible sources of misinterpretation when performing ^{129}Xe NMR experiments have also been outlined. Whenever possible it is important to try and use multiple experimental techniques to characterize porous materials in order to ensure that no errors are made in the interpretation of the ^{129}Xe chemical shifts.

---

[1] Driehuys, B.; Cates, G. D. Miron, E.; Sauer, K.; Walter D. K.; Happer W. *Appl. Phys. Lett.* **1996**, *69*, 1668-1670.

[2] Moudrakovski, I. L.; Lang, S.; Ratcliffe, C. I.; Simard, B.; Santyr G.; Ripmeester, J. A. *J. Magn. Reson.* **2000**, *144*, 372-377.

[3] van Gorkom, L. C. M.; Hook, J. M.; Logan, M. B.; Hanna J. V.; Wasylishen, R. E. *Magn. Reson. Chem.* **1995**, *33*, 791-795.

[4] Ripmeester, J. A.; Ratcliffe C. I.; Tse, J. S. *J. Chem. Soc.-Faraday Trans. I* **1988**, *84*, 3731-3745.

[5] Goodson, B. M. *J. Magn. Reson.* **2002**, *155*, 157-216.

[6] Jeener, J.; Meier, B. H.; Bachmann P;. Ernst, R. R. *J. Chem. Phys.* **1979**, *71*, 4546-4553.

[7] Bax A.; Marion, D. *J. Magn. Reson.* **1988**, *78*, 186-191.

[8] Ohuchi, M.; Hosono, M.; Furihata K.; Seto, H. *J. Magn. Reson.* **1987**, *72*, 279-297.

[9] States, D. J.; Haberkorn, R. A.; Ruben, D. J. *J. Magn. Reson.* **1982**, *42*, 286-292.

[10] Hull, W. E. in *Two-Dimensional NMR Spectroscopy: Applications for Chemists and Biochemists*; 2 ed.; Croasmun, W.R.; Carlson, R. M. K. Eds.; VCH Publishers, Inc., New York, 1994, 67-456.

[11] Perrin, C. L.; Swyer, T. J. *Chem. Rev.* **1990**, *90*, 935-967.

[12] Frisch, M. J.; Trucks, G. W.; Schlegel, H. B.; Scuseria, G. E.; Robb, M. A.; Cheeseman, J. R.; Zakrzewski, V. G.; Montgomery, J. A., Jr.; Stratmann, R. E.; Burant, J. C.; Dapprich, S.; Millam, J. M.; Daniels, A. D.; Kudin, K. N.; Strain, M. C.; Farkas, O.; Tomasi, J.; Barone, V.; Cossi, M.; Cammi, R.; Mennucci, B.; Pomelli, C.; Adamo, C.; Clifford, S.; Ochterski, J.; Petersson, G. A.; Ayala, P. Y.; Cui, Q.; Morokuma, K.; Malick, D. K.; Rabuck, A. D.; Raghavachari, K.; Foresman, J. B.; Cioslowski, J.; Ortiz, J. V.; Stefanov, B. B.; Liu, G.; Liashenko, A.; Piskorz, P.; Komaromi, I.; Gomperts, R.; Martin, R. L.; Fox, D. J.; Keith, T.; Al-Laham, M. A.; Peng, C. Y.; Nanayakkara, A.; Gonzalez, C.; Challacombe, M.; Gill, P. M. W.; Johnson, B. G.; Chen, W.; Wong, M. W.; Andres, J. L.; Head-Gordon, M.; Replogle, E. S.; Pople, J. A.; revision A. 7 ed.; Gaussian Inc.: Pittsburgh, PA, 1998.

[13] Lee, C.; Yang W.; Parr, R. G. *Phys. Rev. B* **1988**, *37*, 785-789

[14] Becke, A. D. *J. Chem. Phys.* **1993**, *98*, 5648-5652.

[15] Sears D. N.; Jameson, C. J. *J. Chem. Phys.* **2004**, *121*, 2151-2157.

[16] Partridge H.; Faegri, K. *NASA Tech. Memo.* 1992, 103918

[17] Bishop D. M.; Cybulski, S. M. *Chem. Phys. Lett.* **1993**, *211*, 255-258.

[18] HyperChem(TM) Professional 6.0, Hypercube, Inc. 1115 NW 4th Street, Gainesville, Florida 32601, USA (1996).

[19] Allinger, N. L. *J. Am. Chem. Soc.* **1977**, *99*, 8127-8134.

[20] MM2(1991) Parameter set, as provided by Allinger.

[21] Jameson, C. J.; Jameson, A. K.; Baello B. I.; Lim, H.-M. *J. Chem. Phys.* **1994**, *100*, 5965-5976.

[22] Aziz R. A.; Slaman, M. *J. Mol. Phys.* **1986**, *57*, 825-840.

[23] Raftery, D.; Long, H.; Meersmann, T.; Grandinetti, P. J.; Reven, L.; Pines, A. *Phys. Rev. Lett.* **1991**, *66*, 584-587.

[24] Kritzenberger, J.; Caede, H. C.; Shore, J. S.; Pines, A.; Bell, A. T. *J. Phys. Chem.* **1994**, *98*, 10173-10179.

[25] Raftery, D.; Reven, L.; Long, H.; Pines, A.; Tang, P.; Reimer, J. A. *J. Phys. Chem.* **1993**, *97*, 1649-1655.

[26] Long, H. W.; Haede, H. C.; Shore, J.; Reven, L.; Bowers, C. R.; Kritzenberger, J.; Pietrass, T.; Pines, A. *J. Am. Chem. Soc.* **1993**, *115*, 8491-8492.

[27] Pietraß, T.; Seydoux, R.; Pines, A. *J. Magn. Reson.* **1998**, *133*, 299-303.

[28] Brunner, E.; Seydoux, R.; Kaake, M.; Pines, A.; Reimer, J. A. *J. Magn. Reson.* **1998**, *130*, 145-148.

[29] MacNamara, E.; Fisher, G.; Smith, J. Rice, C. V.; Hwang, S.-J.; Raftery, D. *J. Phys. Chem. B* **1999**, *103*, 1158-1160.

[30] Smith, J.; Knagge, K.; Smith, L. J.; MacNamara, E.; Raftery, D. *J. Magn. Reson.* **2002**, *159*, 111-125.

[31] Stahl, D.; Mannstadt, W.; Gerhard, P.; Koch, M.; Jänsch, H. J. *J. Magn. Reson.* **2002**, *159*, 1-12.

[32] Jänsch, H. J.; Gerhard, P.; Koch, M.; Stahl, D. *Chem. Phys. Lett.* **2003**, *372*, 325-330.

[33] Terskikh, V. V.; Seidl, M.; Knözinger, H. *Colloids Surf., A* **1999**, *158*, 249-254.

[34] Jameson, C. J.; Jameson, A. K.,; Gerald, R. E. Jr.; Lin. H.-M. *J. Phys. Chem. B* **1997**, *101*, 8418-8437.

[35] Ripmeester, J. A.; Ratcliffe, C. I. *Anal. Chim. Acta* **1993**, *283*, 1103-1112.

[36] Nossov, A. V.; Soldatov, D. V.; Ripmeester, J. A. *J. Am. Chem. Soc.* **2001**, *123*, 3563-3568.

[37] Moudrakovski, I. L.; Nossov, A.; Lang, S.; Breeze, A. R.; Ratcliffe, C. I.; Simard, B.; Santyr, G.; Ripmeester, J. A. *Chem. Mater.* **2000**, *12*, 1182-1183.

[38] Moudrakovski, I. L.; Ratcliffe, C. I.; Ripmeester, J. A.; Wang, L.-Q.; Exarhos, G. J.; Baumann, T.; Satcher, J. H. Jr.; *J. Phys. Chem. B* **2005**, *109*, 11215-11222.

[39] Terkikh, V. V.; Moudrakovski, I. L.; Du. H.; Ratcliffe, C. I.; Ripmeester, J. A. *J. Am. Chem. Soc.* **2001**, *123*, 10399-10400.

Chapter 4: ^{129}Xe NMR spectroscopy used to monitor the formation of $AlPO_4$-18

4.1 Introduction

Numerous metal phosphate zeolites have been synthesised since 1982 when researchers at Union Carbide reported the preparation of an aluminum phosphate zeolite with an Al/P ratio of one.[1] Most of the aluminum phosphates are microporous after the removal of the water and organic templating agents used to prepare the open frameworks. Many of the other metal phosphates do not retain their structure upon removal of the water and organic molecules and only a few of these materials show adsorption properties.[2] The formation mechanism of aluminum phosphate zeolites has been a subject of inquiry for many years. The hydrothermal synthesis of these zeolites involves reacting an aluminum and phosphorus source, typically Al_2O_3 or $Al(OH)_3$ and phosphoric acid, with an organic templating agent under acidic or basic conditions. By using different templating agents and different pH conditions, a wide range of open framework structures can be obtained.[1,2] While the general synthetic procedures are understood, details about the structure during the synthesis are still unclear.

Research has demonstrated that the formation of $AlPO_4$-18 proceeds through a series of intermediate phases. The ^{27}Al and ^{31}P solid-state NMR spectra as well as the powder X-ray diffraction, XRD, patterns of samples at different stages of the formation process indicate that the synthesis proceeds through an amorphous aluminum phosphate stage, then the one-dimensional porous material $AlPO_4$-5 and finally, after 72 hours, is converted to the three dimensional pore system of $AlPO_4$-18, see Figure 4.1.[3]

While the structure of the framework could be characterized using SSNMR and X-ray diffraction, it was unclear if the pore structure would be maintained upon calcination to remove the organic templating agent and water from the material. Xe-129 NMR spectroscopy was used to determine whether the intermediate materials were porous after calcinations and what pore geometries were present at different stages of synthesis. Information about Xe exchange between different phases in the intermediate materials was also obtained. This work has been reproduced in part with permission

from *Chem. Mater.* **2005**, *17*, 5481-5488, copyright 2005 American Chemical Society; only the research performed by the candidate is discussed here unless otherwise stated.

4.2 Sample preparation

The samples used in this study were previously synthesized by Bryan Demko and Dr. Yining Huang at the University of Western Ontario and followed the procedure of Simmen et al.,[1,4] using pseudo-boehmite (Catapal-B) and phosphoric acid (85 wt% H_3PO_4) as the aluminum and phosphorus sources, respectively. Tetraethylammonium hydroxide, TEAH, was used as the templating agent. The alumina and phosphoric acid were stirred with the templating agent and concentrated aqueous HCl for 2 hours and then sealed in a Teflon lined bomb and heated at 150 °C. After a specified time (0, 1, 2, 6, 24, 60, and 72 hrs) the samples were quenched in cold water and the solid and liquid phases were separated via centrifugation. The solids were then air dried at room temperature before being calcined at 500 °C for 24 hrs; this removed the templating agent and water molecules within the frameworks. Powder XRD patterns were recorded on all the samples and confirmed that the structural features of the framework were maintained after calcinations.

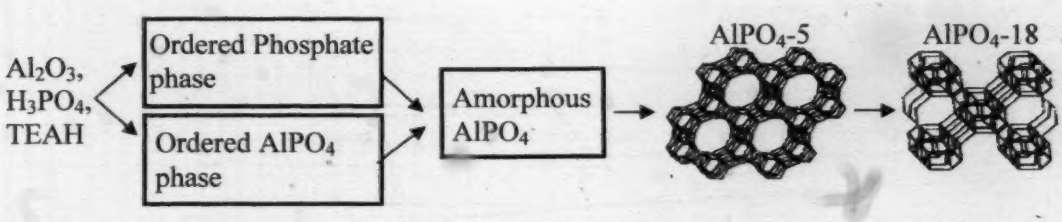

Figure 4.1: The different phases formed during the synthesis of $AlPO_4$-18 as determined by SSNMR and powder X-ray diffraction.[3]

4.3 1-D ^{129}Xe NMR spectra

The ^{129}Xe NMR spectra of HP ^{129}Xe in the samples are shown in Figure 4.2. The intensities of the spectra were scaled according to the weight of the sample used for each experiment so that the integrated intensities could be compared from sample to sample. All ^{129}Xe NMR spectra show distinct peaks resulting from Xe adsorbed in the different

aluminophosphate environments, Figure 4.2. All spectra, except for the sample not heated in the oven, 0 hrs, show ^{129}Xe peaks that are characteristic of Xe occupying pore spaces within the frameworks. These peaks confirm that the intermediate samples are porous after calcination; the structures do not collapse or form impenetrable frameworks that block access by Xe gas.

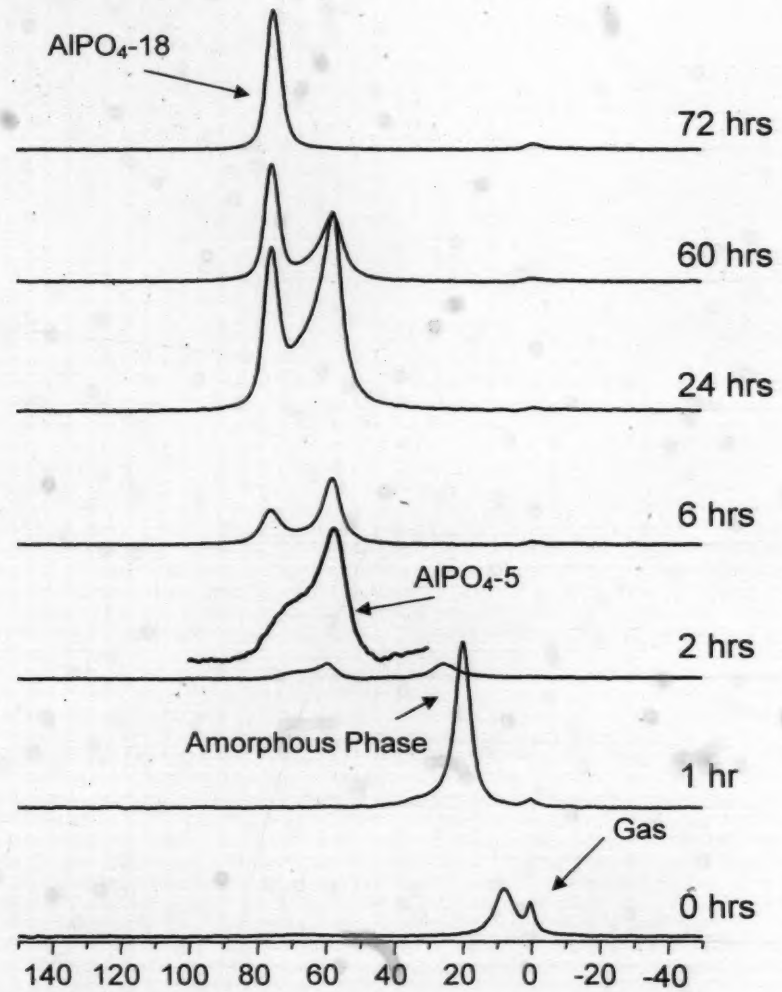

Figure 4.2: ^{129}Xe NMR spectra of HP ^{129}Xe in calcined aluminum phosphate samples after various heating times collected at 4.7 T. The inset spectrum is an expansion of the $AlPO_4$-5 peak in the two hour spectrum.

Information about the general size of the void spaces can be obtained simply by examining the chemical shift of the different peaks. The ^{129}Xe NMR spectrum acquired for the unheated sample shows a broad peak at 7 ppm in addition to the gas peak. The small chemical shift value of this peak suggests that it arises from Xe in the inter-crystallite space;[5] the crystallinity of the sample was confirmed using powder X-ray diffraction. The lack of higher frequency peaks suggests the absence of any porous structure within the frameworks of this phase. This is not an unexpected result since the sample is composed of crystalline phosphate and aluminum phosphate phases.[3]

The ^{129}Xe NMR spectrum of the sample that was heated for one hour is moderately different, Figure 4.2. According to previous work,[3] this sample corresponds to an aluminum phosphate structure that lacks long range order. The amorphous nature of the sample was confirmed by the powder X-ray diffraction pattern which exhibited no narrow diffraction peaks. Despite the lack of order, the peak observed in the ^{129}Xe NMR spectrum near 23 ppm suggests that the heated amorphous phase possesses void spaces which Xe can occupy. The shift is significantly higher than that observed in the 0 hr sample and is too large to be caused by the inter-crystallite space. The chemical shift suggests that the Xe is sampling large mesopores (20 – 500 Å).[6] If the walls of the pores are assumed to be primarily oxygen atoms and the electronic structure of these atoms is similar to that of the silica oxygen atoms, the correlation proposed by Terskikh et al. (see Section 2.6.2) can be used to determine that the approximate pore diameter of the mesoporous space is 470 Å.[7] The isotropic lineshape of the peak indicates that the Xe is rapidly exchanging between different sites within the pore space, as is expected for mesoporous materials. This averages any differences in the isotropic chemical shifts of Xe that arise from Xe sampling different environments within the pore space; the motion also will average any chemical shift anisotropy that may be present.

The third spectrum in Figure 4.2 is that of the sample heated for two hours at 150 °C and shows a small peak around 63 ppm. The peak shows an axially symmetric lineshape characteristic of Xe occupying space in a 1-D channel. The shape and position of this peak are characteristic of Xe in $AlPO_4$-5 (see Section 2.5.2). The components of the Xe magnetic shielding tensor that lie perpendicular to the channel (57.5 ppm) are significantly more shielded than the component that runs parallel to the channel (74.0

ppm). The same lineshape and chemical shifts have been observed for the iso-structural SSZ-24 which is a purely silacious zeolite.[5] Unlike previous thermally polarized ^{129}Xe NMR spectra of Xe in $AlPO_4$-5,[8] the spectrum in Figure 4.2 corresponds to Xe at extremely low pressure and therefore Xe-Xe interactions are negligible. Essentially, the spectrum represents Xe at zero loading and therefore δ_{iso}, 63 ppm, represents the value of δ_s; previous work determined the value of δ_s to be 56 ppm based on an extrapolation of variable pressure results to zero density.[9] Since the channel of $AlPO_4$-5 is microporous, using a fast-exchange two-site model for interpreting the ^{129}Xe chemical shifts is likely to be inadequate. GCMC simulations of Xe in SSZ-24 revealed that the Xe occupies a region along the walls, rarely sampling regions in the center of the channels. Jameson was able to reproduce the span and the skew of the Xe chemical shift tensor using the GCMC method, although the isotropic shift was approximately 20 ppm too small.[10] Subsequent GCMC calculations on $AlPO_4$-5 have revealed a similar behavior.[11]

The fourth spectrum in Figure 4.2, obtained after 6 hrs of sample heating, has a peak at 74 ppm in addition to the peak arising from Xe in $AlPO_4$-5. The powder XRD patterns indicate that this sample contains both $AlPO_4$-5 and $AlPO_4$-18. We assign the peak at 74 ppm to Xe residing in channels of $AlPO_4$-18. The peak increases in intensity as the sample is heated for longer times and shows no obvious powder lineshape indicating that either the chemical shift anisotropy is small or there is exchange that averages the anisotropy. The pore structure of $AlPO_4$-18 is significantly different from that of $AlPO_4$-5 in that it consists of a three dimensional pore system, the intersections of these channels form an asymmetric cage with 3.8 Å windows; at low loadings Xe is expected to occupy these cages.[4] While the cages are not perfectly spherical, the small asymmetry does not produce observable variations in the components of the ^{129}Xe magnetic shielding tensor because the Xe atom will average over all the space within the cage during the NMR experiment. This conclusion has been verified by GCMC simulations which modeled the distribution of Xe within the cages of $AlPO_4$-18.[11] The spectrum of Xe in $AlPO_4$-18 represents one of the few examples of ^{129}Xe NMR in ordered 3-D microporous channel systems.

The variation in intensity between the spectra of the 1 hr sample and the 6 hr sample provides an insight into the transformation process. The intense peak in the 1 hr

spectrum indicates that a large proportion of the solid material is mesoporous. With subsequent heating, the mesoporous phase is destroyed and only when the rearrangement has formed the $AlPO_4$-5 structure does porosity return; this suggests the presence of a non-porous transition phase. The intensity of the ^{129}Xe NMR signal increases from 2 to 24 hrs as more of this non-porous phase is transformed into the microporous aluminum phosphates. After 24 hrs, it is likely that all of the non-porous transition phase is converted to microporous aluminum phosphate, either $AlPO_4$-5 or -18. The spectra indicate that the amount of $AlPO_4$-5 reaches a maximum at 24 hrs after which time the ^{129}Xe NMR peak from Xe in $AlPO_4$-5 decreases as the $AlPO_4$-5 is converted to $AlPO_4$-18. The intensity of the ^{129}Xe NMR peak of Xe in $AlPO_4$-18 increases throughout the process, reaching a maximum intensity after 72 hours, at which time all the $AlPO_4$-5 has been converted to $AlPO_4$-18. The spectrum acquired at 60 hrs represents an $AlPO_4$-5 to $AlPO_4$-18 ratio close to one.

These results clearly show that the pore structure of the aluminum phosphate undergoes the same transitions as were observed for the framework using powder XRD, ^{31}P and ^{27}Al NMR.[3] The ^{129}Xe NMR spectra indicate that the Xe initially resides in the interstitial space prior to heating and no pores are present. After one hour of heating, the Xe resides in the large voids of the amorphous phase. The samples likely go through a non-porous intermediate phase before being converted to $AlPO_4$-5, which begins to form after two hours of heating and provides a one dimensional cylindrical channel in which the Xe resides and exhibits an axially symmetric ^{129}Xe NMR lineshape. Finally, after six hours of heating, $AlPO_4$-18 channels form and continue to form until, after 72 hours of heating, only $AlPO_4$-18 is present.

4.4 2-D ^{129}Xe EXSY spectra

In order to gain insights into the mechanism of the conversion from $AlPO_4$-5 to $AlPO_4$-18, the exchange of the Xe in the sample that was heated for 24 hours was investigated. Two-dimensional exchange spectroscopy (EXSY) spectra are shown in Figure 4.3.[12] Each spectrum consisted of 128 points in the t_1 dimension and 2 k points in the t_2 dimension, and was symmetrized in order to overcome distortions caused by low signal-to-noise and t_1 noise.[13]

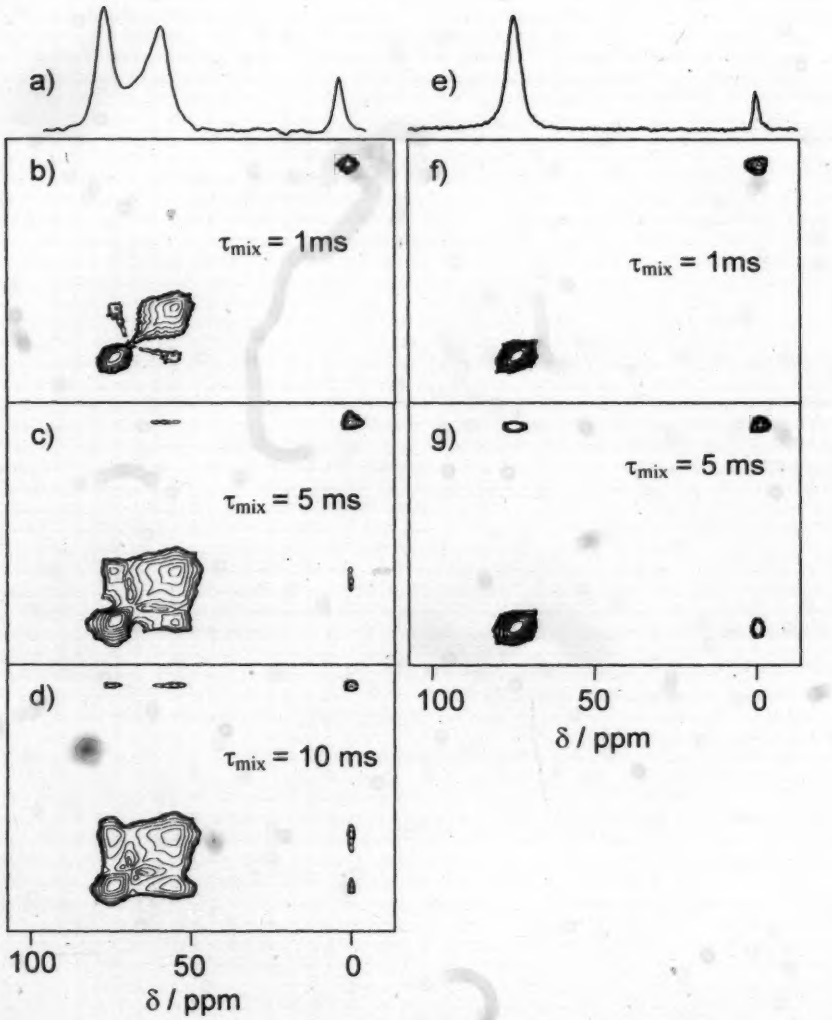

Figure 4.3: ^{129}Xe EXSY spectra of Xe in the 60 hr sample (a – d) and the 72 hr sample (e-g). The 1-D spectra for the respective samples are presented in (a) and (e) while the 2-D EXSY spectra at the indicated mixing times are presented in (c-d) and (f and g).

In the EXSY experiment the diagonal contains the one dimensional spectrum and is equivalent to the spectrum shown in Figure 4.3a, while the cross-peaks indicate that exchange of Xe atoms between the corresponding sites on the diagonal within the timescale of τ_{mix}.[14,15] Figure 4.3b shows the spectrum acquired with τ_{mix} = 1 ms. This spectrum shows the presence of cross-peaks between the two aluminophosphate sites. Surprisingly there are no cross-peaks between either of the sites and the Xe gas peak. This result indicates that on the 1 ms timescale, the exchange of Xe between $AlPO_4$-5 and

$AlPO_4$-18 occurs without transport through the bulk gas. The ^{129}Xe NMR spectrum in Figure 4.3c, acquired with τ_{mix} = 5 ms, shows the Xe exchange between the aluminum phosphate sites as well as a small cross-peak between the $AlPO_4$-5 site and the free Xe gas peak. The presence of this cross-peak indicates that $AlPO_4$-5 exchanges with the bulk gas on the 5 ms timescale, however, the $AlPO_4$-18 site shows no sign of exchanging with the gas peak. The spectrum in Figure 4.3d was acquired with τ_{mix} = 10 ms and indicates that Xe gas exchanges between all three environments on this timescale. Based on these results the exchange of Xe between the two different $AlPO_4$ frameworks is faster than the exchange of either framework with the free gas. This indicates that the two frameworks are in contact with each other, either as domains within the same crystallite or as physically joined crystallites of $AlPO_4$-5 and $AlPO_4$-18.

The EXSY spectra of Xe in a pure $AlPO_4$-18 sample reveal that exchange between the $AlPO_4$-18 pores and the free gas occurs on a timescale of 5 ms, Figure 4.3g. Since there is no exchange peak between the $AlPO_4$-18 and the free gas in the 5 ms EXSY spectrum of the mixture, the exchange dynamics between the $AlPO_4$-18 and the free gas are hindered by the presence of $AlPO_4$-5 in the 60 hr sample. One possible explanation for this is that the $AlPO_4$-18 domains form on the inside of the $AlPO_4$-5 crystallites.

4.5 Conclusions

The ^{129}Xe NMR spectra indicate that all of the samples that undergo heating contain porous space within the solid frameworks. At first, the amorphous $AlPO_4$ phase contains mesoporous void spaces which result in a Xe chemical shift of 23 ppm. Using the correlation for mesoporous silica, an approximate mean pore diameter of 470 Å is obtained. As the sample is heated, the framework initially loses its porosity, forming a nonporous transition phase that is subsequently converted to the microporous structure of $AlPO_4$-5. The peak observed at 63 ppm indicates a microporous cavity and the lineshape reveals that the geometry of the cavity is axially symmetric, consistent with the 1-D cylindrical channels of $AlPO_4$-5. With further heating the final structure, $AlPO_4$-18 is formed; the lack of lineshape in the ^{129}Xe NMR spectrum being consistent with the nearly symmetric cages formed at the intersections of the 3-D channel network. Finally 2-D

EXSY spectra have provided insights into the exchange process of Xe between the gas phase and the $AlPO_4$-5 and $AlPO_4$-18 channel networks in the intermediate, 60 hr, sample.

---

[1] Wilson, S. T.; Lok, B. M.; Messina, C. A.; Cannan, T. R.; Flanigen, E. M. *J. Am. Chem. Soc.* **1982**, *104*, 1146-1147.

[2] Patarin, J.; Paillaud, J.-L.; Kessler, H. *In Handbook of Porous Solids Vol. 2 Proceedings* Schüth, F.; Sing, K. S. W.; Weitkamp, J. Eds. Wiley-VCH, Weinheim, Germany. 2002.

[3] Huang, Y.; Demko, B. A.; Kirby, C. W. *Chem. Mater.* **2003**, *15*, 2437-2444.

[4] Simmen, A.; McCusker, L. B.; Baerlocher, C.; Meier, W. M. *Zeolites* **1991**, *11*, 654-661.

[5] Moudrakovski, I. L.; Nossov, A.; Lang, S.; Breeze, S. R.; Ratcliffe, C. I.; Simard, B.; Santyr, G.; Ripmeester, J. A. *Chem. Mater.* **2000**, *12*, 1181-1183.

[6] Bonardet, J.L.; Fraissard, J.; Gédéon, A.; Springuel-Huet, M.A. *Catal. Rev.-Sci. Eng.* **1999**, *41*, 115-225.

[7] Terskikh, V. V.; Moudrakovski, I. L.; Breeze, S. R.; Lang, S.; Ratcliffe, C. I.; Ripmeester, J. A.; Sayari, A. *Langmuir* **2002**, *18*, 5653-5656.

[8] Koskela, T.; Jokisaari, J.; Satyanarayana, C. *Microporous Mesoporous Mater.* **2004**, *67*, 113-122.

[9] Chen, Q. J.; Springuel-Huet, M. A.; Fraissard, J. *Chem. Phys. Lett.* **1989**, *159*, 117-121.

[10] Jameson, C. J. *J. Am. Chem. Soc.* **2004**, *126*, 10450-10456.

[11] Sears, D. N.; Demko, B. A.; Ooms, K. J.; Wasylishen, R. E. *Chem. Mater.* **2005**, *17*, 5481-5488.

[12] Jeener, J.; Meier, B. H.; Bachmann, P.; Ernst, R. R. *J. Chem. Phys.* **1979**, *71*, 4546-4553.

[13] Hull, W. E. in *Two-Dimensional NMR Spectroscopy: Applications for Chemists and Biochemists*; 2 ed.; Croasmun, W.R.; Carlson, R. M. K. Eds. VCH Publishers, Inc., New York, 1994, pp 67-456.

[14] Moudrakovski, I. L.; Ratcliffe, C. I.; Ripmeester, J. A. *J. Am. Chem. Soc.* **1998**, *120*, 3123-3132.

[15] Kritzenberger, J.; Gaede, H. C.; Shore, J. S.; Pines, A.; Bell, A. T. *J. Phys. Chem.* **1994**, *98*, 10173-10179.

Chapter 5: ^{129}Xe NMR spectroscopy of potentially porous organic macrocycles

5.1 Introduction

There are almost weekly reports of new porous materials prepared using organic or metal-organic building blocks.[1,2,3,4,5,6,7,8,9,10,11] By varying the organic molecules used, chemists can introduce chemical functionality into pores which can increase the applicability of materials for molecular sensing, separation, and gas storage.[2,3,4,5]

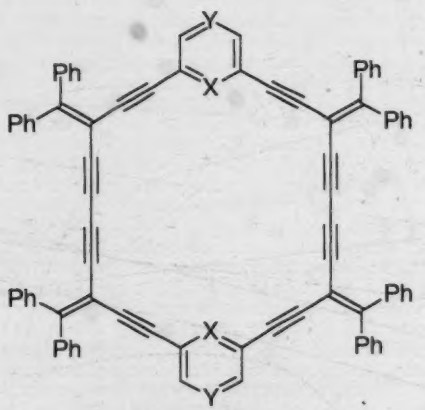

1: X = N, Y = CH
2: X = Y = CH
3: X = CH, Y = N

Figure 5.1: The structure of the three organic macrocycles studied.

One approach to synthesizing porous organic materials is to use conjugated macrocycles as "building blocks" that can form porous channels when the molecules self-assemble in the solid state.[12,13,14,15] One material that has recently been prepared, **1** (Figure 5.1), showed the potential for porosity based on single-crystal X-ray diffraction analysis (Figure 5.2).[15] The conjugated macrocycles stack in the solid state forming one-dimensional channels along the crystallographic *a*-axis. The X-ray diffraction results indicate that there are two solvent molecules present between each pair of macrocycles; although it could not be determined whether the solvent was dichloromethane or 1,2-dichloroethane.

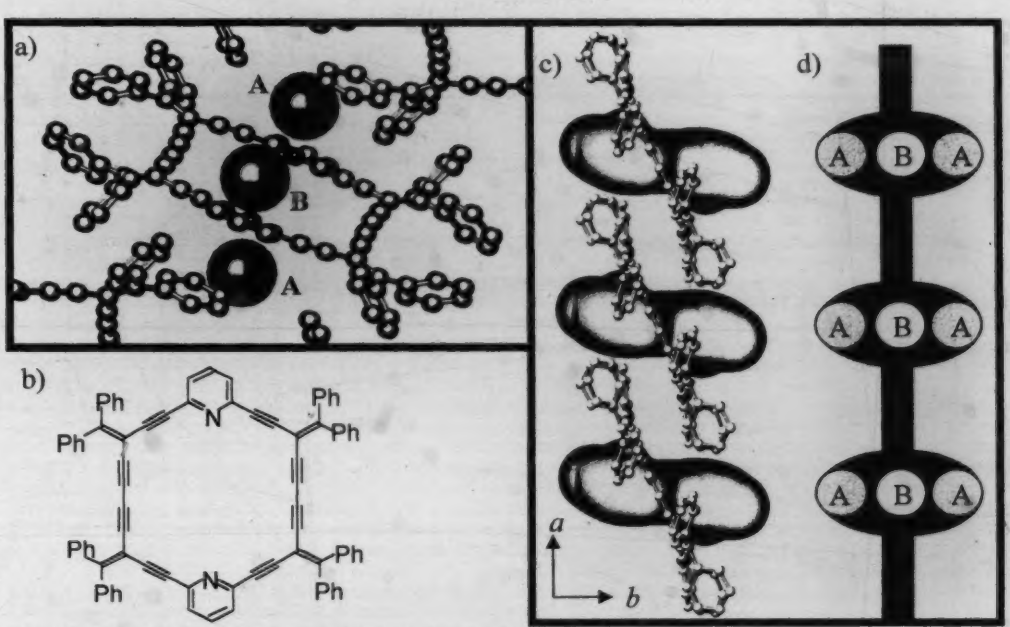

Figure 5.2: The crystal structure of **1** determined by X-ray diffraction. Hydrogen atoms and solvent molecules have been omitted for clarity. (a) The view along the crystallographic *a*-axis showing the channel and two possible sites for Xe atoms. (b) The structure diagram of **1**. (c) Side on view along the crystallographic c-axis showing the framework structure and the van der Waals surfaces of the solvent molecules which illustrate the approximate position, size and shape of the solvent cavities. (d) A schematic diagram of the channel structure formed by the interconnected solvent cavities and the positions of sites **A** and **B**.

One of the challenges facing the development of porous organic materials is the limited number of methods available for characterizing materials in the solid state. In many cases, obtaining suitable single crystals for X-ray diffraction is difficult. Even if single crystals are accessible, they generally contain co-crystallized solvent molecules that occupy the pores, as is the case for **1**, blocking any accessible porosity in the material. Removal of the solvent, if possible, often results in the collapse of the porous framework and shattering of the crystal, making it difficult to determine whether the porous framework remains intact.[9] Therefore, the development of other techniques capable of assessing the presence of pores in these solid materials is desirable.

One experimental challenge that separates classic inorganic porous materials such as aluminum phosphates from these macrocycle compounds is the quantity of sample that can be readily synthesized. Many organic materials are often synthesized in limited quantities (tens to hundreds of milligrams); for example, only 29 mg of macrocycle **2** were isolated, requiring more than a liter of various solvents for the synthesis due to its low solubility. This can make the application of thermally polarized ^{129}Xe gas NMR extremely difficult, even if isotopically enriched Xe is used. The use of optical-pumping spin-exchange to produce highly nuclear spin polarized ^{129}Xe, with an NMR signal increase of 10,000 times, allows the challenges associated with low sample quantity to be overcome.

In this study, continuous-flow HP ^{129}Xe NMR is used to investigate the presence and nature of the pores in three closely related organic materials, **1-3** (Figure 5.1). Variable-temperature (VT) ^{129}Xe NMR studies have been undertaken for the three macrocycles and exchange spectroscopy,[16] (EXSY) experiments were performed on one of the samples. The results demonstrate that valuable information can be obtained by employing this technique to investigate small quantities of potentially porous macrocyclic compounds. These studies, combined with molecular dynamics (MD) simulations and density functional theory (DFT) magnetic shielding calculations, allow us to determine the presence of porosity in the absence of the co-crystallized solvent guests and provide structural information about the porosity of all three materials. This work has been published in *J. Mater. Chem.* **2005**, *15*, 4318-4327, and only the research performed by the candidate is discussed here unless otherwise indicated.

5.2 Preparation of macrocycles

All three macrocycles were synthesized by Dr. Katie Campbell, a collaborator working in the Tykwinski organic synthesis laboratory, using a combination of palladium–catalyzed cross–coupling and copper–catalyzed acetylenic homocoupling strategies, as previously described for macrocycles **1**[15] and **3**.[12] The unfunctionalized macrocycle **2** was prepared using analogous methods, as shown in Figure 5.3. 3,5-Diethynyl benzene **4** was cross–coupled with diphenylalkylidene–substituted triflate **5** using palladium catalysis, to form oligomer **6**, which was purified on a silica gel column

with a yield of 98%. Deprotection of **6** was achieved by treating with tetrabutylammoniumfluoride in wet tetrahydrofuran and the resulting desilylated tetrayne was treated with CuI/*N,N,N'N'*-tetramethylethylenediamine (TMEDA) at high dilution in dry CH_2Cl_2 in the presence of air for 14 hours. Subsequent to aqueous workup, reduction of the solvent volume by approximately 90% and then layering the resulting solution with acetone (1:1 v/v) led to the selective precipitation of **2**. Upon filtering and drying, pure **2** was isolated in 39% yield as an orange–yellow solid.

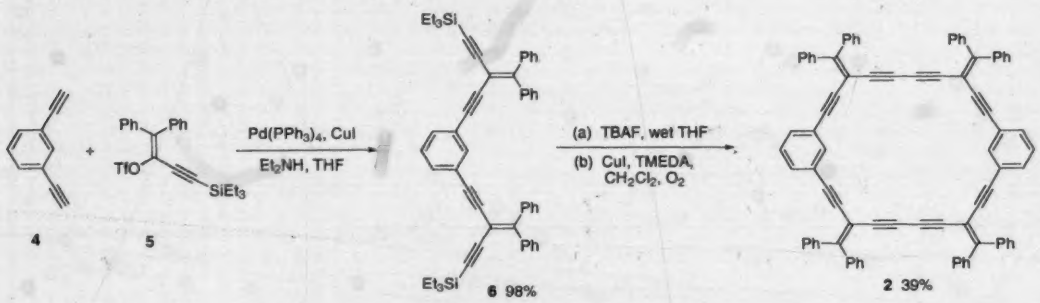

Figure 5.3: Scheme of the synthesis of **2.**

Crystals of **1**, suitable for crystallographic analysis, were obtained by boiling a solution of the macrocycle in CH_2Cl_2/1,2-dichloroethane and allowing slow evaporation at room temperature. Macrocycles **2** and **3** were obtained as microcrystalline solids by allowing slow diffusion/evaporation of an acetone/CH_2Cl_2 solution (9:1, v/v) at 277 K or a concentrated CH_2Cl_2 solution at 277 K, respectively. Macrocycles **2** and **3** did not possess sufficient solubility for the growth of X-ray quality single-crystals, even at elevated temperatures.

Removal of the solvent molecules from solid samples **1-3** occurred when nitrogen gas or the N_2/He/Xe gas mixture flowed over the solid. This was verified using solution-state ^{1}H NMR. The fact that the solvent dichloromethane or 1,2-dichloroethane are readily displaced from the structures suggests that the channel dimensions are large enough to allow Xe to diffuse through the material under flow conditions.

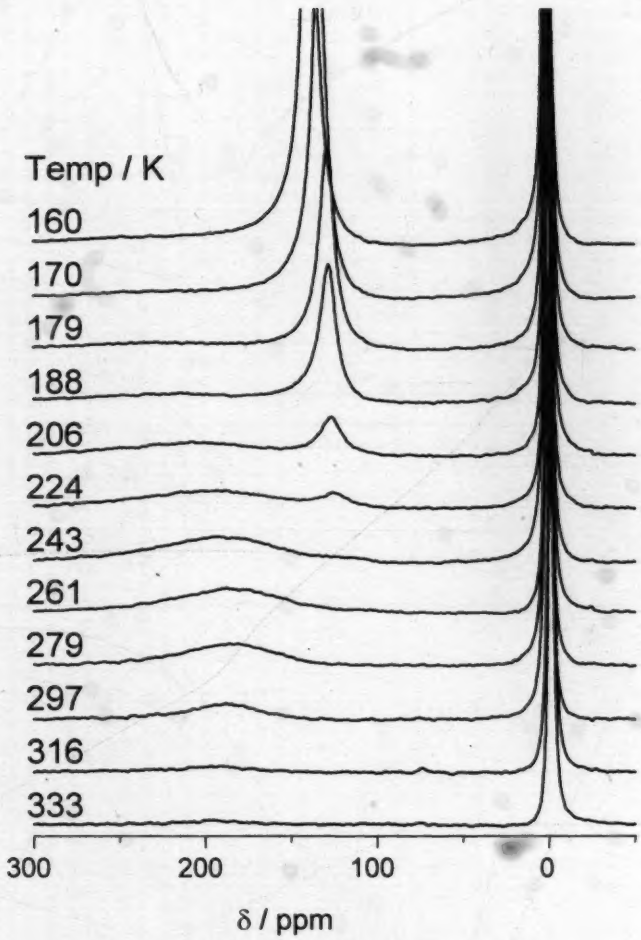

Figure 5.4: VT HP ^{129}Xe NMR spectra of **1**. At each temperature, 1280 scans were acquired using a 1 s pulse delay.

5.3 ^{129}Xe NMR spectroscopy

Compound **1** is a cross-conjugated planar macrocycle containing two pyridine rings oriented such that the nitrogen atoms are on the inside of the large macrocycle ring (Figure 5.1). The periphery of the macrocycle core is appended with diphenylalkylidene groups. The solid-state structure of **1**, as determined by single-crystal X-ray diffraction, shown in Figure 5.2, consists of stacks of planar macrocycles tilted at an angle of 60°

from the *b*–axis. The stacking results in the creation of one-dimensional channels along the crystallographic *a*-axis, through the centre of the macrocycles (Figure 5.2a). When viewed along the crystallographic *c*-axis (Figure 5.2c) it is apparent that the channels are made up of cavities, occupied by the co-crystalized solvent molecules, with approximate van der Waals dimensions of 5.5 x 6.0 x 14.0 Å. These cavities are centred in the middle of the macrocycles and connected by narrower openings between the nitrogen atoms of two neighboring macrocycles, Figure 5.2d. Figure 5.2c also shows the van der Waals surface of the disordered solvent molecules. As already indicated, the solvent molecules are removed from the structure when the $Xe/N_2/He$ gas mixture flows over the solid. The ability to easily remove the solvent molecules suggests that guest molecules or atoms can move between these cavities. In the absence of the solvent, these sites provide an ideal location for the adsorption of Xe atoms.

Figure 5.4 shows ^{129}Xe NMR spectra of Xe in **1** at temperatures between 160 K and 333 K. Peaks with three different chemical shifts are observed, the appearance of which depends on the temperature. The first peak, at 0 ppm, is the peak obtained for "free" Xe in the gas mixture above the solid sample. Since the spectra were acquired using ~ 50 mg of sample, a significant amount of empty space is present in the sample holder (volume ≈ 125 µl). The remaining two peaks correspond to Xe atoms that occupy the pore space within **1** and will each be discussed separately.

5.3.1 The ^{129}Xe NMR peak at $\delta \approx$ 190 ppm

A broad ^{129}Xe NMR peak near 190 ppm is observed at temperatures above ~ 188 K. This large chemical shift value suggests that the Xe is in a highly confined space. The solvent cavity is an elongated pore centred on the channel, Figure 5.2c, with enough space to accommodate several Xe atoms. The channel sites, i.e., the sites in the centre of the solvent cavity that are at the channel-cavity intersection, Figure 5.2a, Site **B**, are relatively large compared to the size of the Xe atoms and it is unlikely that the large chemical shift of 190 ppm would result from Xe occupying these sites. The ends of the solvent cavity, Site **A**, are outside of the channel and are surrounded primarily by the phenyl groups of the neighbouring macrocycles. These end sites offer a more confined space than is available at the channel sites. The size of the cavity can be approximated by

analyzing the van der Waals free space available after the solvent molecules are removed from the crystal structure. The chemical shift value near 190 ppm is similar to that reported for ^{129}Xe in calixarene-based solid lipid nanoparticles where the Xe is apparently "dissolved" in long alkyl chains.[17] Xe chemical shift values close to 200 ppm are also observed for Xe dissolved in organic solvents such as benzene, 193 ppm, and toluene, 188.5 ppm,[18] and for Xe in C_{60}, 188.1 ppm.[19]

The breadth of the ^{129}Xe NMR peak at $\delta \approx 190$ ppm is attributed to the fact that the Xe atoms can occupy a distribution of slightly different positions near the end of the solvent cavity, all of which have approximately equal cavity dimensions. In many cases spinning the sample at the magic angle can confirm whether broadening is due to chemical shift anisotropy or other reasons such as a distribution of sites; however, we were unable to carry out these experiments at this time on the small sample volumes available to us. Additionally, a size distribution of the crystallites has been shown to result in a broadening of the ^{129}Xe NMR lineshape due to differences in the exchange rates between the pore space and the free gas (see Section 3.2.3).[20,21] Disorder and thermal motion of the phenyl groups and anisotropy in the Xe magnetic shielding tensor may also contribute to the broadening.

The peak near 190 ppm changes substantially as the temperature is varied. As the temperature is reduced from 333 K to 279 K, the total integrated peak intensity increases, indicating that as the temperature is lowered more Xe atoms spend time in the end sites. As the temperature is lowered below 279 K, the breadth of the peak near 190 ppm increases and there is an increase in the chemical shift. The intensity of this peak also decreases with decreasing temperature, and below 188 K, disappears entirely. Ripmeester and coworkers observed a similar trend for the ^{129}Xe NMR peak of Xe in the microporous, interlamellar space of montmorillonite, which they attributed to condensation of Xe in the micropores.[22] The inability of freshly hyper-polarized ^{129}Xe to enter the end sites causes a loss of signal intensity due to the "one shot" nature of the hyperpolarized ^{129}Xe NMR experiment.[23] The broadening of the peak and its movement to higher chemical shift values is likely caused by subtle changes in the solid-state structure or Xe dynamics in the cavities as the temperature decreases. The increase in the

average chemical shift could also result from an increase in Xe-Xe interactions as adjacent end sites become filled with Xe.[24,25,26,27]

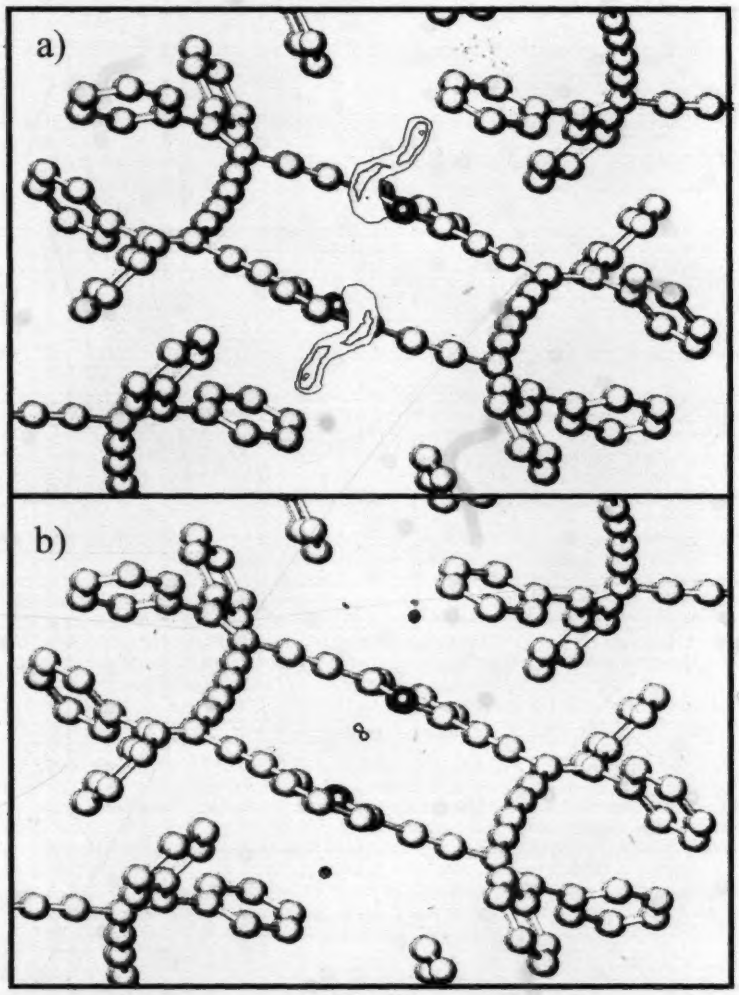

Figure 5.5: Xe one-body distribution plot of Xe in **1**. The contour plots represent the distribution of Xe over the course of the MD simulations. a) One Xe atom at room temperature, b) three Xe atoms at 160 K.

Molecular dynamics simulations were performed in order to provide support for the above explanation; simulations were performed using the MM+ force field as available in the Hyperchem computational chemistry program.[28] The atomic positions of the organic framework were obtained from the X-ray diffraction data; it is assumed that there are no major structural changes to the framework upon removal of the solvent

molecules. One Xe atom was placed in the centre of the solvent cavity and the simulation was performed. The results of the simulation, illustrated in Figure 5.5a, predict that the Xe atom moves around the cavity, spending most of its time at the ends, Figure 5.2a, Site **A**. As the simulation temperature was lowered, the fraction of time that the Xe spent near the ends of the cavity increased (not shown). When two Xe atoms were placed in each cavity, the distribution did not change significantly but the two Xe atoms occupied opposite ends of the cavity, Site **A**.

In summary, by analyzing the van der Waals free space in the cavity the most confined regions in the pores that can accommodate Xe atoms are clearly at the ends of the cavities. Since the ^{129}Xe NMR chemical shift of 190 ppm is characteristic of Xe atoms occupying low volume cavities, this peak is attributed to Xe in the highly confined region of the solvent cavity, Site **A**. Additionally, the MD simulations provide evidence that the lowest energy positions for Xe in the solvent cavity, and therefore the regions preferentially occupied correspond to the regions at the two ends of the cavities.

5.3.2 The ^{129}Xe NMR peak with δ between 125 and 138 ppm

As the intensity of the peak near 190 ppm begins to decrease at T $\approx$ 230 K, Figure 5.4, another peak, close to 125 ppm, appears. This peak steadily increases in intensity and shifts to higher frequency as the temperature decreases, reaching a value of 138 ppm at 160 K. The movement to higher chemical shifts could be attributed to a decrease in the exchange rate between the Xe adsorbed in **1** and the free gas. The smaller chemical shift value suggests that the Xe atoms responsible for this peak reside in a less confined space than those discussed for the peak near 190 ppm. The only possible sites with enough "free" space to result in the observed chemical shift values near 138 ppm are those near the channel-cavity intersections, Site **B** in Figure 5.2a. The chemical shift values of this peak are similar to those reported for Xe in Dianin's compound, 4-*p*-hydroxyphenyl-2,2,4-trimethylchroman; 134 ppm when there is one Xe per unit cell and 152 ppm when there were two Xe atoms per unit cell.[29] Dianin's compound has a cage of similar dimensions to the sites created at the centre of the solvent cavity in **1** when the end sites, Site **A**, are occupied by Xe atoms. Therefore, we assign the peak near 138 ppm to Xe at the **B** Sites of **1**.

The peak at 125 ppm appears only when the intensity of the peak near 190 ppm begins to decrease. This suggests that the Xe atoms only occupy Site **B** when Site **A** becomes inaccessible to freshly polarized ^{129}Xe nuclei. The potential energy surface for Xe in various pore sites depends on the number of close contacts that Xe can make with the host. Generally the greater the number of close contacts, the deeper the potential energy well and therefore the tighter the Xe binding. This explains why Xe preferentially occupies the tight end sites, Sites **A**, and only when these become inaccessible do the Xe atoms begin to occupy the larger channel cavities.[22] An MD simulation was performed as described above but with the addition of a third Xe atom to the structure. The results of this MD simulation are illustrated in Figure 5.5b and show that the three Xe atoms occupy the space indicated in Figure 5.1a. Since, at low temperature, the first two Xe atoms were shown to preferentially reside near the ends of the solvent cavity, Site **A**, the inclusion of subsequent Xe atoms results in the filling of the centre position of the cavity, Site **B**, which has a larger free volume than the end sites. The difference in the calculated potential energy between the two sites is 13.8 kJ mol^{-1} when there is only one Xe per cavity, with the end sites being lower in energy. This correlates well with the dynamic model which was proposed on the basis of the NMR experiments. The distribution of the Xe in Site **B,** Figure 5.5b, is significantly smaller than that of the Xe in Site **A** before the third Xe is added, Figure 5.5a. This is likely the reason for the much narrower ^{129}Xe NMR line-width of the peak near 138 ppm and further suggests that the breadth of the peak near 190 ppm is a result of Xe occupying a distribution of positions within the cavity.

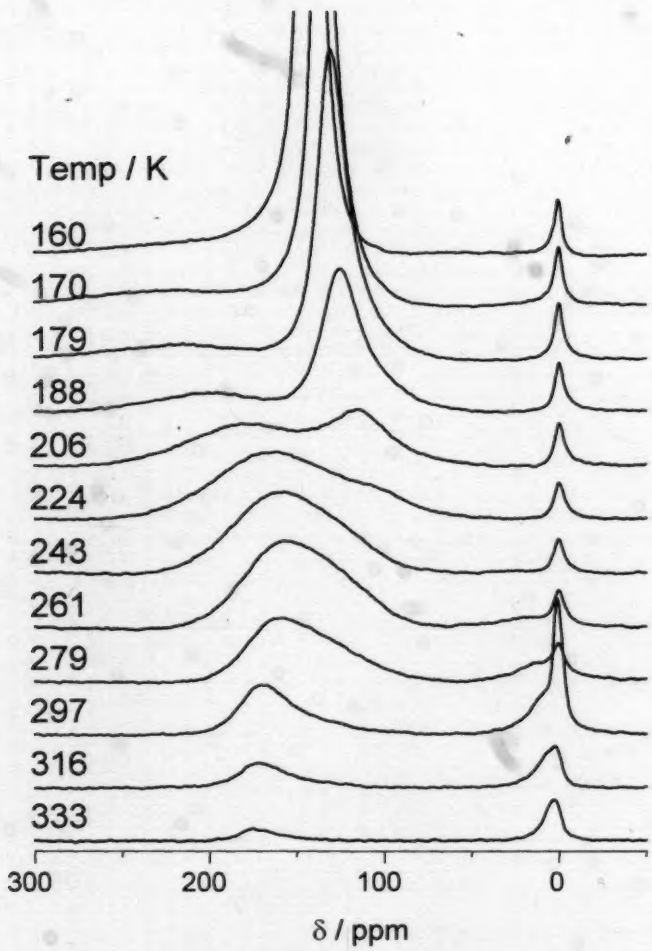

Figure 5.6: VT HP ^{129}Xe NMR spectra of **2**. At each temperature, 1280 scans were acquired using a 1 s pulse delay.

5.3.3 Compounds 2 and 3

The molecular structure of compounds **2** and **3** are analogous to that of **1**, Figure 5.1. In **2** the pyridine rings at the ends of the macrocycle are replaced by phenyl rings. In **3** the orientation of the pyridine group is inverted such that the nitrogens of the pyridines are on the exterior of the macrocycle.

With the connections between chemical shift and structure made above, the ^{129}Xe NMR spectra obtained for compounds **2** and **3** can be analyzed. As previously mentioned, X-ray quality crystals of these two compounds could not be obtained as a

result of their extreme insolubility. The ^{129}Xe NMR VT spectra for Xe in **2** and **3** are presented in Figures 5.6 and 5.7, respectively. The behaviour of the spectra as a function of temperature is similar to that of **1**. This immediately suggests that the crystal packing and pores responsible for the peaks described for **1** are also present in the extended structures of **2** and **3**.

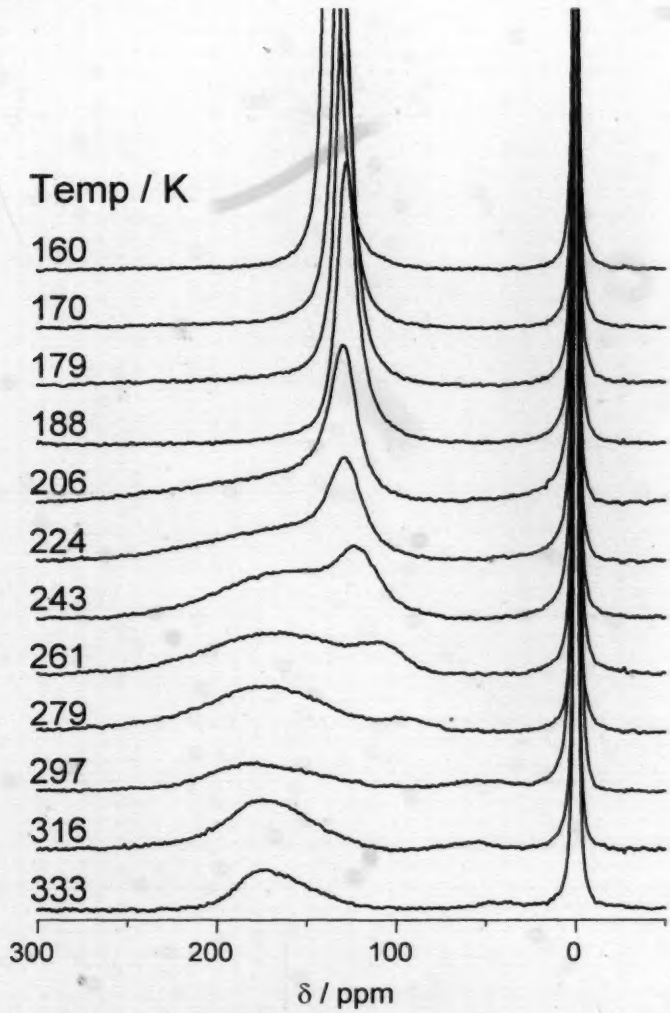

Figure 5.7: VT HP ^{129}Xe NMR spectra of **3**. At each temperature, 1280 scans were acquired using a 1 s pulse delay.

The peak with the larger chemical shift in the spectra acquired for **2** is at slightly lower chemical shift values compared to that of **1**. The difference, however, is small and

does not change the assignment of this peak to Xe trapped in highly confined sites that are analogous to Site **A** in **1**.

The peak with the lower chemical shift in **2** appears when the temperature is decreased to 224 K and is at a lower chemical shift, ~108 ppm, compared to that of **1**. At 160 K, however, the chemical shift is nearly the same, 141 ppm. This different chemical shift *vs.* temperature profile can be attributed to a greater rate of exchange of Xe between the channels and the free gas for **2**. Assuming that the peak with $\delta \approx 141$ ppm results from Xe in a site analogous to **B**, the difference in the chemical shift at 160 K between samples **1** and **2** arises from either subtle differences in the solid-state structure or differences in the phenyl-Xe and pyridine-Xe interactions.

The ^{129}Xe NMR spectra for Xe in **3** show a similar behaviour to the other two compounds, Figure 5.7. The peak with the higher chemical shift appears near 174 ppm and the lower chemical shift peak moves from ~ 95 ppm at 279 K to 136 ppm at 160 K. The main difference between the VT ^{129}Xe NMR spectra of **3** and **1** is that the peak with the lower chemical shift appears before the intensity of the peak near 174 ppm begins to decrease. This indicates that Xe spends significant time in the channel cavities even before the end sites become inaccessible.

We were able to prepare approximately 100 mg of **3** and therefore ^{129}Xe NMR signal intensities were sufficient for 2-D exchange spectroscopy experiments to be attempted. It is rare, when working with these limited sample amounts, that 2-D experiments are feasible because of the time required to acquire a 2-D spectrum. In the case of 2-D exchange experiments, it is further necessary to acquire several 2-D spectra with different mixing times. However, in the case of compound **3**, EXSY spectra were acquired at 293 K and 215 K using three mixing times. The spectra, shown in Figure 5.8, suffer from poor signal-to-noise, especially at longer mixing times, and also suffer from significant t_1 noise, primarily on the peaks attributed to Xe in the pores. At 293 K, the 1-D spectrum consists of a gas peak and the broad peak assigned to Xe in the end sites, Sites **A,** Figure 5.2. In the EXSY experiment, the mixing time corresponds to the amount of time Xe is allowed to move between these two sites. Figure 5.8 indicates that, when the mixing time is 1 ms, there is rapid exchange between the gas phase and the end sites at 293 K, signified by the cross peaks between the two diagonal peaks. The slightly

elongated rectangular shape of the peak near 174 ppm in the 2-D spectrum indicates that the Xe atoms that occupy the end sites are also exchanging between slightly different environments within the cavities. As the mixing time is increased to 10 ms the slight elongation is removed.

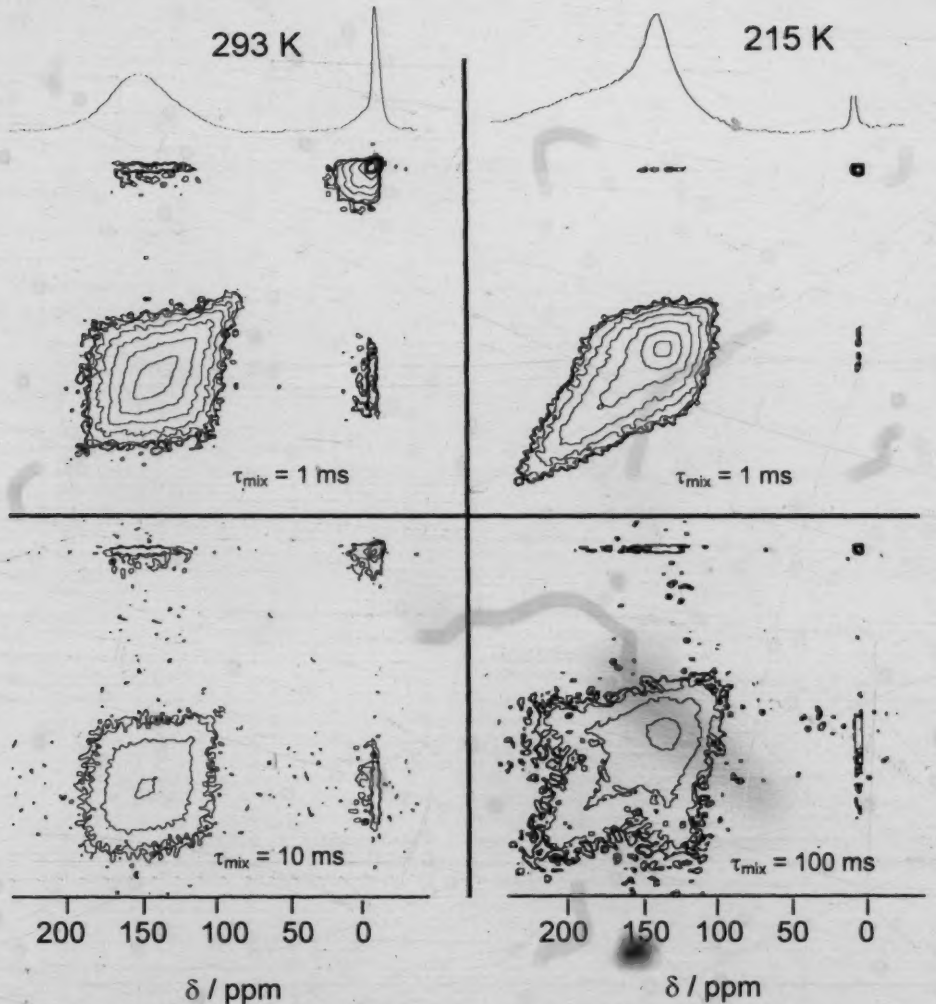

Figure 5.8: The 2-D EXSY HP ^{129}Xe NMR spectra of **3**. Left: the spectra collected at 293 K using mixing times of 1 ms (top) and 10 ms (bottom). Right: the spectra collected at 215 K using mixing times of 1 ms (top) and 100 ms (bottom). The spectra were symmetrized in order to overcome T_1 noise.

A benefit of using **3** for the exchange study is that both the peaks that originate from Xe in Sites **A** and **B** are present at the same temperature, 215 K. At a mixing time of 1 ms, the spectrum clearly shows exchange between the gas phase and the channel

sites, while there is no obvious evidence for direct exchange between the gas and the end sites, Site **A**. The elongated oval shape of the 2-D contour plot suggests that there is also little exchange between the different positions in the end sites at 215 K in contrast to the spectrum obtained at 293 K where nearly complete exchange occurs. When the mixing time is increased to 100 ms, the shape of the peaks changes dramatically. The peak near 174 ppm maintains its elongated shape, signifying minimal exchange, but exchange peaks appear between the peak at $\delta \approx 135$ ppm, Site **B**, and the peaks from Xe in the end site, Site **A**.

These results support the dynamic model proposed based on the 1-D spectra and MD simulations. At 293 K the Xe atoms move between the free gas and the end sites, passing through the channels so rapidly that they are not observed in the channels. When the temperature is reduced, the rate of Xe exchange decreases and the Xe atoms can be traced, passing from the gas into the channels on a time scale less than 1 ms, and then exchanging from the channels into the end sites on a time scale of ≈ 100 ms.

5.4 Magnetic Shielding Calculations

Whereas the chemical shift of Xe depends on the shape and size of the pores that the Xe occupies, it is also intimately related to the electronic structure of the framework. It is reasonable to assume that the solid-state packing of the molecules for the three different compounds, **1-3**, is similar. Changes in the orientation of the pyridine rings in **1** and **3** are not expected to significantly affect the intermolecular interactions that hold the molecules together in the solid state. Replacing a pyridine ring by a phenyl ring, **2**, is expected to cause minimal structural changes in compounds **1** *vs.* **2**. The similarities in the ^{129}Xe NMR spectra discussed above support these conclusions. Therefore, assuming that the solid-state packing and thus the pores are analogous, the differences observed in the ^{129}Xe chemical shift between the three compounds can be attributed to "electronic effects" that arise from the orientation of the pyridine rings, **1** *vs.* **3**, or the replacement of the pyridine rings by phenyl rings. This should have the largest influence on the ^{129}Xe NMR peak arising from the Xe atoms in Site **B**. In order to understand these contributions to the chemical shift, magnetic shielding calculations were performed for Xe near the nitrogen of a pyridine, the C4 carbon of a pyridine and a benzene carbon,

both in the molecular plane and perpendicular to it in all cases. The chemical shift results of these calculations are shown in Figure 5.9 and are referenced to a calculated magnetic shielding value of a free Xe atom.

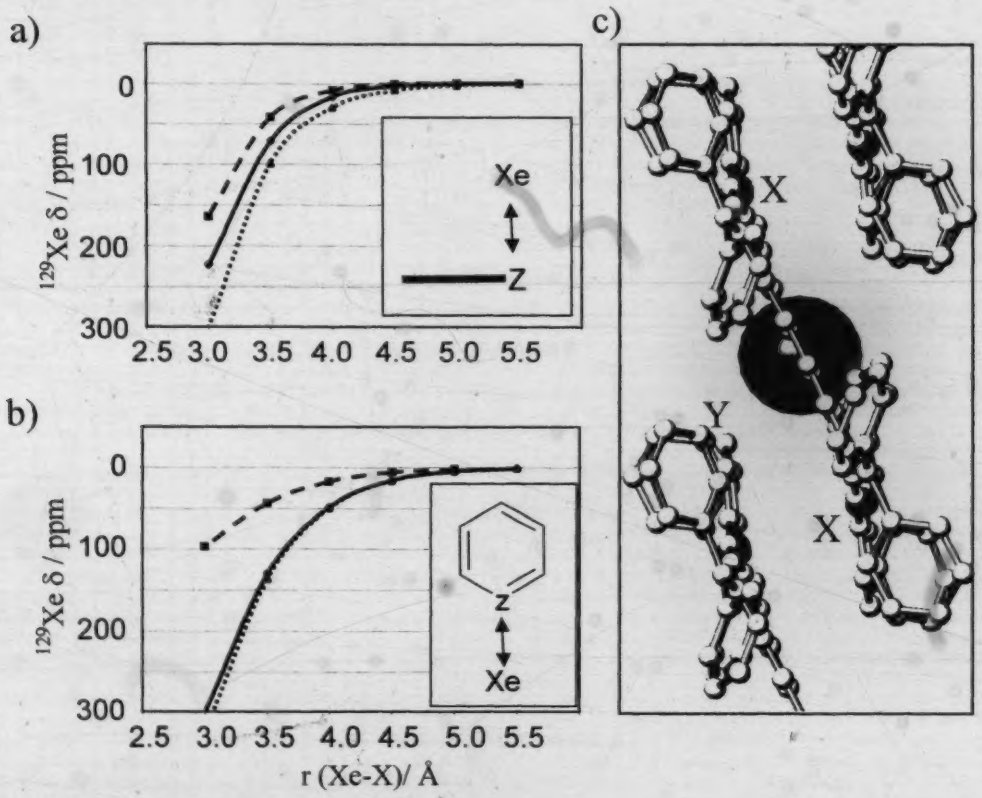

Figure 5.9: Plots of the isotropic Xe chemical shift as a function of distance from the nitrogen (dashed) and C4 of pyridine (solid) and a carbon of benzene (dotted), Z. a) Xe approaching Z perpendicular to the molecular plane. b) Xe approaching Z along the C_2 symmetry axis of the six member rings. Chemical shift values are referenced to the calculated shielding of an isolated Xe atom. c) A view of **1** along the crystallographic *c*-axis (same as Figure 1b) identifying the central Xe atom, Site **B**, in relation to positions X and Y on the structure.

It is immediately apparent from the calculations that the Xe - CH interactions result in a greater Xe chemical shift than do the Xe - nitrogen interaction as a function of distance for both approach orientations. Given the assumptions made above about the structure of the frameworks these results suggest that the change in the chemical shifts of the peaks resulting from Xe in Site **B** can be attributed to the changing functionality of

the macrocycle backbones. Based on the position of the Xe in the centre of the solvent cavity, Site **B**, it can be seen from Figure 5.9c that there are four close contact atoms that are different between compounds **1-3**. Two of the atoms are on the inside position of the macrocycle which surrounds the Xe, Figure 5.1 and Figure 5.9c, position X, and are between 4.2 to 5.0 Å from the central Xe position. The other two atoms are on the outside position of the two neighboring macrocycles, Figure 5.1 and Figure 5.9c, position Y, and are between 3.4 to 3.9 Å from the central Xe position. Compound **2**, contains CH groups at both positions X and Y which causes the greater ^{129}Xe chemical shift, 141 ppm at 160 K. Compound **1** has a nitrogen at position X, which will decrease the chemical shift of the Xe and could be responsible for the smaller shift value, 138 ppm. Finally, **3** has a CH at position X and a nitrogen at position Y. Given the fact that position Y atoms are closer to the Xe than position X atoms, changing Y from CH to nitrogen will cause a greater shielding of the ^{129}Xe nucleus than changing the X atoms will, thus the lowest observed shift value, 136 ppm, for **3** can be rationalized. The changes in the Xe dynamics, as expressed by the different temperature behaviours of the peaks in the spectra of the three compounds may also be explained by the changes in the macrocycle functionality described. However, a complete understanding of the effect these changes would have on the Xe interaction potential is not feasible at this time.

5.5 Conclusions

The application of continuous flow hyperpolarized ^{129}Xe NMR spectroscopy to investigate porous organic materials can provide a wealth of information that would not be obtainable otherwise. We have shown that all three of the macrocyclic materials studied here are porous to Xe gas and that the pores are microporous in size. The results from the VT ^{129}Xe NMR experiments for **1** correlate well with solid-state structural features that were determined crystallographically and suggest that the solid-state packing and pores of the three materials are similar. In the case of **1**, it appears that the crystal structure with guest solvent molecules included in the pores provides a reasonable model of the framework structure after guest removal. Two different porous sites have been identified: tightly bound end sites that typically give rise to broad ^{129}Xe peaks between 160 and 200 ppm, and channel sites which are responsible for sharper ^{129}Xe NMR peaks

in the range of 100 to 140 ppm. 2-D EXSY ^{129}Xe NMR results for **3** and molecular dynamics studies for Xe in **1,** in combination with the VT spectra, suggest a model for Xe adsorption. At high temperatures, Xe gas exchanges rapidly from the gas phase through the channels, and into the end sites. As the temperature is lowered, Xe becomes trapped in the ends of the solvent cavity and freshly polarized Xe atoms are forced to occupy the channel sites. Magnetic shielding calculations have provided insight into the possible reason for the differences in the Xe chemical shifts in the three compounds based on the presence and position of nitrogen atoms in the macrocycles.

---

[1] Stepanow, S.; Lingenfelder, M.; Dmitriev, A.; Spillmann, H.; Delvigne, E.; Lin, N.; Deng, X. B.; Cai, C. Z.; Barth J. V.; Kern, K. *Nature Mater.* **2004**, *3*, 229-233.

[2] Davis, M. E. in *Sci. Tech. Catal. 1998*, **1999**, *121*, 23-32.

[3] Bong, D. T.; Clark, T. D.; Granja J. R.; Ghadiri, M. R.; *Angew. Chem. Int. Ed.* **2001**, *40*, 988-1011.

[4] Davis, M. E. *Nature* **2002**, *417*, 813-821.

[5] Stein, A. *Adv. Mater.* **2003**, *15*, 763-775.

[6] Höger, S. *J. Polym. Sci. Part A: Polym. Chem.* **1999**, *37*, 2685-2698.

[7] Eddaoudi, M.; Li H.; Yaghi, O. M. *J. Am. Chem. Soc.* **2000**, *122*, 1391-1397.

[8] Rosi, N. L.; Eckert, J.; Eddaoudi, M.; Vodak, D. T.; Kim, J.; O'Keeffe M.; Yaghi, O. M. *Science* **2003**, *300*, 1127-1129.

[9] Férey, G.; Mellot-Draznieks, C.; Serre C.; Millange, F. *Acc. Chem. Res.* **2005**, *38*, 217-225.

[10] Kitagawa S.; Uemura, K. *Chem. Soc. Rev.* **2005**, *34*, 109-119.

[11] Malek, N.; Maris, T.; Simard M.; Wuest, J. D. *J. Am. Chem. Soc.* **2005**, *127*, 5910-5916.

[12] Campbell, K.; McDonald R.; Tykwinski, R. R. *J. Org. Chem.* **2002**, *67*, 1133-1140.

[13] Campbell, K.; McDonald, R.; Ferguson, M. J.; Tykwinski, R. R. *Organometallics* **2003**, *22*, 1353-1355.

[14] Campbell, K.; McDonald, R.; Ferguson, M. J.; Tykwinski, R. R. *J. Organomet. Chem.* **2003**, *683*, 379-387.

[15] Campbell, K.; Tiemstra, N. M.; Prepas-Strobeck, N. S.; McDonald, R.; Ferguson, M. J.; Tykwinski, R. R. *Synlett.* **2004**, 182-186.

[16] Jeener, J.; Meier, B. H.; Bachmann P.; Ernst, R. R. *J. Chem. Phys.* **1979**, *71*, 4546-4553.

[17] Dubes, A.; Moudrakovski, I. L.; Shahgaldian, P.; Coleman, A. W.; Ratcliffe C. I.; Ripmeester, J. A. *J. Am. Chem. Soc.* **2004**, *126*, 6236-6237.

[18] Stengle, T. R.; Reo N. V.; Williamson, K. L. *J. Phys. Chem.* **1981**, *85*, 3772-3775.

[19] Syamala, M. S.; Cross R. J.; Saunders, M. J. *J. Am. Chem. Soc.* **2002**, *124*, 6216-6219.

[20] Jameson, C. J.; Jameson, A. K. Gerald R. E.; Lim, H.-M. *J. Phys. Chem. B* **1997**, *101*, 8418-8437.

[21] Ripmeester J. A.; Ratliffe, C. I. *Anal. Chim. Acta* **1993**, *283*, 1103-1112.

[22] Moudrakovski, I. L.; Nossov, A.; Lang, S.; Breeze, S. R.; Ratcliffe, C. I.; Simard, B.; Santyr G.; Ripmeester, J. A. *Chem. Mater.* **2000**, *12*, 1181-1183.

[23] Goodson, B. M. *J. Magn. Reson.* **2002**, *155*, 157-216.

[24] Ripmeester, J. A. *J. Am. Chem. Soc.* **1982**, *104*, 289-290.

[25] Jameson C. J.; de Dios, A. C. *J. Chem. Phys.* **2002**, *116*, 3805-3821.

[26] Moudrakovski, I. L.; Ratcliffe, C. I.; Ripmeester, J. A. *J. Am. Chem. Soc.* **1998**, *120*, 3123-3132.

[27] Jameson, C. J.; Jameson, A. K.; de Dios, A. C.; Gerald, R. E.; Lim H.-M.; Kostikin, P. in *ACS Symposium Series 732: Modeling NMR Chemical Shifts*, Facelli, J.C.; de Dios, A.C, Eds; American Chemical Society: Washington, 1999,; 259-276.

[28] HyperChem (TM) Professional 6.0, Hypercube, Inc.: 1115 NW 4th Street, Gainesville, Florida 32601, USA, 1996.

[29] Lee, F.; Gabe, E.; Tse J. S.; Ripmeester, J. A. *J. Am. Chem. Soc.* **1988**, *110*, 6014-6019.

Chapter 6: ^{129}Xe NMR spectroscopy of potentially porous metal-organic macrocycles

6.1 Introduction

The ability to prove that organic macrocycles are porous to Xe gas using hyperpolarized ^{129}Xe NMR spectroscopy suggests that the technique is generally applicable to other potentially porous macrocyclic complexes. Many well ordered crystalline frameworks possess channels that allow gas atoms to enter the void spaces within the crystal lattice. In some cases the existence of channels is not obvious from single crystal X-ray analysis but the solid can still adsorb gas molecules. This is the case for calixarenes, Figure 6.1, and other similarly shaped molecules which can adsorb guest molecules such as toluene or nitrobenzene as well as larger organic molecules such as tetradecane.[1,2,3,4]

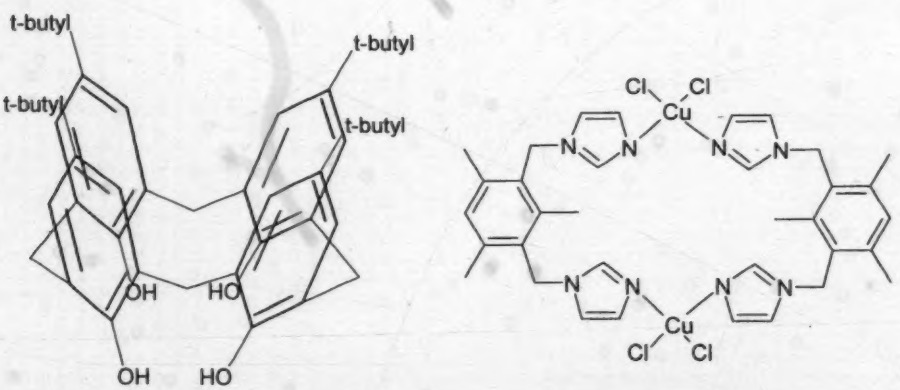

Figure 6.1: Left, the molecular structure diagrams of t-butyl calixarene. Right, the metal-organic macrocycle investigated in Ref 5 which shows the ability to adsorb molecules even though there are no clear channels in the structure determined by single-crystal X-ray diffraction.

Recently, similar behavior has been observed for a cyclic metal-organic molecule, see Figure 6.1, that forms stacks in the solid state.[5] The single crystal X-ray diffraction studies revealed that there were solvent cavities in the solid, similar to those observed for the organic macrocycles discussed in Chapter 5, but with much narrower openings between cages; the free diameter of the openings after solvent-guest removal is

approximately 0.9 Å. Despite the lack of clear channels between the solvent cavities, the solvent molecules can escape from the structure, even at room temperature and ambient pressure. In addition to solvent-guest removal, small molecular gases were taken up by the material. This presents a fascinating example of a material that does not appear to have "accessible" porosity based on the structure determined by single crystal X-ray diffraction, but in fact displays interesting adsorption properties, including gas selectivity.[5]

While this study is interesting, it raises a troubling question, how does one define porosity and what methods can be used to characterize the porous nature of solid frameworks? A related question is: does the "static" structure derived from diffraction studies serve as a reliable model for predicting porosity? The most general answer to the question of porosity is that a material is porous when it can adsorb guest molecules into void spaces within the solid in a reversible manner. While gas adsorption isotherms are useful for characterizing the macroscopic adsorption properties, details about the adsorption process, different adsorption sites, and host-guest interactions cannot be easily obtained from such experiments. On the other hand, ^{129}Xe NMR studies of Xe adsorbed in such materials would provide definitive proof of porosity as well as microscopic information about the pore space and gas adsorption.

We examined five different metal-organic macrocycle compounds, Figure 6.2, and investigated their porosity using HP ^{129}Xe NMR spectroscopy. Unlike the organic macrocycles discussed in Chapter 5, the packing of the metal-organic macrocycles results in void spaces with a greater variation in pore geometry and pore wall functionality. In addition to the phenyl groups on the macrocycle rings, all the metal-organic macrocycles contain bulky triphenyl- or triethylphosphine groups which increase the complexity of the crystal packing. This makes determining regions for Xe adsorption more difficult because free space exists throughout the lattice much of which is large enough for Xe to reside in. Defining the geometry, connectivity, and exact size of the pores nearly impossible based on the structure obtained from single-crystal X-ray diffraction. The solvent cavities usually provide the largest voids in the solid and are positioned between stacks of macrocycles, unlike the organic macrocycles where they were positioned through the center of each macrocyclic core. The increased molecular complexity also

provides more ways in which the solid structure can flex or shift in order to accommodate guest species. This has the advantage of allowing guests to enter the framework even when no channels can be identified, but also decreases the ability to predict adsorption regions based on the solvated structure determined by single-crystal X-ray diffraction.

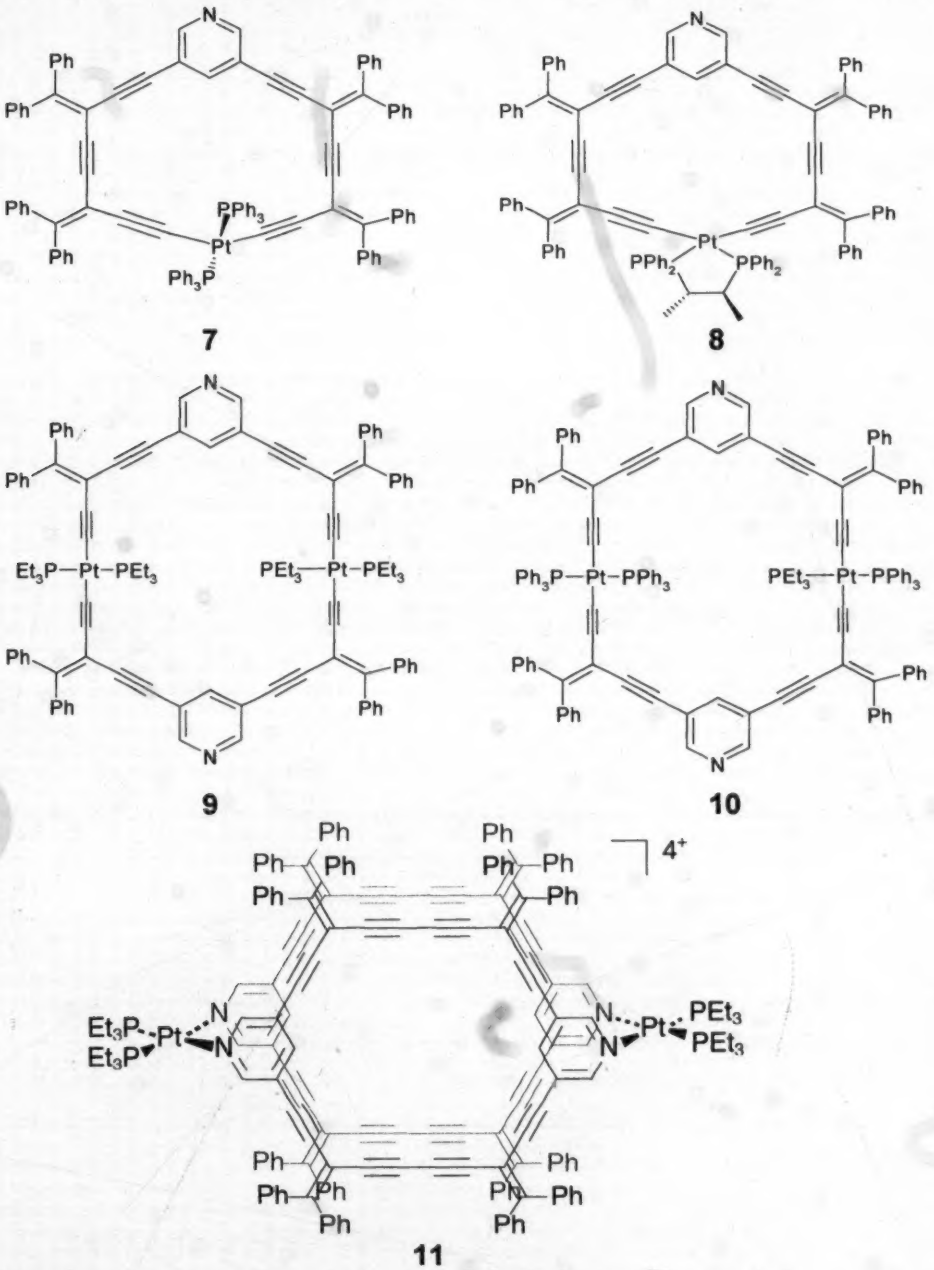

Figure 6.2: The structure of the metal-organic macrocycles studied.

HP ^{129}Xe NMR is an ideal technique to determine whether these materials are porous, to provide information about the pore sizes, adsorption dynamics, and adsorption energies, all on sample quantities less than 100 mg. Some of this work has been reproduced in part with permission from *Org. Lett.* **2005**, 7, 3397-3400, copyright 2005 American Chemical Society; only the research performed by the candidate is discussed here unless otherwise stated.

6.2 Sample preparation

All samples in Figure 6.2 were synthesized by Dr. Katie Campbell. An example of the synthetic process is shown in Figure 6.3.[6] The oligomer **6**, see Chapter 5, is reacted with diphenylalkylidene–substituted triflate to form **12**. The resulting hexayne, **12**, was then desilylated and reacted with stoichiometric amounts of *trans*-$PtCl_2(PPh_3)_2$ to close the macrocycle ring, Figure 6.3.[7] Similar synthetic procedures were used to obtain the other macrocycles.

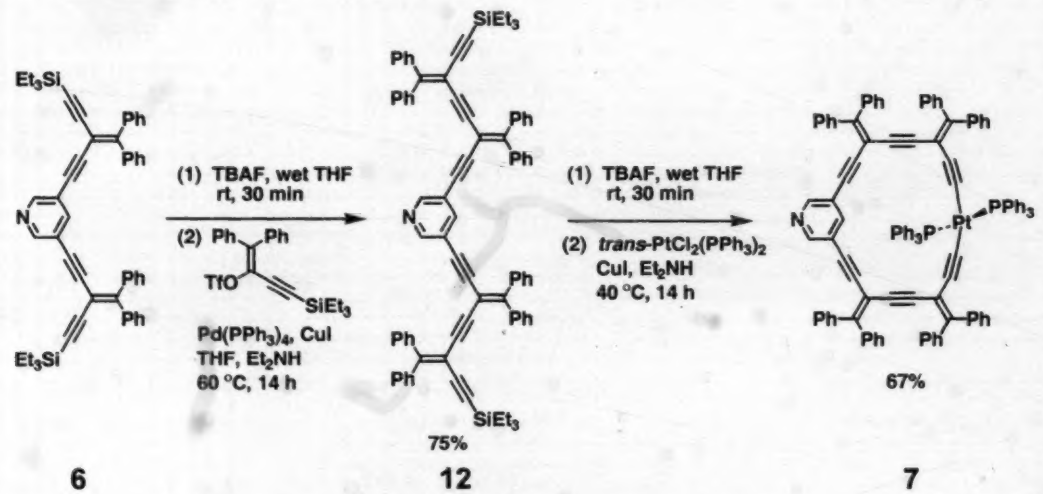

Figure 6.3: Scheme of the synthesis of **7**

Single crystals of macrocycle **7** were obtained from CH_2Cl_2/acetone at 4 °C. The macrocycle backbone is nearly planar and the PPh_3 groups are orientated perpendicular to the plane of the macrocycle ring; the coordination geometry about the Pt is square planar.[7]

Crystals of macrocycle **8** were obtained from boiling 1,2-dichloroethane. The macrocycles have a bend in the backbone at the Pt end of the macrocycle which places the C≡ C-Pt-C≡ C segment nearly perpendicular to the rest of the macrocycle plane. The Pt is in a square planar environment with the P atoms of the ligand *cis* to one another.[8]

Single crystals of macrocycles **9** and **10** were obtained by slow evaporation of a CH_2Cl_2/acetone and a CH_2Cl_2/1,2-dichloroethane/acetone solution at 4 °C, respectively. Both macrocycles were nearly planar in the solid state. The Pt centers are in a square planar environment with the PEt_3 and PPh_3 groups oriented at an angle of 50° to 60° and 33° to 36° from the macrocycle plane for **9** and **10**, respectively.

Macrocycle complex **11** was crystallized from CH_2Cl_2/1,2-dichloroethane at room temperature. The two macrocycles are each bent at the pyridine ends of the macrocycle and the N atoms are coordinated to the Pt atoms of the $Pt(PEt_3)_2^{2+}$ linker groups, See Figure 6.2. The +4 charge on the molecule is balance by triflate counter ions.[9]

Further information about the preparation and characterization of the macrocycles can be found in Dr. Campbell's Ph.D. Thesis.[10]

Removal of the solvent molecules from solid samples occurred when nitrogen gas or the N_2/He/Xe gas mixture flowed through the sample holder. This was verified using solution-state ^{1}H NMR. For samples **7** to **10** approximately 50 to 100 mg of sample were used available for ^{129}Xe NMR experiments. For sample **11** approximately 15 mg was available.

6.3 ^{129}Xe NMR spectroscopy

6.3.1 Mono-platinate macrocycle 7

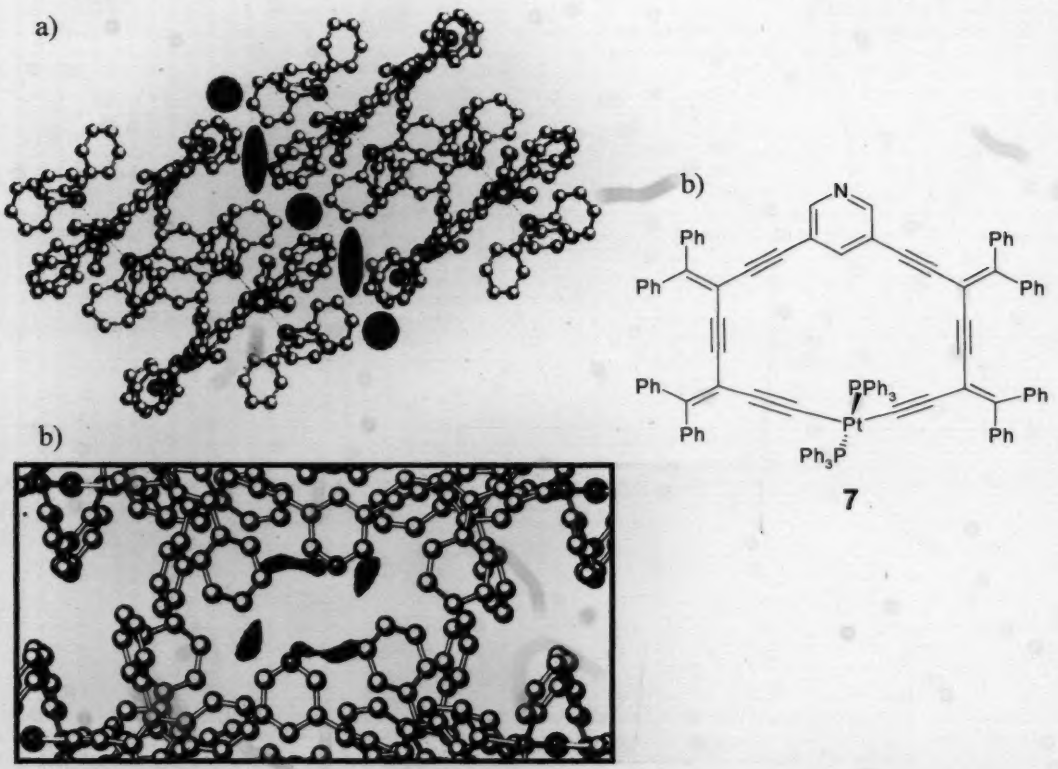

Figure 6.4: (a) Crystal packing diagram of **7** as determined by single-crystal X-ray diffraction, viewed down the *c*–axis; N atoms are pink, Pt atoms are blue and P atoms are turquoise. Co–crystallized solvent is not illustrated and H atoms have been omitted for clarity. Light blue ellipses indicate the acetone cavities and the circles indicate the CH_2Cl_2 cavities. (b) The molecular structure diagram of **7**. (c) The structure of the "channel" viewed down the *c*–axis with contours showing the expected distribution of Xe within the pore structure, as predicted by molecular dynamics simulations. The rounder contours correspond to the acetone solvent sites while the elongated contours correspond to the CH_2Cl_2 sites.

The single crystal X-ray diffraction structure of macrocycle **7** has four types of co-crystallized solvent molecules included in the structure, two acetone molecules, and two CH_2Cl_2 molecules (the two CH_2Cl_2 sites each have a 50% occupancy).[7] The macrocycles stack in columns and the solvent molecules occupy space between the stacks of macrocycles, Figure 6.4a. The triphenylphosphine groups which are coordinated to

the platinum atoms block access to the center of the macrocycles, making it unlikely that Xe atoms can pass through the center of the macrocycles.

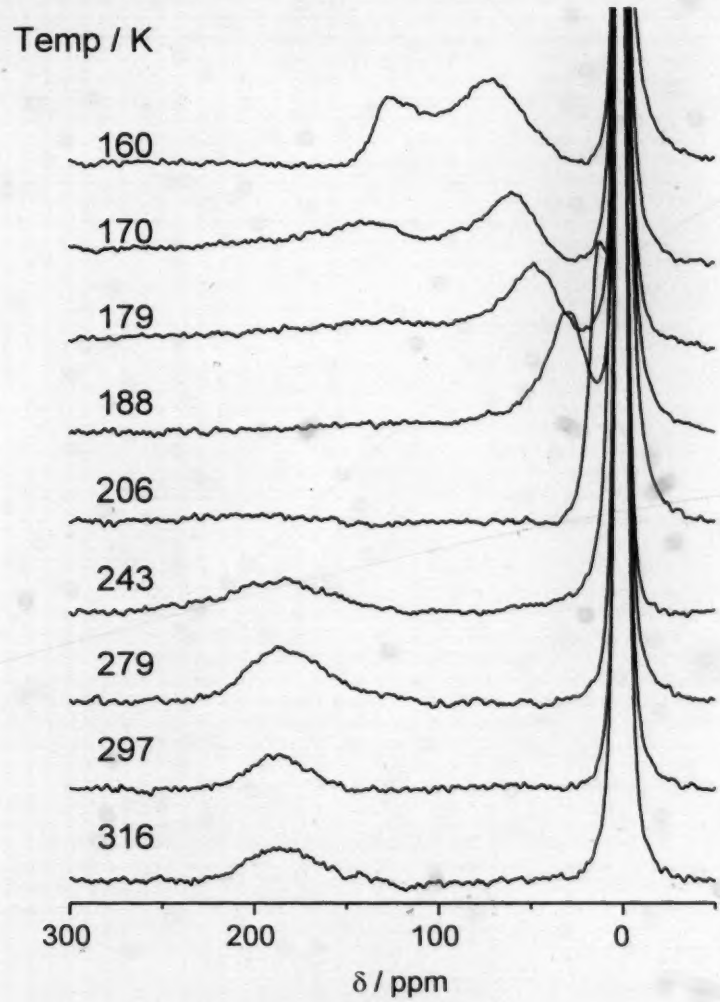

Figure 6.5: VT ^{129}Xe NMR spectra of HP ^{129}Xe in solid **7**. Each spectrum is the sum of 320 scans acquired with a 1.0 s pulse delay.

The ^{129}Xe NMR spectra of HP ^{129}Xe in compound **7** acquired at multiple sample temperatures are presented in Figure 6.5. The intensity of the spectra is low in part because of the small amount of sample used, ~50 mg, but also because the sample absorbs much less Xe than the organic macrocycles discussed in Chapter 5. The spectra show two temperature regimes where Xe adsorption occurs. At temperatures above 224

K a broad peak is observed at $\delta \approx 185$ ppm. Below 188 K other peaks are observed with lower chemical shift values.

The ^{129}Xe NMR peaks observed above 224 K have a similar chemical shift to those observed previously for Xe residing at the ends of the solvent cavities in the organic macrocycles. The shift is also similar to that of Xe in solution or dissolved in polymers and suggests that the Xe is in an environment that is not much larger than the Xe van der Waals diameter, 4.4 Å. [11,12,13,14] The breadth of the peak suggests that different Xe atoms are sampling slightly different environments. The solvent cavities that would be formed by the removal of the acetone and CH_2Cl_2 molecules in the structure would be significantly larger than 4.4 Å and are unlikely to result in such a large chemical shift value. Therefore, either the structure of the solvent cavities has collapsed, or Xe is occupying other free space within the structure, not related to the solvent cavities.

Many of the phenyl groups on the macrocycle are not near the solvent cavities but are near smaller voids which could provide regions for Xe adsorption. For example, the space formed by the two triphenylphosphine groups and the two closest phenyl groups on the edges of the macrocycle creates a void region that has a van der Waals void space of ~ 4.5 × 4.5 × 3.5 Å. This space could accommodate Xe with only small structural changes in the orientation of the phenyl groups and would provide an environment similar to that at the ends of the solvent cavities of the organic macrocycles described in Chapter 5. Other void spaces formed by phenyl groups could also be formed between the macrocycle molecules, leading to a variety of similar microporous sites all surrounded by phenyl groups. The structure of these sites is expected to be somewhat flexible, i.e. small rotations in the phenyl groups are possible, and therefore the Xe adsorption giving rise to the NMR peak at 185 ppm can best be described as a polymer-like-adsorption, see Section 2.3.2. This would also explain how Xe can access these regions in the absence of discreet channels.

When the temperature is lowered from 316 K, the chemical shift remains constant and the signal intensity increases until it reaches a maximum at approximately 279 K. At temperatures less than ~ 261 K, the intensity of the peak decreases until at ~ 206 K the peak disappears. This temperature is much higher than when Xe becomes trapped in the

ends of the solvent cavities in the organic macrocycles. This, combined with the lack of change in the chemical shift, suggests that instead of Xe becoming trapped in a condensation-like mechanism, the Xe is being excluded from accessing these tight spaces by a decrease in the flexibility of the framework. This could result in the adsorption sites becoming too small for the Xe or the passages by which the Xe gains access to the sites becoming no longer flexible enough for Xe to pass through.

When the temperature is decreased below 224 K, a new peak appears at $\delta \approx 13$ ppm. The chemical shift of this peak increases as the temperature is lowered. At 179 K another peak appears near $\delta \approx 130$ ppm. At 160 K two distinct peaks are observed near 125 and 70 ppm. The progression of the chemical shift of these peaks as a function of temperature suggests that Xe in the gas phase begins to sample adsorption sites at 206 K and becomes increasingly more confined to these sites as the temperature is lowered. The chemical shifts indicate that these low temperature adsorption sites are much larger than the microporous sites associated with the phenyl groups.

This behavior would arise from Xe sampling relatively large cavities within the solid or from Xe adsorbing on the surface of the crystals. In order to determine which adsorption is responsible for the peaks, a fresh sample of macrocycle **7** was prepared and the sample temperature was lowered to 160 K before and gas flow was introduced to the sample holder. This "froze" the acetone and CH_2Cl_2 molecules in the structure eliminating the possibility that Xe could adsorb into the solvent cavities. When the HP ^{129}Xe gas flow was turned on and the NMR spectrum was acquired there was no evidence from the NMR of ^{129}Xe gas adsorption, i.e., only the ^{129}Xe in the free gas was observed. The sample was then heated, the solvent molecules removed by the gas flow passing over the sample, and the spectrum at 160 K was rerecorded, reproducing the spectrum shown in Figure 6.5. This confirms that the peaks observed at low temperature in Figure 6.5 are from Xe atoms occupying the space created when the acetone and CH_2Cl_2 guest molecules are removed from the structure.

Based on the size of the two solvent cavities, we tentatively have assigned the peak at $\delta \approx 125$ ppm to Xe in the CH_2Cl_2 cavities and the peak at $\delta \approx 70$ ppm to Xe in the acetone cavities. MD simulations of Xe in these two sites revealed that there is a sufficient space for Xe to adsorb and sample a distribution of positions within each

cavity, Figure 6.4c (see Chapter 3 for simulation details). The two CH_2Cl_2 sites in the unit cell are close to each other and Xe may be able to move between the two cavities; the same is true for the two acetone sites, Figure 6.4c. The different cavities are close to each other in the crystal structure and it could be that the cavities form a pseudo-channel by which the Xe can gain access to the solid structure, thereby accessing the highly confined regions that give rise to the ^{129}Xe NMR peak near 185 ppm. Due to the low signal-to-noise, 2-D EXSY experiments were not feasible.

6.3.2 Chiral mono-platinate macrocycle ***8***

In the solid state, macrocycle **8** has a bend in the macrocycle ring which results in a more open framework than many of the other macrocycles studied here; each ring within a stack of macrocycles is separated by ~10.2 Å, Figure 6.6a. Solid macrocycle **8** has co-crystallized 1,2-dichloroethane and water molecules in the structure. The water molecules occupy positions in the center of the macrocycles while the 1,2-dichloroethane molecules occupy space between the stacks of **8,** Figure 6.6c.

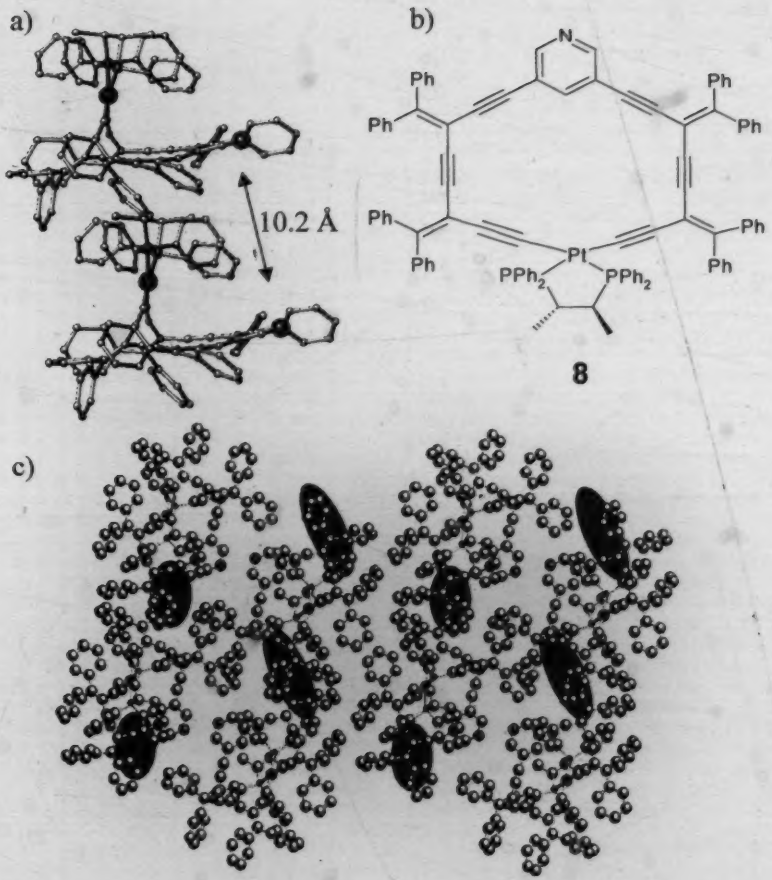

Figure 6.6: (a) The structure of **8** in the solid state as determined by single-crystal X-ray diffraction showing how the bend in the macrocycle backbone results in an open framework structure; N atoms are pink, Pt atoms are blue and P atoms are turquoise. Co–crystallized solvent is not illustrated and H have been omitted for clarity. (b) The molecular structure diagram of **8**. (c) Crystal packing diagram of **8**, viewed down the *a*–axis. Blue ellipses indicate the two types of large void spaces; the larger ellipses correspond to the position of the 1,2-dichloroethane molecules.

The ^{129}Xe NMR spectra obtained of HP ^{129}Xe gas in macrocycle **8** as a function of sample temperature are shown in Figure 6.7. The spectra were acquired using approximately 20 mg of sample and accumulating 320 scans. Immediately it is clear that much more Xe gas is adsorbed by this material than by macrocycle **7**. The spectra show ^{129}Xe NMR signals that can be divided into two different temperature regimes, at

temperatures above 188 K a broad peak is observed near 190 ppm and at temperatures below 224 K a sharper peak is observed with a chemical shift that changes from $\delta \approx 108$ to $\delta \approx 140$ ppm.

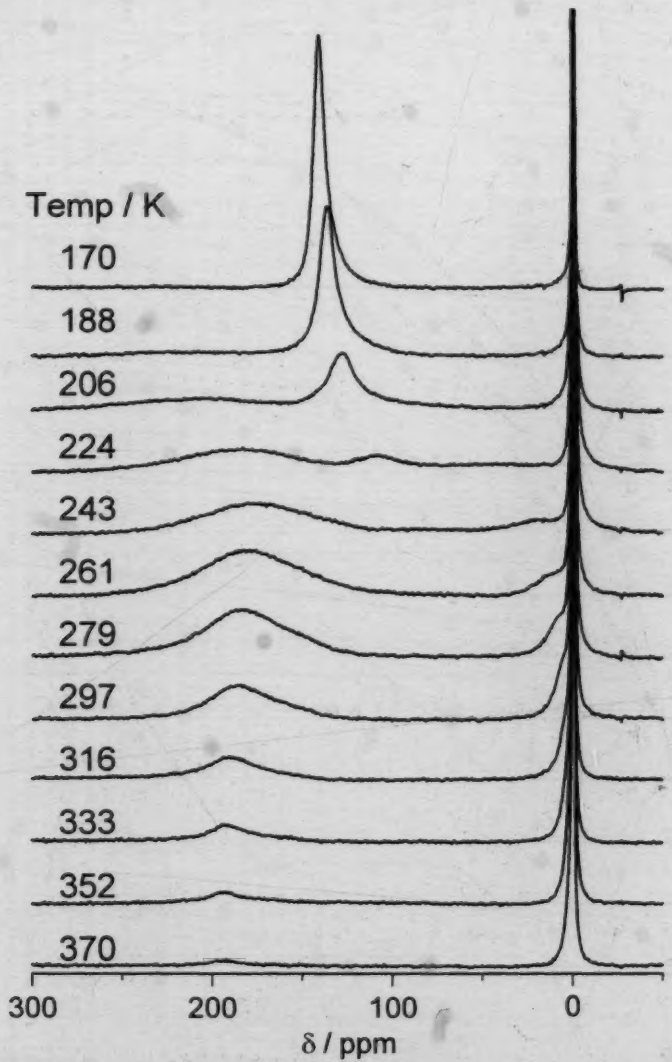

Figure 6.7: VT ^{129}Xe NMR spectra of HP Xe in solid **8**. Each spectrum is the sum of 320 scans acquired with a 1.0 s pulse delay.

These spectra are very similar to those recorded for Xe in the porous organic macrocycles discussed in Chapter 5. This is remarkable since the structure of the two samples is completely different and suggests that the void space in **8** is composed of both highly confined domains and more open cavities. The signal observed near 190 ppm

increases in intensity as the temperature is lowered to 279 K and then begins to decrease in intensity. The breadth and chemical shift increase slightly as the temperature is lowered suggesting that the drop in signal intensity may be caused by a condensation mechanism similar to that observed for the organic macrocycles, i.e., all the sites become filled with Xe atoms and the rate at which the Xe can be replenished with new HP ^{129}Xe gas is slow.

Compound **8** has the most open framework of the monocyclic platinocycles investigated. Much of the free space can be associated with small pockets in the structure near phenyl groups, similar to those discussed for **7**. The open structure of **8** would make more of these sites accessible to Xe atoms, leading to the increased signal intensity observed in the ^{129}Xe NMR spectra.

An analysis of the void space in the crystal packing diagram when the co-crystallized solvent molecules are removed reveals that there are two large cavities between three adjacent stacks of molecules. One of these sites is beside the Pt end of the macrocycle and is where the 1,2-dichloroethane solvent molecules reside before they are removed by the gas flow; the larger ellipses in Figure 6.6c. The other large void is on the pyridine side of the macrocycle stacks and does not contain solvent molecules. Both the cavities have similar van der Waals dimensions, approximately 6 × 5 × 4 Å. These cavities are most likely responsible for the ^{129}Xe NMR signal observed at 140 ppm in the spectrum acquired at 170 K. Since only one, narrow peak is observed in the ^{129}Xe NMR spectra, Xe must be rapidly exchanging between the two different cavities. This rapid exchange is possible because of the open framework structure of **8**. Above 224 K there is a shoulder on the peak from Xe in the gas phase. This is likely from Xe atoms that exchange rapidly between the gas and larger void spaces.

The ability of macrocycle **8** to adsorb more Xe and the rapid exchange of the Xe between the larger cavities compared to that observed for macrocycle **7** has important implications for designing porous materials based on metal-organic macrocycles. By using molecules that can expand the framework, separating the macrocycles in the stacks, an increase in the adsorption ability and the rate of exchange of small gases within the sample can be achieved.

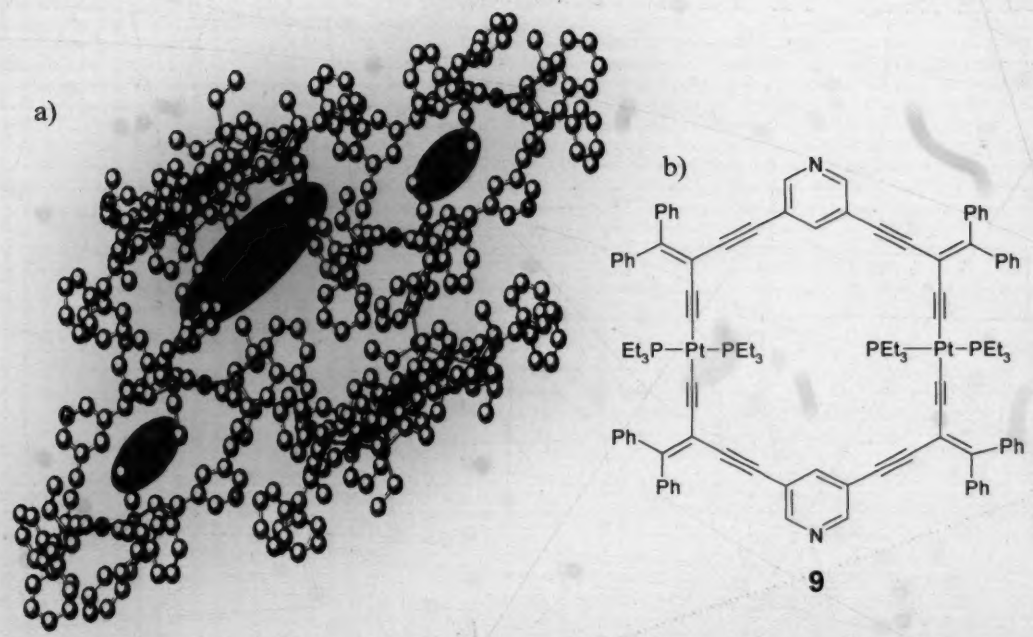

Figure 6.8: (a) Crystal packing diagram of **9** as determined by single-crystal X-ray diffraction, viewed down the *b*–axis; N atoms are pink, Pt atoms are blue and P atoms are turquoise. Co–crystallized solvent is not illustrated and H atoms have been omitted for clarity. Blue ellipses indicate the solvent channels and red circles indicate the possible pocket sites in the center of the large macrocycles that are surrounded by ethyl groups. (b) The molecular structure diagram of **9**.

*6.3.3 Di-platinate macrocycle **9***

Compound **9** has solvent channels that form along the crystallographic *b*-axis between the stacks of macrocycles. The channels are formed by the inclusion of CH_2Cl_2 molecules and have cross-section dimensions of approximately 7 × 5 Å, Figure 6.8. Figure 6.9 shows the ^{129}Xe NMR spectra of HP ^{129}Xe in macrocycle **9** at different sample temperatures (approximately 50 mg of sample was used). In contrast to the other macrocycles studied, the ^{129}Xe NMR spectrum of Xe in compound **9** at 333 K contains an intense peak at 166 ppm. This peak is narrower than the peaks observed above room temperature in the other macrocycle compounds. The intensity of this peak decreases as the temperature is lowered and completely disappears at 188 K.

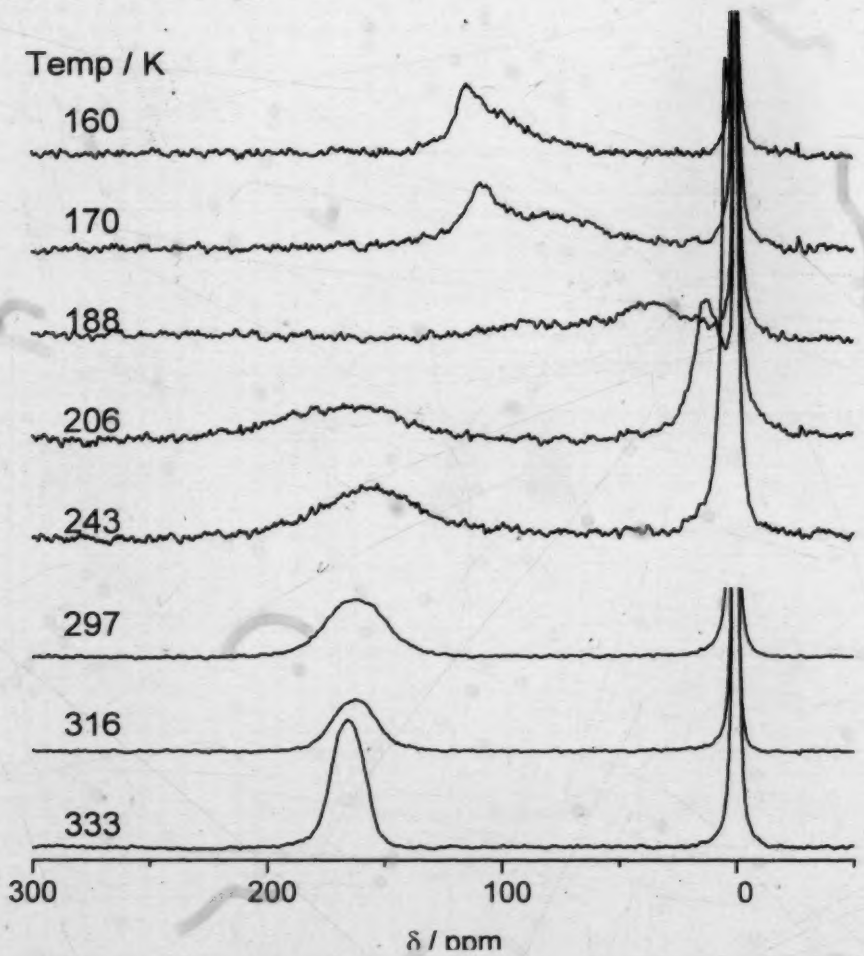

Figure 6.9: ^{129}Xe NMR spectra of HP Xe in solid **9**. The bottom three spectra are scaled by 20 %. Each spectrum is the sum of 320 scans acquired with a 1.0 s pulse delay.

Examining the structure of compound **9** reveals that the planar macrocycles lie nearly parallel to the channel axis. The macrocycles themselves are large enough to accommodate Xe atoms in the center of the macrocycles, in principle offering highly confined side cavities that the Xe atoms can adsorb to, red ellipses in Figure 6.8. These side "pockets" are surrounded by the ethyl groups of the triethylphosphines, which are tilted into the center of the macrocycle. This changes the chemical environment in the pockets from an aromatic environment, as has been postulated for the high temperature sites of the other macrocycles, to an alkyl environment. The chemical shift of Xe dissolved in ethanol, is 161.1 ppm,[15] Xe in diethyl ether is 159.0 ppm, [16] and Xe in n-

pentane is 154.1 ppm at room temperature[16] compared to 193 ppm for Xe in benzene;[16] therefore, Xe in a confined alkyl environment may be expected to have a lower chemical shift than Xe in a confined aromatic environment. The narrower line width indicates that the environment of Xe adsorbed in the pocket sites is much more uniform than for Xe in the tight adsorption sites in other macrocycles. Since there is no increase in the chemical shift at temperatures above 243 K, which would be characteristic of a condensation mechanism, the loss of signal intensity is probably due to a decrease in framework flexibility and subsequent exclusion of Xe from the "pocket" sites. The broadening of the peak may be due to a similar phenomenon to that observed in polymers where, because of the decreased chain mobility, the ^{129}Xe NMR peaks broaden due to the existence of multiple environments.

At temperatures below 243 K another peak appears in the ^{129}Xe NMR spectra. It separates from the gas peak and the chemical shift steadily increases as the temperature is lowered. This behavior is characteristic of Xe undergoing fast exchange with the gas phase, sampling the void space in the solid for longer times as the temperature is lowered. This behavior is similar to that observed for the low temperature peaks of compound **7** and, combined with the low chemical shift values, suggests that the Xe is sampling void spaces significantly larger than the Xe diameter; the solvent channels provide such an environment. There appears to be a distribution of Xe environments within the channels resulting in a broad ^{129}Xe NMR signal at 170 K with a shape that suggests different adsorption regions with different Xe populations; this is not surprising given the disordered nature of the channel walls. At temperatures greater than 188 K this distribution is averaged by fast exchange between the different environments and the gas phase (variations in exchange rate caused by different crystallite sizes could also play a role in the breadth, see Section 3.2.3). The channels adsorb significantly less Xe than the pockets sites as is evidenced by the much lower signal intensity in the ^{129}Xe NMR spectra.

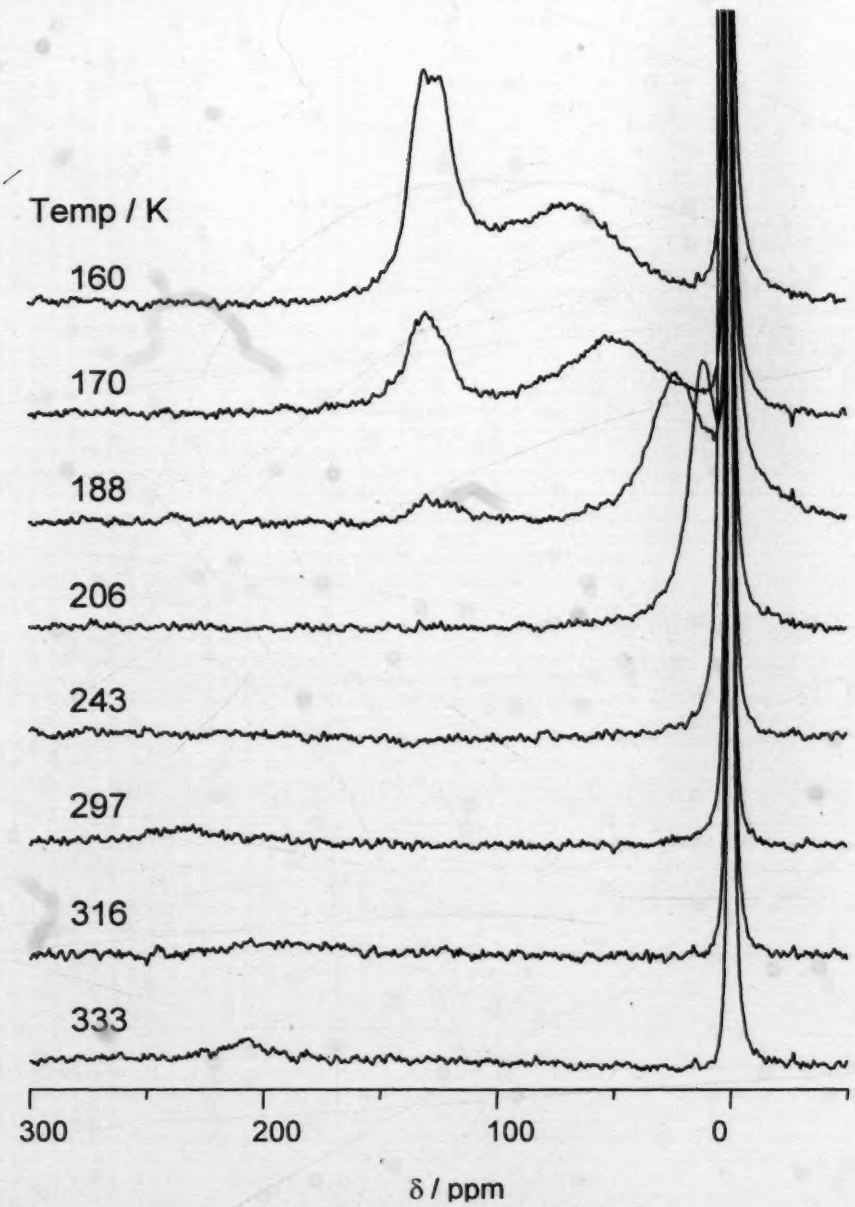

Figure 6.10: VT ^{129}Xe NMR spectra of HP Xe in solid **10**. Each spectrum is the sum of 640 scans acquired with a 1.0 s pulse delay.

*6.3.4 Di-platinate macrocycle **10***

The triphenylphosphine analogue of compound **9** shows different Xe adsorption, as reflected in the ^{129}Xe NMR spectra of Xe in compound **10**, Figure 6.10. Macrocycle

10 shows almost no Xe adsorption at temperatures above 243 K. This suggests that Xe cannot access any binding sites associated with the phenyl rings and that, due to the larger size of the phenyls groups compared to the ethyl groups of **9**, the center of the macrocycles are largely inaccessible to Xe.

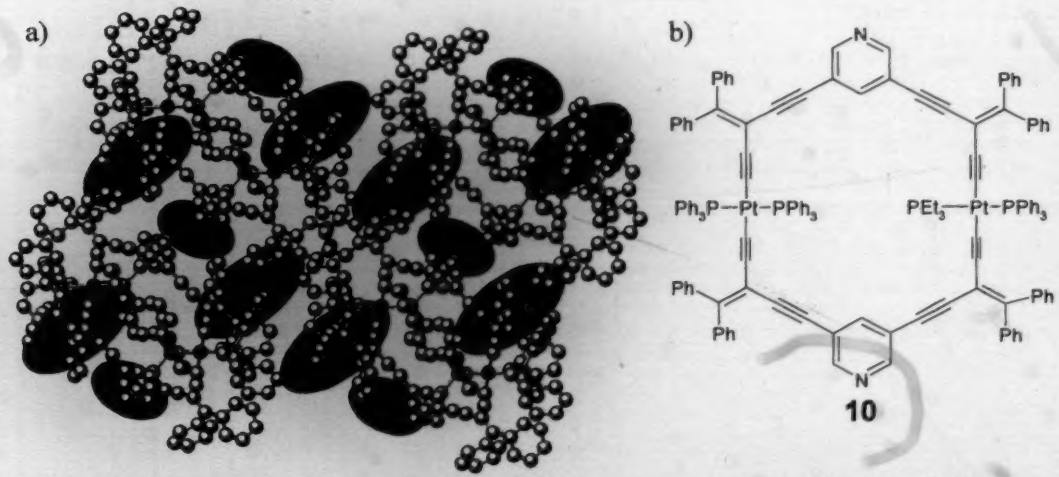

Figure 6.11: Crystal packing diagram of **10** as determined by single-crystal X-ray diffraction, viewed down the *a*–axis; N atoms are pink, Pt atoms are blue and P atoms are turquoise. Co –crystallized solvent is not illustrated and H atoms have been omitted for clarity. Blue ellipses indicate the two types of solvent cavities. (b) The molecular structure diagram of **10**.

X-ray crystallography indicates that macrocycle **10** contains no obvious channel system. The co-crystallized 1,2-dichloroethane molecules are positioned between the stacks of macrocycles but no large openings connect the cavities, Figure 6.11. Each cavity is formed around two 1,2-dichloroethane molecules leading to two types of large cavities, Figure 6.11. At the lowest temperature for which ^{129}Xe NMR spectra were recorded, two peaks are observed arising from Xe occupying two different cavities with large free space volumes. The chemical shifts are similar to those observed for the other macrocycles where Xe is postulated to occupy large cavities created by the removal of solvent molecules. Since the cavities are unconnected, it is unclear why the ^{129}Xe NMR spectra show a trend that would be characteristic of Xe in fast exchange with the free gas at 243 K, with the Xe sampling the cavities for longer times as the temperature is lowered.

One possible explanation for this apparent fast exchange at 243 K may be that Xe atoms adsorb into cavities that are close to the crystal surface and then rapidly exchange back into the free gas, resulting in short residence times in the near-surface cavities. When the temperature is lowered, the Xe residence times increase leading to an increase in the chemical shift and an increased probability that the Xe will penetrate deeper into the structure. Once past the first few layers of the crystal, Xe exchanges between the different cavities at a rate slow enough for different NMR signals from Xe in the two types of cavities to be resolved.

6.3.5 Super-molecular structure ***11***

The final macrocycle studied was a super-molecular assembly created by grafting two organic macrocycles together using two $[Pt(PEt_3)_2]^{2+}$ linker groups. The resulting structure has large, oval shaped channels along the crystallographic c-axis, parallel to the plane of the macrocycles, which have a minimum van der Waals free space cross-section of approximately 12.8 × 4.1 Å, Figure 6.12a. These large channels are connected by windows that pass through the center of the macrocycles and have cross-section dimensions of 4.6 × 6.3 Å. There are six 1,2-dichloroethane molecules in each of the main channels.

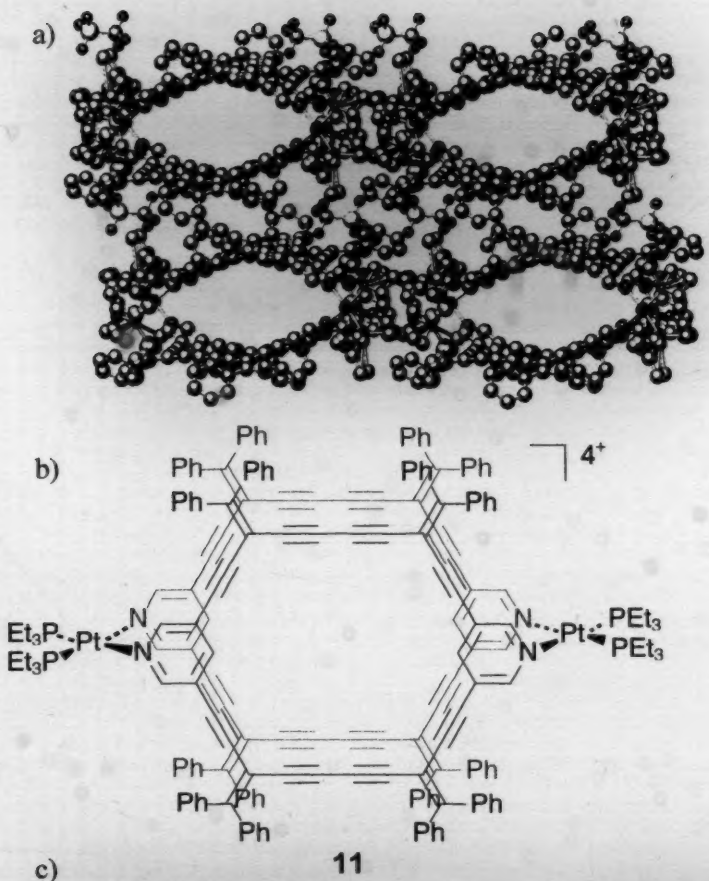

Figure 6.12: (a) Crystal packing diagram of **11** as determined by single-crystal X-ray diffraction, viewed down the *c*–axis; N = pink, Pt = blue, P = turquoise, F = green, S = yellow and O = red. Co–crystallized solvent in the channel is not illustrated and H atoms have been omitted for clarity. (b) The molecular structure diagram of **10**. (c) Contour map showing the expected distribution of Xe within the pore structure, as predicted by molecular dynamics simulations.

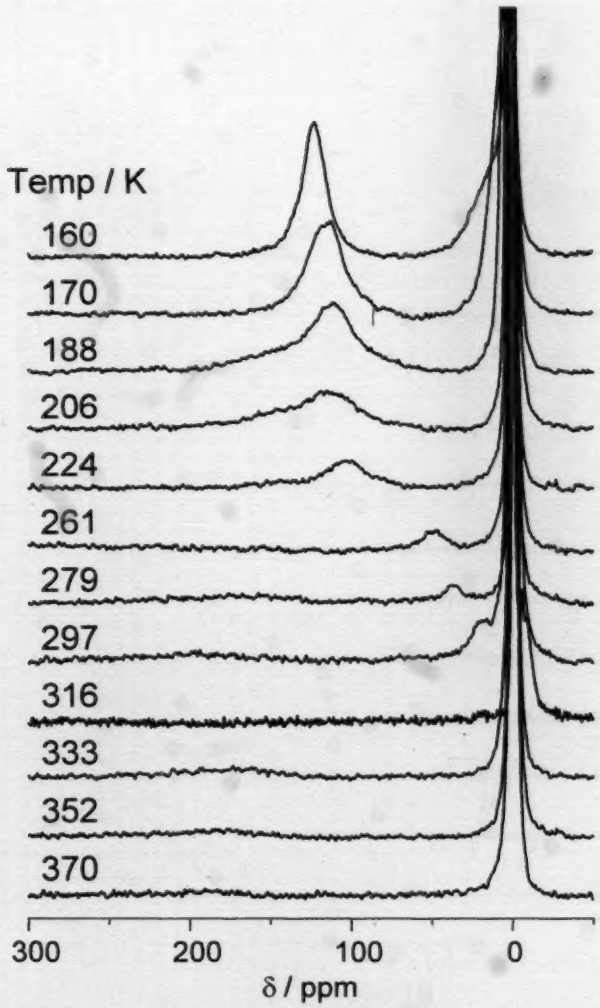

Figure 6.13: ^{129}Xe NMR spectra of HP Xe in solid **11**. Each spectrum is the sum of 1280 scans acquired with a 1.0 s pulse delay.

The ^{129}Xe NMR spectra of HP ^{129}Xe in **11** acquired at multiple temperatures are shown in Figure 6.13. The spectra are different than those observed for any of the previous materials in that there is only one peak observed in addition to the gas peak at 0 ppm. The peak appears at 297 K as a shoulder on the gas peak and, as the sample temperature is lowered, the intensity and chemical shift of the peak increase. The chemical shift, $\delta \approx 112$ ppm, is independent of temperature between 170 and 206 K, and then at 160 K the peak shifts to $\delta \approx 123$ ppm. The presence of ^{129}Xe NMR peaks from

Xe in large pores is clear evidence that despite the removal of the co-crystallized solvent guests, the structure of compound **11** does not collapse and remains porous.

Molecular dynamics simulation of Xe in **11** indicate that while the Xe can move freely throughout the channel system, it spends a majority of its time in the narrows section of the channels, between the individual macrocycle units that form the channel; Figure 6.12b shows the position. The two regions depicted by the contour plots coincide with the position of two of the six 1,2-dichloroethane molecules that occupy the channels before removal of the co-crystallized solvent molecules. Although the contours look different in Figure 6.12b this is a result of the angle at which they are oriented inside the channel; the contour on the left is viewed approximately side-on while the contour on the right is viewed end-on.

The behavior of the ^{129}Xe NMR signal above 206 K for **11** is characteristic of Xe in fast exchange between the adsorption regions and the free gas. Since the channel dimensions are large the changes in chemical shift can be analyzed assuming the fast-exchange low-loading regime, see Section 2.6.2. Because there is no clear indication that Xe-Xe interactions are causing increased shifts as a result of the decrease in temperature, we can assume that there is only a small amount of Xe adsorbing in **11**. It is assumed that when the chemical shift remains constant over a significant temperature range, the Xe can be considered adsorbed and the fast exchange with the free gas is minimal; therefore, δ_s is taken to be 112 ppm. Equations 2.28 to 2.30 can be rewritten as a linear equation

$$\ln\left[\left(\frac{\delta_s}{\delta}-1\right)T^{1/2}\right]=\ln\left(\frac{D}{RK_0\eta}\right)-\frac{\Delta H_{ads}}{RT} \qquad 6.1$$

By plotting $\ln\left[\left(\frac{\delta_s}{\delta}-1\right)T^{1/2}\right]$ vs. 1/T the effective heat of adsorption, ΔH_{ads}, can be obtained from the slope.[17] Using equation 6.1 to analyze the ^{129}Xe NMR spectra of **11**, one obtains an effective heat of adsorption of approximately 28 kJ mol^{-1}. The same analysis could in theory be used for the other samples for which fast exchange is evident between Xe in the solvent cavities and free Xe gas, except that an estimate for δ_s is

problematic since there is no region where the chemical shift does not change over a significant temperature range.

6.4 Conclusions

Xe-129 NMR spectroscopy has been used to prove that five different solid metal-organic macrocycles are porous to Xe gas. This is true even when no clear channels can be identified in the structure determined by single-crystal X-ray diffraction. Experiments were performed on ≤ 100 mg sample quantities which make other techniques used to characterize porosity extremely difficult if not impossible to use. Three of the solids show Xe adsorption in highly confined "pocket" sites at the higher sample temperatures and Xe adsorption into larger cavities at lower sample temperatures; the large cavities are likely formed when the co-crystallized solvent molecules are removed from the solid. For macrocycle **10** and the super-molecular macrocycle **11** there is no sign of "pocket" sites while adsorption into the solvent cavities is observed for both. For compounds **7**, **9** and **10** the number of solvent cavities observed in the structure determined from the single-crystal X-ray diffraction is the same as the number of ^{129}Xe NMR peaks observed at lower temperature. For samples **8** and **11**, fast exchange between sites, a result of the more open framework structures, leads to a single observed ^{129}Xe NMR signal at the low temperatures. The ^{129}Xe NMR spectra of Xe in **11** display a temperature dependence that can be analyzed using the fast-exchange two-site model as applied to the low loading regime. From this analysis an estimate of the effective adsorption energy was obtained, 28 kJ mol^{-1}.

---

[1] Brouwer, E. B.; Enright, G. D.; Udachin, K. A.; Lang, S.; Ooms, K. J.; Halchuk, P. A.; Ripmeester, J. A. *Chem. Commun.* **2003**, 1416-1417.

[2] Brouwer, E. B.; Udachin, K. A.; Enright, G. D.; Ripmeester, J. A.; Ooms, K. J.; Halchuk, P. A. *Chem. Commun.* **2001**, 565-566.

[3] Atwood, J. L.; Barbour, L. J.; Jerga, A. *Angew. Chem. Int. Ed.* **2004**, *43*, 2948-2950.

[4] Riddle, J. A.; Bollenger, J. C.; Lee, D. *Angew. Chem. Int. Ed.* **2005**, *44*, 6689-6693.

[5] Dobrzańska, L.; Lloyd, G. O.; Raubenheimer, H. G.; Barbour, L. J. *J. Am. Chem. Soc.* **2006**, *128*, 698-699.

[6] Campbell, K.; Johnson, C.A. II; McDonald, R.; Ferguson, M. J.; Haley, M. M.; Tykwinski, R. R. *Angew. Chem. Int. Ed.* **2004**, *43*, 5967–5971.

[7] Campbell, K.; McDonald, R.; Ferguson, M. J.; Tykwinski, R. R. *Organometallics* **2003**, *22*, 1353-1355.

[8] Campbell, K.; McDonald, R.; Ferguson, M. J.; Tykwinski, R. R. *J. Organomet. Chem.* **2003**, *683*, 379-387.

[9] Campbell, K.; Tiemstra, N. M.; Prepas-Strobeck, N. S.; McDonald, R.; Ferguson, M. J.; Tykwinski, R. R. *Synlett* **2004**, 182-186.

[10] Campbell, K. *Ph.D. Thesis*, University of Alberta, **2004**.

[11] Stengle, T. R.; Williamson, K. L. *Macromolecules* **1987**, *20*, 1430-1431.

[12] Kentgens, A. P. M.; van Boxtel, H. A.; Verweel, R.-J.; Veeman, W. S. *Macromolecules* **1991**, *24*, 3712-3714.

[13] Urban, C.; McCord, E. F.; Webster, O. W.; Abrams, L. *Chem. Mater.* **1995**, *7*, 1325-1332.

[14] Morgan, D. R.; Stejskal, E. O.; Andrady, A. L.; *Macromolecules* **1999**, *32*, 1897-1903.

[15] Lim, Y.H.; Nugara, N.; King A. D. Jr. *Appl. Magn. Reson.* **1995**, *8*, 521-534.

[16] Stengle, T. R.; Reo, N. V.; Williamson, K. L. *J. Phys. Chem.* **1981**, *85*, 3772-3775.

[17] Terskikh, V. V.; Moudrakovski, I. L.; Mastikhin, V. M. *J. Chem. Soc. Faraday Trans.* **1993**, *89*, 4239-4243.

Chapter 7: ^{129}Xe NMR spectroscopy of IRMOFs

7.1 Introduction

In the past five years Yaghi and coworkers have described a series of metal-organic frameworks, MOFs, which have recently gained attention because of their reported high stability and gas adsorption properties which make them potential gas separation and storage materials.[1,2,3,4,5] The most thoroughly investigated metal-organic framework, MOF-5 (also known as IRMOF-1), forms when 1,4-benzenedicarboxylic acid, BDC, and zinc nitrate react in diethylformamide, DEF.[6] The cubic framework of MOF-5 consists of Zn_4O subunits which are linked in octahedral arrays of BDC groups to form a porous material with a cavity diameter of approximately 15 Å, as depicted in Figure 7.1a; the structure of the subunits is shown in Figure 7.2a.[7,8,9] A wide variety of guest molecules have been adsorbed in MOF-5 and have been studied by gas and liquid sorption techniques,[8,9] computational methods,[10,11,12,13] IR spectroscopy,[14] X-ray diffraction and neutron scattering.[4,5]

The structural simplicity of MOF-5 has led to the preparation of a series of MOFs based on aromatic dicarboxylic acids coordinated to Zn_4O subunits.[6,9] These complexes, referred to as iso-reticular metal-organic frameworks or IRMOFs, have demonstrated the control that can be achieved over pore size and functionality. Using different dicarboxylic acids, frameworks with pore diameters as large as 25 Å have been prepared.[6,9]

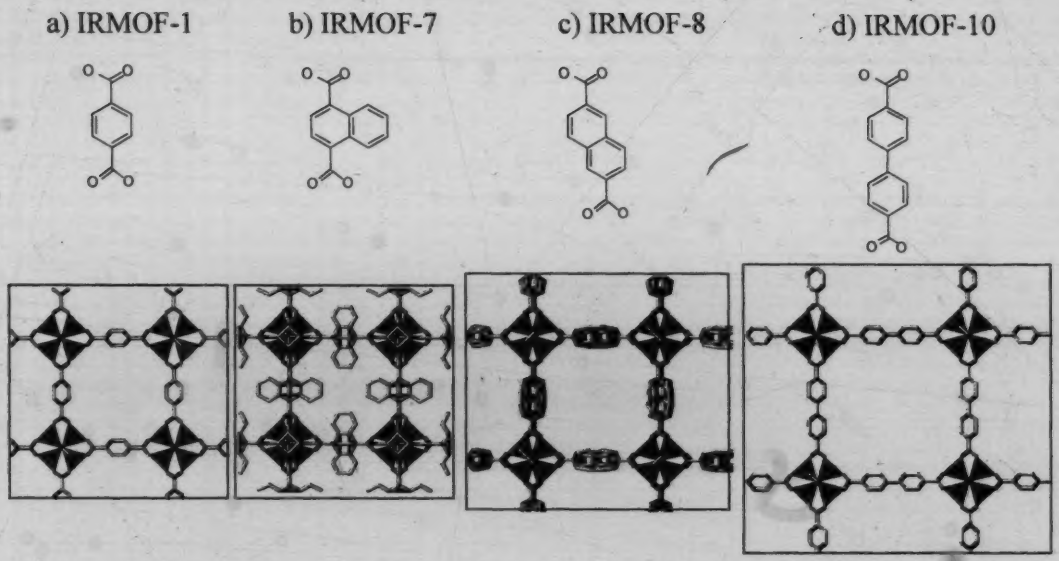

Figure 7.1: The structure of the four cubic frameworks formed when $Zn(NO_3)_2$ is reacted with different aromatic dicarboxylic acids as determined by X-ray crystallography; hydrogen atoms and guest molecules have been omitted for clarity and the four frameworks are depicted to scale. The length of the linker controls the dimensions of the cubic cages. The blue ZnO_4 tetrahedra are composed of three oxygen atoms from the dicarboxylate linkers and one oxygen which is coordinated to all four Zn atoms in each corner.

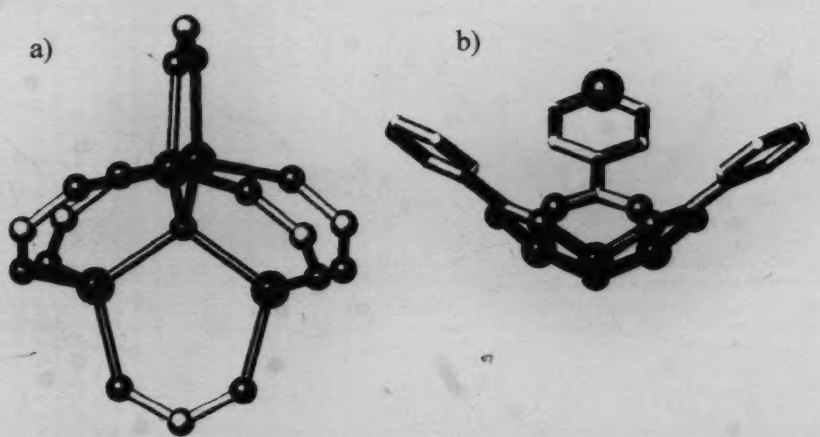

Figure 7.2. (a) The zinc subunit and (b) a corner of an α-cage of IRMOF-1 depicting the lowest energy position for Xe, purple, in the structure. Red spheres are oxygen, grey are carbon, and blue are Zn; hydrogen atoms have been removed for clarity. The blue tetrahedral in Figure 1 correspond to the Zn and four bonded oxygen atoms depicted in (a). The distance between the Xe position and the Zn atoms in (b) is approximately 4.9 Å.

One key to developing new porous materials for the storage of gases or as molecular sieves is to understand how different gas atoms and molecules interact with the framework. Determining the ease with which gases move through the framework and how long they reside within specific regions of the open structure are important. Some theoretical and experimental studies have attempted to answer some of these questions.[4,10,12,14,15,16,17] Perhaps the most insightful results thus far have been provided by computational models which have reproduced experimental gas adsorption isotherms. Based on these experimental adsorption results and computational studies, adsorption energies, details on adsorption sites, and some diffusion data have been obtained.[10,11,12,14,15,17]

Several research groups have demonstrated that ^{129}Xe NMR spectroscopy is an ideal method of characterizing porous materials,[18,19,20,21,22,23,24] largely because Xe chemical shifts are extremely sensitive to the time-averaged environment experienced by Xe atoms. For example, chemical shifts typically range from $\delta \approx 0$ ppm for Xe gas at low pressure to $\delta \approx 315$ ppm for solid Xe.[18] Xenon-129 NMR lineshapes are also dependent on the rate at which Xe exchanges between various adsorption sites. In some cases, ^{129}Xe NMR data can provide information about the mechanism of diffusion, e.g., single file diffusion, unidirectional diffusion, etc.[25,26,27,28,29] Xe has a van der Waals radius of 2.16 Å,[30] making it a reasonable model for small molecular gases such as CH_4. Since there are many physical phenomena that affect the ^{129}Xe chemical shift, interpretation of the NMR spectra can be difficult. The study of ^{129}Xe NMR spectra can however, provide the unique opportunity to gain atomic level information to correlate with theoretical models for gas adsorption.[25,31]

In the present study we have used ^{129}Xe NMR spectroscopy to characterize the adsorption of Xe in a series of IRMOFs. We have selected four frameworks where the linkers are composed of aromatic dicarboxylic acids of different size (aromatic = benzene, 1,4-naphthalene, 2,6-naphthalene, 4,4'-biphenyl). Table 7.1 contains information about the pore size for the four IRMOF samples. NMR spectra of continuous flow HP ^{129}Xe were recorded as a function of temperature in order to determine the effects that the different structures have on the ^{129}Xe NMR chemical shifts

and lineshapes. The research presented in this chapter is essentially a duplicate of a manuscript that will be submitted for publication shortly.

Table 7.1: Relevant structural data for materials studied

	Linker[1]	Space group[2]	Unit cell dimension / Å[2]	# of cage types	Cage free space diameter[3] / Å	Window free space diameter[3] / Å
IRMOF-1	BDC	Fm-3m	25.83	2	15.1	7.8
IRMOF-7	1,4-NDC	Pm-3m	12.91	1	10.2	2.1
IRMOF-8	2,6-NDC	Fm-3m	30.09	2	18.0	9.2
IRMOF-10	4,4'-BPDC	Fm-3m	34.28	2	21.1	12.0

1) BDC = 1,4-benzenedicarboxylate, NDC = naphthalenedicarboxylate, BPDC = biphenyldicarboxylate
2) Crystal structures obtained from Ref. 7 and 9.
3) Free space diameter refers to the diameter of the largest sphere that can fit in the cage or through the window when the van der Waals radii are assumed for all framework atoms.

7.2 Sample preparation and characterization

Samples were prepared based on previously published methods.[6] $Zn(NO_3)_2 \cdot 6$ H_2O and the appropriate dicarboxylic acid linker were dissolved in diethylformamide, DEF, (IRMOF-1: 0.256 g, 0.066 g, 10ml; IRMOF-7: 0.118 g, 0.030 g, 10 ml; IRMOF-8: 0.024 g, 0.122 g, 15ml; IRMOF-10: 0.072 g, 0.010 g, 25 ml). The samples were placed in sealed glass vials and heated at 90 to 95 °C for 48 hrs. Crystals of the IRMOFs formed on the walls of the vials and were filtered and washed with DEF. Co-crystallized DEF was removed from the samples by placing the crystals in CH_2Cl_2 to exchange the included DEF with CH_2Cl_2, and subsequently placed under vacuum at 120 °C to remove the CH_2Cl_2. The IRMOF-1 and IRMOF-7 crystals were crushed lightly for NMR analysis while the IRMOF-8 and IRMOF-10 crystallites did not require crushing.

The crystallinity and structure of the samples were confirmed by powder X-ray diffraction and their compositions determined by elemental analysis. The structure of IRMOF-1 was also confirmed by single-crystal X-ray diffraction. The removal of DEF

and CH_2Cl_2 from the framework was verified by elemental analysis and solid-state ^{13}C NMR spectroscopy. Powder X-ray diffraction was used to monitor the structure during removal of the guest species. Powder X-ray diffraction patterns were collected from the sample included with DEF, the sample with CH_2Cl_2, and the evacuated sample. Small changes in the X-ray diffraction powder pattern were observed after the removal of the DEF. Differences in the powder X-ray diffraction patterns have been previously noted for IRMOFs due to changes in preparation method but may also indicate changes in the structure due to guest removal.[6]

Several samples of each IRMOF were synthesised to ensure sample reproducibility. Some of the samples showed variations in the ^{129}Xe NMR spectra when the synthesis or guest removal conditions were changed slightly, e.g., IRMOF-1 samples that were prepared at higher temperatures yielded similar elemental analysis but different spectra, see Chapter 3 section 3.2.4. The general variation in the ^{129}Xe NMR spectra as a function of temperature shown in Figure 7.3 is representative of that observed for all samples but additional peaks were also observed, suggesting structural variations within the sample. Additional ^{129}Xe NMR peaks were observed for samples stored for several months; this was particularly true for the larger frameworks suggesting that the frameworks may degrade over time.[32,33] Since most of the "extra" ^{129}Xe NMR peaks had lower chemical shift values, it may be that carboxylate oxygen-Zn bonds break, possibly by hydrolysis, resulting in larger cages being formed in the crystal lattice. The spectra presented here are of samples prepared exactly as described, acquired between 2 and 30 days after synthesis and stored in small, sealed vials under air. Each set of spectra presented in this work was reproduced using a minimum of three different samples all prepared as described.

7.3 Structures of IRMOFs

The cubic structure of IRMOF-1 as determined by X-ray crystallography,[7] Figure 7.1a, is composed of two types of cages differentiated by the orientation of the benzene rings; one cage has the faces of the benzene rings facing the centre of the cubic cavity, α-cages, while the other cage has the edge of the benzene rings pointing towards the centre, β-cages. The windows between the cages of IRMOF-1 have a van der Waals space that

can accommodate a sphere with diameter of 7.8 Å (in the discussion that follows, this will be referred to as the "free space" diameter). Deuterium NMR investigation of the motion of the benzene rings in IRMOF-1 have revealed that at room temperature the benzene rings are stationary, while at temperatures significantly above room temperature the rings undergo 180° jumps about the dicarboxylate axis.[34]

Within each cage there is a distribution of adsorption potentials that depend on the nature of the gas entering the IRMOF-1 and the interaction of the gas with the different parts of the framework. X-ray diffraction studies and molecular dynamics simulations have identified a number of different sites that can be associated with the corners of the cubic cages, the linkers, and the windows.[4,11] All three of these general regions have different adsorption energies due to the varying number of possible close contacts that the adsorbing gas can make with the framework and the different atoms in the different regions. In general, the more close contacts that exist between the solid and the gas, the greater the adsorption potential. It is not surprising then that the lowest energy adsorption sites in the solid are in the corners of the cubic cages, Figure 7.2. In particular, the corners of the α-cage provide ideal sites for Xe adsorption, Figure 7.2b. Based on molecular mechanics geometry optimizations of the Xe within the cage the lowest energy position for Xe is only 4.9 Å from the three corner Zn atoms, see Figure 7.2b. The corners, therefore, provide a very different chemical environment than any of the cage space associated with the organic linkers. When interpreting the ^{129}Xe chemical shift, the relative population of Xe in the corners as opposed to the rest of the cage is important; the distribution of Xe will be determined by the relative adsorption energies in the different regions.

Results from a single crystal X-ray diffraction study have confirmed that both Ar and N_2 first adsorb in the corners of the α-cages.[4] The next most favourable adsorption site is in the corner of the β-cages, followed by the window sites that would allow Xe to exchange between two adjacent corners, and then adsorption regions around the linkers. Similar conclusions have been obtained from theoretical calculations.[17]

The structures of IRMOF-8 and IRMOF-10 obtained from X-ray diffraction studies, Figures 7.1c and 7.1d, are comparable to that of IRMOF-1.[9] Both frameworks have similar α- and β-cages that are formed when the aromatic linker is oriented with its

face or edges pointing towards the center of the cubic cage, respectively. IRMOF-8 has larger cage and window dimensions than IRMOF-1 whereas IRMOF-10 has the largest dimensions of the four frameworks studied here (Table 7.1). IRMOF-7 [9] has the same size cage as IRMOF-1 (Figure 7.1b) but the presence of the additional aromatic ring on the naphthalene reduces the free space in the cage and the window diameters. The X-ray diffraction structure of IRMOF-7 shows a four-site disorder in the orientation of the naphthalene, which makes it difficult to determine the dimensions of the window. The most favourable orientation of the naphthalene linkers is when two naphthalenes on opposite sides are directed into the window; this makes the largest free space diameter of the window 2.1 Å. A consequence of the orientation of the naphthalenes in IRMOF-7 is that there is only one type of cage in the crystal structure; this is reflected in the unit cell parameters (Table 1). For all the samples, the same basic adsorption regions exist with the different linker structures changing the adsorption energies of the regions.

7.4 ^{129}Xe NMR spectroscopy

7.4.1 IRMOF-1

The variable temperature ^{129}Xe NMR spectra of IRMOF-1 exposed to the HP ^{129}Xe are presented in Figure 7.3. At all the temperatures except 126 K two peaks are observed one very small peak from Xe in the free gas, 0 ppm, and one from Xe inside the framework. The ^{129}Xe NMR peak from the adsorbed Xe has a nearly constant chemical shift of 106 ppm at temperatures between 278 and 392 K. The width-at-half-height of the peak in this temperature range is approximately 220 Hz and the shape is Lorentzian suggesting that the Xe atoms responsible for this peak are rapidly exchanging between different adsorption sites within the structure. If the Xe atoms were trapped in specific sites a much broader Gaussian peak would be expected because a distribution of adsorption sites would influence the lineshape.[35] The ^{129}Xe NMR peak intensity increases as the temperature is lowered, consistent with the increased adsorption of Xe by the framework.

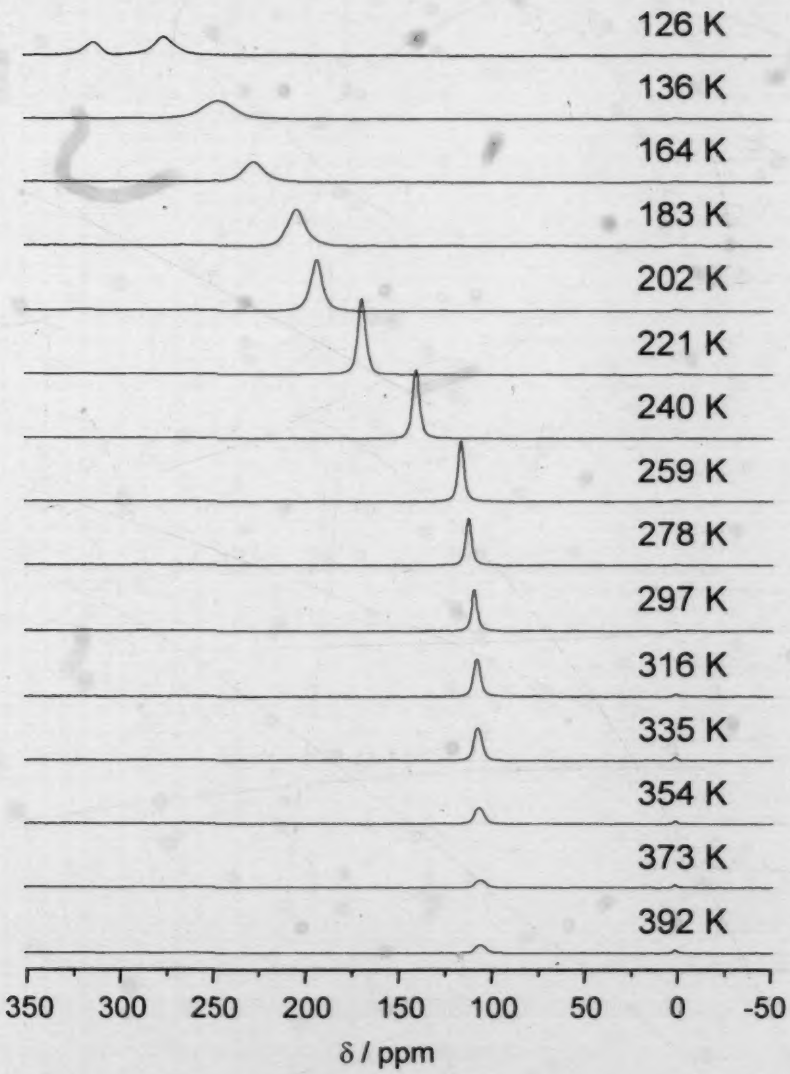

Figure 7.3: ^{129}Xe NMR spectra of HP Xe in IRMOF-1 as a function of sample temperature. Each spectrum is the result of 128 scans.

The chemical shift value of the adsorbed peaks is constant over a temperature range of 100°. This is surprising and indicates that even at 392 K the exchange rate between Xe in the framework and in the free gas is relatively slow. By simulating the ^{129}Xe NMR spectra using a two-site exchange model an upper limit for the exchange rate at 297 K is estimated to be 200 Hz, see Ref. 36 as well as Appendix B.[37,38] In many open framework materials the exchange between Xe adsorbed and in the free gas is relatively

fast, particularly at elevated temperatures.[39,40,41,42] Rapid Xe exchange averages the ^{129}Xe NMR chemical shift to a value between Xe in the free gas and the chemical shift characteristic of Xe interacting with the framework, δ_s. As the temperature is lowered the fraction of adsorbed Xe increases resulting in an increase in the ^{129}Xe chemical shift as the temperature is lowered, tending towards the value of δ_s.[39,40,41] In the case of IRMOF-1 the slow exchange process means that the chemical shift observed at 106 ppm can be interpreted as the shift characteristic of a lone Xe interacting with the walls of framework, δ_s. The isotropic lineshapes observed at all temperatures indicate that despite the slow exchange between Xe in the free gas and Xe adsorbed by IRMOF-1, the exchange between the different sites within the IRMOF-1 cages is rapid. If the exchange within the cage was slow, different peaks from the different adsorption sites would be expected and anisotropic powder linshapes would be observed for Xe atoms in anisotropic environment, i.e. anywhere except the center of the cages.

The observed value of the chemical shift depends on the proportion of time the Xe spends in the gas and adsorbed phases, or alternatively the fractional populations n_i of Xe in the different sites at any given temperature, Equation 7.1.

$$\delta_{obs}(T) = n_G(T)\delta_G + n_A(T)\delta_A + n_B(T)\delta_B + n_C(T)\delta_C \ldots \qquad 7.1$$

The subscript G denotes gas phase and A, B, C, …, denote different adsorption regions within the framework, i.e., corners, along the linkers, or in the windows as discussed above; δ_i is the chemical shift of Xe in the indicated site. Previous studies have shown that the entire internal void space accessible to Xe must be properly averaged, making the actual number of adsorbed terms very large.[26] However, as a starting point, we can limit Equation 7.1 to Xe sites with very different adsorption energies and chemical shifts.

Since the partial pressure of Xe in the gas mixture is small, at elevated temperatures the Xe loading is low even for strongly adsorbing materials. As the temperature is lowered, however, the number of Xe atoms adsorbed increases. By performing a calibration of the ^{129}Xe NMR signal intensity it was determined that near 259 K the Xe loading is approximately one Xe atom per α and β-cage; the effect of signal loss due to long Xe residence times was accounted for (see below). Since the average

loading is expected to increase as the temperature is lowered, Xe-Xe interactions will begin to play a role in determining the observed chemical shift.[43,44] It has been shown that the contribution to the Xe chemical shift from Xe-Xe interactions is substantial. The increasing ^{129}Xe chemical shift observed in Figure 7.3 below 259 K occurs largely because the average Xe loading is increasing above one Xe per cage. Additionally, the distribution of the Xe within the cages will be dominated more by the stronger adsorption sites as the temperature is lowered, leading to larger chemical shifts since typically strong adsorption sites give larger δ values. With the increase in ^{129}Xe chemical shift an increase in the breadth of the peak is also observed, particularly below 202 K. The increased breadth suggests that the peak may be a result of Xe in multiple chemical shift environments caused by small differences in the average loading of each cage; the peak also takes on a Gaussian lineshape at the lower temperatures consistent with a random distribution of nonequivalent sites.

At 136 K the chemical shift of Xe in the framework is 245 ppm, 139 ppm greater than the chemical shift of an isolated Xe within the framework. This suggests that there are several Xe atoms inside each cage, resulting in a large deshielding due to the increased number of Xe-Xe interactions. For comparison, zeolite NaA which has an α-cage with a diameter of approximately 11.4 Å,[45] shows a change in chemical shift from 74.8 to 272.3 ppm when the loading is increased from one to eight Xe atoms per cage.[46] The Xe loading of IRMOF-1 can not be estimated based on the ^{129}Xe NMR signal intensity in Figure 7.3 due to the time it takes to replace all the spin-depolarized Xe atoms with fresh HP ^{129}Xe and the effects of relaxation during this time. Previous studies using hyperpolarized ^{129}Xe have shown that high Xe loadings can be achieved even when very low Xe partial pressures are used in a continuous-flow system. For example, the study of silicalite revealed that at 140 K the one-dimensional channels were fully loaded and 16 Xe atoms per unit cell were adsorbed employing the same gas mixture used here.[47] Using hyperpolarized ^{129}Xe and a gas mixture with 2.5% Xe, Meersmann and coworkers showed that Xe-Xe contributions to the anisotropic ^{129}Xe NMR lineshape of Xe in TPP cause a 60 ppm increase in the perpendicular components of the chemical shift tensor in the 313 to 203 K temperature range.[29]

At 126 K a third peak at 312 ppm is observed from solid Xe. At the same temperature the peak from Xe adsorbed into the framework is at 275 ppm. This is close to the ^{129}Xe chemical shift observed for 8 Xe atoms in zeolite NaA and suggests that at this temperature Xe has fully condensed in the framework and has filled the available porous space.

7.4.2 IRMOF-7

Variable temperature ^{129}Xe NMR spectra of Xe adsorbed in IRMOF-7 are presented in Figure 7.4. The spectra show the same basic pattern observed for IRMOF-1. Between 259 and 297 K the ^{129}Xe NMR peak arising from Xe adsorbed in the framework remains at a relatively constant chemical shift of approximately 95 ppm. This chemical shift value is less than that observed for Xe in RMOF-1 over the same range of temperatures. This is initially surprising because in general, the chemical shift of ^{129}Xe in porous materials can be related to the volume of the pores; qualitatively, the larger the free space within the pore, the smaller the chemical shift. However, variation in this trend can be caused by Xe exchange, which can play an important role in determining the chemical shift when there are positions within the cavity that yield different ^{129}Xe chemical shifts. The chemical shift observed for IRMOF-7 could result from Xe sampling sites with smaller chemical shifts more frequently than is the case for IRMOF-1, for example sampling positions along the linkers more often. In terms of Equation 7.1 this would mean that sites with smaller δ values have larger n values in IRMOF-7 than in IRMOF-1.

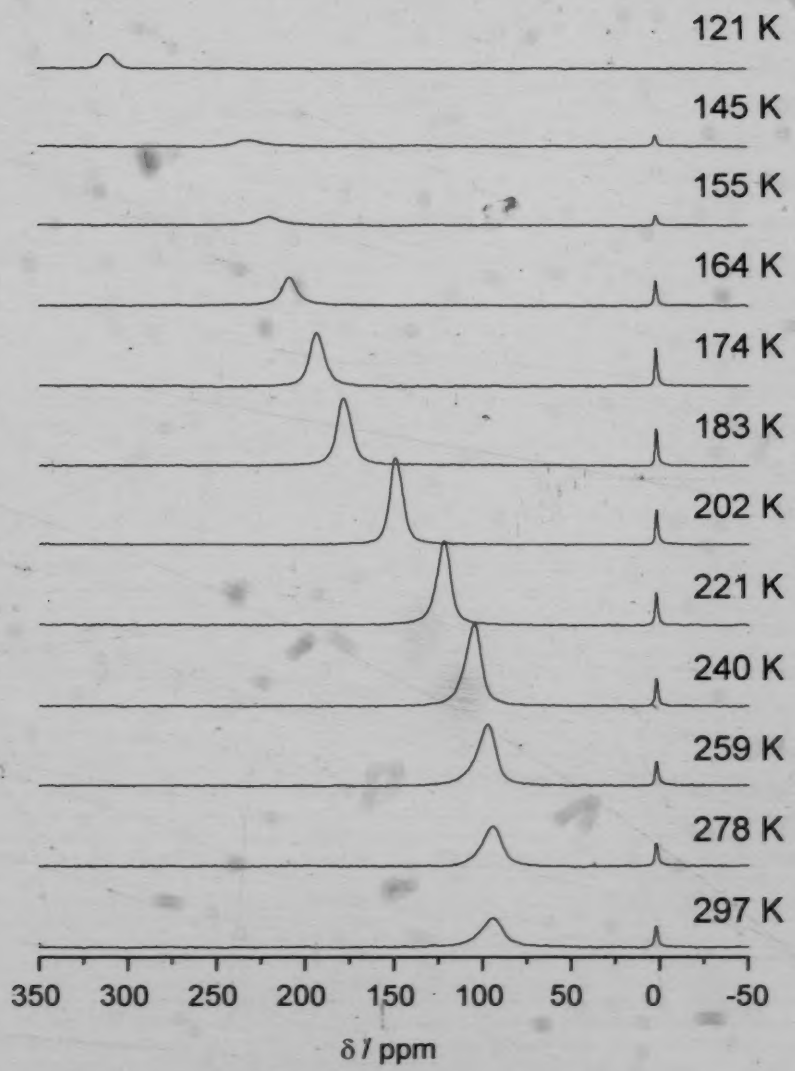

Figure 7.4: ^{129}Xe NMR spectra of HP Xe in IRMOF-7 as a function of sample temperature. Each spectrum is the result of 128 scans.

At temperatures less than 240 K the chemical shift of the peak from Xe adsorbed in IRMOF-7 increases. As with IRMOF-1, this is characteristic of the onset of Xe-Xe interactions as the Xe loading rises above one Xe per cage. For IRMOF-1, evidence of Xe-Xe interactions were first resolved at higher temperature than for IRMOF-7, suggesting that the average heat of adsorption for Xe in IRMOF-7 is lower than for IRMOF-1, i.e., Xe is more strongly adsorbed in IRMOF-1 than IRMOF-7. As mentioned

above, the corner sites will have the greatest adsorption potential; by changing the orientation of the linkers the binding potential of the corners will change in IRMOF-7 compared to IRMOF-1. Since it is expected that the corners will play a significant role in determining the average adsorption energy, the structural difference between the two IRMOFs likely makes the corners of IRMOF-7 weaker adsorption sites than the α-corners in IRMOF-1; this would also explain why the ^{129}Xe chemical shifts are smaller in IRMOF-7 than in IRMOF-1 since δ_{corner} is expected to be the largest chemical shift, any decrease in n_{corner} would result in a smaller value of δ_{obs}.

The chemical shift increases further as the temperature is lowered until 145 K when a chemical shift value of 232 ppm is reached. This value is again slightly smaller than that of IRMOF-1 at the same temperature. The striking feature about the spectra presented in Figure 7.4 is that the signal intensity of the peak from Xe in the framework decreases as the temperature is lowered and completely disappears below 145 K; using longer pulse delays did not increase the signal intensity significantly. Usually this loss of signal is associated with the rate of exchange between Xe in the pore and Xe in the gas being so slow that Xe in the pore cannot be replenished by fresh HP Xe, this phenomena is often referred to as Xe condensation because it is usually accompanied by large Xe loadings.[35,48] Increased ^{129}Xe NMR linewidths are usually observed when condensation occurs because the motional averaging of multiple magnetically nonequivalent sites is slowed or stopped. This explanation seems unlikely in the case of IRMOF-7 since the structure is similar to IRMOF-1 and there was no corresponding loss in signal intensity for IRMOF-1.

A more likely explanation is that the framework motion or flexibility mentioned above is sufficiently slow that HP ^{129}Xe is unable to access the pore space before relaxation results in a loss of nuclear spin-polarization. As discussed above the windows of IRMOF-7 are on average much smaller than for IRMOF-1. The most sterically favorable orientation of the naphthalenes pointing into the windows makes the largest opening in the windows ~ 2.1 Å, smaller than the van der Waals diameter of Xe (Figure 7.1). Based on the large ^{129}Xe NMR peak observed at $\delta \approx 95$ ppm, above 145 K, it is clear that Xe is able to access the cages. This suggests that either there are windows that adopt more sterically hindered orientations of the naphthalenes or that there is some

torsional motion of the naphthalene linkers. From the X-ray crystal structure it can be seen that there is four-fold disorder of the naphthalenes about the dicarboxylate axis. Four-fold hops of the naphthalene rings about the linker axis would allow for Xe atoms to pass through the windows. Even at temperatures where such motion becomes slow, Xe atoms could pass through the windows provided the framework exhibited some flexibility. This would be analogous to the way gases can diffuse into materials even though there are no clear channels, as was seen in Chapter 6.[49,50,51] At the lowest temperatures studied here the framework likely becomes sufficiently rigid that HP ^{129}Xe will be completely precluded from entering the framework.

7.4.3 IRMOF-8

The NMR spectra of ^{129}Xe adsorbed on IRMOF-8 at a series of temperatures are shown in Figure 7.5. The orientation of the linkers in IRMOF-8 is the same as for IRMOF-1 and therefore similar α- and β-cages are present. Both the cage diameters and the window diameters of IRMOF-8 are larger than for IRMOF-1. The ^{129}Xe NMR spectrum at 297 K, which remains relatively constant down to 240 K, reveals that there is a broad ^{129}Xe NMR peak centered at 91 ppm with a width-at-half-height of 900 Hz. This chemical shift is less than that observed for IRMOF-1 suggesting that unlike IRMOF-7, the chemical shift is related more strongly to changes in pore dimension than to changes in Xe exchange dynamics; i.e., the adsorption energies in the various regions of the cage are similar for IRMOF-1 and IRMOF-8.

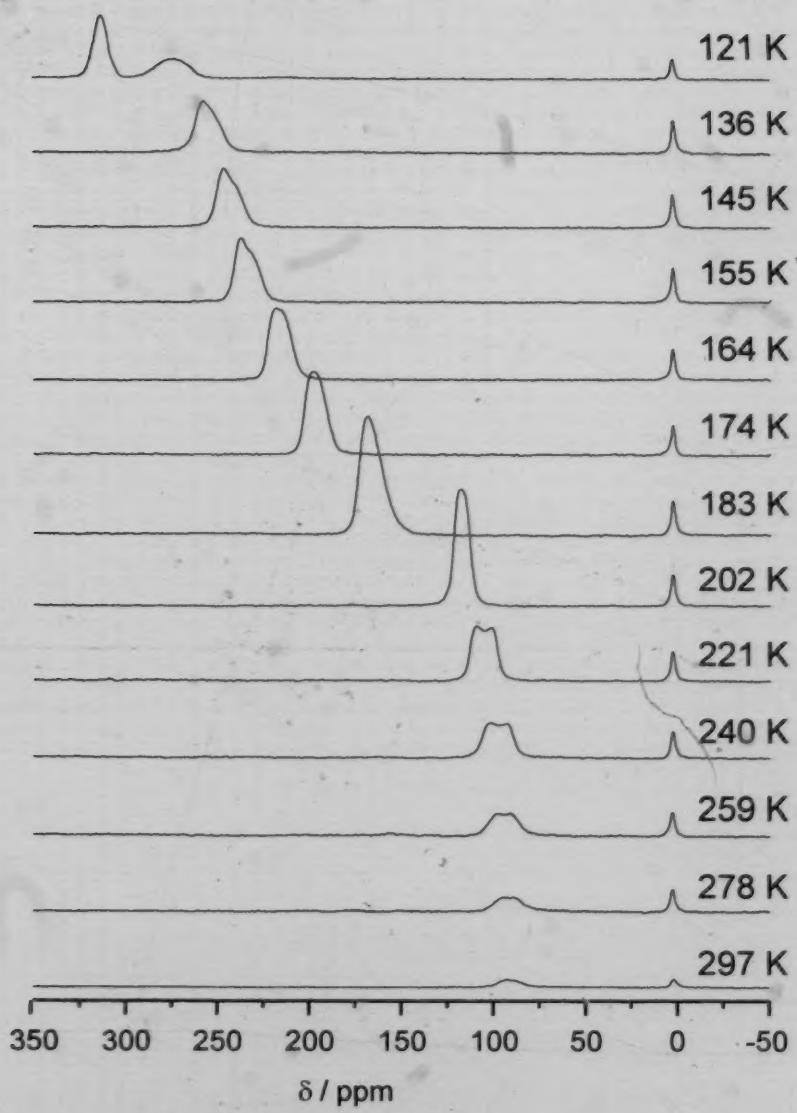

Figure 7.5: ^{129}Xe NMR spectra of HP Xe in IRMOF-8 as a function of sample temperature. Each spectrum is the result of 128 scans.

The peak is split by 9 ppm indicating that there are two distinct adsorption regions in IRMOF-8 with approximately the same populations. Clearly Xe exchange between these two regions is slow at 240 K; according to spectral simulations using the two-site chemical exchange model the exchange rate between the two sites must be slower than

2000 s^{-1};[37] faster exchange would result in a single motionally averaged peak as is observed for IRMOF-1.

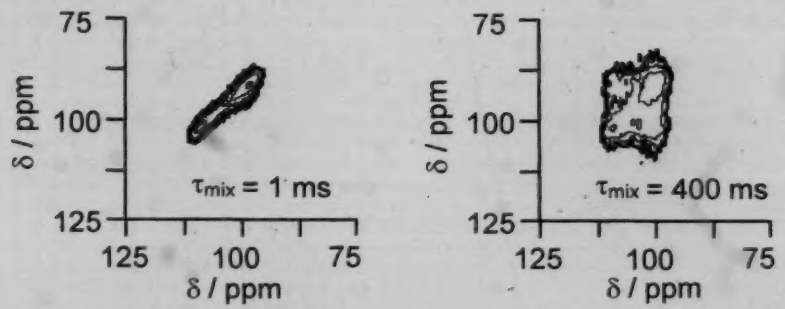

Figure 7.6: The ^{129}Xe NMR EXSY spectra of HP Xe in IRMOF-8 at mixing times of 1 ms and 400 ms.

In order to obtain more information about the rate of exchange between the two sites and to confirm that the two sites are in the same framework and not different crystallites, two-dimensional exchange (EXSY) spectra were acquired. Figure 7.6 shows the spectra acquired at two different mixing times, 1 ms and 400 ms. The spectra indicate that, when the mixing time is 1 ms, there is no exchange between the two sites that give rise to the different ^{129}Xe NMR signals, consistent with the exchange rate being slower than 1000 s^{-1}. However at longer mixing times, *i.e.* 10 ms, cross peaks begin to develop between the two sites. These cross peaks indicate that Xe is exchanging between the two sites during the mixing time. At 400 ms, Figure 7.6, there is significant exchange between the two sites. It should be noted that even at a mixing time of 400 ms no cross-peaks between the peaks from adsorbed Xe and the free gas could be detected, confirming the hypothesis made based on the relatively constant chemical shift values that this exchange is slow, probably on the order of seconds. EXSY experiments at 5 or 6 different mixing times were acquired at 212, 221, 231, and 240 K. By measuring the cross peak intensities as a function of mixing time,[52] and fitting the intensity to a single exponential rate equation, exchange rates as a function of temperature were calculated to be in the range of 10 to 17 s^{-1} for 212 to 240 K, respectively. While the values are only approximate given the difficulty in accurately measuring the cross-peak intensities and the poor signal-to-noise in some of the longer mixing time experiments, the rates showed Arrhenius behavior as a function of temperature. Based on the experiments, an approximate activation energy of 8 ± 3 kJ mol^{-1} could be determined for the exchange

process. Since no exchange was observed with the free gas, it can be concluded that the two peaks arise from Xe in two different environments within the same structure; they could arise from the two types of cages making the measured free energy of activation equivalent to the energy barrier between the α– and β–cages.

As the temperature is lowered below 221 K the peaks begin to shift to higher chemical shift values and the splitting is obscured due to increased line widths caused by Xe-Xe interactions. The chemical shift increases to a value near 257 ppm at 136 K, about 12 ppm greater than was observed for IRMOF-1 at the same temperature. This may result from the ability of IRMOF-8 to accommodate more Xe atoms than IRMOF-1 due to the larger cage dimensions. At 121 K, a peak characteristic of solid Xe is observed; the chemical shift of Xe in the framework is 274 ppm, nearly the same as for IRMOF-1 and consistent with a fully loaded framework.

It was surprising that two sites could be observed in IRMOF-8 but not in IRMOF-1 since the structures are so similar. One possibility is that for IRMOF-1 at temperatures where the exchange is sufficiently slow to allow observation of the two peaks, the splitting is obscured by the peak broadening brought on by increased Xe-Xe interactions.

The thermally polarized ^{129}Xe NMR spectra of a sample of IRMOF-1 sealed under 5 atm of Xe were recorded between 297 and 183 K, this allowed for Xe exchange to be slowed without significantly increasing the Xe loading; the ^{129}Xe NMR peak did shift to slightly higher chemical shifts due to a small increase in Xe loading, 132 ppm at 293 K to 148 ppm at 183 K. The two sites could not be detected within the temperature range accessible; the lowest temperature obtainable using the solution spectrometer temperature controller was 183 K. In order to obtain a lower temperature the spectrum was acquired immediately after removing the sample from liquid nitrogen which it had been submerged in for 16 hrs; the spectrum was acquired at 110.6 MHz. While the exact temperature of the sample is difficult to determine the spectrum did show two peaks split by 9 ppm.

7.4.4 IRMOF-10

IRMOF-10 is the largest and most open framework investigated in this study. The ^{129}Xe NMR spectra of Xe in IRMOF-10 are presented in Figure 7.7. No ^{129}Xe NMR

peaks were observed for Xe adsorbed in the framework above 240 K. At 240 K a small signal is observed at 65 ppm, the intensity of which increases as the temperature is lowered. The chemical shift also increases dramatically as the temperature is lowered approaching a constant value near 122 ppm at 174 K and is relatively constant between 180 and 160 K. The increase in chemical shift between 140 and 183 K is attributed to rapid exchange between Xe in the framework and in the free gas which slows as the temperature is lowered. The chemical shift versus temperature profile can be modeled using a modified form of Henry's law if one assumes only weak adsorption and low Xe loading.[39,40]

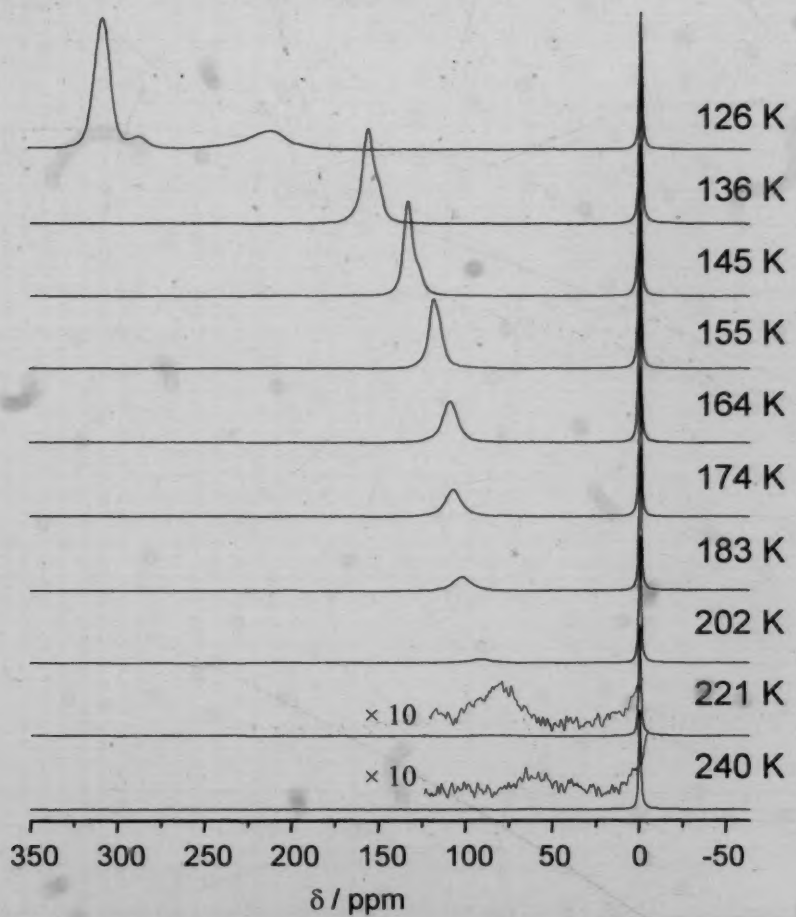

Figure 7.7: The ^{129}Xe NMR spectra of HP Xe in IRMOF-10 as a function of temperature. Each spectrum is the result of 512 scans. The inset spectra is a magnification of the spectra acquired at 240 and 221 K.

In the low loading limit under conditions of rapid exchange between adsorbed Xe and Xe in the free gas the chemical shift, δ, as a function of temperature, *T*, can be expressed as[39,40]

$$\delta = \delta_s / (1 + D/\eta KRT) \qquad 7.2$$

where *D* is the pore diameter, η is dependant on the pore geometry, *K* is Henry's constant, *R* is the gas constant, and δ_s is the chemical shift characteristic of Xe interacting with the framework (δ_s can be thought of as the population weighted average of all the δ values in the different adsorbed sites, δ_A, δ_B, δ_C... in Equation 7.1 and is assumed to be 122 ppm). Henry's constant is also temperature dependant and can be expressed as[39]

$$K = K_0 \exp(\Delta H_{ads} / RT) / \sqrt{T} \qquad 7.3$$

where K_0 is a pre-exponential that is temperature independent, and ΔH_{ads} is the effective heat of adsorption. The full equation for the temperature dependence of the chemical shift rearranged in a linear form is thus[39]

$$\ln\left[\left(\frac{\delta_s}{\delta} - 1\right)T^{1/2}\right] = \ln\left(\frac{D}{RK_0\eta}\right) - \frac{\Delta H_{ads}}{RT} \qquad 7.4$$

Using this model, Equation 7.4 indicates that from a plot of $\ln\left[(\delta_s/\delta - 1)T^{1/2}\right]$ versus $1/T$, a straight line should be obtained with a slope of $\Delta H_{ads}/R$. For IRMOF-10 there are five points in the low loading regime, despite the limited amount of data the plot yields an effective heat of adsorption of 12 ± 2 kJ mol^{-1}. The effective heat of adsorption of CH_4 in IRMOF-10 obtained from simulations which reproduced the experimental adsorption isotherm was 9 kJ mol^{-1}.[12] Since the heats of adsorption for Xe are generally greater than for CH_4 the value obtained here is reasonable; for comparison Xe adsorbed on graphite has a ΔH_{ads} value of 15.6 ± 0.4 kJ mol^{-1}, whereas that of CH_4 is 12.5 ± 1 kJ mol^{-1}.[53]

As mentioned, a relatively constant chemical shift value near 122 ppm is observed between 174 K and 155 K. This chemical shift is the largest observed for Xe in the four IRMOFs studied here. As with IRMOF-7 this value does not follow the usual trend of decreased chemical shift with increased pore size. One possible explanation for the larger chemical shift is that for IRMOF-10 the Xe atoms spend more time in the corners, where the chemical shift of Xe is greater, than in the other regions of the cages; n_{corner} is greater in IRMOF-10 than in either IRMOF-1 or IRMOF-7. This could be a result of the greater separation between the corner sites brought about by the larger linker. The longer linkers could increase the energy barrier for Xe exchange between different corners resulting in Xe atoms spending more time in the corners.

Xe-Xe interactions do not become evident until the temperature is lowered to145 K. As with the other IRMOFs, the chemical shift increases in the low temperature regime but the chemical shift only reaches 170 ppm at 136 K. This value is lower than for the previous samples, indicating that there are less Xe-Xe interaction in IRMOF-10 at 136 K than in the other three samples studied here. This suggests that the average adsorption potential of IRMOF-10 for Xe is weaker than any of the other samples. At the lowest temperature where solid Xe is present the peak from Xe in the framework is only at 227 ppm, indicating that even at this low temperature the framework is not completely filled with Xe atoms.

In the lowest temperature spectrum there is a small ^{129}Xe NMR peak at $\delta \approx$ 290 ppm that does not correspond to pure solid Xe or Xe in the framework. This peak is only 20 ppm away from the solid Xe peak suggesting that this signal may be from Xe frozen between or on the surface of the IRMOF-10 crystallites.

7.4.5 Signal recovery experiment

In the variable temperature ^{129}Xe NMR experiments it was apparent that at lower temperatures the signal intensity of the peak from adsorbed Xe decreased despite increased Xe loading. Hyperpolarization of the ^{129}Xe nuclei means that if $\pi/2$ excitation pulses are used, hyperpolarized ^{129}Xe nuclei can only be "observed" once.[19] Therefore, if the Xe atoms are not replaced by freshly polarized ^{129}Xe nuclei from the optical pumping system, no signal enhancement will be observed when signal averaging is performed; the

experiments were typically conducted with an experimental recycle time of 1.0 s. If the rate at which Xe adsorbed in the framework can exchange with the free gas is significantly longer than 1.0 s, a loss in signal is expected, proportional to the exchange rate at a given temperature. This also means that the rate at which the HP ^{129}Xe is replenished, k_{rep}, can be determined by monitoring the signal intensity as a function of the experimental pulse delay. The signal intensity obtained will be lower if the pulse delay is below the replenishment time, $t_{rep} = 1/k_{rep}$. If the experimental recycle time is long enough, all of the de-polarized ^{129}Xe atoms in the solid can be replaced by freshly hyperpolarized ^{129}Xe and the signal intensity will be at a maximum. At long recycle delays the signal intensity may be reduced because of the ^{129}Xe T_1 but this is unlikely to become important unless there are paramagnetic impurities in the framework.

The signal intensity curves as a function of pulse delay were recorded for all the samples at a minimum of 7 different temperatures and fit with single exponentials. Overall the replenishment time, t_{rep}, varied from 0.2 to 13 seconds. Due to the influence that crystallite size will have on this replenishment rate, it is meaningless to compare the rates between different samples. However, the temperature dependence of the rates should not depend on the crystallite size and therefore plots of the rates as a function of temperature should provide some valuable information. When plots of $\ln(1/t_{rep})$ versus $1/T$ were made the data showed a linear dependence. The activation energies obtained from these Arrhenius plots were 3.5 kJ mol^{-1} for IRMOF-1, 5.5 kJ mol^{-1} for IRMOF-7, 7.2 kJ mol^{-1} for IRMOF-8 and 9.4 kJ mol^{-1} for IRMOF-10; errors are estimated to be on the order of 1 to 2 kJ mol^{-1}.

The activation energies are all below the expected heats of adsorption for these materials. In addition, the order of the activation energies does not follow the expected ordering of the heats of adsorption based on the results for CH_4 adsorbed on IRMOF-1, IRMOF-8, and IRMOF-10.[12] This indicates that the rate of replenishment is not determined by the heat of adsorption but by some other activation energy barrier. The close correlation between the activation energy measured in this experiment and that obtained from the EXSY experiment for IRMOF-8 suggests that the energy that determines the replenishment rate may be the cage-to-cage jump activation energy,

although given the errors associated with the two experiments, this result may be fortuitous.

7.5 Conclusions

We have used continuous-flow HP ^{129}Xe NMR spectroscopy to compare the Xe adsorption characteristics of four iso-reticular metal-organic frameworks, IRMOF-1, 7, 8, and 10. All four samples show similar patterns in their temperature dependent ^{129}Xe NMR spectra and, based on the onset of Xe-Xe interaction which correspond to Xe loadings in excess of one Xe per cage, reveal that in general the effective heats of adsorption can be ranked IRMOF-1 $\approx$ IRMOF-7 > IRMOF-8 > IRMOF-10. Only IRMOF-10 showed significant exchange of Xe between the adsorbed and free gas states; analysis of the ^{129}Xe chemical shift as a function of temperature in the low loading regime of IRMOF-10 reveals an effective heat of adsorption of 12 ± 2 kJ mol^{-1}.

There is no obvious relationship between the cage size and the Xe chemical shift in the four IRMOFs, indicating that the ^{129}Xe chemical shift is determined not only by the geometry of the material but also significantly by the exchange of Xe between different adsorption sites within the pores. The exchange processes will be dictated by the potential energy surface for Xe within the framework. One type of exchange is the two site exchange between the α- and β-cages in IRMOF-1, 8, and 10. For IRMOF-8 peaks from Xe in these two cages could be resolved and an approximate activation energy for the exchange could be determined using EXSY experiments, 8 ± 3 kJ mol^{-1}. IRMOF-7 is unique among the samples studied here in that at low temperatures Xe is blocked from entering the framework, most likely due to reduced motion of the naphthalene linker which effectively blocks access to the cages by Xe.

Finally the process of Xe replenishment can be connected to the diffusion of Xe within the solid rather than the effective heats of adsorption. The activation energy for this process may correspond to the activation energy for the cage-to cage exchange. These results provide initial information about the adsorption of Xe in IRMOFs and illustrate how ^{129}Xe NMR can be used to obtain information about the adsorption process in these potentially important materials.

[1] Rosi, N. L.; Eckert, J.; Eddaoudi, M.; Vodak, D. T.; Kim, J.; O'Keeffe M.; Yaghi, O. M. *Science* **2003**, *300*, 1127-1129.

[2] Chae, H. K.; Siberio-Pérez, D. Y.; Kim, J.; Go, Y.; Eddaoudi, M.; Matzger, A. J.; O'Keeffe, M.; Yaghi, O. M. *Nature* **2004**, *427*, 523-527.

[3] Yaghi, O. M.; O'Keeffe, M.; Ockwig, N. W.; Chae, H. K.; Eddaoudi, M.; Kim, J. *Nature* **2003**, *423*, 705-714.

[4] Rowsell, J. L. C.; Spencer, E. C.; Eckert, J.; Howard, J. A. K.; Yaghi, O. M. *Science* **2005**, *309*, 1350-1353.

[5] Rowsell, J. L. C.; Eckert, J.; Yaghi, O. M. *J. Am. Chem. Soc.* **2005**, *127*, 14904-14910.

[6] Yaghi, O. M. World Intellectual Property Organization Patent, WO 02/088148 A1, November 7, 2002.

[7] Li, H.; Eddaoudi, M.; O'Keeffe, M.; Yaghi. O. M. *Nature* **1999**, *402*, 276-279.

[8] Eddaoudi, M.; Li H.; Yaghi, O. M. *J. Am. Chem. Soc.* **2000**, *122*, 1391-1397.

[9] Eddaoudi, M.; Kim, J.; Rosi, N.; Vodak, D.; Wachter, J.; O'Keeffe, M.; Yaghi, O. M. *Science* **2002**, *295*, 469-472.

[10] Düren, T.; Sarkisov, L.; Yaghi, O. M.; Snurr, R. Q. *Langmuir* **2004**, *20*, 2683-2689.

[11] Mueller, T.; Ceder, G. *J. Phys. Chem. B* **2005**, *109*, 17974-17983.

[12] Düren, T. Snurr, R. Q. *J. Phys. Chem. B* **2004**, *108*, 15703-15708.

[13] Garberoglio, G.; Skoulidas A. I.; Johnson, J. K. *J. Phys. Chem. B.* **2005**, *109*, 13094-13103.

[14] Bordiga, S.; Vitillo, J. G.; Ricchiardi, G.; Regli, L.; Cocina, D.; Zecchina, A.; Arstad, B.; Bjørgen, M.; Hafizovic, J.; Lillerud, K. P. *J. Phys. Chem. B* **2005**, *109*, 18237-18242.

[15] Sagara, T.; Klassen J.; Ganz, E. *J. Chem. Phys.* **2004**, *121*, 12543-12547.

[16] Skoulidas A. I.; Sholl D. S. *J. Phys. Chem. B* **2005**, *109*, 15760-15768.

[17] Mulder, F. M.; Dingemans, T. J.; Wagemaker M.; Kearley G. *J. Chem. Phys.* **2005**, *317*, 113-118.

[18] Ratcliffe, C. I. *Annu. Rep. NMR Spectrosc.* **1998**, *36*, 123-221.

[19] Goodson, B. M. *J. Magn. Reson.* **2002**, *155*, 157-216.

[20] Bonardet, J. L.; Fraissard, J.; Gédéon A.; Springuel-Huet, M. A. *Catal. Rev.-Sci. Eng.* **1999**, *41*, 115-225.

[21] Springuel-Huet, M. A.; Bonardet J. L.; Fraissard, J. *Appl. Magn. Reson.* **1995**, *8*, 427-456.

[22] Barrie P. J.; Klinowski, J. *Prog. Nucl. Magn. Reson. Spectrosc.* **1992**, *24*, 91-108.

[23] Brunner, E. *Magn. Reson. Chem.* **1999**, *37*, S14-S22.

[24] Pietraß, T. *Magn. Reson. Rev.* **2000**, *17*, 263-337.

[25] Moudrakovski, I. L.; Soldatov, D. V.; Ripmeester, J. A.; Sears D. N.; Jameson, C. J. *Proc. Natl. Acad. Sci. USA* **2004**, *101*, 17924-17929.

[26] Jameson, C. J. *J. Chem. Phys.* **2002**, *116*, 8912-8929.

[27] Ripmeester J. A.; Ratcliffe, C. I. *J. Phys. Chem.* **1995**, *99*, 619-622.

[28] Sozzani, P.; Comotti, A.; Simonutti, R.; Meersmann, T.; Logan J. W.; Pines, A. *Angew. Chem. Int. Ed.* **2000**, *39*, 2695-2698.

[29] Meersmann, T.; Logan, J. W.; Simonutti, R.; Caldarelli, S.; Comotti, A.; Sozzani, P.; Kaiser L. G.; Pines A. *J. Phys. Chem. A* **2000**, *104*, 11665-11670.

[30] Sears D. R.; Klug, H. P. *J. Chem. Phys.* **1962**, *37*, 3002-3006.

[31] Sears, D. N.; Demko, B. A.; Ooms, K. J.; Wasylishen R. E.; Huang, Y. *Chem. Matter.* **2005**, *17*, 5481-5488.

[32] Huang, L.; Wang, H.; Chen, J.; Wang, Z.; Sun, J.; Zhao D.; Yan, Y. *Microporous Mesoporous Mater.* **2003**, *58*, 105-114.

[33] Greathouse J. A.; Allendorf, M. D. *J. Am. Chem. Soc.* **2006**, 128, 10678-10679.

[34] Gonzalez, J.; Devi, R. N.; Tunstall, D. P.; Cox P. A.; Wright, P. A. *Microporous Mesoporous Mater.* **2005**, *84*, 97-104.

[35] Ooms, K. J.; Campbell, K.; Tykwinski, R. R.; Wasylishen, R. E. *J. Mater. Chem.* **2005**, *15*, 4318-4327.

[36] This assumes that the effective Xe T_2 in the gas is 0.004 s as estimated from the ^{129}Xe NMR line width of the Xe gas when not in exchange with an adsorbed site. The Xe T_2 in the adsorbed site is on the order of 0.002 s which was estimated based on the FID decay rate, and the population ratio is greater than 5 Xe atoms adsorbed for every Xe in the gas.

[37] Sandström, J. *Dynamic NMR Spectroscopy*, Academic Press: London, 1982.

[38] Harris, R. K. *Nuclear Magnetic Resonance Spectroscopy*, Pitman Books Ltd.: London, 1983.

[39] Terskikh, V. V.; Mudrakovski I. L.; Mastikhin, V. M. *J. Chem. Soc. Faraday Trans.* **1993**, *89*, 4239-4243.

[40] Moudrakovski, I. L.; Terskikh, V. V.; Ratcliffe, C. I.; Ripmeester, J. A.; Wang, L.; Shin Y.; Exarhos, G. J. *J. Phys. Chem. B* **2002**, *106*, 5938-5946.

[41] Terskikh, V. V.; Moudrakovski, I. L.; Breeze, S. R.; Lang, S.; Ratcliffe, C. I.; Ripmeester J. A.; Sayari, A. *Langmuir* **2002**, *18*, 5653-5656.

[42] Nossov, A.; Haddad, E.; Guenneau F.; Gédeon, A.*Phys. Chem. Chem. Phys.* **2003**, *5*, 4473-4478.

[43] Jameson C. J.; de Dios, A. C. *J. Chem. Phys.* **2002**, *116*, 3805-3821.

[44] Moudrakovski, I. L.; Ratcliffe C. I.; Ripmeester, J. A. *J. Am. Chem. Soc.* **1998**, *120*, 3123-3132.

[45] Pluth J. J.; Smith, J. V. *J. Am. Chem. Soc.* **1980**, *102*, 4704-4708.

[46] Jameson, C. J.; Jameson, A. K.; Gerald R., II; de Dios, A. C. *J. Chem. Phys.* **1992**, *96*, 1676-1689.

[47] Terskikh, V. V.; Moudrakovski, I. L.; Du, H.; Ratcliffe, C. I.; Ripmeester, J. A. *J. Am. Chem. Soc.* **2001**, *123*, 10399-10400.

[48] Moudrakovski, I. L.; Nossov, A.; Lang, S.; Breeze, S. R.; Ratcliffe, C. I.; Simard, B.; Santyr G.; Ripmeester, J. A. *Chem. Mater.* **2000**, *12*, 1181-1183.

[49] Brouwer, E. B.; Enright, G. D.; Udachin, K. A.; Lang, S.; Ooms, K. J.; Halchuk P. A.; Ripmeester, J. A. *Chem. Commun.* **2003**, 1416-1417.

[50] Atwood, J. L.; Barbour L. J.; Jerga, A. *Angew. Chem. Int. Ed.* **2004**, *43*, 2948-2950.

[51] Dobrzańska, L.; Lloyd, G. O.; Raubenheimer H. G.; Barbour, L. J. *J. Am. Chem. Soc.* **2006**, *128*, 698-699.

[52] The intensities used for the analysis were the maximum peak heights rather than the integrated peak intensities. The total intensity from the measured peaks was scaled to one at all temperatures and for all mixing times; the cross-peak intensity was expressed as a fraction of the total intensity. Plots of relative cross-peak intensity, *I*,

as a function of mixing time were then fit to a simple rate equation, $I = C[1 - \exp(\tau_{mix} / \tau_{ex})]$, where C is a scaling constant, τ_{mix} is the mixing time and τ_{ex} is the characteristic exchange time at a given temperature

[53] Vidali, G.; Ihm, G.; Kim H.-Y.; Cole, M. W. *Surf. Sci. Rep.* **1991**, *12*, 133-181.

Chapter 8: Concluding remarks

In this thesis, HP ^{129}Xe has been used to investigate the pores and Xe adsorption properties of a variety of inorganic, organic, and metal-organic materials. The goal has been to answer questions regarding the presence of accessible porosity, the general size of the pores and, more specifically, the geometry of the pores and dynamics of Xe within them. Answers to these questions provide vital information to chemists that can help determine the possible application of new materials for gas adsorption and separation processes. While many of the conclusions arrived at in this thesis are of a qualitative nature, the extensive knowledge of ^{129}Xe NMR developed over the past thirty years has allowed physical models to be proposed both for the structure of the porous materials and timescale for Xe exchange within the pores of the materials, which could not be arrived at using alternative techniques.

In Chapter 3, the construction and operation of an optical-pumping spin-exchange system has been described and was used to produce HP ^{129}Xe. This technique has allowed ^{129}Xe NMR experiments to be performed on sample quantities as small as 15 mg using low partial pressures of Xe gas. Xe-129 NMR spectra were acquired with sample temperatures ranging from 126 K to 373 K. The ability to perform experiments at low temperature allows for large Xe loadings to be achieved using the low pressure HP ^{129}Xe.

In Chapter 4 the formation of $AlPO_4$-18 has been studied using HP ^{129}Xe NMR spectroscopy. The ^{129}Xe NMR spectra acquired on samples at different stages in the formation process reveal that $AlPO_4$-18 forms *via* intermediate porous structures. First an amorphous mesoscale porous system is formed, followed by the formation of the 1-D channels of $AlPO_4$-5 and finally the $AlPO_4$-5 structure is converted to $AlPO_4$-18. The use of 2-D exchange spectroscopy to study an intermediate sample has provided insight into the connectivity of the $AlPO_4$-5 and $AlPO_4$-18 structures, revealing that the two phases are in contact.

The studies of porous macrocycles presented in Chapters 5 and 6 represent an ideal approach to the integration of ^{129}Xe NMR spectroscopy and synthetic chemistry. In collaboration with the Tykwinski research group, this research has been able to provide information about the presence and nature of porosity in eight different organic and

metal-organic macrocycles. The ability to acquire spectra on milligram quantities of sample has meant that ^{129}Xe NMR spectroscopy can be used as a part of the synthetic development of such materials and not only as a post-synthetic characterization technique. HP ^{129}Xe NMR also offers unique opportunities for determining porosity and characterizing the size of pores for materials that do not exhibit discernible channels based on the X-ray crystallography. These studies have demonstrated that all eight macrocycles studied are porous, the solvent cavities created when co-crystalized solvent is removed from the solid provides locations for Xe adsorption, and for many of the samples Xe can penetrate into tightly confined pore spaces in the solid.

Studies of metal-organic frameworks have been presented in Chapter 7 for IRMOFs-1, -7, -8, and -10. The ^{129}Xe NMR spectra reveal the complex interplay between the chemical shift, pore size and geometry, and the exchange averaging of the Xe over the porous environment. Based on the changes in chemical shift as a function of temperature relative adsorption energies have been estimated. Experiments that offer information about Xe exchange and diffusion have suggested that the diffusion of Xe through the material is not controlled by the average adsorption energy but by some other process, probably associated with cage-to-cage exchanges.

The application of ^{129}Xe NMR spectroscopy to the study of porous materials is entering a new and powerful period. This is evidenced by the continued publication of studies using ^{129}Xe NMR to explore new material and the existence of a specialized ^{129}Xe NMR conference, XeMAT. The knowledge gained over the past thirty years by studying the interaction of Xe with well ordered inorganic and organic porous materials has provided a basic understanding of the processes involved in determining the ^{129}Xe chemical shifts. The challenge in the coming years is to take this knowledge and extend the utility of ^{129}Xe NMR to study more complex porous systems and pores for which the structure can not be determined using other techniques. The results presented in this thesis provide a step in that direction. Clearly ^{129}Xe NMR spectroscopy holds a unique place in the characterization of materials as it can provide both general measurements and more specific atomic level information about any material that can absorb Xe atoms.

Chapter 9: Future and Ongoing Research

Based on the work presented here, ongoing and future research in our lab utilizing HP ^{129}Xe NMR spectroscopy could take a number of different directions. Some of these directions will be highlighted here.

9.1 Continued studies of metal-organic frameworks

The four MOF samples studied in this thesis represent only a small fraction of the MOFs currently in the literature. On an almost weekly basis new porous materials are being reported based on the coordination of organic linker molecules to metal centers. Clearly, very few of the materials can be examined to the extent that some of the IRMOFs have been studied using a wide range of experimental and theoretical techniques. It has been shown that HP ^{129}Xe NMR is an efficient method for characterizing the void space and guest dynamics in these materials. Therefore, ^{129}Xe NMR spectroscopy could serve as a valuable cornerstone technique for characterizing these materials.

The study of functionalized MOFs using ^{129}Xe NMR spectroscopy could prove insightful. An example of a functionalized MOF is IRMOF-2, which has the same structure as IRMOF-1 but has 2-bromo-1,4-benzendicarboxylic acid as the linker. Initial ^{129}Xe NMR spectra, Figure 9.1, indicate a very similar temperature behavior as when IRMOF-1 served as the host. Interestingly, the ^{129}Xe chemical shifts appear to be smaller than IRMOF-1, possibly suggesting that adsorption sites that are less deshielding are more important in IRMOF-2 than IRMOF-1, i.e., adsorption along the linkers which could become more important due to the presence of the Br. Further studies into the stability and degradation of MOFs and IRMOFs using HP ^{129}Xe, thermally polarized ^{129}Xe, and ^{13}C NMR spectroscopy are also warranted.

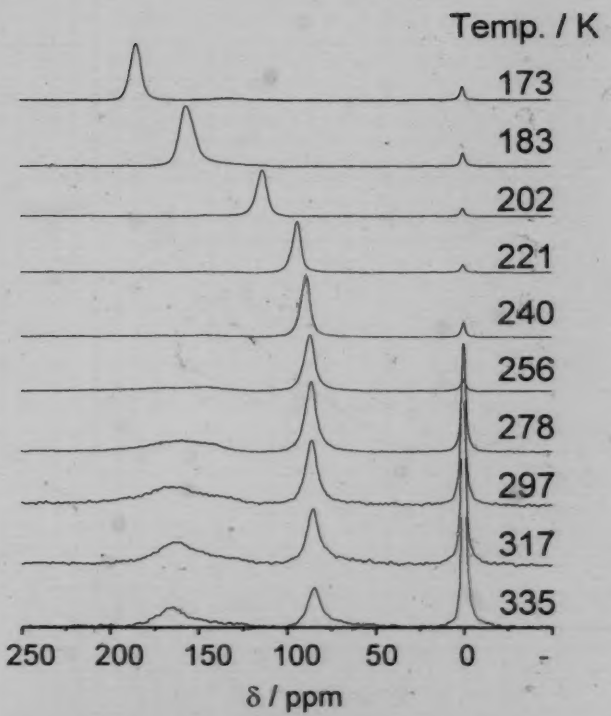

Figure 9.1: Variable temperature ^{129}Xe NMR spectra of HP ^{129}Xe in IRMOF-2. It is unclear if the High frequency peaks near 180 ppm is from impurities or the sample.

Of particular interest are MOFs prepared with paramagnetic metal centers.[1,2,3] These materials are often structurally analogous to diamagnetic MOFs. It is unclear how the presence of paramagnetic centers will affect the ^{129}Xe NMR spectrum. Some previous results have shown that broad peaks can be expected but further work in this area would be of both fundamental and practical interest.[4,5,6] Recent results of Jameson using GCMC simulations of Xe in model paramagnetic channels have revealed that the paramagnetic centers should influence the ^{129}Xe NMR signal.[7] The lineshapes obtained for Xe in one-dimensional paramagnetic channels are predicted to be reversed compared to Xe in diamagnetic analogues, with the paramagnetic shift of the unique component of the shielding tensor shifted to lower δ values. My attempts to prepare and analyze a paramagnetic Ni analogue of IRMOF-1 have as yet proven unsuccessful.

9.2 HP ^{129}Xe NMR of titanosilicates

An interesting class of porous inorganic materials is composed of SiO_4 tetrahedra and TiO_6 octahedra and has been given the general name Englehard Titanosilicates, ETS. One structure formed undergoes distortions in the framework dimensions as a function of both temperature and heat treatment.[8,9] These materials, the model compound being termed strontium-ETS-4, should be able to adsorb Xe gas. Xe-129 NMR as a function of temperature should prove capable of registering the change is structure that occurs during heating. Also ^{129}Xe NMR will be able to differentiate the variations in pore size as a function of heat treatment.

ETS-10 is another titanosilicate that has shown interesting gas adsorption properties due to its three-dimensional pore structure.[10] Previous ^{129}Xe NMR studies of ETS-10 have illustrated the sensitivity of the Xe chemical shift to the counter ions included in the structure.[11] Initial ^{129}Xe NMR studies show the expected axially symmetric line shape. Of particular interest is the adsorption properties of ETS-10 with Ag metal clusters included in or on the framework. Initial adsorption studies indicate an extremely high Xe adsorption potential, on the order of 50 kJ mol^{-1}! Xe-129 NMR studies of the Na/K and Ag-cluster ETS-10 should provide valuable information about the interaction between the Xe gas and the host framework. Fu Chen will be continuing this research.

9.3 HP ^{129}Xe NMR studies of clays and minerals

Many naturally occurring minerals and clays are porous and can act as gas adsorption materials. Some of these solids, such as montmorillonite and mordenite, have been previously studied using HP and thermally polarized ^{129}Xe NMR spectroscopy.[12,13] Many types of clay are micro-crystalline or amorphous and therefore their structure can not be determined using single crystal X-ray diffraction. Consequently, any other technique that can provide structural information is extremely valuable. As has been

shown in this thesis and the literature, ^{129}Xe NMR spectroscopy is an invaluable tool for studying pore space.

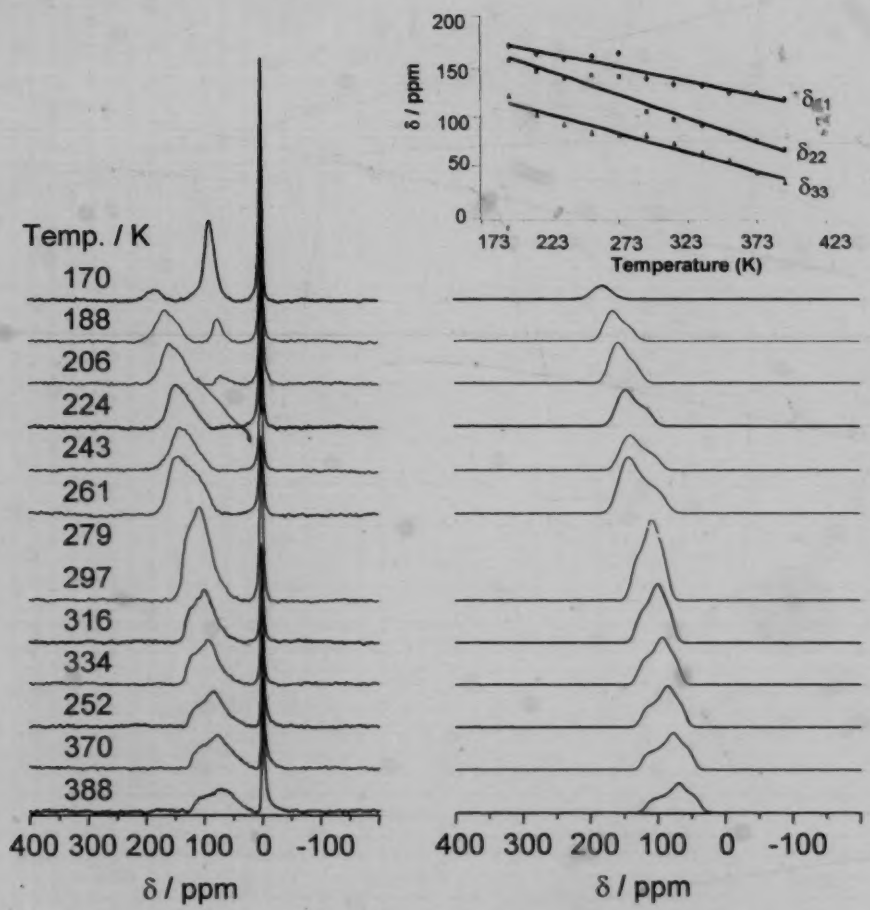

Figure 9.2: Left) ^{129}Xe NMR spectra as a function of temperature of HP Xe in sepiolite. Right) simulations of the ^{129}Xe NMR lineshapes. Inset) plots of the principal components of the ^{129}Xe chemical shift tensor as a function of temperature.

Initial studies performed on the porous mineral sepiolite, provided by Dr. Christian Detellier of the University of Ottawa, have shown promise for determining unique information about the structure of the solid. Figure 9.2 shows initial variable temperature ^{129}Xe NMR spectra of HP ^{129}Xe in sepiolite. The change in lineshape of the main adsorption peak is intriguing and either correlates to increases in Xe loading as the temperature is decreased or changes in the framework structure. Further studies of this

material are warranted in order to determine the origin of the line shape changes. The low frequency peak observed at low temperature likely arises from Xe atoms that sample the channels on the surface of the crystallites and are in fast exchange with Xe in the free gas.

9.4 Development of a variable pressure NMR probe for thermally polarized ^{129}Xe NMR studies

In many cases it is desirable to perform thermally polarized ^{129}Xe NMR experiments when adequate amounts of sample are available. The value of these experiments arises from the ability to control Xe loadings accurately using the pressure of Xe gas. To conduct such experiments porous samples are typically sealed in glass tubes at different pressures of Xe gas. This can however be time consuming if many pressures are desired or if the preparation of large amounts of sample is required. An alternative is to develop an NMR probe that can change the partial pressure of Xe using the same sample. A Bruker 7 mm double resonance MAS probe has been modified to house a pressure cell that can be used to hold the sample and allow pressures in the cell to be changed and monitored, see Appendix C. The pressure cell is designed to be attached to a Xe gas cylinder and the pressure can be adjusted using separate inlet and outlet gas lines that extend out of the bottom of the probe. A pressure sensor is connected along the stainless steal tubes to monitor the pressure. The cell has been tested up to 10 atm of pressure. Tests are underway to investigate the stability of the pressures over long acquisition times and difficulties with the coil electronics are currently unresolved.

---

[1] Kim, J.; Chen, B.; Reineke, T. M.; Li, H.; Eddaoudi, M.; Moler, D. B.; O'Keeffe, M.; Yaghi, O. M. *J. Am. Chem. Soc.* **2001**, *123*, 8239-8247.

[2] Chen, X.-Y.; Zhao, B.; Shi, W.; Xia, J.; Cheng, P.; Liao, D.-Z.; Yan, S.-P.; Jiang, Z.-H. *Chem. Mater.* **2005**, *17*, 2866-2874.

[3] Férey, G.; Mellot-Draznieks, C.; Serre, C.; Millange, F.; Dutour, J.; Surblé, J.; Margiolaki, I. *Science* **2005**, 23, 2040-2042.

[4] Soldatov, D. V.; Ripmeester, J. A. *Stud. Surf. Sci. Catal.* **2002**, *141*, 353-362.

[5] Soldatov, D. V.; Moudrakovski, I. L.; Ratcliffe, C. I.; Dutrisac, R.; Ripmeester, J. A. *Chem. Mater.* **2003**, *15*, 4810-4818.

[6] Böhlmann, W.; Pöppl, A.; Sabo, M.; Kaskel, S. *J. Phys. Chem. B.* **2006**, *110*, 20177-20181.

[7] Jameson, C. J. results presented at *XeMAT3*, **2006**, Ottawa, Canada.

[8] Kuznicki, S. M.; Bell, V. A.; Nair, S.; Hillhouse, H. W.; Jacubinas, R. M.; Braunbarth, C. M.; Toby, B. H.; Tsapatsis, M. *Nature*, **2001**, *421*, 720-724.

[9] Nair, S.; Tsapatsis, M.; Toby, B. H.; Kuznicki, S. M. *J. Am. Chem. Soc.* **2001**, *123*, 12781-12790.

[10] Anderson, M. W.; Terasaki, O.; Phsuna, T.; Philippou, A.; MacKay, S. P.; Ferreire, A.; Rocha, J.; Lidin, S. *Nature*, **1994**, *367*, 347-351.

[11] Yang, X.; Truitt, R. E. *J. Phys. Chem.* **1996**, *100*, 3713-3718.

[12] Moudrakovski, I. L.; Nossov, A.; Lang, S.; Breeze, A. R.; Ratcliffe, C. I.; Simard, B.; Santyr, G.; Ripmeester, J. A. *Chem. Mater.* **2000**, *12*, 1182-1183.

[13] Ripmeester, J. A. *J. Am. Chem. Soc.* **1982**, *104*, 290-291.

Appendix A: Optical-pumping spin-exchange apparatus: safety considerations

There are a number of sources of danger when using the optical-pumping spin-exchange apparatus.

A.1 Laser safety

The laser is a 60 W diode laser that emits light between 792 and 798 nm. The beam divergence from the source of the laser light, through the polarizer, to the cell is approximately 4 cm m^{-1}. Despite the large divergence the laser light hitting the cell has enough power to burn combustibles and to do serious damage to eyes and skin, Laser safety glasses must be worn whenever the laser is on. The beam path is contained within the matte black stainless steal casing that surrounds the apparatus. There are very few times that the operator is exposed to the laser beam under normal operating conditions (the only time under normal circumstances is during initial laser alignment). The only reason for opening the cover door on the laser chamber is to open and close the Rb well/optical cell valves. When the door is open the laser must be turned off to avoid any chance of harm to the operator. The operator should avoid looking into any of the holes in the casing or the open end of the chamber; a possible exception is during the alignment of the laser.

Before operating the laser, all users must first obtain laser eye exams and undergo a 30 min trainings session with the Department of Health and Safety of the University of Alberta (contact Carl Schumaker at Health and Safety for more information: carl.schumaker@ehs.ualberta.ca).

A.2 Electronics safety

This is a high-power laser and as such there are considerable risks of electric shock if the laser unit is mishandled. Under no circumstances should the operator ever open the laser or polarizer cases. A proper CO_2 extinguisher should be used in case of an electrical fire. The operator should note the general condition of the laser unit and cords before powering up the laser.

A.3 Rubidium safety

The Rb well is the most error prone and dangerous part of the apparatus for two reasons. First, the Rb well/optical cell is covered by heaters so it is difficult to inspect the condition of the glass before start up. Second, rubidium is extremely sensitive to moisture; any serious exposure to the air will cause the rubidium to ignite, blowing up the cell and well and lighting combustibles on fire. Care must be taken whenever the Rb well/optical cell is being opened or closed. This is the most dangerous time of operation because the door to the protective case is open and too much pressure applied while turning the valves could cause the glass of the apparatus to crack; always open these valves very slowly. The face shield should be worn whenever the metal casing surrounding the apparatus is open. If the user is unsure of what to do, they should consult with someone who has been trained to operate the apparatus.

During operation the stainless steal casing should be closed which will protect the operator from any explosions that may occur. However, the operator should be aware that this also may hide problems in laser alignment or the cell performance. The user should always be aware of sounds and smells near the apparatus and monitor the adsorption spectrum using the Ocean Optics fiber optic spectrometer to ensure that polarization is stable.

If the Rb is exposed to the air and a fire starts the following procedures should be followed.

1) If the laser is on press the emergency shut off button.
2) If the fire is small use the calcium carbonate (in the plastic container and the big bucket) to extinguish the fire and quickly move the cell to the glove box.
3) Never use water to fight a fire near the apparatus. Rb reacts with H_2O to form H_2 and O_2 while water conducts electricity.
4) Follow standard fire safety procedures. If you are unfamiliar with what to do contact the University Safety Advisor.

A.4 Pressure in the gas lines

The operator must ensure that proper start-up and shut-down procedures have been followed. This will keep the apparatus in good working condition and prevent any pressure explosions.

The glass Rb well/optical cell should be tested up to 120 psi (8.2 atm) before it is filled with Rb. Despite this, under no circumstances should the operator exceed 80 psi of gas pressure in the lines. This should ensure that the cell does not explode.

Be extremely careful when adjusting the pressure at the tank, either during start-up, shut-down or optimization. This is the most likely point at which the operator can over pressurize the lines. The gas flow rate should also be monitored. Extreme jumps in flow could disturb the apparatus. High flow rates can also result in extensive amounts of Rb being swept into and through the optical cell.

A.5 Startup and shutdown checklist

Startup

1) Inspect the system and note any possible safety concerns that may require adjustment of the following procedures.

2) Move the optical pumping cell close to the magnet by pivoting the cart

3) If the system has been idle for an extended period of time and the gas line pressure has dropped below 20 psi, the line will need to be purged. Remove the connection immediately before the Rb well valve.

4) Open all the valves on the line (on either side of the two filters, *not the optical cell/Rb well valves*)

5) Open the Gas cylinder and adjust the pressure to 50 to 70 psi, let gas flow through the line for 5 min to ensure no moisture or O_2 is in the line (only done if the line needs to be purged.

6) Re-attach the line to the Rb well valve while maintaining the pressure in the line.

7) Turn power on to the system (switch is on the power bar)

8) Set heaters to 0 and turn them on.

9) Adjust both heaters until an initial temperature of 80 to 100 °C is reached.

10) Check line pressure to ensure it is at 50 to 70 psi.

11) Open the inlet valve to the Rb well slowly. Bubbling will occur for a short time and should then cease when the pressure equalizes.

12) Open the Optical cell outlet valve.

13) Adjust needle valve until flow is 0.4 on the flow readout

14) Turn on the laser using the keys, adjust power on the laser and align the laser beam as described in the operations section, Chapter 3.

15) The system may take up to 15 min to equilibrate.

Shutdown

1) Turn laser off

2) Turn off heaters and to allow the temperature to decrease to approximately 80 °C

3) Turn off the needle valve, then outlet valve on the optical cell, then the inlet valve on the Rb well.

4) For short periods (overnight or a few days) the rest of the line can be left open at pressure. If left longer the valves should be closed and the gas regulator shut.

5) Power down the system; turn the power bar off.

6) After the system has cooled down check the condition of the optical cell and note any changes or problems.

Above all, it must be remembered that this is a home-built system that is prone to problems particularly in the Rb well/optical cell, see Chapter 3. If for any reason the user feels unsure about the condition of the system, the procedures described here, or problems that may arise during operation it is their responsibility to talk to the person with the most experience in the lab.

Appendix B: Maple script for calculating two-site exchange spectra

This program takes the values Pa and Pb which are the relative populations of the two site sin exchange, T2A and T2B which are the effective T_2 values for the two sites, na and nb which are the chemical shifts (in Hz) of the two peaks and kB which is the exchange rate (in Hz). (C0 is simply a magnitude scale constant for the graph)

This program is based on the equation given on page 14 of *Dynamic NMR Spectroscopy* By J. Sandstrom. Academic Press: London, 1982.

```
restart:
define values
Pa:=1: Pb:=1: T2A:=0.002: T2B:=0.002:na:=0:nb:=500:kB:=1000:C0:=1:

the calculation
dn:=na-nb:Dn:=0.5*(na+nb)-n:t:=Pa/kB:
P:=evalf(t*((1/(T2A*T2B))-4*Pi*Pi*(Dn^2)+Pi*Pi*(dn^2))+(Pa/T2A)+(Pb/T2B)):
Q:=evalf(t*(2*Pi*Dn-Pi*dn*(Pa-Pb))):
R:=evalf(2*Pi*Dn*(1+t*(1/T2A+1/T2B))+Pi*dn*t*(1/T2B-1/T2A)+Pi*dn*(Pa-Pb)):
top:=P*(1+t*(Pb/T2A+Pa/T2B))+Q*R:
v:=C0*top/(P^2+R^2):
plot(v,n=10000..-2000,axes=FRAMED);
```
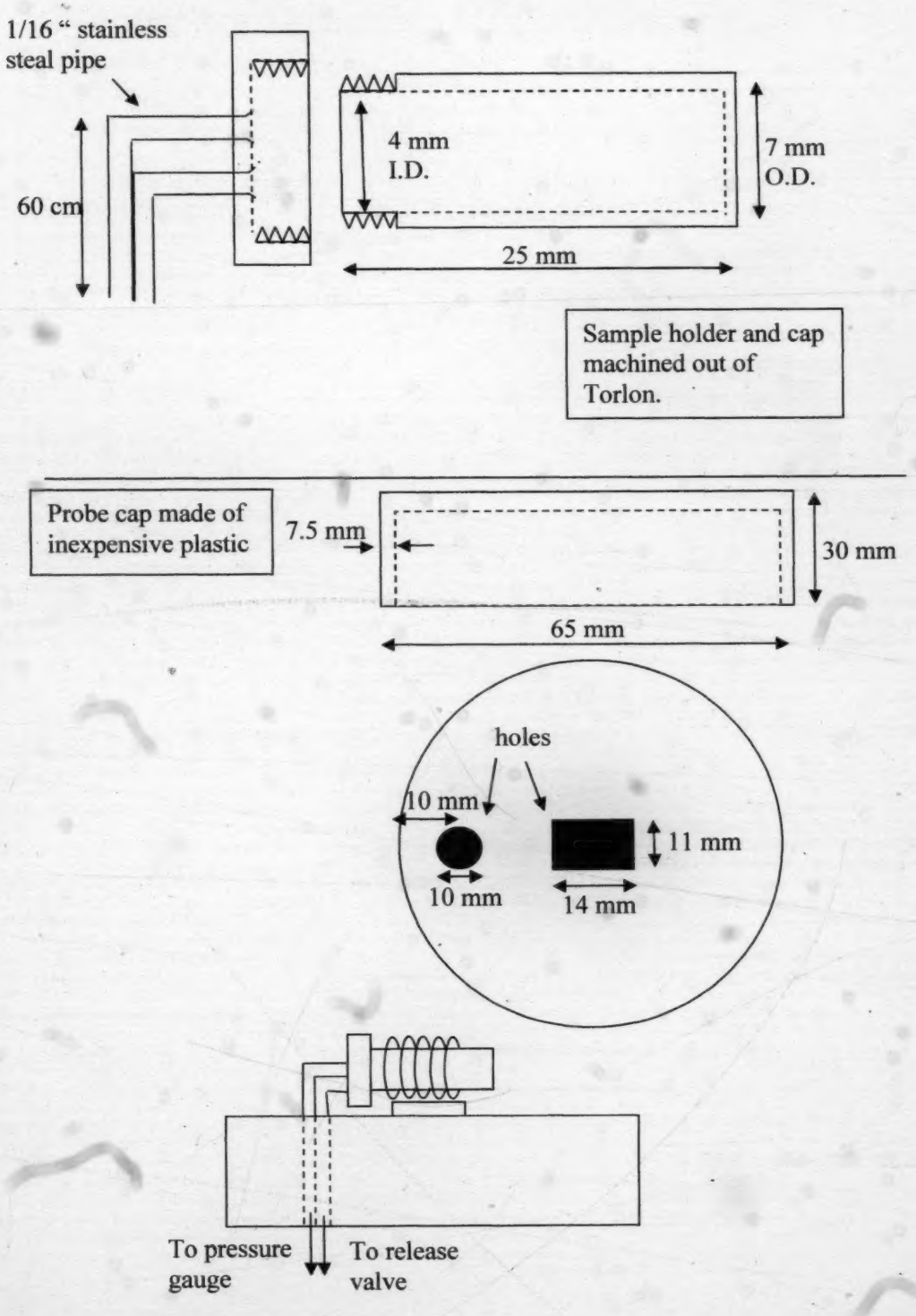
Appendix C: Pressure cell for elevated pressure gas NMR